Doctoral Thesis

Search for Θ^+ pentaquark using a hadron beam at J-PARC

Kotaro Shirotori

Department of Physics, Tohoku University

2011

Abstract

We have searched for Θ^+ via $\pi^- p \to K^- X$ reaction using 1.92 GeV/c π^- beam at the K1.8 beam line of the J-PARC 50 GeV Proton Synchrotron. This experiment was the first experiment in the J-PARC hadron experimental facility. We used the K1.8 beam line spectrometer and the SKS spectrometer both of which have an excellent momentum resolution of $\Delta p/p \sim 10^{-3}$. The SKS spectrometer, which was previously used at KEK, was reconstructed for the J-PARC experiments with new detectors and a new data acquisition system. In the experiment, we irradiated 7.8×10^{10} π^- mesons on the liquid hydrogen target. For the calibration of the spectrometer system, the $\Sigma^\pm$ production data were taken via the $\pi^\pm p \to K^+\Sigma^\pm$ reactions. The missing mass resolution for the Θ^+ is estimated to be 1.4 MeV/c^2 (FWHM) from the $\Sigma^\pm$ data.

In the missing mass spectrum, any prominent peak in the Θ^+ mass region has not been observed. Therefore, we have obtained the upper limit of the production cross section of the $\pi^- p \to K^-\Theta^+$ reaction at the beam momentum of 1.92 GeV/c. The upper limit of the differential cross section averaged for the scattering angle over 2° to 15° in the laboratory frame has been obtained to be 0.2 μb/sr at the 90 % confidence level in the missing mass region of 1.52$-$1.54 GeV/c.

From the results of the present experiment along with the previous experiment at KEK, we found the Θ^+ production cross section using hadron beams of both π^- and K^+ with beam momenta less than 2 GeV/c is quite small. To explain these small cross sections, the width of Θ^+ should be possibly less than several hundred keV/c^2. The high sensitivity of the present experimental result strongly constrains the production mechanism of Θ^+, if it exists.

Contents

1 Introduction **1**
- 1.1 Exotic hadrons . . . 1
- 1.2 The Θ^+ pentaquark baryon . . . 2
- 1.3 Search for Θ^+ using hadron beams . . . 6
  - 1.3.1 Production of Θ^+ . . . 6
  - 1.3.2 Previous experiments: KEK E522 and KEK E559 . . . 10
  - 1.3.3 J-PARC E19 experiment . . . 14

2 Experiment **15**
- 2.1 Outline . . . 15
- 2.2 K1.8 beam line . . . 18
- 2.3 K1.8 beam line spectrometer . . . 25
- 2.4 Scattered-particle spectrometer (SKS) . . . 32
- 2.5 Trigger . . . 40
- 2.6 Data-acquisition system . . . 45
- 2.7 Liquid hydrogen target . . . 47
- 2.8 Data summary . . . 48

3 Data Analysis **50**
- 3.1 Outline . . . 50
- 3.2 Analysis of π^- beam . . . 53
  - 3.2.1 Identification of π^- . . . 53
  - 3.2.2 Beam track reconstruction . . . 54
- 3.3 Analysis of scattered particles . . . 63
  - 3.3.1 Hodoscope cut . . . 63
  - 3.3.2 Momentum reconstruction of scattered particles . . . 66
  - 3.3.3 Particle identification in the SKS . . . 71
- 3.4 Vertex reconstruction . . . 72
- 3.5 Cross section . . . 74
  - 3.5.1 Efficiency . . . 76
- 3.6 Acceptance of SKS . . . 89
- 3.7 Background . . . 92
  - 3.7.1 Empty target data . . . 92
  - 3.7.2 Associated reactions . . . 94
- 3.8 The Σ production cross section . . . 96

3.9 Systematic errors 98
3.10 Energy precision and resolution 99
3.11 Missing mass resolution 108

4 Experimental results and discussion **110**
4.1 Missing mass spectrum of the $\pi^- p \to K^- \Theta^+$ reaction 110
4.2 Upper limit of production cross section 112
4.3 Discussion 116

5 Conclusion **117**

A Field map calculation **121**

B Efficiency time dependence **130**

List of Figures

1.1 The anti-decuplet of baryons with $J^P = 1/2^+$ by chiral soliton model. . . 2
1.2 The first reported Θ^+ spectrum by the LEPS collaboration. 3
1.3 The updated experimental result reported by the LEPS collaboration in 2009. 4
1.4 Diagrams for the $\pi^- p \to K^- \Theta^+$ reaction and the $K^+ p \to \pi^+ \Theta^+$ reaction. 7
1.5 Calculated cross sections for the $\pi^- p \to K^- \Theta^+$ reaction. 8
1.6 Differential cross section of the $K^+ p \to \pi^+ \Theta^+$ reaction calculated at $\sqrt{s}$ = 2.4 GeV 9
1.7 The cross section of the $\pi^- p \to K^- \Theta^+$ reaction using the small coupling constant of $g_{K^* N \Theta}$. 10
1.8 The missing mass spectrum of the $\pi^- p \to K^- \Theta^+$ reaction at the beam momentum of 1.92 GeV/c obtained in the KEK-E522 experiment. 11
1.9 The missing mass spectrum of the $K^+ p \to \pi^+ \Theta^+$ reaction at the beam momentum of 1.2 GeV/c obtained in the KEK-E559 experiment. 13

2.1 A schematic view of J-PARC 16
2.2 The schematic view of hadron experimental facility (Phase-1). 17
2.3 The schematic view of K1.8 Beam line. 19
2.4 The upstream section. 20
2.5 The mass separation section. 21
2.6 Typical beam profile at the experimental target. 22
2.7 The beam envelopes for the condition of the beam momentum of 1.8 GeV/c. 22
2.8 Typical single rate per 100 μsec of a BH1 counter segment. 23
2.9 The schematic view of K1.8 beam spectrometer. 25
2.10 The schematic view of GC. 27
2.11 The schematic view of BH1. 28
2.12 The schematic view of BH2. 28
2.13 The cell structure of BC3. 30
2.14 The plateau curve of one of the MWPC(BC1) and BC3 layer as a function of the cathode plane high voltage. 31
2.15 Detector components of SKS. 34
2.16 The schematic view of TOF. 35
2.17 Threshold and reflection index for Čerenkov radiation as a function of the momentum. 36
2.18 The schematic view of AC2. 37

2.19 The schematic view of LC. 38
2.20 The cell structure of SDC3·4. 39
2.21 The plateau curve of one of the SDC3 layer as a function of the anode wire high voltage. 40
2.22 The PIK trigger logic diagram. 41
2.23 The beam trajectories in the SKS magnet with the beam momentum of 1.92 GeV/c. 42
2.24 The hit pattern of TOF for the (π^-, K^-) reaction data. 43
2.25 Typical trajectories of the background particles and the relation between the TOF and LC segment. 43
2.26 The selected region for the matrix trigger was indicated in red lines. . . . 44
2.27 The diagram of the data-acquisition system. 45
2.28 Schematic view of the liquid hydrogen target (unit in mm). 47

3.1 Flow chart of the offline analysis. 52
3.2 Typical TOF spectrum of the incident beam particles. 53
3.3 Typical TDC distribution of a BC1 layer. 55
3.4 Typical TDC distributions of one of the BC3 layers and one of the BC4 layers. 56
3.5 A scatter plot between the drift time and the drift length of one of the BC3 layers. 57
3.6 Scatter plots between the drift time and the drift length of one of the BC3 layers and one of the BC4 layers. 57
3.7 Local position coordinate for the local straight tracking. 58
3.8 The VI and VO point. 59
3.9 Typical χ^2 distribution of the BC1·2 tracking and the BC3·4 tracking. . . 60
3.10 Typical residual distribution of one of the BC1 layers and one of the BC3 layers. 60
3.11 Typical χ^2 distribution of the K1.8 track with the beam momentum of 1.37 GeV/c and 1.92 GeV/c. 61
3.12 The missing mass resolution of Σ^+ as a function of the χ^2_{K18}. 62
3.13 Typical distribution of the momentum for a π^+ beam of 1.37 GeV/c and a π^- beam of 1.92 GeV/c. 63
3.14 The hodoscope cut region of TOF-ADC,TDC. 64
3.15 The hodoscope cut region of LC-ADC,TDC. 64
3.16 The hodoscope cut region of the hit segment number difference between the TOF and the LC segment and the time difference between TOF and LC. 65
3.17 Scatter plot between the horizontal scattering angle measured by SDC1·2 and the flight time between BH2 and TOF. 66
3.18 Typical TDC distribution and a scatter plot between the drift time and the drift length of one of the SDC3 layers. 67
3.19 The origin of the coordinates of the local tracking of SDC1·2 and SDC3·4 and the SKS tracking. 68
3.20 Typical χ^2 distributions of SD1·2 tracking and SDC3·4 tracking. 69

3.21 Typical residual distribution of one of the SDC2 layers and one of the SDC3 layers. 69
3.22 Typical distribution of χ^2_{SKS}. 70
3.23 Scattered particle mass distribution for the $p(\pi^-, K^+)\Sigma^-$ data. 71
3.24 Typical distribution of the horizontal and vertical scattering angle difference. 72
3.25 Vertex distribution for the (π^-, K^-) data. 73
3.26 Scatter plot between the scattering angle and z-vertex distribution for the (π^-, K^-) data. 74
3.27 Typical track multiplicity of the BC1·2 and BC3·4 local tracking. 78
3.28 The Σ^+ missing mass spectrum with the single-track selection and the multi-track selection. 79
3.29 The number of photo-electrons detected by AC1 and AC2 for the π^- events. 81
3.30 Scatter plot between the horizontal scattering angle measured by SDC1·2 and the flight time between BH2 and TOF. 82
3.31 The layer's efficiency of one of the SDC4 layers as a function of the horizontal hit position. 83
3.32 The missing mass resolution of Σ^+ as a function of the χ^2_{SKS}. 84
3.33 The SKS tracking efficiency as a function of the scattering angle. 85
3.34 The missing mass resolution of Σ^+ as a function of the SKS scattering angle. 85
3.35 Scattered particle mass distribution for the $p(\pi^-, K^+)\Sigma^-$ data. 86
3.36 The acceptance of SKS in the 2.5 T mode. 90
3.37 The acceptance projection of SKS in the 2.5 T mode. 91
3.38 The z-vertex distribution of scattering angle over 0° to 2° and 2° to 4°. . 92
3.39 The vertex distribution of the empty target data along the beam axis, and the horizontal and vertical directions. 93
3.40 The subtracted vertex distribution from the liquid hydrogen data along the beam axis, and the horizontal and vertical directions. 94
3.41 The angular dependence of the cross section of the ϕ and the $\Lambda(1520)$ production. 95
3.42 The estimated background shape of the associated reactions. 95
3.43 The missing mass spectrum of Σ^+ and Σ^-. 96
3.44 The differential cross sections of Σ^+ production. 97
3.45 The differential cross sections of Σ^- production. 97
3.46 The momentum difference between the two spectrometers as a function of the central momentum of the beam line spectrometer. 100
3.47 The momentum difference between the two spectrometers without any offset correction. 100
3.48 The width of the distribution for the momentum difference between the two spectrometers as a function of the central momentum of the beam line spectrometer. 101
3.49 The simulated missing mass spectra without the target and with the target. 102
3.50 The missing mass spectrum of Σ^+ with the selection of the number of the BH2 hit segments. 103
3.51 The corrected missing mass spectrum of Σ^+ with the selection of the number of the BH2 hit segments. 104

3.52 A scatter plot between the derivatives of horizontal ($\frac{dx}{dz}$) or vertical ($\frac{dy}{dz}$) positions at the target point and the Σ^- missing mass. 105

4.1 The missing mass spectrum for the the $\pi^- p \to K^- \Theta^+$ reaction with the momentum of 1.92 GeV/c. 111
4.2 The background spectrum for the $\pi^- p \to K^- \Theta^+$ reaction with the momentum of 1.92 GeV/c. 112
4.3 The averaged differential cross section of the missing mass spectrum for the $\pi^- p \to K^- \Theta^+$ reaction averaged over 2° to 15° in the laboratory frame. 113
4.4 The missing mass spectrum of the $\pi^- p \to K^- \Theta^+$ reaction with a fitting result. 113
4.5 The differential cross section of the $\pi^- p \to K^- \Theta^+$ reaction with the Θ^+ width fixed at 1.4 MeV/c^2 (FWHM). 114
4.6 The differential cross section of the $\pi^- p \to K^- \Theta^+$ reaction with the Θ^+ width fixed at 2.0 MeV/c^2 (FWHM). 115

A.1 The measured 2.2 T and 2.7 T map. 122
A.2 The schematic view of the SKS coil. 123
A.3 The shorted points of the SKS coil and the removed coil unit. 124
A.4 The B-H curve of iron of the SKS magnet. 125
A.5 The coordinate of the calculation. 126
A.6 The difference of the magnetic field value between the measured map and the several calculated maps. 128
A.7 The distribution of the calculated magnetic field of 2.2 T. 129

B.1 The beam intensity during the Θ^+ production run. 131
B.2 The beam accidental coincidence rate during the Θ^+ production run. . . 131
B.3 The horizontal beam position during the Θ^+ production run. 132
B.4 The vertical beam position during the Θ^+ production run. 132
B.5 The BC1·2 efficiency during the Θ^+ production run. 133
B.6 The BC3·4 efficiency during the Θ^+ production run. 134
B.7 The K1.8 beam line tracking efficiency during the Θ^+ production run. . . 135
B.8 The single beam track efficiency during the Θ^+ production run. 135
B.9 The SDC1·2 efficiency during the Θ^+ production run. 136
B.10 The SDC3·4 efficiency during the Θ^+ production run. 137
B.11 The mean value and width of the pedestal of GC during the Θ^+ production run. 138
B.12 The mean value and width of the pedestal, and the ADC gain of BH1 during the Θ^+ production run. 138
B.13 The mean value and width of the pedestal, and the ADC gain of BH2 during the Θ^+ production run. 139
B.14 The mean value and width of the pedestal, and the ADC gain of TOF during the Θ^+ production run. 139
B.15 The mean value and width of the pedestal, and the ADC gain of AC during the Θ^+ production run. 140

B.16 The mean value and width of the pedestal, and the ADC gain of LC during the Θ^+ production run. 140

List of Tables

1.1 Published experiments with positive result for the Θ^+ baryon 4
1.2 Published experiments with negative result for the Θ^+ baryon 5

2.1 The differences in the experimental conditions between KEK-E522 and J-PARC E19. 16
2.2 Design specifications of the K1.8 beam line spectrometer 26
2.3 Specifications of the trigger counters 29
2.4 Specifications of the MWPC(BC1, BC2) and the drift chambers. 31
2.5 Specifications of the SKS magnet. 32
2.6 Design specifications of the new SKS spectrometer at 2.5 T mode. 33
2.7 Specifications of the liquid hydrogen target. 48
2.8 Data summary. 49
2.9 Data summary of the control data. 49

3.1 The list of the experimental efficiency factors. 75
3.2 The rejection of K decay events and the total survival rate. 87
3.3 Typical materials in the spectrometers along the flight path. 88
3.4 The systematic error of the cross section for each data. 98
3.5 The condition of the calibration process and the obtained values by correcting the parameters. 106
3.6 The estimation of missing mass resolution of Θ^+. 109

A.1 The number of coil turns. The HF1 and LF3 are the most inner and outer side, respectively. 122
A.2 The present SKS coil specification. The 470A data was the quench limit of the SKS coil. 124

Chapter 1

Introduction

1.1 Exotic hadrons

The Quantum Chromodynamics (QCD) is a theory of strong interaction, which describes the color interaction between quarks and gluons. When applying QCD to calculate experimental phenomena, it is important whether the QCD calculation can be treated perturbatively or not. The QCD calculation for the high energy phenomena where QCD can be perturbatively calculated shows good agreements with experimental results. This is one of the most remarkable successes of QCD. For the low energy phenomena where QCD cannot be perturbatively calculated, the models to solve QDC problems are still in progress. The properties of hadrons such as spin, parity, mass, and magnetic moment, which cannot be calculated perturbatively, have been described partly well from effective models. Recently, the progress of the lattice QCD calculation enable to reproduce the mass and other properties of ground-state hadrons have been reproduced well. In the future, the lattice QCD might succeed in complete calculation for the low energy phenomena with a huge computing system. Even if the properties of hadrons are exactly reproduced well by the lattice QCD simulation, it is necessary to "understand" the properties of hadrons from the effective models which respect the symmetry and the feature of QCD. In the effective models, quarks and gluons have the quantum number of "color" with the $SU(3)_{color}$ symmetry, and hadrons, compounds of quarks and gluons, must be a singlet state of the $SU(3)_{color}$ symmetry. By the constituent quark models which comprise the features in QCD and the assumption of the confined constituent quark, called QCD-inspired models, the properties of ground-state hadrons are described well, although excited hadrons are not well reproduced by them.

QCD requires hadrons to be a color singlet, but does not restrict the number of quarks [1] so that exotic hadrons which do not have the same quark content as ordinary hadrons can exist. The existence of exotic hadrons such as "hybrid meson ($q\bar{q}g$)", "baryonium($qq\bar{q}\bar{q}$)", "pentaquark ($qqqq\bar{q}$)" and "dibaryon ($qqqqqq$)" has also been predicted theoretically. There was little evidence for existence of such states until recently. The observation of a tetraquark ($qq\bar{q}\bar{q}$) was recently reported by the Belle collaboration [2]. The understanding exotic hadrons plays an essential role to discriminate and improve the models of hadrons. Similarly, it is important not only for the improvement of the effective models but also the lattice QCD calculation. Therefore, search for ex-

otic hadrons is one of the important subject in hadron physics toward understating of hadrons from QCD.

1.2 The Θ^+ pentaquark baryon

D. Diakonov, Petrov and Polyakov predicted the narrow resonance state with a width of less than 15 MeV/c^2 at 1530 MeV/c^2 using chiral soliton model [3]. The exotic anti-decuplet state including Θ^+ is the 2nd excited state and the members are shown in Fig. 1.1. The spin of the anti-decuplet is 1/2 and the parity is positive. It is same as the octet and decuplet baryons in the chiral soliton model. Diakonov *et al.* assumed the state $N^*(1710)$ to be a member of the proposed anti-decuplet in order to have a prediction for the Θ^+ mass.

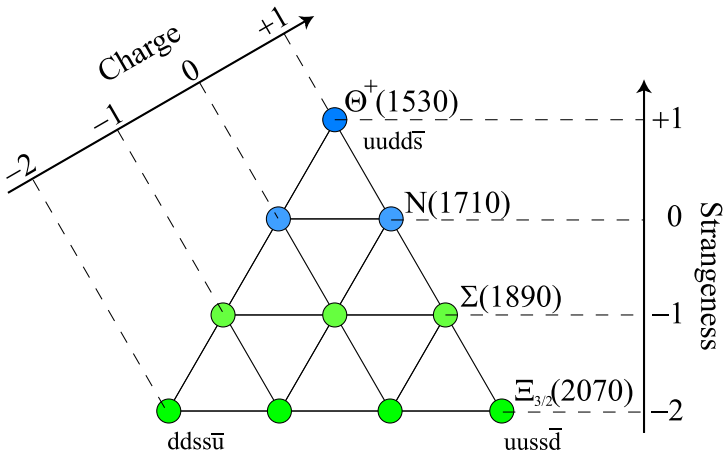

Figure 1.1: The anti-decuplet of baryons with $J^P = 1/2^+$ by chiral soliton model proposed by D. Diakonov *et al.* [3]. The anti-decuplet includes the exotic particle, Θ^+, at the corners of this diagram. The quark content and the predicted masses are shown.

An observation of the Θ^+ pentaquark was firstly reported by the LEPS collaboration [4]. Using a tagged photon beam of ∼2 GeV from the electron beam in SPring-8, they measured the $\gamma n \to K^- K^+$ reaction where the neutron in ^{12}C nuclei were used as a target. A peak obtained in the missing mass of the $\gamma n \to K^- X$ reaction is shown in Fig. 1.2. They reported the peak as the Θ^+ baryon with the mass of 1.54±0.01 GeV/c^2. The observed width is consistent with its experimental resolution and only the upper limit of 25 MeV/c^2 has been obtained. There is a good agreement between the theoretical prediction by Diakonov, Petrov and Polyakov [3] and the experimental result by the LEPS collaboration.

One of the most remarkable property of Θ^+ is its narrow width. The observed width of Θ^+ can not be explained as a loosely bound molecule-like state of K^+n but suggests a pentaquark state. In order to understand the narrow width, several theoretical models are proposed. By one of the models[5], the additional correlation between quarks was considered. When Θ^+ decays, quarks composing Θ^+ is re-arranged from the di-quark-di-quark-antiquark configuration to the KN, quark-antiquark and three quarks,

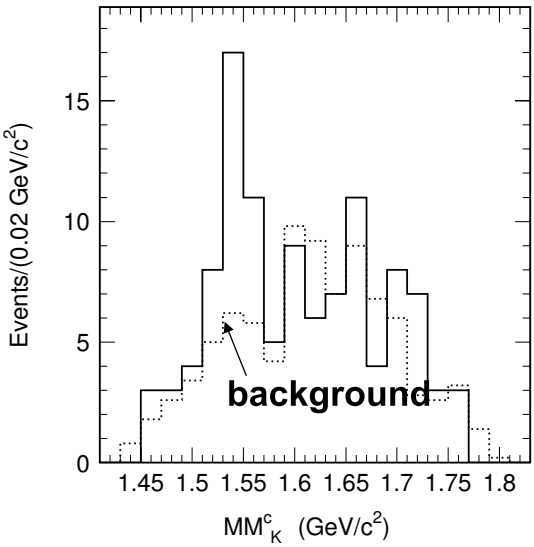

Figure 1.2: The first evidence of Θ^+ reported by the LEPS collaboration. The solid histogram is the missing mass spectrum of $\gamma n \to K^-\mathrm{X}$ reaction. The hatched histogram is the estimated background from $\gamma p \to K^-$ reaction. The peak with a Gaussian significance of 4.6σ was observed at 1540 ± 10 MeV/c^2. The only upper limit of the width was determined to be less than 25 MeV/c^2.

configuration. The re-arrangement of quarks causes the small decay width of Θ^+. Thus, study of Θ^+ provides a key to understand the decay mechanism of hadron resonance and to obtain a new knowledge of the quark dynamics in the low energy region.

Experimental review

After the first report from the LEPS collaboration [4], several experiments reported positive results. However, the statistics of all experiments were not sufficient to establish its existence. On the other hand, from several high energy experiments, negative results have been reported with much higher statistics. In addition, some of the initial positive evidences were denied later by the same collaboration with higher statistics. The positive and negative experimental results are summarized in Table 1.1 and 1.2, respectively.

As shown in Fig. 1.3, the LEPS collaboration also reported the updated experimental result, where the statistics has been improved by a factor of 8 over the previous measurement [6]. They reported a clear peak of Θ^+ with the mass of $1.524\pm0.002+0.003$ GeV/c^2 in the Fermi-motion-corrected nK^+ invariant mass distribution. The differential cross section for the $\gamma n \to K^-\Theta^+$ reaction was obtained to be 12 ± 2 nb/sr. However, the LEPS collaboration reported such a high statistic data. Other having much higher statistics and using different reaction channels or different experimental setups must be needed to conclude the existence of Θ^+.

The search for Θ^+ using hadron beams was previously performed at KEK-PS as well. Those experiments with hadron beams are described in the following section.

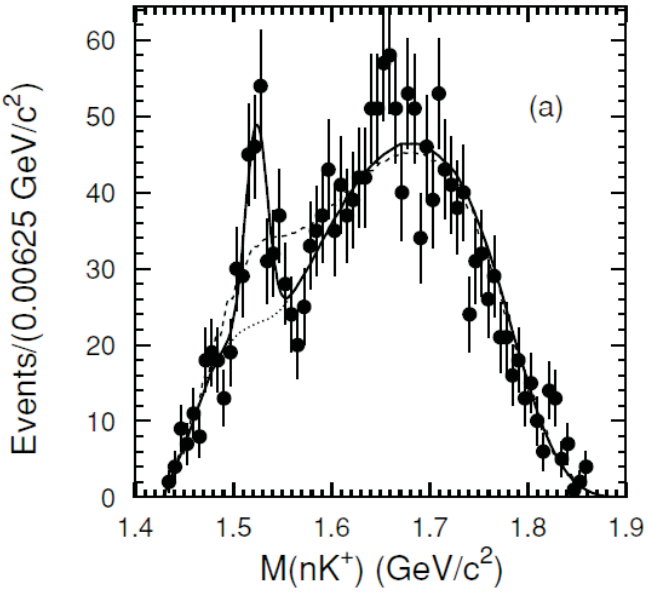

Figure 1.3: The updated experimental result reported by the LEPS collaboration in 2009, where the statistics has been improved by a factor of 8 over the previous measurement [6]. The statistical significance of the peak is 5.1σ, and the differential cross section for the $\gamma n \to K^- \Theta^+$ reaction was obtained to be 12±2 nb/sr. The solid line show a fit to the spectrum with a Gaussian function and the dotted line is the background. The dashed line shows a fit to the randomized minimum momentum method (RMM) background spectrum only.

Reference	Group	Reaction	Mass (MeV)	Width (MeV)	Statistical significance (σ)
[4]	LEPS	$\gamma C \to K^+K^-(n)$	1540 ± 10	<25	4.6
[6]	LEPS	$\gamma C \to K^+K^-(n)$	1524 ± 2	<25	5.1
[7]	DIANA	$K^+Xe \to K^0_s pX$	1539 ± 2	<9	4.4
[8]	DIANA	$K^+Xe \to K^0_s pX$	1538 ± 2	0.39±0.1	8
[9]	CLAS(d)	$\gamma d \to K^+K^-p(n)$	1542 ± 5	<21	(5.2)
[10]	CLAS(p)	$\gamma p \to \pi^+K^+K^-(n)$	1555 ± 10	<26	7.8
[11]	SAPHIR	$\gamma p \to K^+K^0_s nX$	1540 ± 6	<25	4.8
[12]	ITEP	$\nu A \to K^0_s pX$	1533 ± 5	<20	6.7
[13]	HERMES	$e^+d \to K^0_s pX$	1528 ± 3	12±9	4.2
[14]	COSY-TOF	$pp \to K^0_s p\Sigma^+$	1530 ± 5	<18	4.7
[15]	ZEUS	$e^+p \to e^+K^0_s pX$	1522 ± 3	8 ±4	4.6
[16]	NOMAD	$\nu A \to K^0_s pX$	1529 ± 3	2∼3	4.3
[17]	SVD	$pA \to K^0_s pX$	1526 ± 5	<24	5.6
[18]	SVD	$pA \to K^0_s pX$	1523 ± 5	<14	8.0

Table 1.1: Published experiments with positive result for the Θ^+ baryon

Reference	Group	Reaction	Limit
[19]	BES	$e^+e^- \to J/\Psi \to \bar{\Theta}\Theta$	$< 1.1 \times 10^{-5}$ B.R. (90% C.L.)
	BES	$e^+e^- \to \Psi(2S) \to \bar{\Theta}\Theta$	$< 8.4 \times 10^{-6}$ B.R. (90% C.L.)
[20]	ALEPH	$e^+e^- \to Z \to pK_s^0X$	$< 6.2 \times 10^{-4}$ B.R. (95% C.L.)
[21]	BarBar	$e^+e^- \to \Upsilon(4S) \to pK_s^0X$	$< 1.0 \times 10^{-4}$ B.R. (90% C.L.)
[22]	BarBar	$eBe \to pK_s^0X$	not given
[23]	Belle	$e^+e^- \to B^0\bar{B}^0 \to p\bar{p}K_s^0X$	$< 2.3 \times 10^{-7}$ B.R. (90% C.L.)
[24]	Belle	$K^+n \to K_s^0pX$	$\Gamma < 0.64MeV$ (90% C.L.)
[25]	CDF	$p\bar{p} \to K_s^0pX$	$< 0.03 \times \Lambda^*$ (90% C.L.)
[26]	SPHINX	$pC \to K_s^0pX$	$< 0.1 \times \Lambda^*$ (90% C.L.)
[27]	HERA-B	$pA \to K_s^0pX$	$< 2.7\% \times \Lambda^*$ (95% C.L.)
[28]	HyperCP	$pCu \to K_s^0pX$	$< 0.3\%$ K_s^0p
[29]	FOCUS	$\gamma BeO \to K_s^0pX$	$< 0.02 \times \Sigma^*$ (95% C.L.)
[30]	PHENIX	$dAu \to K^-\bar{n}X$	not given
[31]	WA89	$\Sigma^+A \to K_s^0pX$	$< 1.8\mu$b/A (99% C.L.)
[32]	CLAS	$\gamma p \to \bar{K}_s^0K^+n$	< 0.8 nb (95% C.L.)
[33]	CLAS	$\gamma d \to K^-pK^+n$	$< 0.15 - 3$ nb (95% C.L.)
[34]	CLAS	$\gamma d \to K^+n\Lambda$	$< 5 - 25$ nb (95% C.L.)
[35]	COSY-TOF	$pp \to \Sigma^+pK_s^0$	$< 0.15\mu$b/A (95% C.L.)
[36]	NOMAD	$\nu A \to K_s^0pX$	$< 2.13 \times 10^{-3}\nu$CC (90% C.L.)

Table 1.2: Published experiments with negative result for the Θ^+ baryon

1.3 Search for Θ^+ using hadron beams

The present status of Θ^+ is still controversial. Thus, the confirmation of the existence (or non-existence) of the Θ^+ is crucially important.

For the other experiments with positive results, the statistics is not sufficient to claim the existence of Θ^+, while high energy experiments report negative results from much higher statistics and better resolution data. The production cross section of baryons is generally suppressed in the high energy region by about a few orders of magnitude. The suppression of the production cross section of Θ^+ was studied by A. I. Titov *et al.* [37]. They found the large suppression compared with the production of the ordinary three-quark hyperons. Thus, high statistics experiments at low energy region become important.

Since the LEPS collaboration reported Θ^+ via photo-induced reaction, Θ^+ could be produced via hadron-induced reaction. In general, the production cross section for hadrons via hadron-induced reaction is larger than that of photo-induced reaction. Therefore, the experiment with the Θ^+ production using a hadron beam such as π^- and K^+ is important.

1.3.1 Production of Θ^+

Fig. 1.4 shows the diagram for the calculation of the $\pi^- p \to K^- \Theta^+$ reaction and the $K^+ p \to \pi^+ \Theta^+$ reaction. The $K^+ p \to \pi^+ \Theta^+$ reaction is the inverse reaction of the $\pi^- p \to K^- \Theta^+$ reaction. In both reactions, the same coupling constants are used in the production diagrams, where s- or u-channel includes $g_{KN\Theta}$ for intermediate N and t-channel includes $g_{K^*N\Theta}$ for the K^* exchange. The production cross section of the $\pi^- p \to K^- \Theta^+$ reaction is determined by the coupling constant $g_{KN\Theta}$ which is related to the Θ^+ decay width ($\Theta^+ \to KN$ ($\Gamma_{\Theta^+ \to K^+ n + K^0 p} \propto {g^2}_{KN\Theta}$)) [38]. Thus, for understanding the nature of Θ^+ if it exists, it is quite important to measure the production cross section.

Figure 1.5 shows the calculated cross section for the $\pi^- p \to K^- \Theta^+$ reaction taking into account the s-channel and the t-channel diagrams [38]. The parity of Θ^+ was assumed to be positive. They used $g_{KN\Theta} = 2.2$, which corresponds to the Θ^+ width of 5 MeV/c^2. Due to the interference between the amplitudes of s-channel and t-channel, the cross section of the $\pi^- p \to K^- \Theta^+$ reaction dependents on the magnitude of $g_{K^*N\Theta}$. The calculated cross section ranges from about 2 μb to 190 μb as shown in Fig.1.5 (b) and (d).

As shown in Fig. 1.4, the t-channel and the u-channel diagrams in the $K^+ p \to \pi^+ \Theta^+$ reaction is considered. Figure 1.6 shows the differential cross section calculated in [39]. The decay width of Θ^+ was assumed to be 1.03 MeV/c^2 which corresponds to $g_{KN\Theta}$ = 1.0. On the other hand, there is no experimental information about $g_{K^*N\Theta}$. They calculated in three cases where $g_{K^*N\Theta} = 0$, $g_{K^*N\Theta} = g_{KN\Theta}$ and $g_{K^*N\Theta} = -g_{KN\Theta}$. If there is the t-channel process ($g_{K^*N\Theta} = \pm g_{KN\Theta}$), the differential cross section would have a forward peak distribution as shown by the solid and dashed lines in Fig. 1.6. On the other hand, if there is no t-channel process, the differential cross section would have a backward peak distribution.

In addition, the cross section of the $\pi^- p \to K^- \Theta^+$ reaction was calculated using the

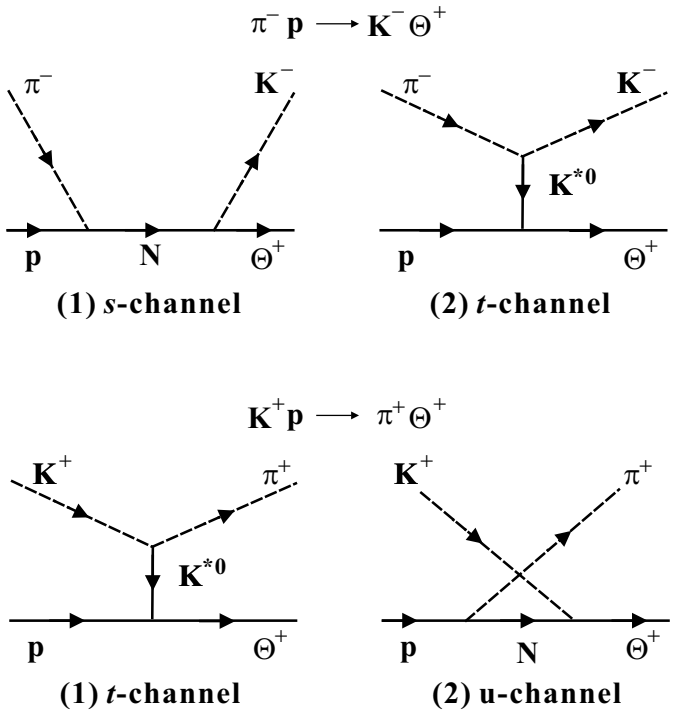

Figure 1.4: Diagrams for the $\pi^- p \to K^- \Theta^+$ reaction (Top) and the $K^+ p \to \pi^+ \Theta^+$ reaction (Bottom).

small coupling constant of $g_{K^* N \Theta}$ [40] as shown in Fig. 1.7. They assumed the width of Θ^+ of 1 MeV/c^2 and positive parity. The cross section of the s-channel process is 0.5 μb at $\sqrt{s} = 2.25$ GeV.

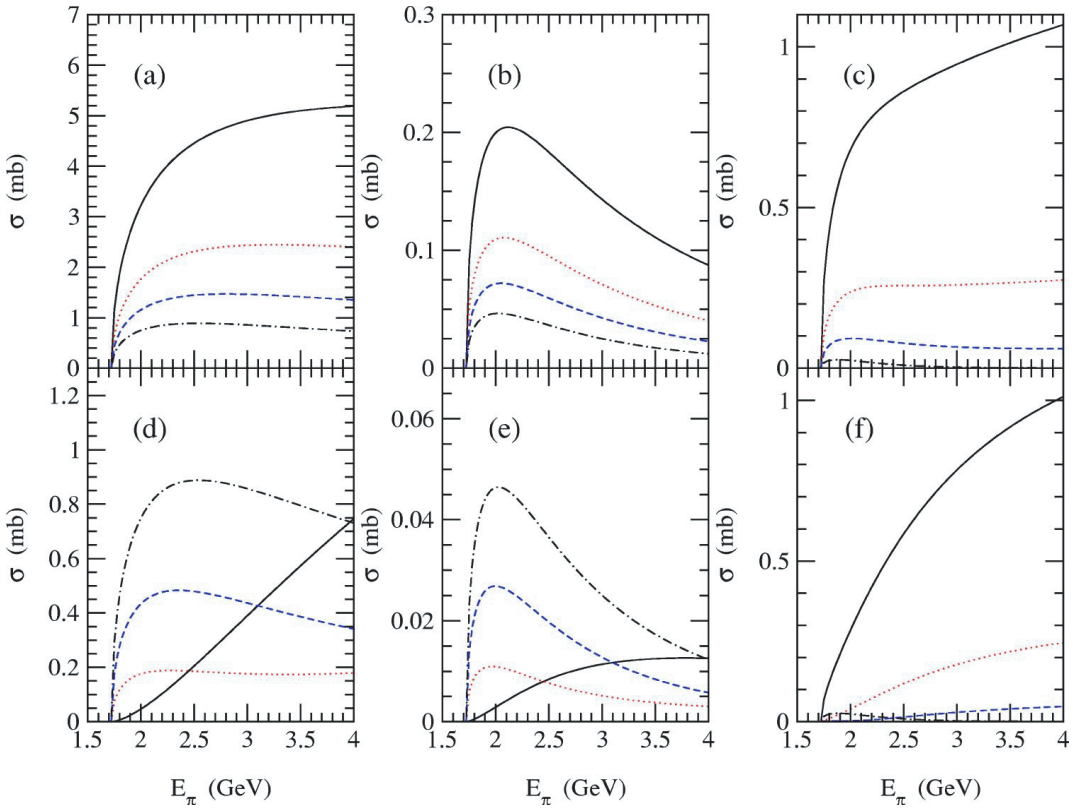

Figure 1.5: Calculated cross sections for the $\pi^- p \to K^- \Theta^+$ reaction [38]. The (a) and (d) are the results without a form factor, (b) and (e) are those with the monopole form factor with $\Lambda = 0.5$ GeV, and (c) and (f) are those with other form factor (See Reference [38]). In (a), (b), (c), the solid, dotted, dashed, and dot-dashed lines are with $g_{K^*N\Theta}$=-2.2, -1.1, -0.5 and 0.0, respectively. In (d), (e), (f), the solid, dotted, dashed, and dot-dashed lines are with $g_{K^*N\Theta}$=2.2, 1.1, 0.5 and 0.0, respectively.

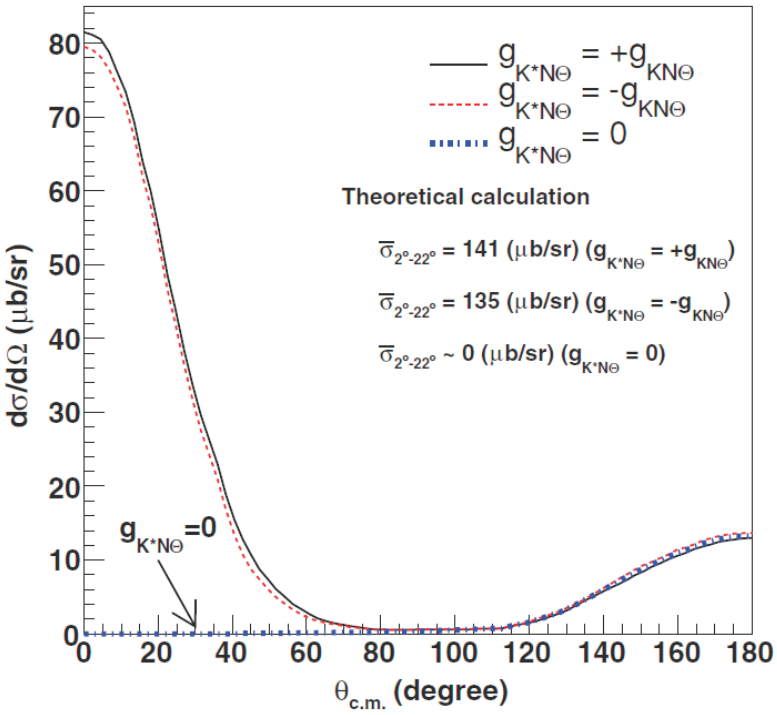

Figure 1.6: Differential cross section of the $K^+p \to \pi^+\Theta^+$ reaction calculated at $\sqrt{s} = 2.4$ GeV [39]. The horizontal axis represents the scattering angle of the π^+ in the c.m. frame of the K^+p system. The solid line is obtained with $g_{K^*N\Theta} = +g_{KN\Theta}$, the dashed line with $g_{K^*N\Theta} = -g_{KN\Theta}$, and the dot-dashedline with $g_{K^*N\Theta} = 0$. The differential cross sections averaged over 2^o to 22^o in the laboratory frame are also listed for each case.

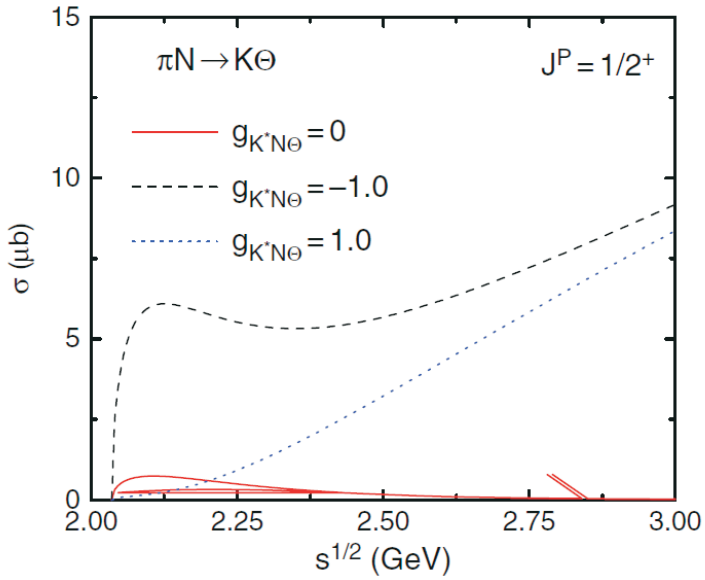

Figure 1.7: The cross section of the $\pi^- p \to K^- \Theta^+$ reaction using the small coupling constant of $g_{K^*N\Theta}$ [40]. They assumed the width of Θ^+ of 1 MeV/c^2 and positive parity. The cross section of the s-channel process is 0.5 μb at $\sqrt{s} = 2.25$ GeV. They used the monopole-type form factor and pseudo-scalar-type couplings between $KN\Theta^+$ and πNN systems as done by Oh *et al.* [38, 39].

1.3.2 Previous experiments: KEK E522 and KEK E559

The search for Θ^+ using hadron beams was performed in the KEK-PS E522 experiment via the $\pi^- p \to K^- \Theta^+$ reaction [41] and the KEK-PS E559 experiment via the $K^+ p \to \pi^+ \Theta^+$ reaction [42].

KEK E522 experiment

The E522 experiment [41] carried out to search for Θ^+ via the $\pi^- p \to K^- \Theta^+$ reaction at the K2 beam line of the KEK-PS. The data was taken with the beam momenta of 1.87 GeV/c and 1.92 GeV/c. In the 1.92 GeV/c data, as shown in Fig. 1.8, a bump with a width consistent with the experimental resolution was found at the mass of $M = 1530.6^{+2.2}_{-1.9}(\text{stat.})^{+1.9}_{-1.3}(\text{syst.})$ MeV/c^2. However, the statistical significance of the bump was only 2.5$\sim$2.7σ, being not sufficient to claim the evidence for Θ^+. Therefore, they have derived an upper limit of the production cross section via the $\pi^- p \to K^- \Theta^+$ reaction. The upper limit of the differential cross sections for the scattering angle from 0^o to 20^o at the laboratory frame was obtained to be 1.6 μb/sr and 2.9 μb/sr at the 90 % confidence level for the beam momenta of 1.87 and 1.92 GeV/c, respectively. The upper limits of the total cross sections were obtained to be 1.8 μb and 3.9 μb at 1.87 and 1.92 GeV/c, respectively, assuming that Θ^+ is produced isotropically in the center of mass system.

The obtained upper limits are quite smaller than the theoretical calculations and give a strong constraint to the unknown parameters such as the coupling constant $g_{K^*N\Theta}$

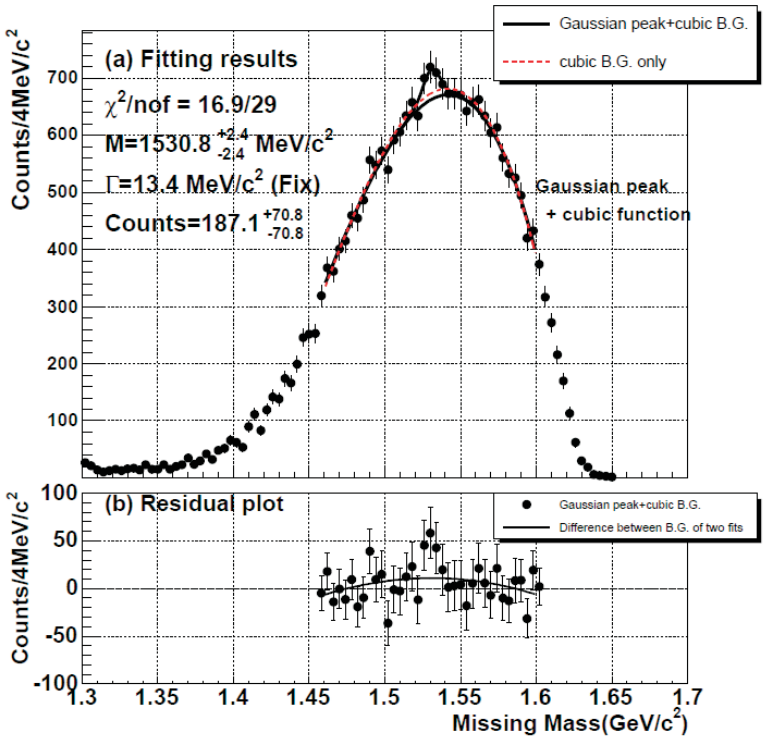

Figure 1.8: The missing mass spectrum of the $\pi^- p \to K^- \Theta^+$ reaction at the beam momentum of 1.92 GeV/c obtained in the KEK-E522 experiment. (a) They fitted this spectrum with third order polynomial background and a Gaussian peak (solid line). The dashed line represents the fitting result with only third order polynomial background assuming that there is no peak structure. (b) Residual plot from the background function obtained from the fitting with third order polynomial background and a Gaussian peak. The fitted curve with the background function is only represented by the solid line.

used in the calculations. Using the E522 results, the cross section of the $K^+p \to \pi^+\Theta^+$ reaction was studied in [43]. They found that the ratio of the cross sections of π^- and K^+ induced reactions are quite different for two J^P assignments of Θ^+. In the case of $J^P = 1/2^+$, $\sigma(K^+p \to \pi^+\Theta^+)/\sigma(\pi^-p \to K^-\Theta^+)$ is $\sim$50, while in the case of $J^P = 3/2^-$ it is $\sim$3.3.

Therefore, it was point out that search for Θ^+ via the $K^+p \to \pi^+\Theta^+$ reaction is necessary to understand the production mechanism of Θ^+. The KEK-E559 experiment was performed to search for Θ^+ via the $K^+p \to \pi^+\Theta^+$ reaction as described in the following.

KEK E559 experiment

After the E522 experiment, the E559 experiment [42] was performed to search for Θ^+ in the $K^+p \to \pi^+\Theta^+$ reaction at the KEK-K6 beam line with high statistics and good missing mass resolution using the Superconducting Kaon Spectrometer (SKS). Although the theoretical prediction expected a large production cross section in this reaction (more than several ten μb) [39], the experiment was designed to have sensitivity to a small production cross section (about 10 μb) because the cross section might be small considering the experimental small cross section via the $\pi^-p \to K^-\Theta^+$ reaction. They obtained a missing mass spectrum of the $K^+p \to \pi^+\Theta^+$ reaction with the mass resolution of 2.4 MeV/c^2 (FWHM), which was comparable to the expected width of Θ^+. Figure 1.9 shows the double differential cross section of the $K^+p \to \pi^+\Theta^+$ reaction averaged for reaction angles over 2^o to 22^o in the laboratory frame, which corresponds to the acceptance of the spectrometer. No peak structure was observed. They obtained a 90% C.L. upper limit less than 3.5 μb/sr for almost all the mass region.

The experimental upper limit of 3.5 μb/sr is much smaller than the theoretical value. Therefore, the t-channel process is excluded by the E559 result. On the other hand, if the contribution of the t-channel process is much smaller than that of the u-channel process, the differential cross section shows a backward peak distribution as shown in Fig. 1.6. In this case, the $\overline{\sigma}_{2^o-22^o}$ is expected to be less than 1 μb/sr. The E559 experiment was not sensitive enough to exclude the u-channel process.

By the E522 experiment, the upper limit of the $\pi^-p \to K^-\Theta^+$ reaction was obtained to be 3.9 μb at the 90% confidence level assuming that Θ^+ is produced isotropically in the center of mass system. By the E559 experiment, the upper limit of 3.5 μb/sr was also obtained. In the theoretical calculation, the s-channel and t-channel processes in the $\pi^-p \to K^-\Theta^+$ reaction were considered, the cross section was controlled by the same coupling constants, $g_{KN\Theta}$ and $g_{K^*N\Theta}$, as the ones used for the $K^+p \to \pi^+\Theta^+$ reaction. From the result of the $K^+p \to \pi^+\Theta^+$ reaction, $g_{K^*N\Theta}$ is considered to be quite small. Therefore, $g_{KN\Theta}$ should be small to explain both experimental results. Consequently, the width of Θ^+ is quite narrow.

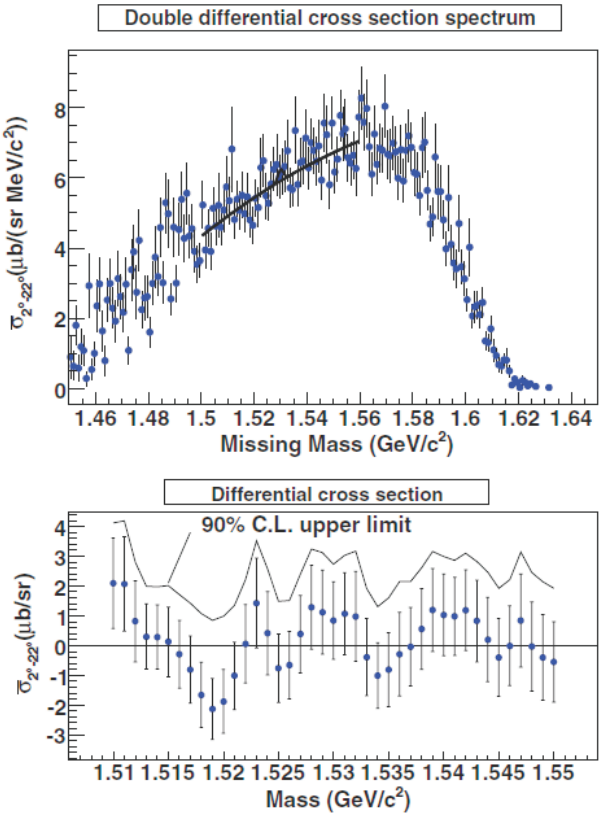

Figure 1.9: Top: double differential cross section of the $K^+p \to \pi^+\Theta^+$ reaction averaged over 2^o to 22^o in the laboratory frame. This spectrum includes a contribution from the K^+ decay events. In order to derive the upper limit of the differential cross section, the spectrum with a background was fitted using a second order polynomial function and a Gaussian peak with a fixed width of 2.4 MeV/c^2 (FWHM). Bottom: the upper limits of the differential cross section of the $K^+p \to \pi^+\Theta^+$ reaction averaged over 2^o to 22^o in the laboratory frame as a function of the mass of Θ^+. The data points show the value and the error of the differential cross section obtained from the area of the fitted Gaussian function. The line shows the 90% C.L. upper limit of the differential cross section.

Study from a photo-induced reaction

The small value of the coupling constant of $g_{K^*N\Theta}$ was also obtained from the experimental result by the CLAS collaboration [33]. They used the exclusive reaction $\gamma p \to \bar{K}^0 K^+ n$ in the photon energy range between 1.6 and 3.8 GeV searching for the decay of $\Theta^+ \to nK^+$. The Θ^+ resonance was not found and the upper limit of the total cross section of 0.8 nb at 90 % confidence level was obtained.

1.3.3 J-PARC E19 experiment

High-resolution search of Θ^+ pentaquark in $\pi^- p \to K^- X$ reactions

From the previous experiments using hadron beams, the information of the production cross section of Θ^+ was obtained. However, there was no evidence for Θ^+ in any of the previous experiments. As mentioned above, the total cross section depends on the decay width, and the s-channel process related to the coupling constant $g_{KN\Theta}$ in the $\pi^- p \to K^- \Theta^+$ reaction is suggested to be dominant. We can expect the cross section for the width of 1 MeV/c^2 amounts to less than 1 μb/sr, which is comparably smaller than that of the usual hadron production. Therefore, experimental information on the cross section is important to study the nature of Θ^+, such as the decay width in particular.

The J-PARC E19 experiment [44] has been carried out at the J-PARC K1.8 beam line from October to November in 2010. The experiment was proposed to confirm Θ^+ using the $\pi^- p \to K^- \Theta^+$ reaction by high-resolution spectroscopy. We measured the missing mass spectrum of the $\pi^- p \to K^- \Theta^+$ reaction with the beam momentum of 1.92 GeV/c using the K1.8 beam line spectrometer and the SKS spectrometer both of which have excellent momentum resolution. This experiment corresponded to a natural extension of the E522 experiment, but the resolution of the missing mass was much better than that of the previous experiment. We accumulated 10 times higher the statistics with much better mass resolution of 1.4 MeV/c^2 (FWHM). If the bump observed in E522 is not a statistical fluctuation but a real one, a peak with a Gaussian significance of 10σ was expected to be observed from the cross section of the bump observed in E522. If Θ^+ is not observed, the upper limit of the cross section will be 10 times smaller than that of E522 (3.9 μb). Compared with the theoretical calculation of the production cross section of the $\pi^- p \to K^- \Theta^+$ reaction [40], the sensitivity of the E19 experiment is better than that of the calculated production cross section, assuming the Θ^+ width of 1 MeV/c^2. In this case, further theoretical studies will be required to understand an extraordinary narrow width of Θ^+ or to explain the suppression of the production.

Chapter 2

Experiment

2.1 Outline

The present experiment was carried out in 2010 as J-PARC E19 [44] in the hadron facility of J-PARC using the K1.8 beam line and Superconducting Kaon Spectrometer (SKS). The purpose of the experiment is to search for the Θ^+ pentaquark with a high-resolution missing mass spectroscopy via the $\pi^- p \to K^- X$ reaction. The operation of the J-PARC accelerators has started in 2009, and this experiment was the first to take place at the K1.8 beam line, which will be a host of several hypernuclear and exotic-hadron experiments. By using a hadron beam such as π and K, these important experiments will be successively performed after the J-PARC E19 experiment.

An experiment to search for the Θ^+ pentaquark using a hadron beam had previously been carried out as the E522 experiment at the KEK 12 GeV Proton Synchrotron. The experiment found no clear evidence for the existence of Θ^+ within its experimental sensitivity. For the J-PARC E19 experiment, we used Superconducting Kaon Spectrometer (SKS) with the momentum resolution of 0.2%(FWHM) and a liquid hydrogen target resulting an improved sensitivity to reinvestigate the search. The beam momentum of the experiment was chosen to be 1.92 GeV/c in order to examine the previous experimental result of the $\sim$2.6σ bump. The incident momenta of pions were measured with the K1.8 beam line spectrometer, and those of kaons were measured with the SKS spectrometer. Using these spectrometers, the missing mass resolution for Θ^+ down to 2 MeV/c^2(FWHM) can be achieved. The differences in the experimental conditions between KEK-E522 and J-PARC E19 are listed in Table 2.1.

The SKS spectrometer had been used at the KEK-PS K6 beam line [47]. The SKS magnet was then moved to the J-PARC K1.8 beam line. The SKS spectrometer was modified and reconstructed for the J-PARC experiments with new detectors to increase the momentum acceptance and the tolerance to high counting rate limit. Using the downstream detectors twice larger than the previously used detectors, the maximum momentum acceptance of SKS is increased up to 1.1 GeV/c from the previous setup of 0.85 GeV/c at the magnetic field strength of 2.5 T, while the solid angle of 100 msr and the angular coverage of up to 20° are kept. The design value of the momentum resolution is of the order of 10^{-3}. By using the larger downstream detectors, the momentum range of scattered kaons widen to 0.75$-$1.00 GeV/c. Considering inseparable background

Table 2.1: The differences in the experimental conditions between KEK-E522 and J-PARC E19. N_{Beam} is the number of π^- beam irradiated to the target.

	E522	E19
Reaction	$p(\pi^-, K^-)\Theta^+$	$p(\pi^-, K^-)\Theta^+$
Momentum	1.87, 1.92 GeV/c	1.92 GeV/c
Resolution	13.6 MeV/c^2 (KURAMA)	<2.0 MeV/c^2 (SKS)
Target	Polyethylene ($(CH_2)_n$)	Liquid hydrogen (H_2)
Thickness	10 g/cm^2 (1.4 g/cm^2 for H_2)	0.85 g/cm^2
N_{Beam}	7.4×10^9	7.8×10^{10}

reactions (the ϕ production and the $\Lambda(1520)$ production), a flat background shape would be desired to search for the Θ^+ peak in the missing mass. From these experimental requirements, the wide momentum range with a high momentum resolution is essential.

J-PARC and Hadron experimental facility

J-PARC (Japan Proton Accelerator Research Complex) (Fig. 2.1) is a high intensity proton accelerator facility which aims to pursue frontier in nuclear physics, particle physics, materials science, life science and nuclear technology, using a new proton accelerator complex with the highest beam power in the world.

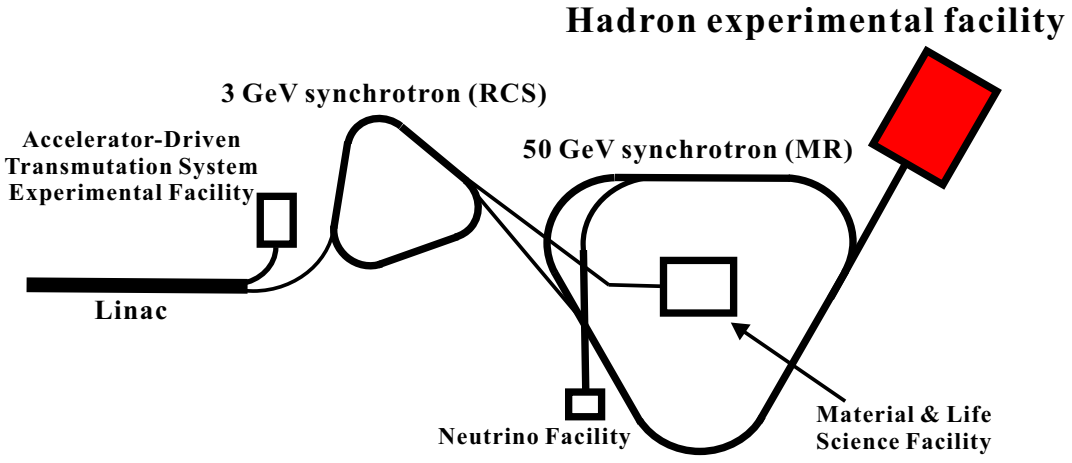

Figure 2.1: A schematic view of J-PARC.

H^- is produced at an ion source and accelerated by Linac to 400 MeV (50 mA). The accelerated H^- is converted to a proton (H^+) and injected to the 3 GeV Rapid-Cycling Synchrotron (RCS) which accelerates protons to 3 GeV (333 μA). Finally, part of protons are injected to Main Ring (MR) and accelerated up to 50 GeV (15 μA). The 50-GeV proton beams are provided to the hadron facility and the secondary hadronic beams are produced for experiments. In 2010, the beam energy after Linac is 189 MeV. In the

phase-1 of the J-PARC construction, the beam energy is 30 GeV and the goal beam intensity is 9 μA (270 kW). Since the operation of the J-PARC accelerator was started in 2009, the beam power of MR has been at $\sim$3 kW in time of the present experiment. The primary proton beam was extracted for a duration of 2.2 second in every 6.0 second, which is synchronized to the J-PARC MR operation cycle. This duration of the beam extraction is called a spill.

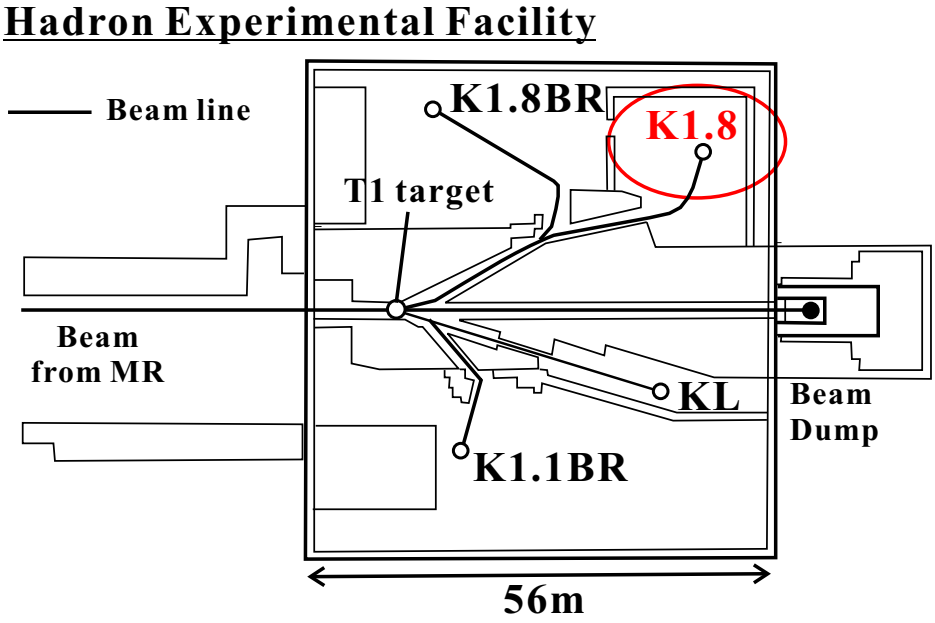

Figure 2.2: The schematic view of hadron experimental facility (Phase-1).

The J-PARC E19 experiment was performed at the K1.8 beam line in the hadron facility (Fig. 2.2). The facility consists of a primary beam line, several secondary beam lines where individual experiments are set up. The proton beam is transported from the Main Ring to the hadron facility and bombarded to the production target, T1. In the present experiment, the production target was a platinum rod (ϕ6$\times$60 mm). The hadronic beams (kaons, pions and so on) produced at T1 are delivered to an experimental area through secondary beam lines. Thus, the secondary beams are available for several lines (K1.8BR, K1.1BR and KL) simultaneously.

2.2 K1.8 beam line

The K1.8 beam line is a general-purpose mass-separated beam line that can supply various secondary hadron beams up to 2.0 GeV/c [45]. The most important design principle is to supply both high-intensity and high-purity kaon beams for an investigation of the $S = -2$ hypernuclei. The K1.8 beam line is designed to achieve the ratio of number larger than 1 of kaon over other particles (pion and muon) mixed in the beam providing the kaon beam intensity of 10 MHz on the experimental target. For the present experiment, the pion beam of enough intensity was used. Thus, the optics of the K1.8 beam line was not fine tuned using beams, but design values of the magnet setting was mostly used.

Figure 2.3 shows a schematic view of the K1.8 beam line. The K1.8 beam is divided into four sections which are the upstream, the first and second mass separation, and the momentum analysis (the K1.8 beam line spectrometer). The total length of the beam line is ∼46 m. The platinum rod target (T1) which is ϕ6 mm×60 mm to produce the secondary beams from the primary proton beam is located at the most upstream of the K1.8 beam line. The primary beam intensity on the production target was typically of 3.5×10^{12} proton/spill for the present experiment.

Upstream section

In the upstream section (Fig. 2.4), the first dipole magnet (D1), two quadrapole magnet (Q1,Q2) and the second dipole magnet (D2) are located. The copper collimator is installed between the T1 target and D1 in order to reduce the thermal deposit to the downstream magnets. Due to its high power of the proton beam from the J-PARC accelerators, thermal deposit to the beam line vacuum pipes and the activation of the cooling water are significant. Those pipes are, therefore, removed at the down stream of the T1 target. Instead, T1, D1 and Q1 are all housed in a large vacuum chamber (∼6 m height and ∼3 m × ∼3 m pentagonal box). The transported beam is vertically focused at the IF point. Then, both horizontal and vertical profiles are shaped by the IF (intermediate focus) slits which have the horizontal (IFH) and the vertical (IFV) components. By the IF slits, the cloud pions which are produced by the decay of K^0_s and the scattered pions by materials of the upstream section are rejected. This is one of the essential components in order to increased the purity of kaon. For the IF slits, the 30-cm brass blocks are used.

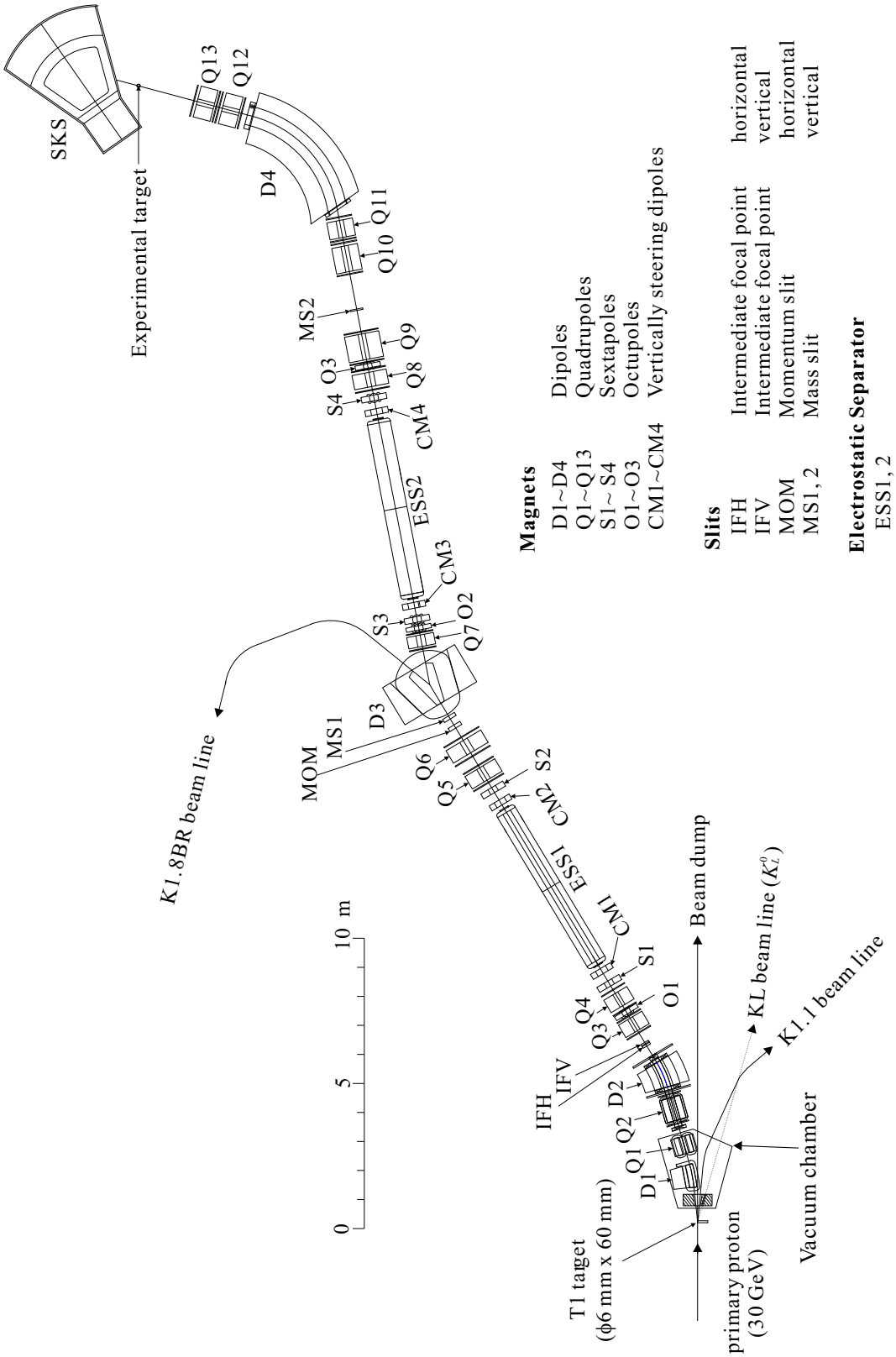

Figure 2.3: The schematic view of K1.8 Beam line.

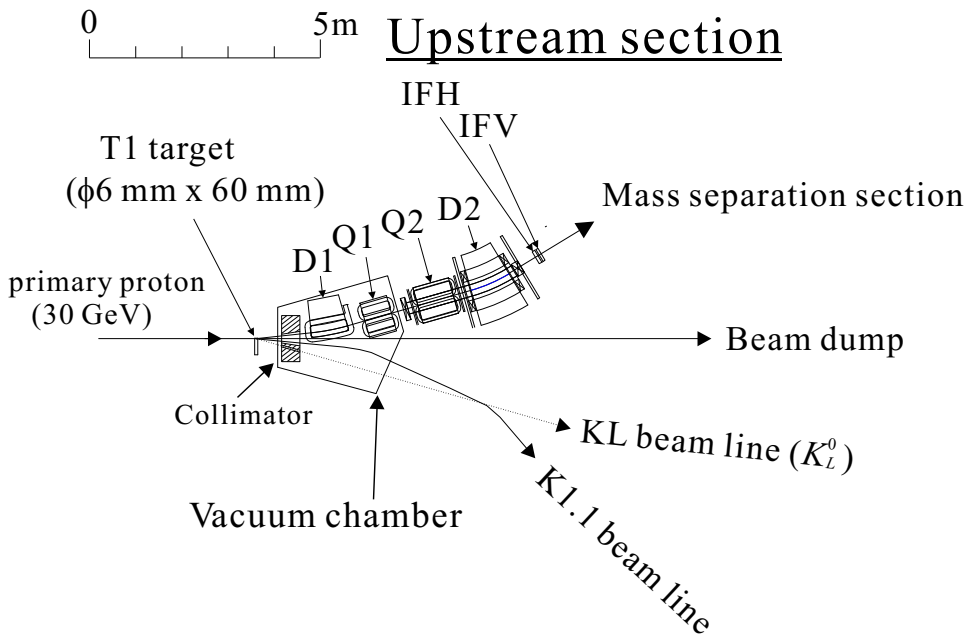

Figure 2.4: The schematic view of the upstream section.

Mass separation section

At the down stream of the upstream section, the first mass separation section (Fig. 2.5) is located. In order to supply the high-purity kaon beam, a set of the electrostatic separator (ESS1) with two correction magnets (CM1,CM2), four quadrapole magnet (Q3−Q6) and a slit for the mass separation (MS1) is a key system. The beam particles after passing through the IF slits are focused to the vertical center by Q3 and Q4 before entering CM1. The particle orbits are corrected by CM1 and CM2 located at both the entrance and the exit of ESS1. The maximum gradient of the electrostatic field of ESS1 is 75 kV/cm between the 10-cm gap. Bended by the high electrostatic field over the 6 m flight length, the secondary particles are separated according to their speed ($1/\beta$). For the present pion beam experiment, the settings of CM1 and CM2 are adjusted to pass through only pions. The pion orbit is brought to the vertical center by CM2 followed by focusing by Q5 and Q6. The horizontal momentum slit (MOM) which selects the beam particle momentum determines the momentum bite of the secondary beam. Then, the beam particles except pions are blocked by a 50 cm-long tungsten slit, MS1. The D3 magnet localed at the down stream of MOM direct the beam either to the K1.8 or K1.8BR experimental area.

After passing through D3, the beam is further separated by the second mass separation section (ESS2, CM3,4, Q7−Q9 and MS2). The sextapoles (S1−S4) and octapoles (O1−O3) in each mass separation section are used to correct the 2nd and 3rd order distortion, respectively. This double-stage mass separation system is an essential component of the K1.8 beam line. That gives the number ratio of kaon over other particles (pion and muon) in the beam to 3.5 at the beam momentum of 1.8 GeV/c.

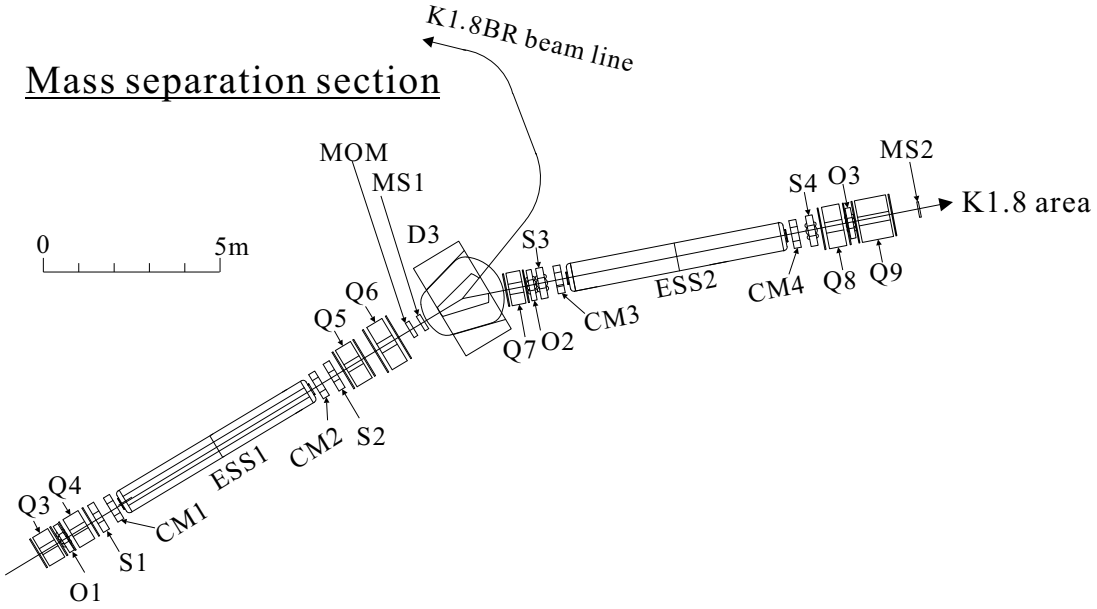

Figure 2.5: The schematic view of the mass separation section.

Momentum analysis part

The final section of the K1.8 beam line is the momentum analysis section (the K1.8 beam line spectrometer) which is described in the next section. After passing through MS2, the mass separated beam is delivered to the K1.8 beam line spectrometer. Then, the beam are focused on the experimental target and their momentum is analyzed.

Beam properties

Beam profile

In the present experiment, the central beam momentum was set at 1.92 GeV/c for the Θ^+ pentaquark search. A typical momentum bite was $\sim$2% determined by the setting of the momentum slit. The measured beam size at the experimental target position by tracking chambers at the down stream of the K1.8 beam line spectrometer was typically 10 mm (horizontal)$\times$5 mm (vertical) in rms, as shown in Fig. 2.6. The derivatives of the horizontal (dx/dz) and vertical (dy/dz) directions on the experimental target position were 0.01 rad and 0.003 rad in rms, respectively. The beam was almost parallel to the target axis. In order to increased the kaon purity, the vertical profile are shaped to be narrow at each slit position. Thus, the vertical size was determined by the slits. The horizontal profile is determined by the combined factors from the settings of the beam line components. In particular, for the present beam momentum of 1.92 GeV/c, the focusing by the combination of Q9 and Q10 determines the horizontal position. Figure. 2.7 shows the beam envelopes calculated with Transport [46] for the condition of the beam momentum of 1.8 GeV/c.

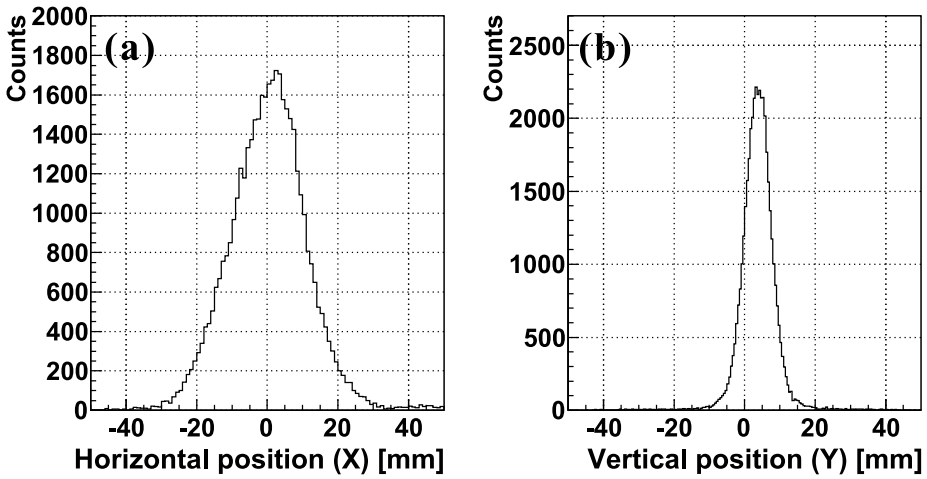

Figure 2.6: Typical beam profile at the experimental target in the E19 experiment measured by tracking chambers at the down stream of the K1.8 beam line spectrometer. The horizontal (a) and vertical (b) positions are shown.

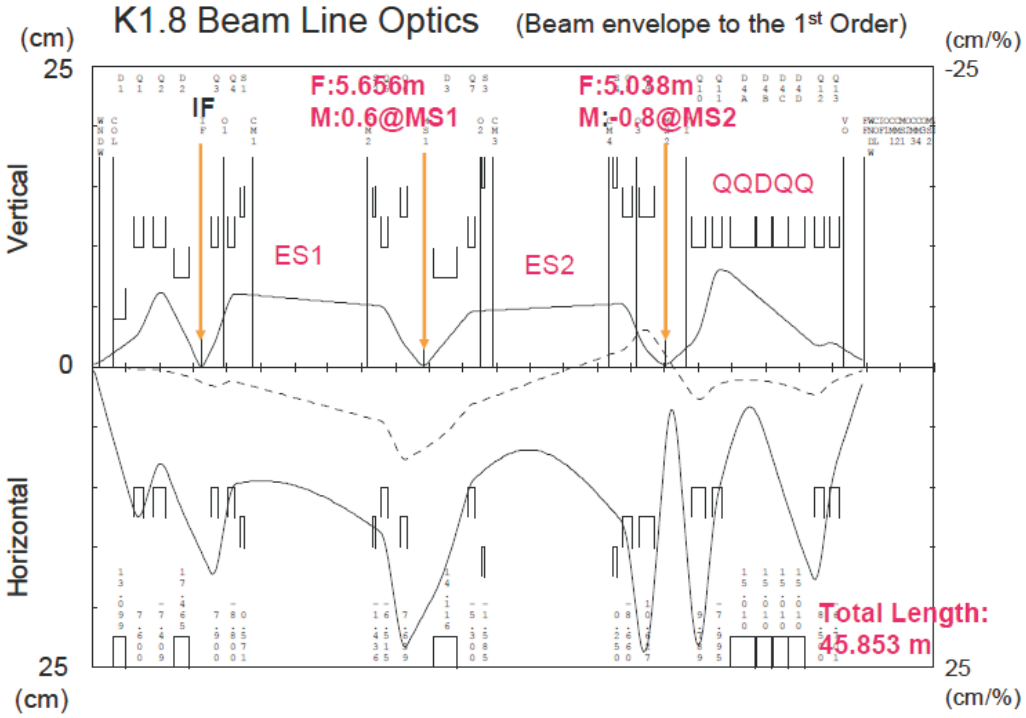

Figure 2.7: The beam envelopes for the condition of the beam momentum of 1.8 GeV/c.

Time structure of the beam

For the fixed target experiments, a uniform beam within an extraction period should be supplied to the experimental area. In the case of the present J-PARC, the beam orbit in MR is not stable and the extracted beam has a non-uniform time structure. It has pulse-like structure with intensity busts which are much higher than the flat distribution. Thus, counting rates of timing counters and tracking chambers often exceeded the limit of their operation. In addition, it was suspected that this caused a broken wires in chambers. Accordingly, the beam intensity was precisely adjusted within the operational level. Figure 2.8 shows a typical single rate per 100 μsec of a BH1 counter segment. BH1 is located just the downstream of the MS2 slit. Thus, the maximum intensity of 500 counts per 100 μsec corresponded to the instantaneous rate of 5 MHz. On the other hand, the horizontal line in the figure indicates average intensity ($\sim$45 counts per 100 μsec).

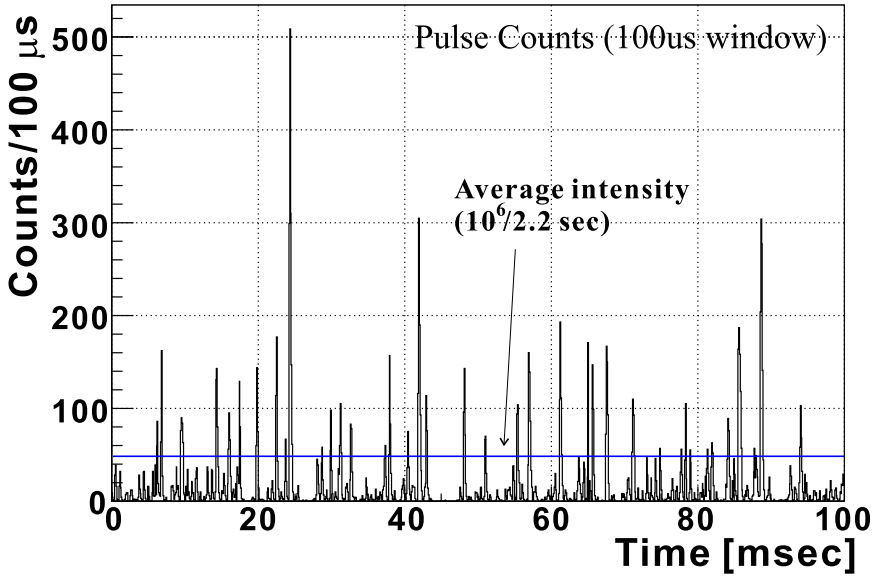

Figure 2.8: Typical single rate per 100 μsec of a BH1 counter segment for a certain spill. One bin was the number of counts in the time gate of 100 μsec.

We estimated an effective extraction time length over the extraction time of 2.2 sec as a duty factor (η) using the accidental coincidence rate between two counters (S_1, S_2) located separately from each other. The total counting number (N_1, N_2) and accidental counting (N_{acc}) between the two counters are described by the single (R_1, R_2) and accidental (R_{acc}) counting rate as,

$$N_1 = R_1 \times T \times \eta$$
$$N_2 = R_2 \times T \times \eta$$
$$N_{acc} = R_{acc} \times T \times \eta,$$

where T is the extraction time length. In addition, the accidental coincidence rate is calculated by

$$R_{acc} = R_1 \times R_2 \times \Delta_T,$$

where Δ_T is the coincidence width between two counters. Then, we obtain the duty factor as,

$$\eta = \frac{\Delta_T}{T} \times \frac{N_1 \times N_2}{N_{acc}}.$$

In the present experiment, the duty factor is $\sim$16%. However, as shown in Fig. 2.8, the ratio between the average and the maximum intensity was less than 10%. To avoid the drop of detection efficiency and the damage to the wire chambers due to high counting rates, the beam intensity was limited to $\sim 1.0 \times 10^6$/spill for the present experiment.

The duty factor is one characterizes of the beam structures. The realistic beam quality was needed to be estimated from multiplicity and accidental events by an offline analysis such as the beam line tracking and the scattered particle identification.

2.3 K1.8 beam line spectrometer

Overview

The end-part of the K1.8 beam line is used as a beam spectrometer [48] to analyze momentum and trajectory of each beam particle. The beam spectrometer is comprised of a QQDQQ magnet system and a set of tracking wire chambers and trigger counters located at the entrance and exit of the magnet system. Figure 2.9 shows the schematic view of the K1.8 beam spectrometer.

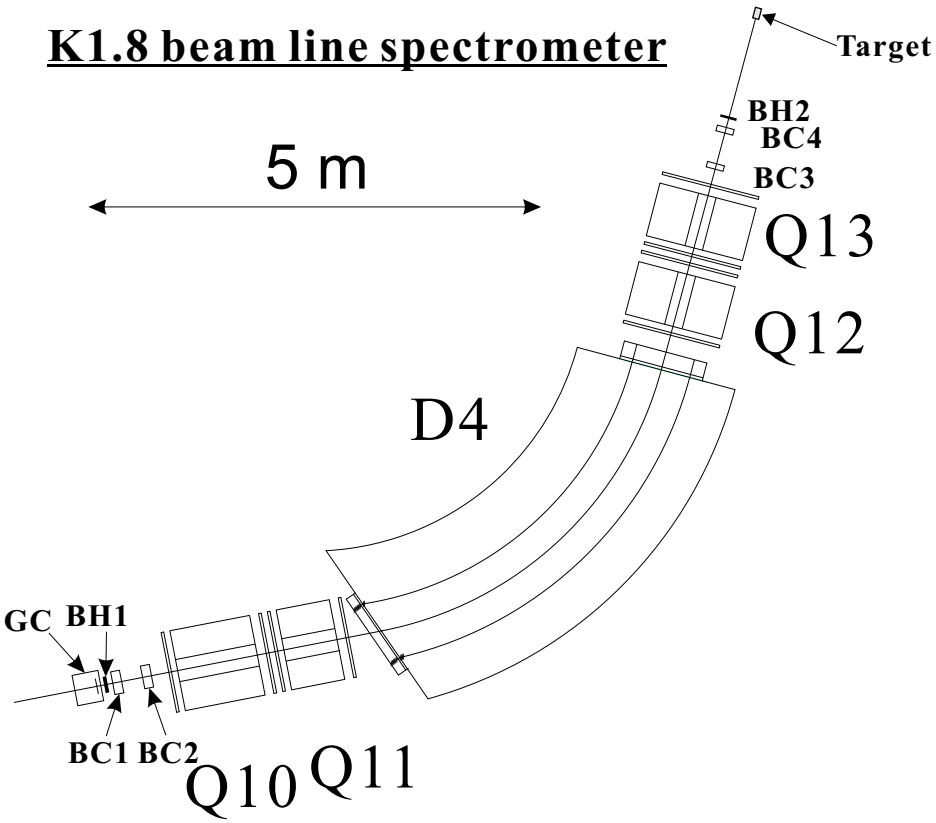

Figure 2.9: The schematic view of K1.8 beam spectrometer.

Beam trajectories are measured by two sets of wire chambers at the entrance (BC1,2) and exit (BC3,4) of the K1.8 beam line spectrometer for momentum analysis and reaction vertex reconstruction. The trigger counters consist of a isobutane-gas Čerenkov counter (GC) and two sets of horizontally segmented plastic scintillation counters (BH1, BH2). For the momentum reconstruction, a third-order transfer matrix was used. In order to minimize the multiple scattering effect on the momentum resolution, the $\langle x|\theta\rangle$ term of the transport matrix was tuned to be zero. The design momentum resolution is expected to be 3.3×10^{-4}(FWHM) with the position accuracy of 0.2 mm(rms) [48]. The magnetic field of the dipole magnet (D4) was monitored during the experiment with a high-precision Hall probe [Digital Teslameter 151 (DTM-151)] in order to correct its fluctuation in the offline analysis. The accuracy of the Hall probe is 1.7×10^{-6} [49]. The

observed fluctuation was less than 0.05%. Design specifications of the K1.8 beam line spectrometer are listed in Table 2.2.

Table 2.2: Design specifications of the K1.8 beam line spectrometer

Momentum resolution	3.3×10^{-4}(FWHM)
Maximum momentum	2.0 GeV/c
Bending angle	64°
Flight path (BH1−BH2)	10.4 m
Effective length (D4)	4 m

Trigger counters

Specifications of the trigger counters are listed in Table 2.3. Three sets of trigger counters (GC, BH1, BH2) are installed for particle identification.

Gas Čerenkov counter

The Čerenkov counter, GC [50], is installed at the most upstream of the K1.8 beam line spectrometer in order to reject electrons. Although the beam particles are selected by using the time-of-flight between BH1 and BH2, electrons (or positrons) cannot be separated from pions over the beam momentum of 1 GeV/c. Due to the narrow space between MS2 and BH1, the length of GC along the beam direction was needed to be less than 30 cm. The shorter length causes the smaller emission of the Čerenkov radiation. Thus, the pressured isobutane-gas (0.15 MPa) which has the higher transmittance was chosen. In addition, to increase the detection efficiency of GC, the UV transparent window PMT was used. The reflection mirror was a borosilicate glass evaporated with aluminum. In order to resist the oxidation of aluminum, the surface is coated by the manganese fluoride (MgF_2) which is transmissive to the ultraviolet-light region. The angles of the mirror and the PMT were optimized to converge the Čerenkov radiation. Figure 2.10 shows the schematic view of GC.

The number of photo-electron detected by GC was ∼5 to the electron with the momentum of more than 0.5 GeV/c. The efficiency of GC for electrons and positrons was found to be 99.5%. It was enough efficiency to reject the electron (or positron) contamination of 12−14% in the beam.

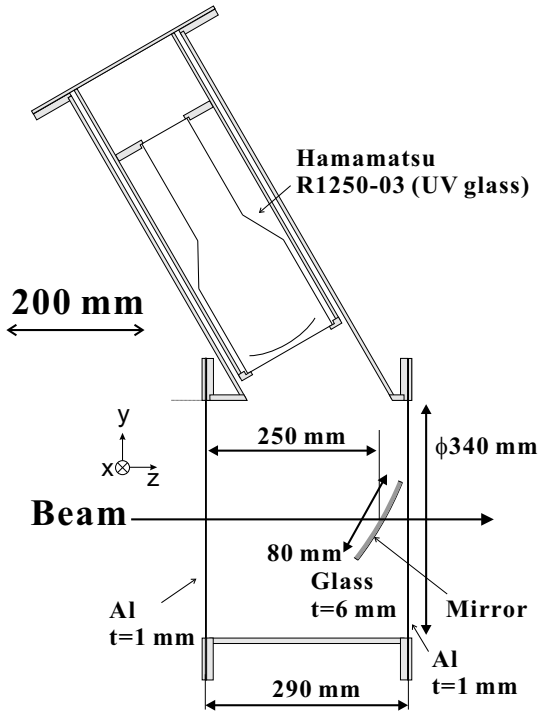

Figure 2.10: The schematic view of GC.

The BH1 and BH2 counter

By the time-of-flight measurement between BH1 and BH2, beam particles were identified. The required time-of-flight resolutions of both counters were less than 150 ps(rms) to separate kaons from pion at the momentum of 1.8 GeV/c.

BH1 (Fig 2.11) was a segmented plastic scintillation counter located just downstream of GC. It was segmented into 11 vertical pieces of 5 mm-thick plastic scintillators. The horizontal size of each segment was adjusted for the single counting rate of each segment to be uniform. Each segment was overlapped with its adjacent segments by 1 mm to avoid a dead space. Phototubes were connected on both ends of each segment and a high voltage power with a three-stage booster was supplied.

BH2 (Fig 2.12) was a segmented plastic scintillation counter located 120-cm upstream of the target to define the time zero for the timing measurement. It was segmented into 7 vertical pieces of 5 mm-thick plastic scintillators. BH2 was designed in a similar concept to BH1. The horizontal size of each segment was adjusted to equalize the single counting rate and each segment was overlapped with its adjacent segments by 2 mm. Phototubes with a three-stage booster were connected on both ends of each segment.

The time-of-flight resolution between BH1 and BH2 was measured to be $\sim$140 ps(rms) with the pulse-height correction. The required resolution was achieved.

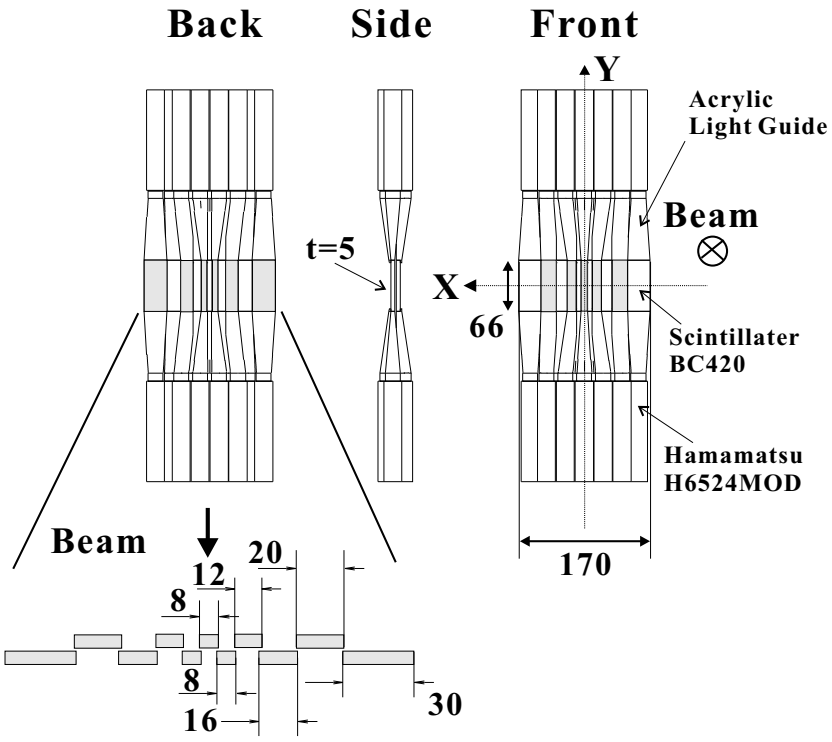

Figure 2.11: The schematic view of BH1.

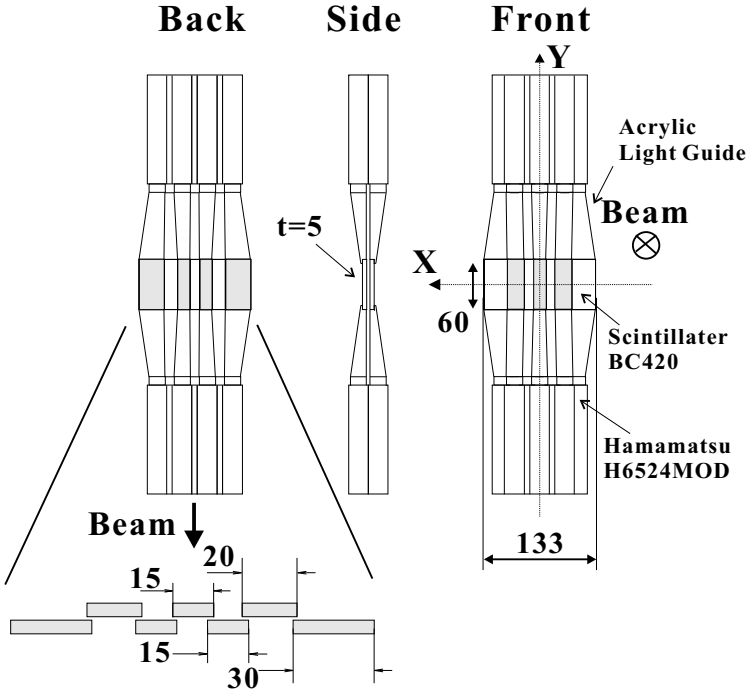

Figure 2.12: The schematic view of BH2.

Table 2.3: Specifications of the trigger counters

Name	Sensitive area W×H×T (mm)	Spec.	PMT (Hamamatsu)
GC	340×80(mirror), 290^L	iso-C_4H_{10}, n∼1.002 (1.5 atm)	R1250-03 (UV glass)
BH1	170×66×5	11 segments, 3-stage booster	H6524MOD
BH2	133×60×5	7 segments, 3-stage booster	H6524MOD
TOF	2240×1000×30	32 segments	H1949
AC1	1050×1200×113	Aerogel; n=1.06	R1584-02
AC2	1400×1400×113	Aerogel; n=1.06	R1584-02
LC	2800×1400×40	28 segments, Acrylic; n=1.49	H1949, H6410

Tracking chambers

Specifications of the tracking chambers are summarized in Table 2.4. MWPCs (BC1, BC2) were placed at the entrance of the K1.8 beam spectrometer and drift chambers (BC3, BC4) at the exit.

BC1·2(MWPC)

At the entrance of the K1.8 beam spectrometer, particle trackers should be operated under a very high counting rate of 10−20 MHz. In the previous KEK experiment, the chamber whose drift space was 2.5 mm was used at the entrance of the beam line spectrometer. The maximum counting rate of ∼0.2 MHz per wire was the limit of the operation without the efficiency drop at the total beam counting rate of 1.5 MHz. The expected horizontal and vertical beam size were 200 mm and 10 mm, respectively. The required wire spacing with the maximum counting rate of ∼0.2 MHz corresponded to 1 mm pitch, which could not be achieved by the drift chamber. Thus, MWPC with the anode pitch size of 1 mm and the cathode gap size of 3 mm was designed. The wire pitch size of 1 mm is near the technical limit to allow some space for soldering. The sense wire was a gold-plated 15 μm-diameter tungsten wire. In order to suppress damage of the cathode by discharge, the cathode planes are made of 20 μm-thick graphite pasted on 12 μm-thick aramid film. The cathode pitch size of 3 mm was determined by the balance between preventing discharge and keeping the gain with the lower voltage. The MWPCs had 6 layers (x, u, v, x, u, v), where u and v wires were tilted by $\pm 15^\circ$ with respect to the x wires. The front-end read-out electronics for both MWPC and MWDC were made of ASD (Amplifier-Shaper-Discriminator) chips with 16 ns integration time developed for ATLAS Thin Gap Chamber [51]. The timing information of the BC1·2 hit was digitized by the MWPC encoder installed in the COPPER modules [54] as described in Sec. 2.6.

BC3·4

At the exit of the K1.8 beam spectrometer, the wire chambers have to be operated under several MHz. The expected horizontal and vertical beam size were 150 mm and 10 mm, respectively. The required wire spacing with the maximum counting rate of ∼0.2 MHz corresponded to 3 mm. Thus, we made a new drift chamber (MWDC) with an anode wire pitch of 3 mm, which was used for BC3. Figure 2.13 shows the cell structure of BC3. For BC4, we used a drift chamber with the anode wire pitch of 5 mm used in the previous KEK-PS experiments [47]. For both BC3 and BC4, the sense wire was a gold-plated 12.5 μm-diameter tungsten wire and the field wire was a gold-plated 75 μm-diameter copper-beryllium wire. The cathode planes of BC3 are made of 20 μm-thick graphite pasted on 12 μm-thick aramid film. The optimal cathode pitch size was 1.7 mm based on the studies from the previously used drift chamber with the anode wire pitch of 5 mm. By considering the manufacturing accuracy, the pitch size was determined to be 2 mm. The drift chambers have 6 layers (xx', uu', vv'), where u and v wires were tilted by $\pm 15^\circ$ with respect to the x wires. The wire position of each pair plane was shifted by a half of the cell size. The timing information of the BC3·4 hit was digitized by the TKO Multi-hit TDC module as described in Sec. 2.6.

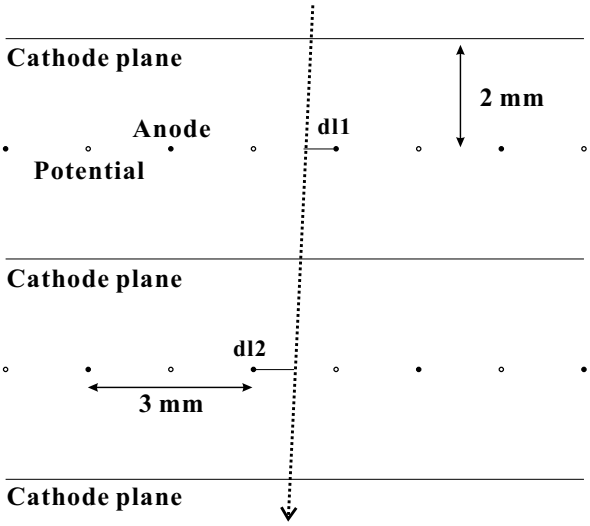

Figure 2.13: The cell structure of BC3.

Operation of MWPC and MWDC

Figure 2.14 shows the plateau curve of one of the MWPC(BC1) (a) and MWDC(BC3) (b) layer as a function of the cathode plane high voltage. The curve was measured by the low intensity π beam (∼10 kHz). The gas mixture for both MWPCs and drift chambers was Ar(76%)+C_4H_{10}(20%)+Methylal(4%). At first, the operation voltage of MWPC was set to be −2.55 kV, but the over current and the broken wire occurred at this high voltage because of the poor beam structure. Thus, we set the MWPC high voltage to −2.51 kV which kept the stable operation. In the present experiment, the MWPCs could

be operated under the counting rate of ∼8 M/spill. MWDC was operated at the cathode and potential wire high voltage of −1.23 kV and the−1.25 keV, respectively. The BC4 which was previously used in the KEK experiment was operated at both cathode and potential wire high voltage of −1.40 kV. The same high voltage as of the previous KEK experiment was used.

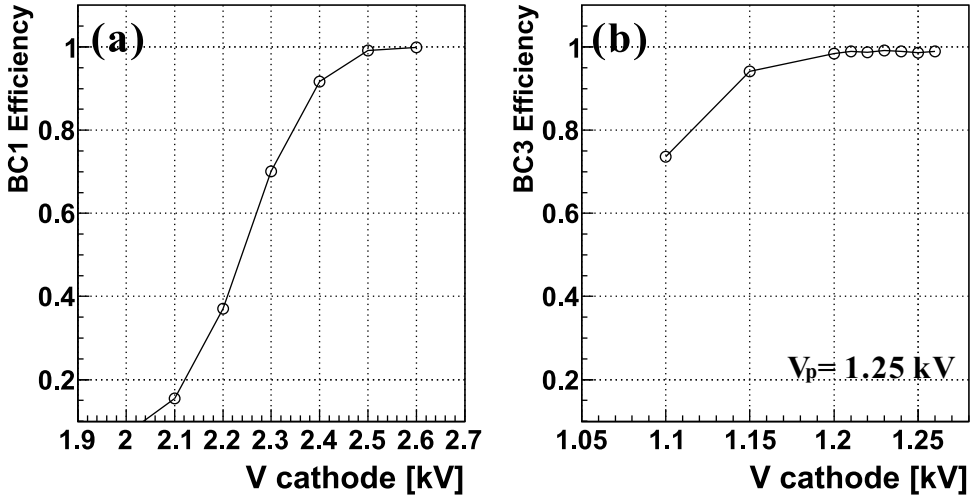

Figure 2.14: The plateau curve of one of the MWPC(BC1) (a) and BC3 (b) layer as a function of the cathode plane high voltage.

Table 2.4: Specifications of the MWPC(BC1, BC2) and the drift chambers.

Name	Area W×H (mm)	Anode pitch or Drift length (mm)	Wires	Angle (x, u, v) (°)	Resol. (μm in r.m.s)
BC1	256×150	1 mm pitch	$xuvxuv$	0, +15, −15	300
BC2	256×150	1 mm pitch	$vuxvux$	0, +15, −15	300
BC3	192×150	1.5	$xx'uu'vv'$	0, +15, −15	200
BC4	240×150	2.5	$vv'uu'xx'$	0, +15, −15	200
SDC1	192×150	1.5	$vv'uu'$	0, +15, −15	200
SDC2	400×150	2.5	$vv'uu'xx'$	0, +15, −15	200
SDC3	2140×1140	10	$vxuvxu$	0, +30, −30	300
SDC4	2140×1140	10	$vxuvxu$	0, +30, −30	300

Gas mixture (BC1−4, SDC1·2); Ar(76%) + C_4H_{10}(20%) + Methylal(4%)
Gas mixture (SDC3·4); Ar(50%) + C_2H_6(50%)

2.4 Scattered-particle spectrometer (SKS)

Overview

The SKS spectrometer had been originally used in the KEK-PS K6 beam line [47]. It was designed to be optimal for the Λ hypernuclear spectroscopy experiment. SKS has a good momentum resolution of an order of 10^{-3} ($\Delta p/p$) together with a large acceptance of 100 msr. In order to decrease the in-flight decay of kaon, the flight path was designed to be as short as 5 m. Those characteristics were achieved by the unique specification of the SKS magnet as listed in Table 2.5. The high energy resolution and high statistic experiments were realized by the SKS spectrometer.

Table 2.5: Specifications of the SKS magnet.

Maximum magnetic field	2.5 T
Stored energy	6.3 MJ
Pole gap	49.75 cm
Conductor	NbTi/Cu
Ampere turn	2.1 MA·T
Maximum current	400 A
Total weight	280 t

The SKS magnet was moved to the J-PARC K1.8 beam line. The cooling system was changed to be a GM-JT cryo-coolers [45]. The SKS spectrometer was modified and reconstructed for the J-PARC experiments with new detectors to increase the momentum acceptance and the tolerance to high counting rate, while keeping the design concept of the previous SKS spectrometer (high resolution and large acceptance). Figure 2.15 shows the present SKS spectrometer. The design parameters of the new SKS are summarized in Table 2.6. Using the downstream detectors having the twice larger horizontal size than the previously used detectors, the maximum momentum acceptance of SKS is increased up to 1.1 GeV/c from the previous setup of 0.8 GeV/c at the magnetic field strength of 2.5 T, while the solid angle of 100 msr and the angular coverage of up to 20 degree are kept. The design value of the momentum resolution is of the order of 10^{-3}. From the experimental requirements, such a wide momentum range with high momentum resolution is essential. The SKS consists of drift chambers (SDC1−4) for the momentum reconstruction, a plastic scintillation counter wall (TOF), two stage of silica aerogel Čerenkov counters (AC1,2), and a Lucite (Acrylic) Čerenkov counter (LC) for a particle identification (Fig. 2.15). The effective areas of the TOF and LC counters were increased, but AC1 and AC2 were installed without a modification.

The particle momentum was reconstructed by Runge-Kutta calculation method from the hit information of drift chambers and a calculated magnetic field map (Appendix A). In order to reduce multiple scattering effects on the momentum resolution, we installed helium bags in the spaces along the particle trajectory (the SKS pole gap and the space between SDC3 and the SKS magnet). The magnetic field was monitored with an NMR

probe during the experiment to correct for the fluctuation of the field in the offline analysis. The accuracy of the NMR probe is 1.0×10^{-6} [52]. For this experiment, the magnetic field strength of 2.5 T (400A) was mainly used.

Table 2.6: Design specifications of the new SKS spectrometer at 2.5 T mode.

	Present SKS	Original SKS
Momentum resolution	0.1% FWHM (0.8 GeV/c)	0.1% FWHM (0.8 GeV/c)
Maximum momentum	1.1 GeV/c	0.85 GeV/c
Momentum range	0.75−1.10 GeV/c	0.75−0.85 GeV/c
Bending angle	100°	100°
	for central trajectory	for central trajectory
Solid angle	120 msr	100 msr
Flight path	∼6.0 m	∼5.5 m
	for central trajectory	for central trajectory

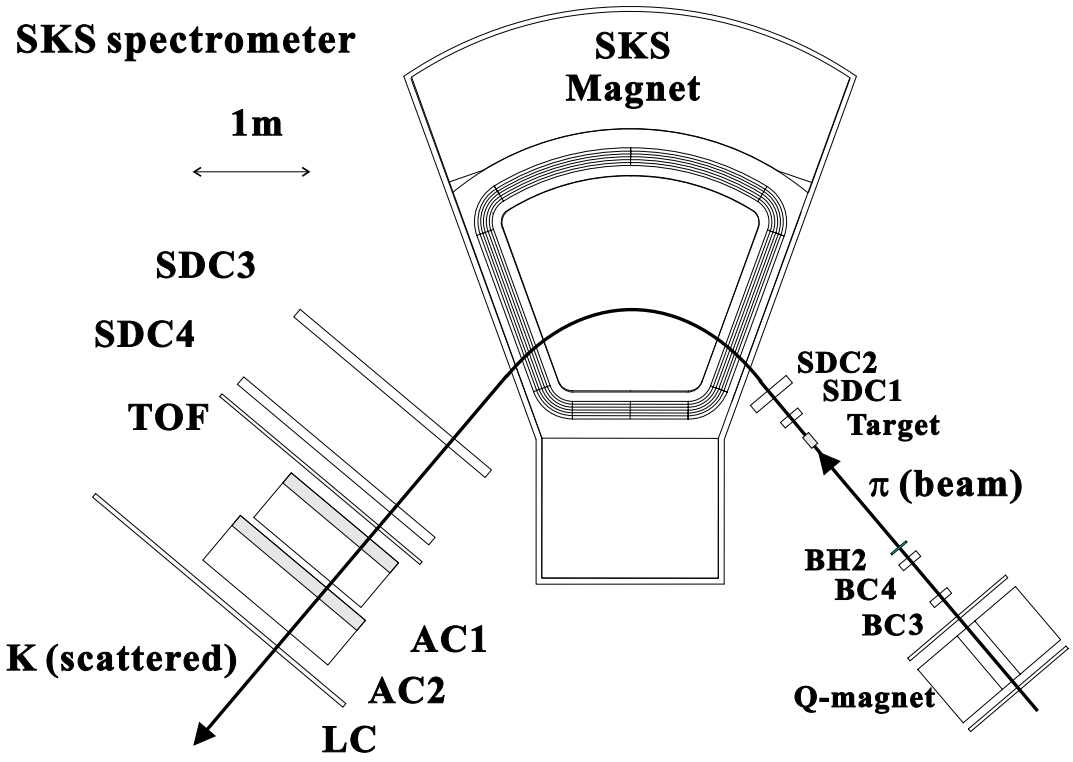

Figure 2.15: Detector components of SKS. The downstream detectors were about twice larger than the previous setup [47] for increasing the maximum momentum acceptance. SDC1–4 were drift chambers. TOF was a plastic scintillation counter hodoscope for the Time-Of-Flight measurement. AC1, 2 were aerogel Čerenkov counters (n=1.06). LC was a Lucite (Acrylic) Čerenkov counter (n=1.49).

Trigger counters

Specifications of the trigger counters are listed in Table 2.3. In the trigger, a combination of three kinds of trigger counters were used to identify pions, kaons and protons. The TOF counter is sensitive to charged particles, AC1 and AC2 are sensitive only to pions, and LC is insensitive to protons. In order to increase the acceptable momentum range, the TOF and LC counter of twice larger in the horizontal size than that of the previous KEK experiment were constructed.

TOF

TOF is a segmented plastic scintillation hodoscope located at just a downstream of SDC4 to identify scattered particles by the time-of-flight measurement with BH2. The TOF counter was horizontally segmented into 32 pieces of $70\times1000\times30$ mm^3 scintillators. The present TOF consisted of 17 new and 15 previously used counters in KEK. The signal of each segment was detected by fast phototubes (H1949) on the top and bottom sides. The typical time-of-flight resolution between TOF and BH2 was measured to be 150 ps(rms), including the time resolution of both counters. This is enough to separate the scattered pions, kaons and protons.

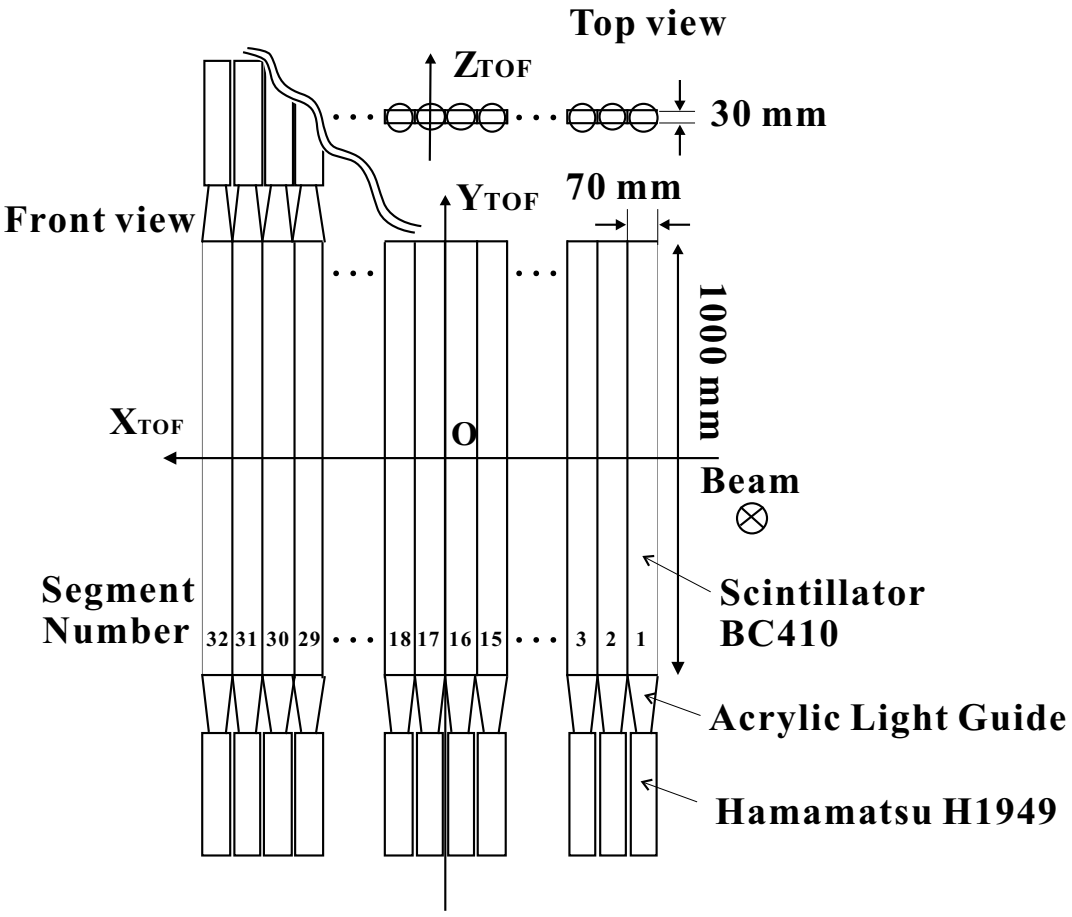

Figure 2.16: The schematic view of TOF.

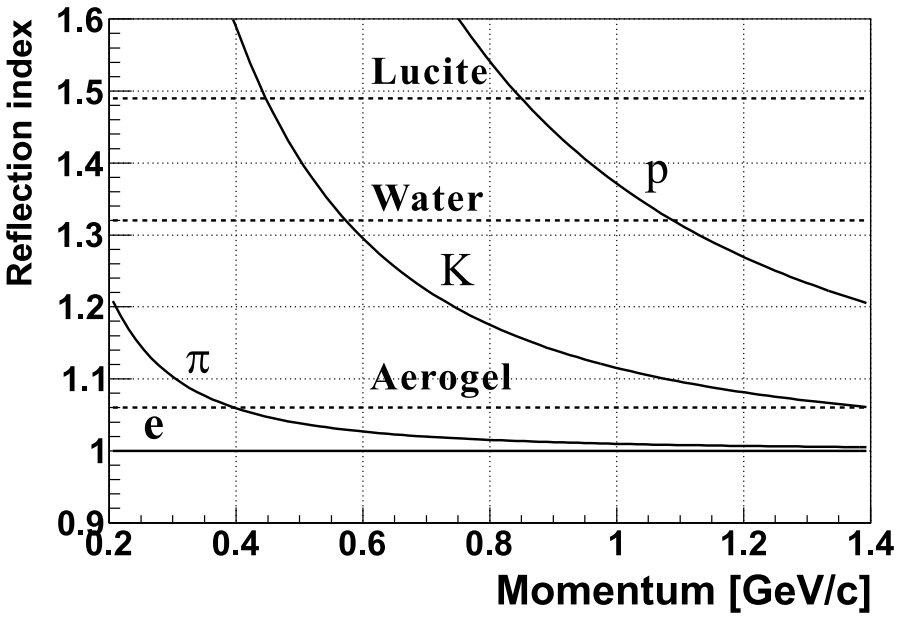

Figure 2.17: Threshold and reflection index for Čerenkov radiation as a function of the momentum.

AC1·2

AC1·2 are threshold-type silica aerogel Čerenkov counters to reject pions in the trigger level. As shown in Fig. 2.17, pions with a threshold of 0.4 GeV/c were rejected by the reflection index of silica aerogel of 1.06. AC1 and AC2 were installed just behind the TOF counters. Figure 2.18 shows a schematic view of AC2. The sensitive area of AC1 was 1050×1200×113 mm^3 and that of AC2 was 1400×1400×113 mm^3. For the uniform efficiency without any dead space over a large sensitive area, AC2 was not segmented but of a large one-box type. On the other hand, the AC1 radiator box has a horizontal partition which makes an insensitive region. Phototubes which were sensitive to a single photon were placed on both side. The number of photoelectrons was typically ∼6 over the whole area for 0.85 GeV/c π.

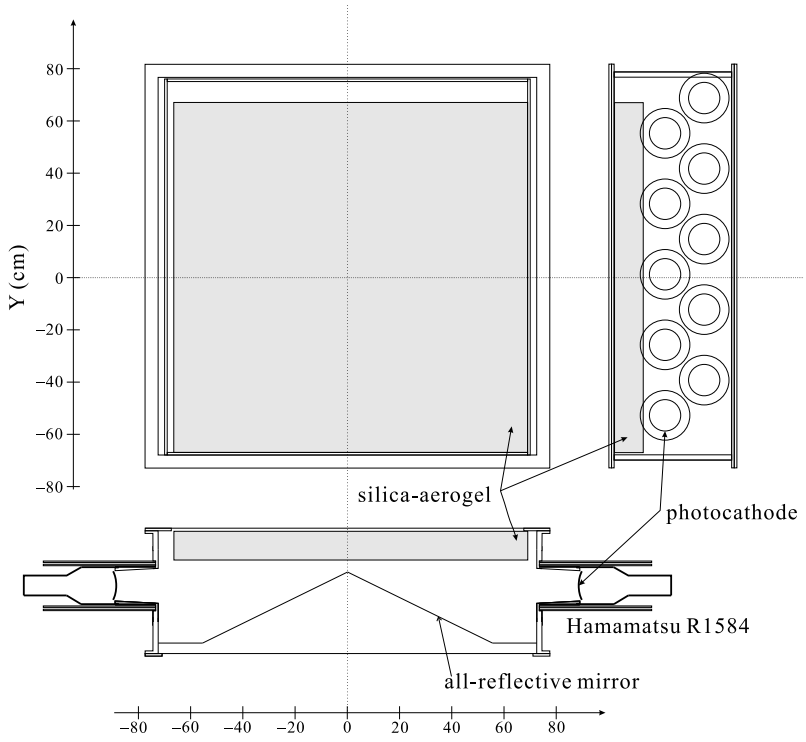

Figure 2.18: The schematic view of AC2.

LC

LC is a threshold-type Čerenkov counter installed just downstream of AC2. It was segmented into 28 vertical pieces of 100×1400×40 mm^3 Lucite (Acrylic) radiator with the reflection index of 1.49. The present LC consists of 14 new and 14 previously used counters in KEK. Each segment is equipped with fast phototubes on the top and bottom sides. In the Acrylic radiator, a wavelength shifter of bis-MBS was mixed by 10 ppm in weight in order to uniformly radiate photons to keep the detection efficiency for various incident angles. On the other hand, due to the scintillating radiation of the wavelength shifter, several percent of protons were detected below the threshold. As shown in Fig. 2.17, most of protons slower than 0.85 GeV/c were rejected.

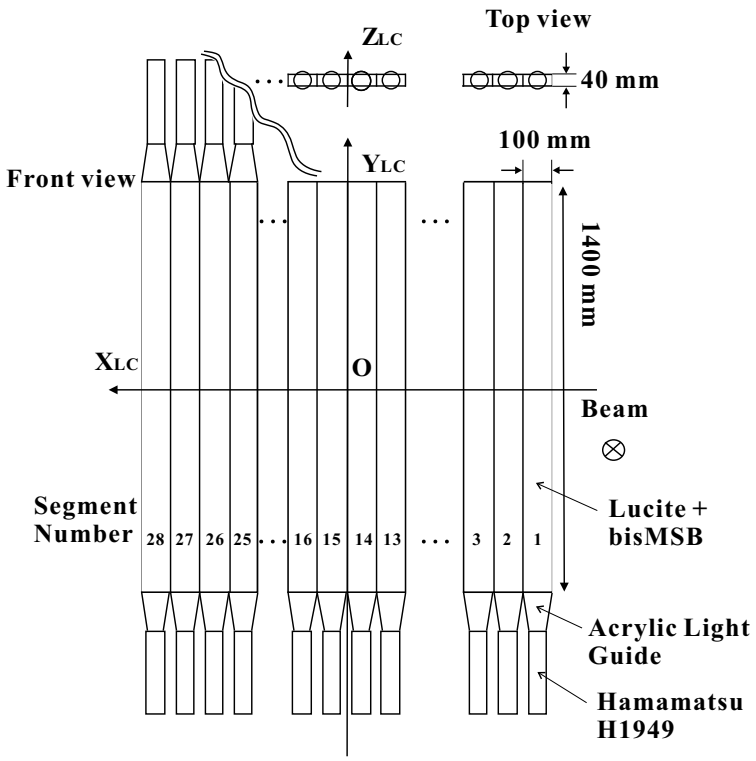

Figure 2.19: The schematic view of LC.

Tracking chambers

Specifications of the tracking chambers are summarized in Table 2.4.

SDC1·2

SDC1 and SDC2 are the new drift chambers installed at the entrance of the SKS magnet. The anode wire pitch of the SDC1 was 3 mm and that of the SDC2 was 5 mm. The structure of the SDC1 was the same as that of the BC3. The SDC2 is similar to SDC1 except for its wire spacing. For both SDC1 and SDC2, the sense wire was gold-plated 12.5 μm-diameter tungsten wire, and the field wire was gold-plated 75 μm-diameter copper-beryllium wire, and the cathode planes were made of 20 μm-thick graphite pasted on 12 μm-thick aramid film. The SDC1 had 4 layers of uu', vv' and the SDC2 had 6 layers of xx', uu', vv', where u and v wires were tilted $\pm 15^\circ$ with respect to the x wires. Since the SDC1 and SDC2 were in line with the beam, the gas mixture and read-out electronics were the same as those of beam line chambers.

SDC3·4

SDC3 and SDC4 are located at the exit of SKS. In order to increase the acceptable momentum range and to cover a large scattering angle, it was necessary to install large drift chambers at the exit of the SKS magnet. For this propose, we moved drift chambers which had been used in the AGS-BNL experiments to the J-PARC K1.8 beam line as

SDC3 and SDC4. The size of the effective area was 2140×1140 mm^2, being twice larger in length than in the previous SKS. All anode wires were replaced to the larger diameter (20μm $\rightarrow$ 25μm) wires for more strength. The drift space was 10 mm and its cell structure is shown in Fig. 2.20. The anode wire was a gold-plated 25 μm-diameter tungsten wire, and both field wire and cathode wire were gold-plated 80 μm-diameter copper-beryllium wire. The pith of the cathode wires was 2 mm. SDC3 and SDC4 had 6 layers (x, x, u, u, v, v), where u and v wires were tilted $\pm 30^\circ$ with respect to the x wires. The front-end read-out electronics of SDC3·4 was made of ASD chips. The timing information of the SDC3·4 hit was digitized by the TKO Dr.TII TDC module as described in Sec. 2.6.

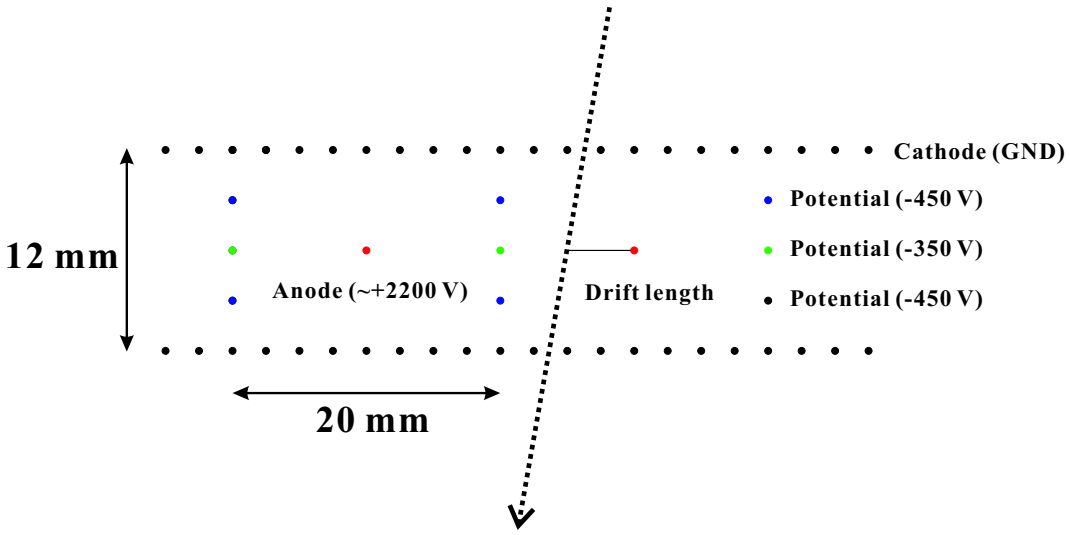

Figure 2.20: The cell structure of SDC3·4.

Operation

Figure 2.21 shows the plateau curve of one of the SDC3 and SDC4 layers as a function of the anode wire high voltage. The curve was measured by the low intensity π beam (~10 kHz). The high voltage of potential wires was -350 V and -450 V. In the experiment, the anode high voltage was set at +2.2 kV. The gas mixture was Ar(50%)+C_2H_6(50%).

The beam particles with momentum less than 1.5 GeV/c passed through SDC3 and SDC4. In the present experiment, the instantaneous beam intensity was over the operational limit of SDC3·4. The area where the beam passed through could not be used. The high voltage lines of the anode wires were divided and the high voltage was not supplied to some anode wires where the beam passes through. By identifying precisely the beam passing area, the chamber acceptance was not affected. Therefore, the momentum range and acceptance were not significantly reduced.

The operation of SDC1·2 were the same as of BC3·4.

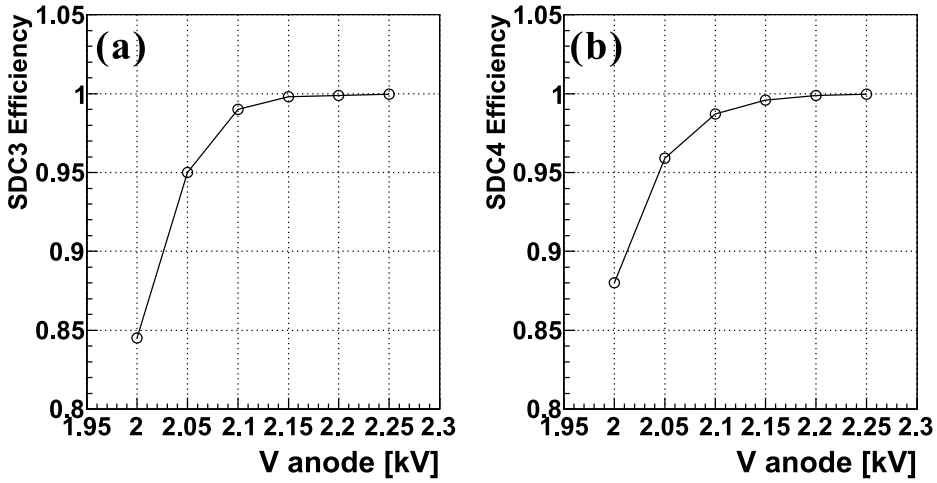

Figure 2.21: The plateau curve of one of the SDC3 (a) and SDC4 (b) layer as a function of the anode wire high voltage.

2.5 Trigger

In this experiment, we used the (π, K) and several other triggers for obtaining various kinds of calibration data. For the (π^-, K^-) reaction, the 2-dimensional matrix trigger was used. This trigger is made of a particular combination of the TOF and LC segment and help to reduce the DAQ dead time.

The (π, K) trigger

To select the true (π, K) reaction event from large backgrounds, such as the (π, π) and (π, p) reactions, the trigger system of the SKS was constructed as follows. A typical cross section of the background reactions were two or three orders of magnitude larger than that of the (π, K) reaction. In addition, muons from beam decay had to be rejected if the non-charge exchange reaction was used.

The π beam trigger was defined as:

$$BEAM \equiv \overline{GC} \times BH1 \times BH2.$$

BH1 and BH2 had two PMTs at both end, and then mean timer modules were used to remove the incident position dependence of the trigger timing. The coincidence timing between BH1 and BH2 was adjusted with a coincidence width less than 5 ns. The proton contamination was completely rejected by precisely adjusting the coincidence timing between BH1 and BH2 for pions. This was possible for the momentum of less than 1.5 GeV/c, which corresponds to the time difference between BH1 and BH2 of $\sim$7 ns.

The (π, K) trigger was defined as:

$$PIK \equiv BEAM \times TOF \times \overline{AC1} \times \overline{AC2} \times LC.$$

Mean timer modules were also used for the same reason for the TOF and LC counters. The PIK trigger logic diagram is shown in Fig. 2.22.

In addition, the size of AC1·2 was smaller than that of TOF and LC. For the present experiment, the TOF and LC segments used in the trigger were restricted after precise adjustment of their coverages considering the scattered particle momentum and the trigger rate. The coverages of TOF and LC were from the segment number 11 to 32 (last) and from 10 to 28 (last), respectively

The BH2 timing was used as the STOP signal of the TDC's for BCs and SDC1,2, while the TOF timing was used as stop for SDC3,4 because the flight time from BH2 to TOF varies according to the flight path and momenta of scatted particles.

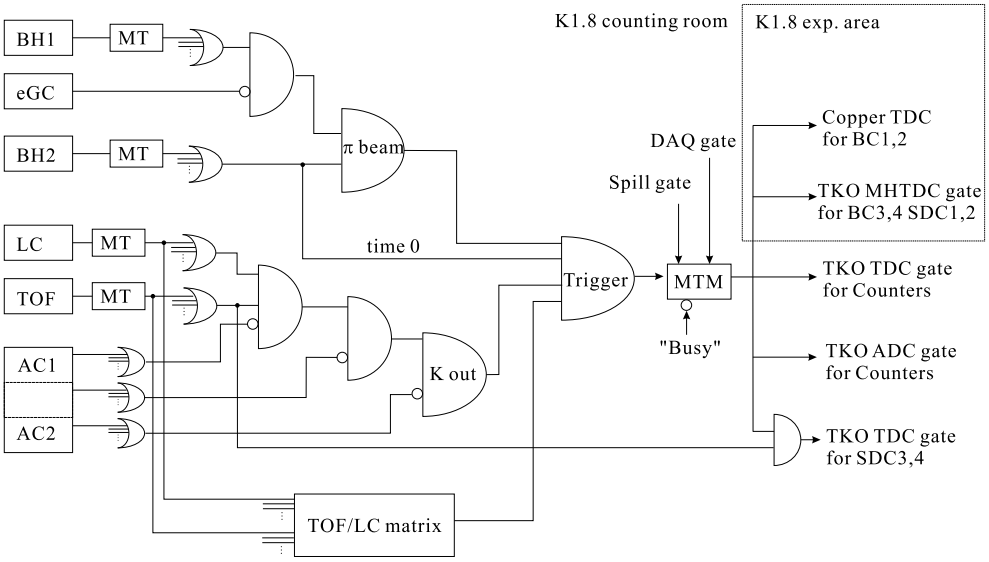

Figure 2.22: The PIK trigger logic diagram.

The matrix trigger

For the (π^-, K^-) reaction with the momentum of 1.92 GeV/c, we found background particles which were produced after the beam hits the coil vessel of the SKS magnet. Those particles passed the TOF and LC counters and contaminated the (π^-, K^-) trigger, because they were mostly of low momentum pions whose velocity was higher than that of the LC threshold, but below the threshold of AC1 and AC2 resulting in as a fake kaon. Figure 2.23 shows beam trajectories with a beam momentum of 1.92 GeV/c which are generated by the Geant4 code by taking account of the beam profile and momentum bite measured in the experiment. The beam was found to hit the edge of the coil vessel. From this simulation, the ratio between the number of beams hitting the SKS magnet and the total beam number was estimated to be ∼10%.

Figure 2.24 shows the hit pattern of TOF for the (π^-, K^-) reaction data. The black and red lines were all the PIK trigger and the true scattered K events, respectively. The true K events were selected by the SKS tracking analysis. The typical trigger rate of the

(π^-, K^-) reaction with the beam momentum of 1.92 GeV/c was ∼1 k/spill, which could not be acceptable for the DAQ system. The trigger rate had to be less than 0.4 k/spill.

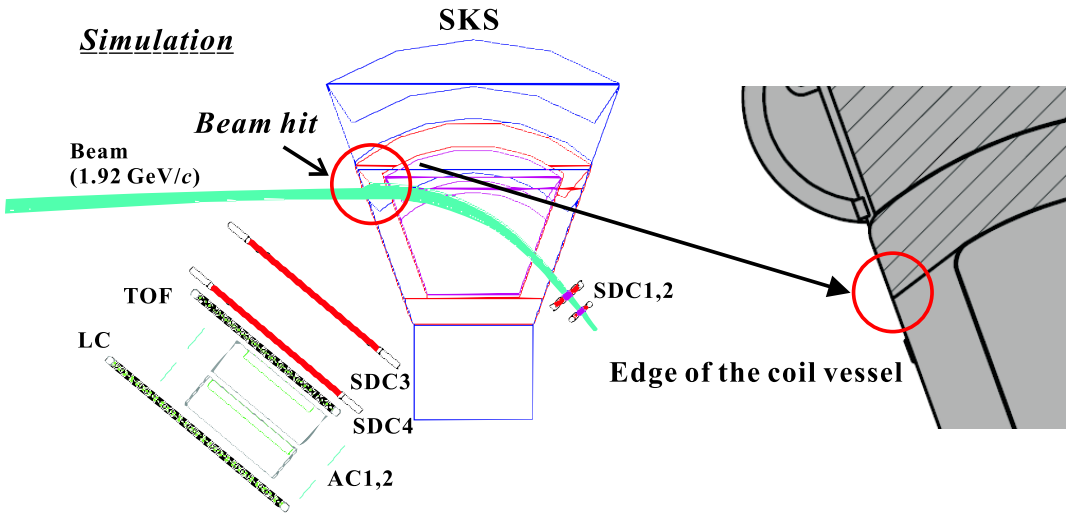

Figure 2.23: The beam trajectories in the SKS magnet with the beam momentum of 1.92 GeV/c (simulation).

Since those events could not be rejected by using the PIK trigger only, we applied a matrix coincidence trigger using the combinations between the TOF and LC counter. The trajectories of the background particles were localized and thus are reflected as a particular position of TOF and LC counters. Figure 2.25 shows typical trajectories of the background particles and the relation between the segment ID of TOF (TOF_i) and LC (LC_j) counters. This positions corresponded to a particular segment ID of TOF and LC counters and their combination. Due to the beam hitting the edge of the coil vessel, this hitting point can be regarded as a point source of the background particles. Thus, the particles were radially emitted. In the figure, the segment ID of the TOF and LC counter are shown. The central track of scattered K was also shown (0.85 GeV/c). The main contribution of the background events distributed over $TOF_i - LC_j = -1 \sim 1$, while the true K events $TOF_i - LC_j = 1 \sim 10$. By requiring the coincidence between those special combination of TOF and LC segments, we can reject the background events from the PIK trigger, because the incident angles of the background particles were different from those of true scatted particles. The combination of TOF and LC segments were determined segment by segment.

For constructing a matrix trigger, we used a FPGA module called TUL (Tohoku Universal Logic Module) [53]. All K^- hit combinations between particular segments were examined in TUL and a "true hit" signal was generated with a delay of 20 ns. It was much faster than the PIK trigger generated by NIM modules. Figure 2.26 shows the selected combination of the TOF and LC segments. In the figure, the selected region is indicated by solid lines and the background events are located out of the region. The number of the background events was scaled to be 1/1000. The trigger rate was decreased from ∼800 /spill to ∼150/spill at the beam intensity of 1 M/spill for the

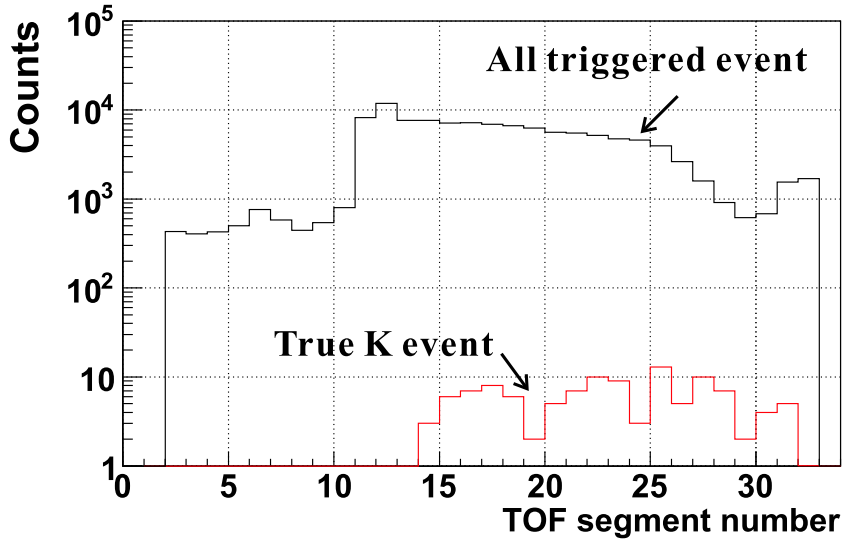

Figure 2.24: The hit pattern of TOF for the (π^-, K^-) reaction data. The data of one run (number of irradiated π^-: 3×10^8) are shown.

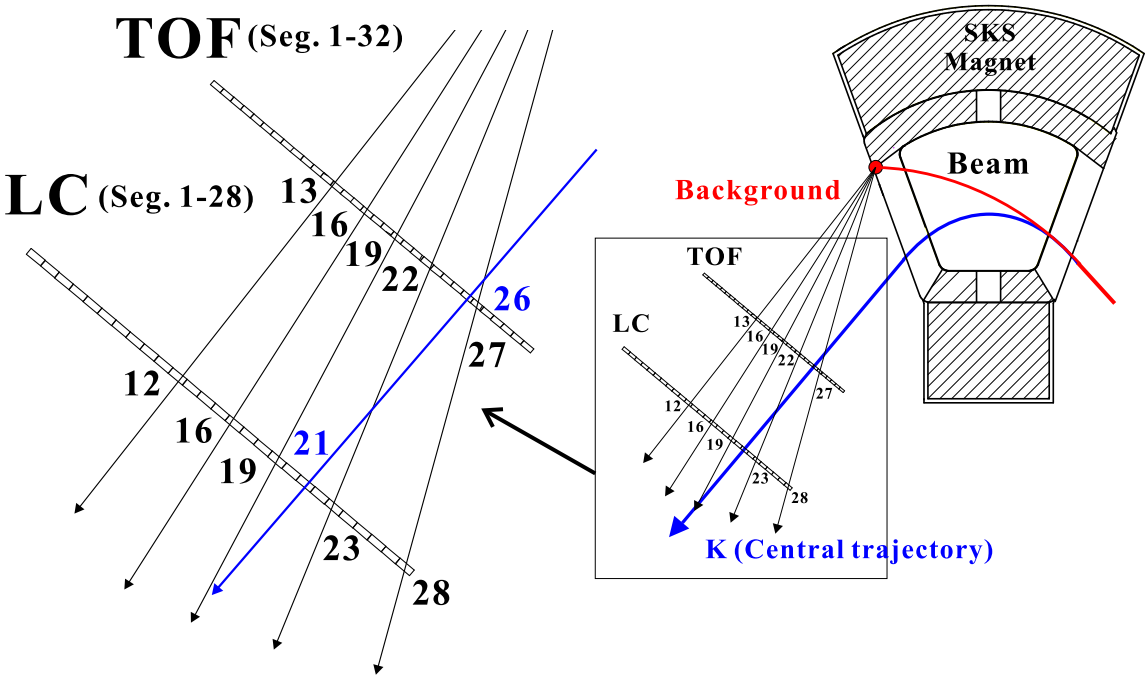

Figure 2.25: Typical trajectories of the background particles and the relation between the TOF and LC segment. The number of hit segments of the TOF and LC counter are shown. The background particles only passed through the special combination between the TOF and LC segment ($TOF_i - LC_j = -1 \sim 1$). The central track of scattered K was also shown (0.85 GeV/c).

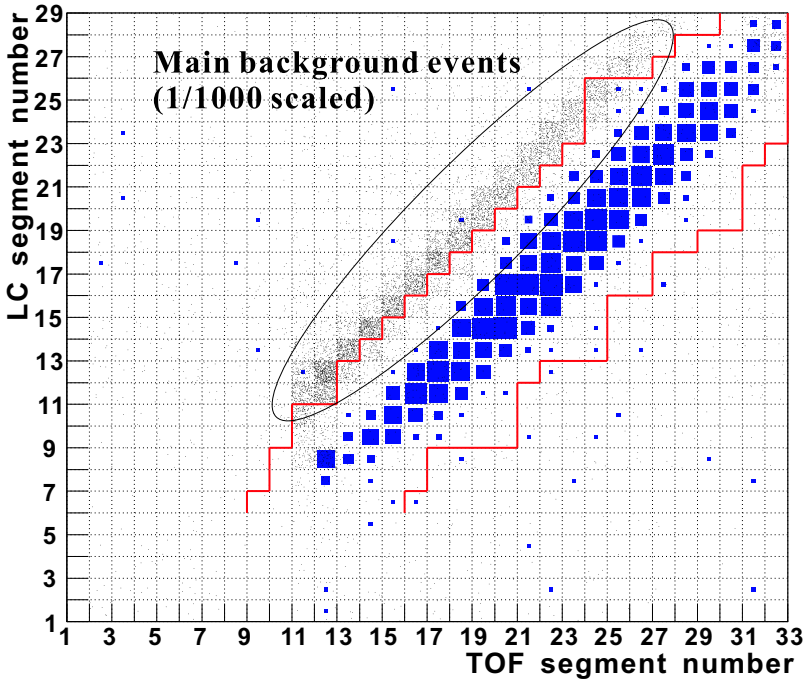

Figure 2.26: The selected region for the matrix trigger was indicated in red lines. The K^- events are shown in blue squares. The main distribution of the background events ($N_{TOF\ seg.} - N_{LC\ seg} = -1 \sim 1$) are indicated by circle.

(π^-, K^-) reaction with the liquid hydrogen target. This trigger rate was lower than the acceptable rate of the DAQ system. In the (π^-, K^-) data, we included the pre-scaled PIK trigger (1/10) without the matrix coincidence to study inefficiency of the matrix trigger.

The typical trigger rate for the (π^-, K^-) data was ∼350 /spill including the pre-scaled PIK, the (π^-, π^-) and the BEAM trigger.

2.6 Data-acquisition system

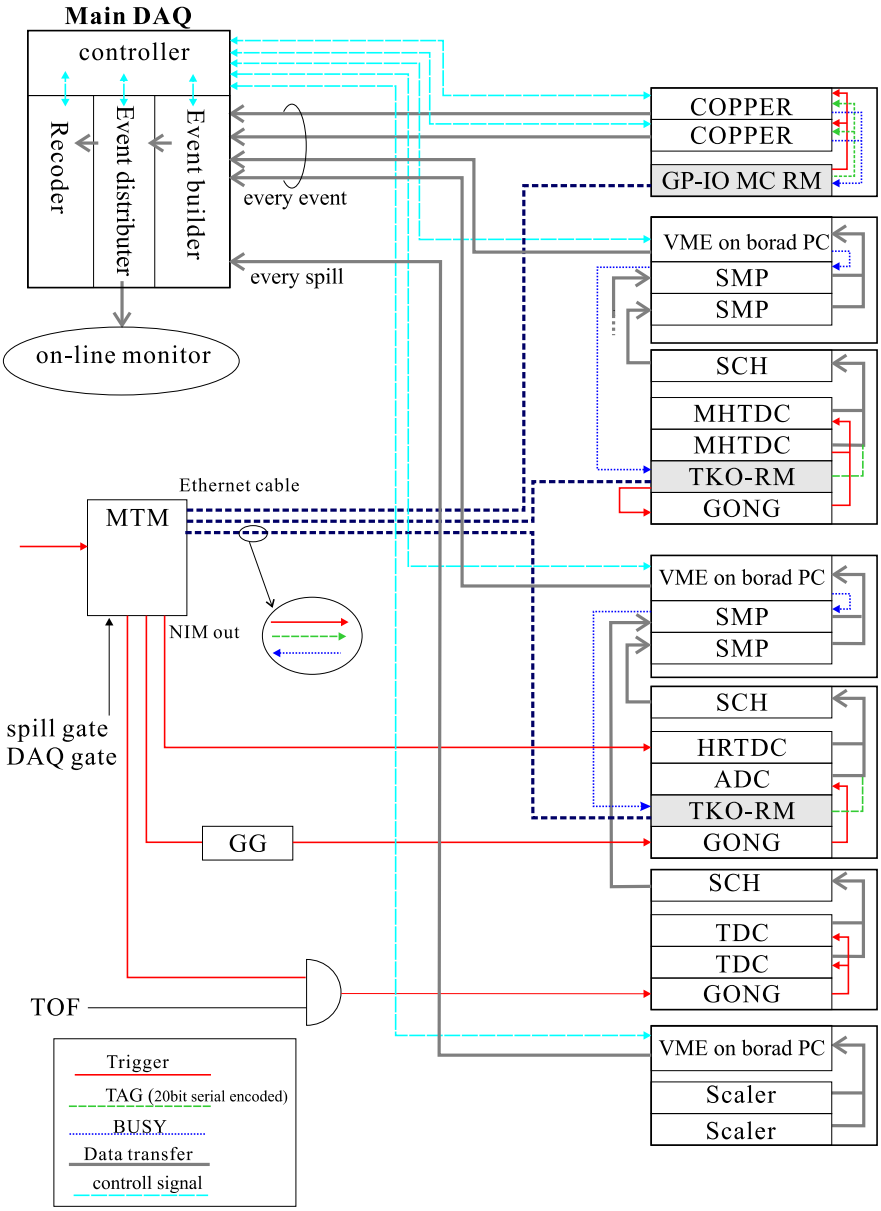

Figure 2.27: The diagram of the data-acquisition system.

Figure 2.27 shows a diagram of the data-acquisition system. The raw signals of trigger counters and SDC3·4 were digitized with the TKO TDC and ADC modules and the TKO TDC (Dr.TII) modules, respectively, while the signals of BC3·4 were digitized with the TKO Multi-hit TDC (MHTDC) modules. For the TKO modules, those digitized signals were transfered to the VME-SMP (Super Memory Partner) which was installed in the VME box together with a VME-CPU module. Then, the data were read out by the VME-CPU module and transfered to the host computer. This TKO system was a conventional one used by the previous KEK experiment [47]. The timing information of the BC1·2

hit was digitized by the MWPC encoder installed in the COPPER modules. COPPER (COmmon Pipelined Platform for Electronics Readout) [54] is a new platform module for the KEK-VME specification that realizes various types of analog-to-digital conversion and pipelines digital data processing functions within a unified scheme. Although the COPPER is a slave VME module, it works as a standalone system without any additional VME processor on the VME bus. The BC1·2 data on the COPPER modules were directly transfered to the host computer. The data-acquisition cycle was processed event by event. The single counting of each trigger counter was recorded by VME scalars. The scale data were transfered at the end of spill.

For the early stage of J-PARC hadron experiments, we needed to use several conventional DAQ subsystems, such as CAMAC, FERA and TKO, together with a new network oriented DAQ module, KEK-VME/COPPER. It was necessary to integrate these different data acquisition readouts. In addition, most readout systems (VME-CPU and COPPER) have network interfaces and communicate via the TCP/IP protocol. Under this situation, we developed a network-based DAQ system [55] with a DAQ software using the TCP/IP protocol and a trigger/tag distribution system.

For building up an event by combining data sets coming from the different modules, we needed to write the event number and the spill number to each data set and to check their consistency event by event in the event building. For this purpose, we developed a trigger/tag distribution system. When the trigger (e.g. the PIK trigger) signal was generated, the Master Trigger Module (MTM) accepted the trigger signal and distributed the event and spill numbers to Receiver Modules (RM) in each node by using the Ethernet cables. After finishing the analogue to digital conversion of all the modules in each node, MTM distributed the read-out signal to all the RMs and the event data with the same event and spill numbers were transfered to the host computer. The event and spill numbers were distributed to the data bus by RM in each node. The information of those numbers were transfered together with the digitized raw data to the host computer. However, in the present experiment, we did not use these event and spill numbers for an event building in the host computer, because the data read-out was successfully carried out without any event slipping.

The data transfered from each module to the host computer were at first processed by the Event-Builder. Then they were transfered to the Event-Distributor and to HDD data storages as well as to the on-line analyzer.

2.7 Liquid hydrogen target

For the previous KEK-E522 experiment, a polyethylene target $[(CH_2)_n]$ was used and the quasi-free K^- production from the ^{12}C nucleus was a background in the missing mass spectrum. We leaned from the second experiment at KEK, E559 in which the $p(K^+, \pi^+)$ reaction was used, that it is advantageous to use a pure proton target for suppressing the background. Thus, J-PARC E19 used a liquid hydrogen target which was used in E559 [42].

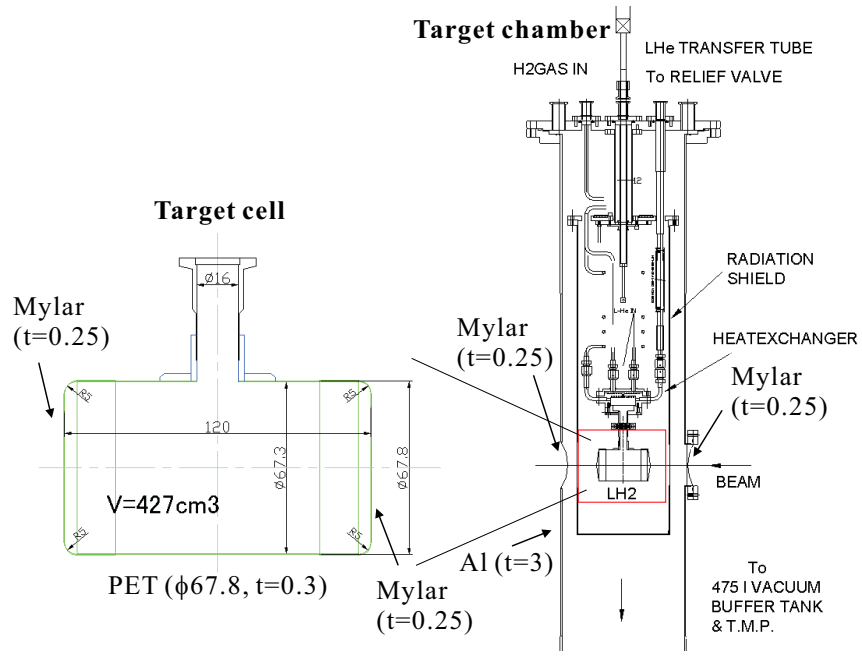

Figure 2.28: Schematic view of the liquid hydrogen target (unit in mm).

Figure 2.28 shows a schematic view of the liquid hydrogen target. Its cooling system uses liquid helium. The hydrogen vessel was made from PET (polyethylene terephthalate) of 0.30 mm thick for the cylinder part, and Mylar of 0.25 mm thick for the end cap. The target dimensions were 67.3 mm in diameter and 120 mm in length. During the experimental period, the volume and the pressure of the target were monitored. The stability of the density was $\Delta\rho/\rho \sim 10^{-5}$ during the beam time. Specifications of the liquid hydrogen target were listed in Table 2.7.

Table 2.7: Specifications of the liquid hydrogen target.

Size	$\phi 67.3 \times 120^L$ mm
Capacity	427 cm^3
Material	PET(cylinder), Mylar(end cap)
Average thickness	0.3 mm(cylinder), 0.25 mm(end cap)
Target chamber	Aluminium; t=3 mm, ϕ270 mm
	Window(Mylar); t=0.25 mm
Vacuum	$\sim 1.0 \times 10^{-7}$ mbar
LH_2 thickness	0.85 g/cm^2 (0.0708 g/cm^3 $\times$12 cm)
Mylar thickness	0.0695 g/cm^2 (1.39 g/cm^3 $\times$0.025 cm$\times$2)

2.8 Data summary

The Θ^+ production data were taken in two cycles from October to November in 2010, as listed in Table 2.8. The total number of pions irradiated on the liquid hydrogen target was 7.8×10^{10}. At the beginning of the October beam time, we took $\Sigma^\pm$ production data using the liquid hydrogen target. The mass and cross section of $\Sigma^\pm$ are well known and thus the data serve as calibration for the missing mass and check of an entire system. Empty target data were also taken in the October cycle.

In the empty target run, we took beam-through data for the calibration of both spectrometers. Since the π beam passed through both spectrometers, we could estimated the difference of the scale and offset of the reconstructed momenta between the beam line spectrometer and SKS. The beam-through data were also taken with the liquid hydrogen target to check the energy loss effect in the target. To check the alignment of chambers at the upstream and downstream of the target, we took the beam-through data without exciting the SKS magnet. The beam-through data were taken with the trigger in which the LC counter hit was not required so that the LC efficiency could be checked by this data. To check the efficiency of TOF and the over kill ratios of AC1·2, we took data with the trigger in which the hits of TOF or AC1·2 were not required. The control data were listed in Table 2.9.

Table 2.8: Data summary. P_{Beam} is the beam momentum and N_{Beam} is the number of pions irradiated on the target. The $\Sigma^{\pm}$ production data, the empty target data and the 1st Θ^{+} production data were taken in October. The 2nd Θ^{+} production data was taken in November after a week interval.

Data	P_{Beam} [GeV/c]	Reaction	Target	N_{Beam} ($\times 10^9$)	Data taking time (hours)
Σ^{+}	1.37	(π^{+}, K^{+})	LH_2	2.9	5
Σ^{-}	1.37	(π^{-}, K^{+})	LH_2	12	20
Empty	1.92	(π^{-}, K^{-})	–	4.6	10
Θ^{+} 1st	1.92	(π^{-}, K^{-})	LH_2	30	50
Θ^{+} 2nd	1.92	(π^{-}, K^{-})	LH_2	48	82

Table 2.9: Data summary of the control data. "BT" means beam-through data.

Data	P_{Beam} [GeV/c]	Reaction	Target	Comments
BT (Negative)	$0.75 \sim 0.95$	(π^{-}, π^{-})	–	Calibration
BT (Negative)	0.85	(π^{-}, π^{-})	LH_2	Target energy loss
BT (Positive)	0.85	(π^{+}, π^{+})	–	Calibration
BT (Positive)	0.85	(π^{+}, π^{+})	LH_2	Target energy loss
BT (without SKS)	0.85	(π^{-}, π^{-})	–	Alignment of chambers
TOF efficiency	1.92	(π^{-}, π^{-})	LH_2	TOF not required
AC1·2 over kill	1.37	(π^{-}, K^{+})	LH_2	AC1·2 not required

Chapter 3

Data Analysis

3.1 Outline

The mass of the producted particle (M) was obtained as a missing mass in the (π, K) reaction from

$$M = \sqrt{(E_\pi + M_A - E_K)^2 - (p_\pi^2 + p_K^2 - 2p_\pi p_K \cos\theta_{\pi K})}$$

where E_π and p_π are the total energy and momentum of a pion, E_K and p_K are those of a kaon, M_A is the mass of a target nucleus, and $\theta_{\pi K}$ is the scattering angle of the reaction. Here, three kinematic variables, p_π, p_K and $\theta_{\pi K}$, were measured by the beam and SKS spectrometers through the track reconstruction.

Figure 3.1 shows a flow chart of the offline analysis. (π, K) reaction events were roughly selected from a large number of background reaction events by the PIK trigger. An incident beam π was selected by using the time-of-flight between BH1 and BH2. A scattered K was roughly selected by using the information of the TOF and LC counters. Then, the π momentum and K momentum were reconstructed from the tracking information on BCs and SDCs, respectively. At the first stage of the tracking analysis, straight-line track candidates were determined both at the entrance and the exit of the spectrometer system. Then the best track candidates were selected by the combination of the straight-line tracks so as to give the least chi-square in the track reconstruction. For the track reconstruction of the K1.8 beam spectrometer, a third-order transport matrix was used. In the track reconstruction of SKS, we used a calculated magnetic field map and the SKS track was reconstructed by the Runge-Kutta method. After the track reconstruction, the identification of K was carried out by using the time-of-flight between BH2 and TOF with the flight path and the reconstructed momentum of SKS. Then, a vertex point of the (π, K) reaction event was reconstructed from the trajectories of π and K, and finally the missing mass was obtained.

In order to estimate those values such as the decay factor, the acceptance of the spectrometer, the background level in the (π^-, K^-) missing mass spectrum, and the missing mass resolution for Θ^+, a Monte Carlo simulation program was developed based on the GEANT4 code [56]. All materials in the spectrometers were included in this program. For trajectories of particles through the experimental apparatus, decay in

flight, energy loss, multiple scattering and hadronic reactions of the particles were taken into account.

Then the missing mass spectrum was corrected for the acceptance and its vertical scale was converted to the cross section. Finally, a peak of Θ^+ was searched for in the spectrum.

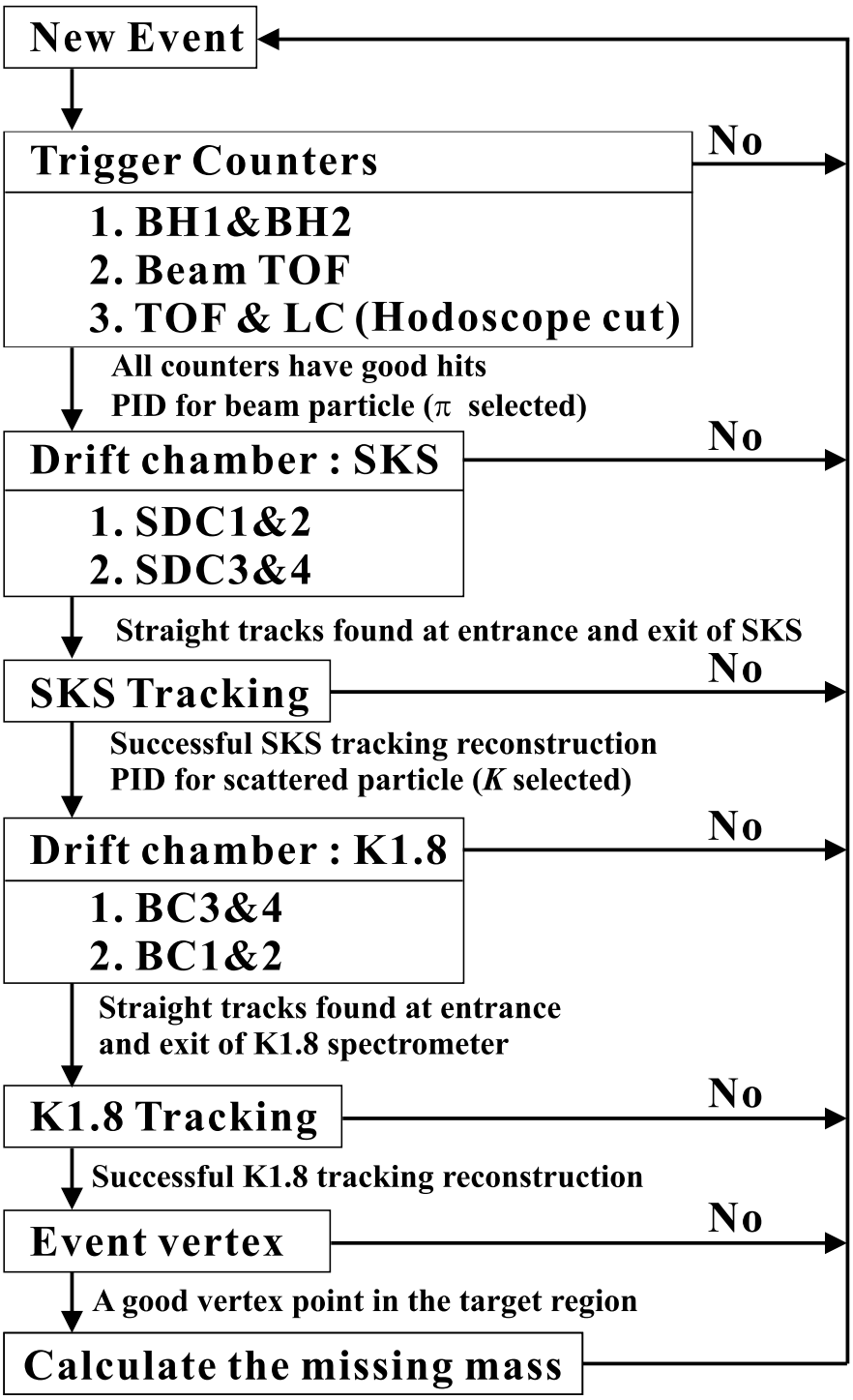

Figure 3.1: Flow chart of the offline analysis. The order of the analysis is shown in each box. Due to the high multiplicity of the beam, the tracking of the beam line chambers was carried out in the last stage.

3.2 Analysis of π^- beam

3.2.1 Identification of π^-

An incident π was selected by using the time-of-flight between BH1 and BH2. Figure 3.2 shows the time-of-flight spectrum for the negatively charged beam. Only π was observed and its flight time between BH1 and BH2 was adjusted to be at the origin. The continuous background around the π peak was due to accidental hits on BH1 and BH2. The typical time resolution without the ADC pulse height correction was 0.3 ns(rms). The electrons remaining in the beam due to the inefficiency of GC could not be separated by the time-of-flight analysis. In the case of using the positive beam, the flight time difference between pions and protons was 3.8 ns with the beam momentum of 1.92 GeV/c. The protons were separated by requiring this time window.

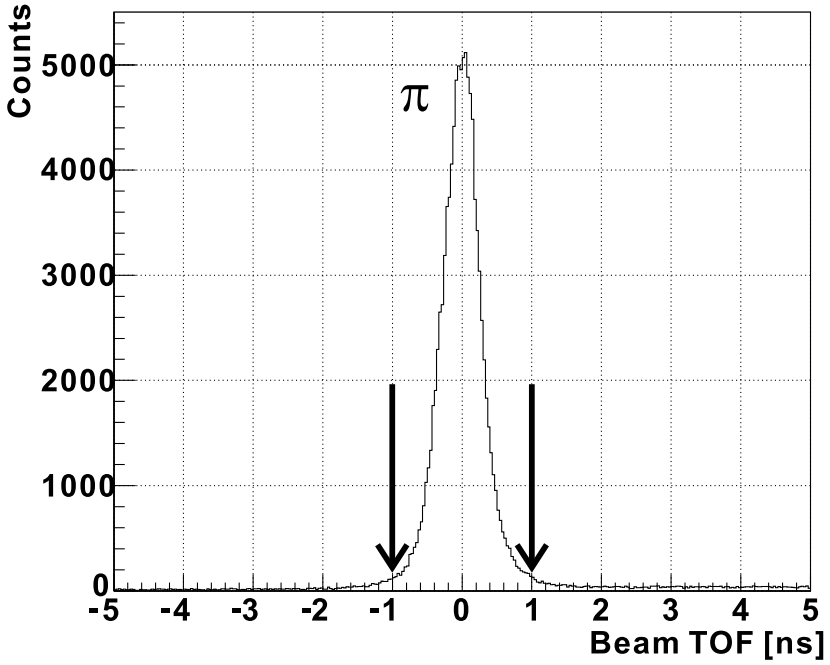

Figure 3.2: Typical TOF spectrum of the incident beam particles. The selected time window was indicated by arrows.

3.2.2 Beam track reconstruction

Overview

The beam momentum was calculated from the BC data as follows. At first, local straight tracks were found at the entrance and the exit of the K1.8 beam line spectrometer by BC1·2 and BC3·4 using the least square method, respectively. In the BC1·2 tracking, hits on adjoining wires within the proper timing was made up as a cluster hit. As the weight in the least square method on the BC1·2 tracking, we used the spatial resolution calculated from the wire spacing ($\Delta(wire\ space)/\sqrt{12}$ mm). In finding the BC3·4 tracking, all combinations of hit positions on the plane were examined with a pre-tracking routine to reduce the number of possible combinations. In the pre-tracking routine, a two dimensional tracking between the same tilt angle planes, such as u, u', u, u', was only examined at first. Then, good tracks found in those planes (the u, u', u, u' planes, the v, v', v, v' planes, and the x, x', x, x' planes) were combined to be a 3-dimensional track. For multi-hit events, all possible combinations were examined. After determination of the straight tracks at the entrance and the exit of the K1.8 beam line spectrometer, those tracks were connected using a 3rd-order transport matrix calculated by the OR-BIT code [57], and the momentum was determined by minimizing the following χ^2 value. The fitting parameters were the momentum (p), the horizontal (x) and vertical (y) positions and their derivatives (dx/dz, dy/dz) at the entrance of the beam line spectrometer which is the VI position described as later. The χ^2 value was defined as

$$\chi^2_{K1.8} \equiv \frac{1}{n-5}\left(\sum_{i=1}^{12} H_i\left(\frac{P_i - f_i(\vec{X}_{in})}{w_i}\right)^2 + \sum_{i=13}^{24} H_i\left(\frac{P_i - g_i(\vec{X}_{out})}{w_i}\right)^2\right)$$

$$n = \sum_{i=1}^{24} H_i$$

$$H_i = \left\{ \begin{array}{l} 1 \text{ if } i\text{−th plane has a hit} \\ 0 \text{ if } i\text{−th plane has no hit} \end{array} \right\}$$

$$\vec{X}_{out} = M(\vec{X}_{in}, \delta),$$

where P_i and w_i denote the hit position and resolution of the i-th plane in BCs. The calculated position by the transport matrix at the i-th plane is denoted by $f_i(\vec{X}_{in})$ and $g_i(\vec{X}_{out})$, where $\vec{X}_{in}$ and $\vec{X}_{out}$ are the horizontal and vertical positions and their derivatives at the entrance and the exit of the K1.8 beam line spectrometer; $\vec{X} = \left(x, y, \frac{dx}{dz}, \frac{dy}{dz}\right)$. The momentum is denoted by $p = p_0(1+\delta)$, where p_0 is the central momentum. The operator M denotes the transport matrix which combines $\vec{X}_{in}$ and $\vec{X}_{out}$.

BC1·2 cluster search

The timing information of BC1·2 was digitized by the MWPC encoder by the sampling time interval of 10 ns (100 MHz sampling). In the digitalization, both leading edge and trailing edge information of raw signals were taken for making up cluster hits. The time information had a signal width between the timing from the leading edge to the trailing

edge. Figure 3.3 shows a typical raw TDC distribution (leading edge timing) of one of the BC1 layer, where 1 ch corresponded to 1 ns. In the present analysis, the time gate with a 100-ns width was set as indicated in the figure.

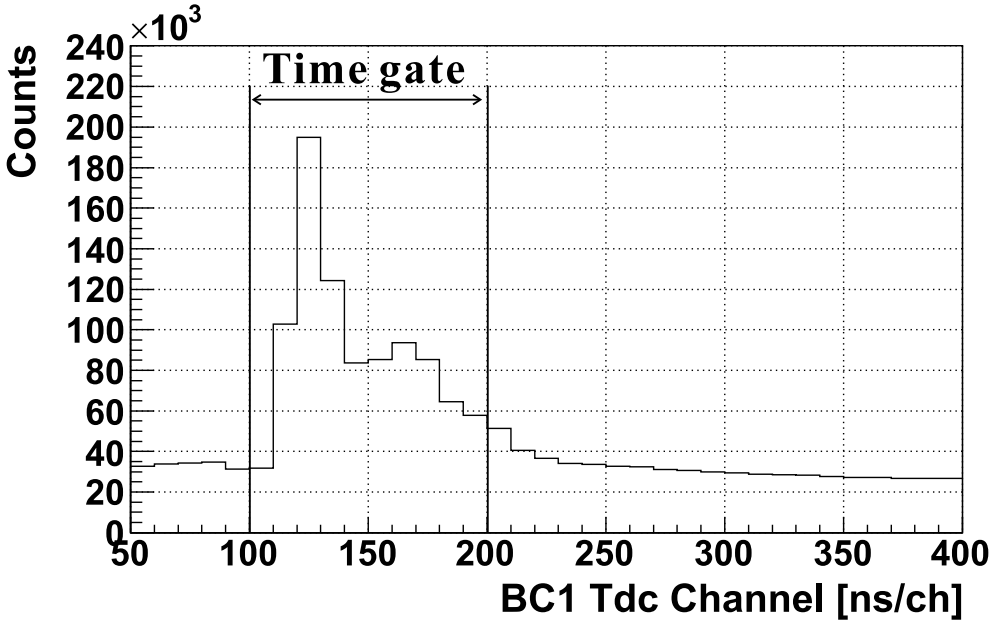

Figure 3.3: Typical TDC distribution of one of the BC1 layer. The TDC distribution was the sum of all hits in a layer. All multi-hit signals were shown in the distribution.

For the clustering, at first, hits on adjoining wires were checked by using signal width. When there were hits on adjoining wires whose signal width overlapped each other in the 100-ns time gate, those wires were made up into a cluster. Then, we searched for another cluster in the same layer. If three or more adjoining wires have hits, they were made up to a larger cluster. Those cluster hits were searched for until finding all cluster combination on each layer. For the tracking analysis, the position of the center wire in the cluster was used.

BC3·4 drift length calculation

The timing information of BC3·4 was digitized by the TKO Multi-hit TDC (MHTDC) modules. The MHTDC module encoded the timing information with the fixed time resolution of 0.78 ns. Figure 3.4 shows typical TDC distributions of one of the BC3 layers (3 mm wire spacing) (a) and one of the BC4 layers (5 mm wire spacing) (b). The bump structure of the tail of the BC3 TDC distribution was the satellite signal due to the ringing of the ASD card. Those satellite signal events were rejected in the tracking process because the timing of the satellite signals was far from the drift time range and their coincidence rate were quite low.

For calculation of the drift length, at first, the TDC information was converted to the drift time information. The origin of the drift timing was roughly determined to the

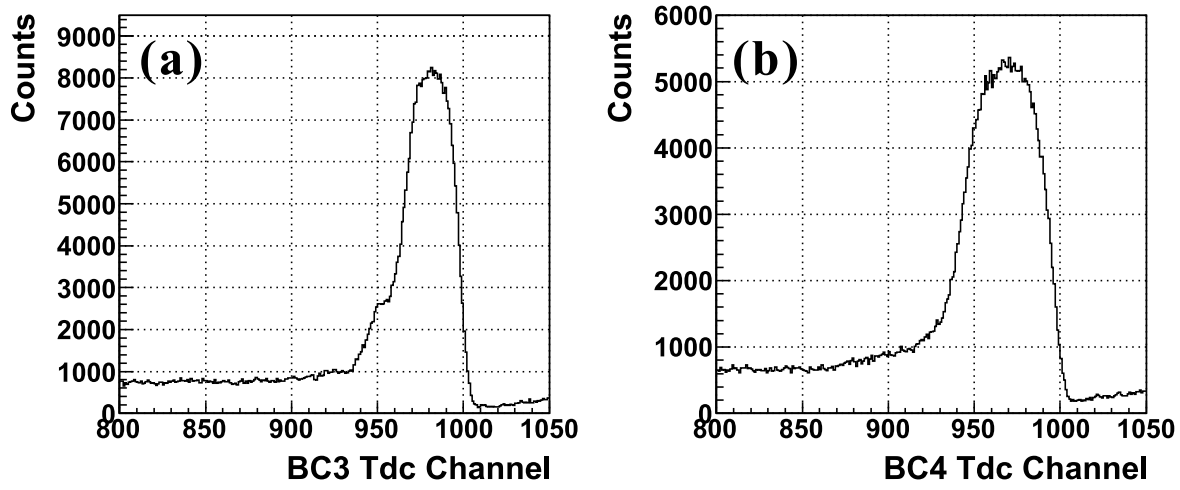

Figure 3.4: Typical TDC distributions of one of the BC3 layers (a) and one of the BC4 layers (b). The TDC distribution was the sum of all hits in a layer. All multi-hit signals were shown in the distribution.

edge of the TDC distribution (∼1000 ch in Fig. 3.4) and TDC channels were converted to the time using the MHTDC channel width of 0.78 ns. Then, in order to obtain the function of the drift velocity, the drift time distribution was integrated from the time origin to the maximum drift time as the following calculation:

$$DL(t) = \frac{m(t)}{n},$$

where t is the drift time, $m(t)$ the number of events integrated from the time origin to the drift time (t) and n the total event in the integration region. Figure 3.5 shows a scatter plot between drift time and drift length ($DL(t)$) for one of the BC3 layers. The scatter plot was fitted by using a 5th-order polynomial,

$$dl(t) = \sum_{i=0}^{5} p_i t^i,$$

and, then, we obtained the function of the drift velocity. To optimize the drift velocity function, we iterated the analysis process which involves the determination of the time origin and the fitting to determine the drift velocity function. We chose the 5th-order polynomial function which gave the best tracking χ^2 value.

Figure 3.6 shows scatter plots between drift time and drift length of one of the BC3 layers (a) and one of the BC4 layers (b). Since a part of events around the maximum drift length were true ones, those events with TDC values exceeding the maximum drift time was not discarded and the values were fixed to be the maximum drift length, while the events with TDC values earlier than the drift time origin were assumed to have the minimum drift length (0 mm). On the other hand, the fake events such as accidental backgrounds around the maximum drift length were rejected by the local tracking process so that the effects of these fake events were negligibly small.

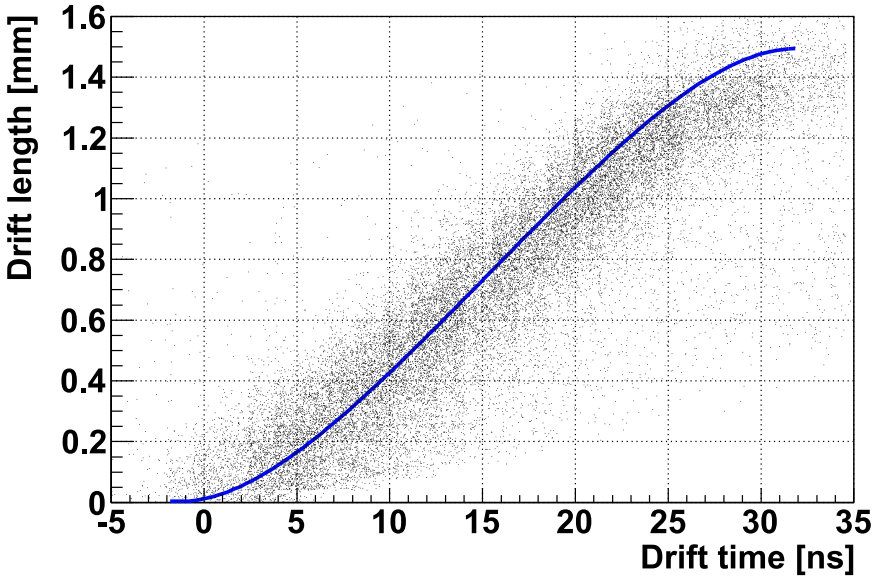

Figure 3.5: A scatter plot between the drift time and the drift length of one of the BC3 layers with the fitting result in blue line. The scatter plot was the sum of all hits in a layer.

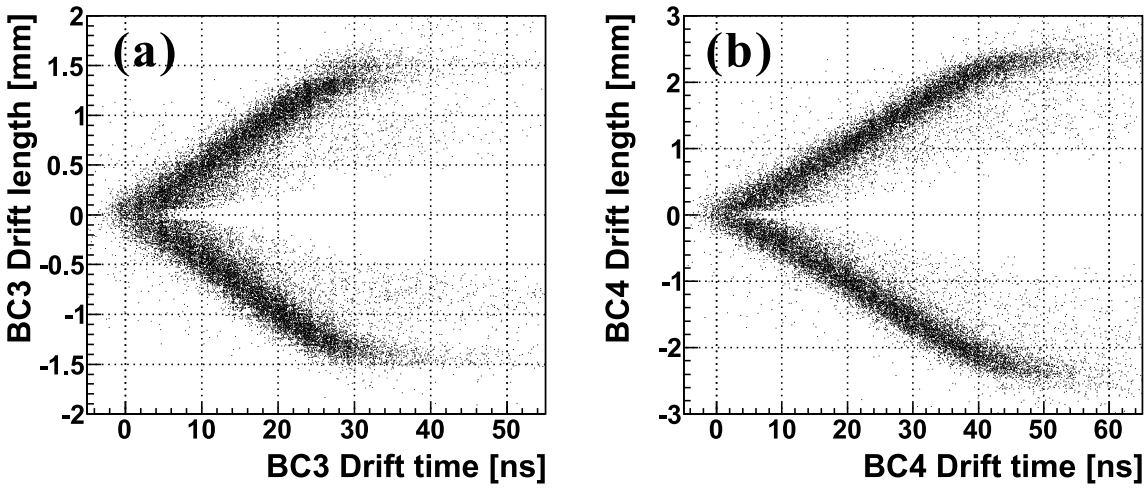

Figure 3.6: Scatter plots between the drift time and the drift length of one of the BC3 layers (a) and one of the BC4 layers (b). The scatter plots were the sum of all hits in a layer.

Local straight track search

In finding both BC1·2 and BC3·4 tracks, all combinations of all the hit positions on each layer were examined. Those local straight tracks were found by using the least square method. The local position coordinate was shown in Fig. 3.7. For the origin of the the local coordinate, we defined the VI and VO points which were 130-mm upstream of the end-guard of the entrance Q-magnet and 130-mm downstream of the end-guard of the exit Q-magnet for the BC1·2 and BC3·4 tracks, respectively. The VI and VO points were shown in Fig 3.8. For the BC3·4 tracking, we used a two-dimensional pre-tracking just to reduce the number of possible combinations. Then, the three-dimensional tracking search started. The tracking routine of the two-dimensional pre-tracking was the same as of the three-dimensional tracking.

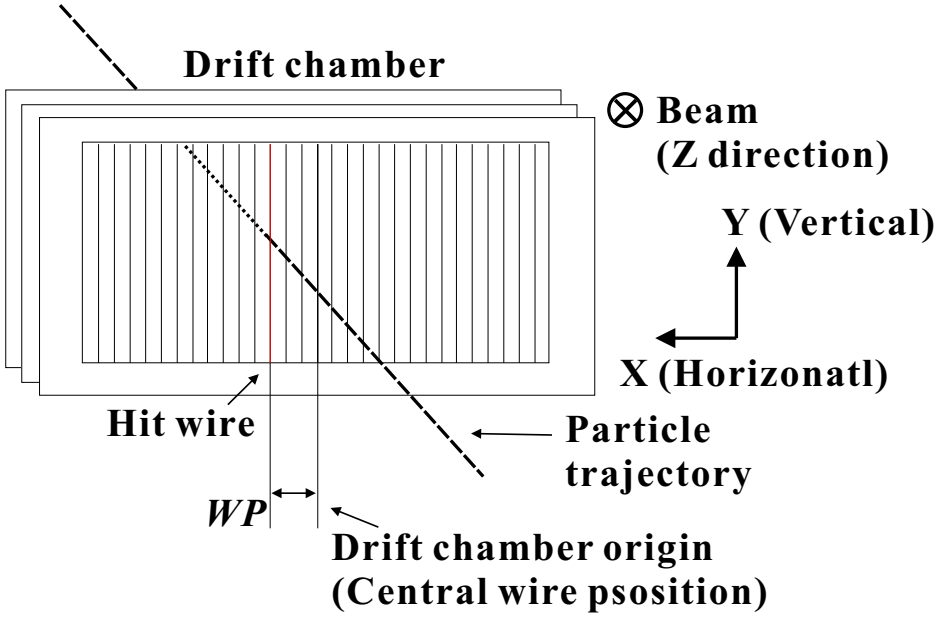

Figure 3.7: Local position coordinate for the local straight tracking.

The tracking χ^2 was defined as following,

$$\chi^2 = \frac{1}{n-5}\sum_{i=1}^{12}\left(\frac{dl_i(t) - f(z_i)}{\sigma_i}\right)^2$$
$$f(z_i) = x(z_i)\cos(\theta) + y(z_i)\sin(\theta) - WP$$
$$x(z_i) = x_0 + u_0 \times z_i$$
$$y(z_i) = y_0 + v_0 \times z_i$$

where $dl_i(t)$ is the drift length (or position of the cluster center wire), σ_i the position resolution of each chamber, θ wire tilt angle of each plane (x, u, v for 0°, 15° −15°), and WP the distance from the central wire position of the drift chamber to the sense wire position closest to the hit position. The track which have parameters (x_0, y_0, $u_0(dx/dz)$, $v_0(dy/dz)$, sign of left or right) with the least χ^2 was determined as local track candidates.

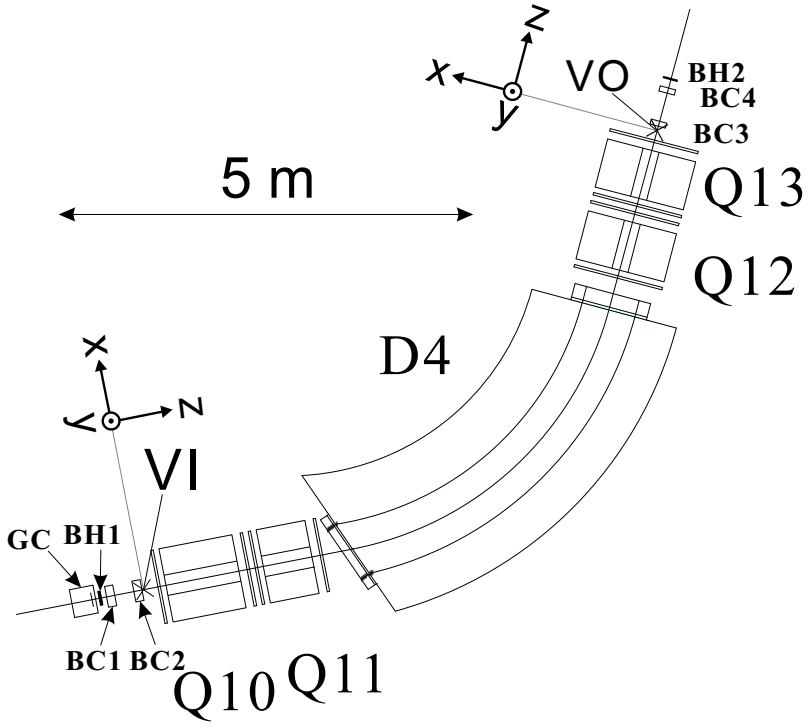

Figure 3.8: The position of VI and VO which were the origin of the local coordinate.

Figure 3.9 shows the χ^2 distribution of the BC1·2 tracking (a) and the BC3·4 tracking (b). The black and the red lines show the total and the single-track events, respectively. In the local track search, the accepted χ^2 value which included more than 99.5% of the single tracks was selected to be less than 30 and 20 for the BC1·2 and the BC3·4 trackings, respectively. The quality of the beam line spectrometer tracking was discussed in the beam momentum reconstruction.

Figure 3.10 shows the residual distribution of one of the BC1 layers (a) and one of the BC3 layers (b). The residual was defined as $Residual = X_{Hit\ position} - X_{Track\ position}$ on the layer. In the calculation of the residual distribution, the calculated layer was not included in the tracking analysis. Typical residual widths of BC1 and BC3 were 300 μm and 200 μm in rms, respectively.

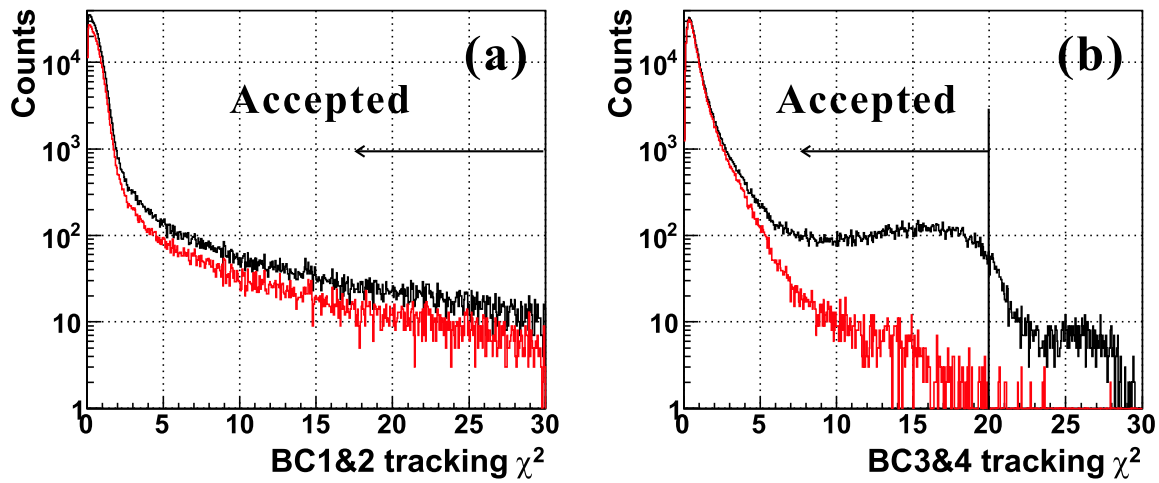

Figure 3.9: Typical χ^2 distribution of the BC1·2 tracking (a) and the BC3·4 tracking (b). The black and the red lines show the total and the single-track events, respectively.

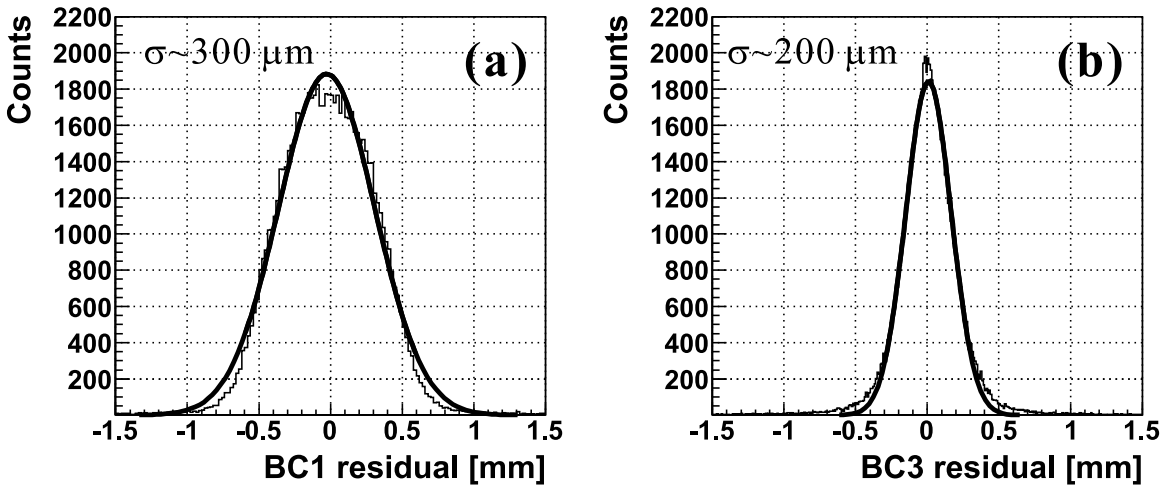

Figure 3.10: Typical residual distribution of one of the BC1 layers (a) and one of the BC3 layers (b).

Beam momentum reconstruction

The straight tracks at the entrance and the exit of the K1.8 beam line spectrometer were connected using a 3rd-order transport matrix calculated by the ORBIT code [57], and the momentum was determined by minimizing the above χ^2 value. The fitting parameters were the momentum, the horizontal and vertical positions and their derivatives at the VI position. The momentum was reconstructed by the horizontal and vertical positions and their derivatives at the entrance and the exit of the K1.8 beam line spectrometer; $\vec{X} = (x, y, \frac{dx}{dz}, \frac{dy}{dz})$.

To the ORBIT code, we input the properties of the K1.8 beam line spectrometer magnets, the effective magnetic length, aperture, field strength of the central lay, and bending angle and the radius of central orbit for the dipole magnet. The effective magnetic length was determined from measured magnetic field distribution. The aperture was taken from the design value of the spectrometer magnets. The properties of the magnetic fields of all the magnets were calculated by using the measured excitation curve. By using those input data, the ORBIT code calculated the transport matrix in a stepwise way. The step width was defined by the input data. The VI and VO points were also used as the origin of the transport matrix. Figure 3.11 shows a typical χ^2 distribution of the K1.8 track with the beam momentum of 1.37 GeV/c (a) and 1.92 GeV/c (b). The black and the red lines show the total and the single track events, respectively. In order to obtain the missing mass spectrum, only single track events were used. The selection of single track is described in the section to estimate the beam line tracking efficiency.

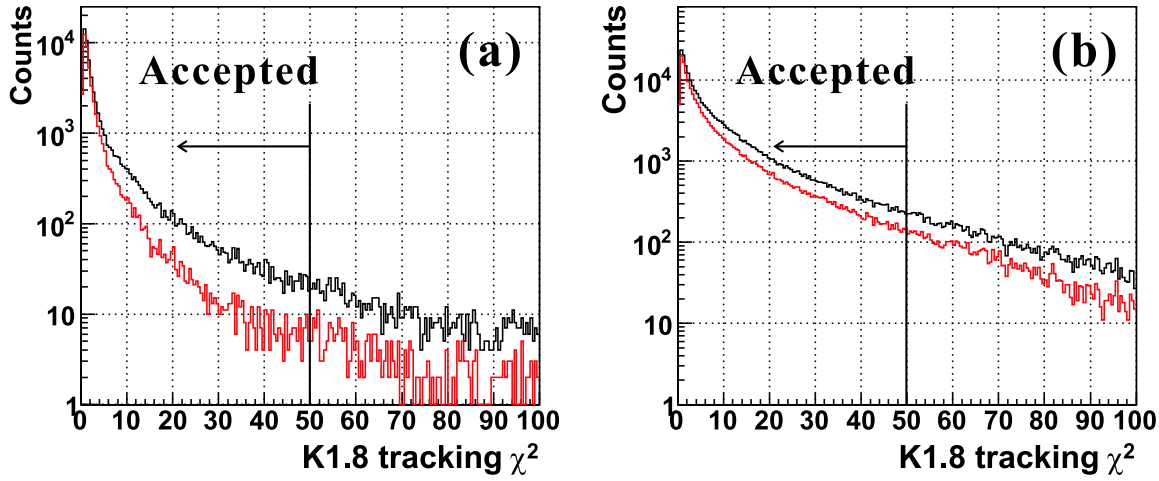

Figure 3.11: Typical χ^2 distribution of the K1.8 track with the beam momentum of 1.37 GeV/c (a) and 1.92 GeV/c (b). The black and the red lines show the total and the single-track events, respectively.

The $\chi^2_{K1.8}$ distribution was worse for the 1.92 GeV/c beam than that for 1.37 GeV/c. The effect of $\chi^2_{K1.8}$ selection was studied by using the Σ^+ data with the beam momentum of 1.37 GeV/c. Figure 3.12 shows the missing mass resolution of Σ^+ as a function of the χ^2_{K18}. The region whose χ^2 was more than 6 was selected to have the same number of events in each region. The χ^2 region of more than 50 could not be studied because the

event number was not enough. It was found that the events whose χ^2_{K18} was less than 50 kept the missing mass resolution of less than 2.5 MeV/c^2 (FWHM), and the central value of the Σ^+ mass was found to be unchanged. In order to keep the achievable sensitivity, the acceptable Σ^+ missing mass resolution which corresponded to the estimated Θ^+ missing mass resolution of less than 2.0 MeV/c^2 (FWHM) was estimated to be less than 2.5 MeV/c^2 (FWHM). In addition, the largest contribution to the missing mass resolution was the momentum resolution of SKS as described in Sec. 3.11. In the present analysis, by selecting the events of χ^2_{K18} less than 50 as a good trajectory, the $\chi^2_{K1.8}$ selection kept the quality of the present experiment. Thus, the same $\chi^2_{K1.8}$ selection was applied to the beam momentum of 1.92 GeV/c.

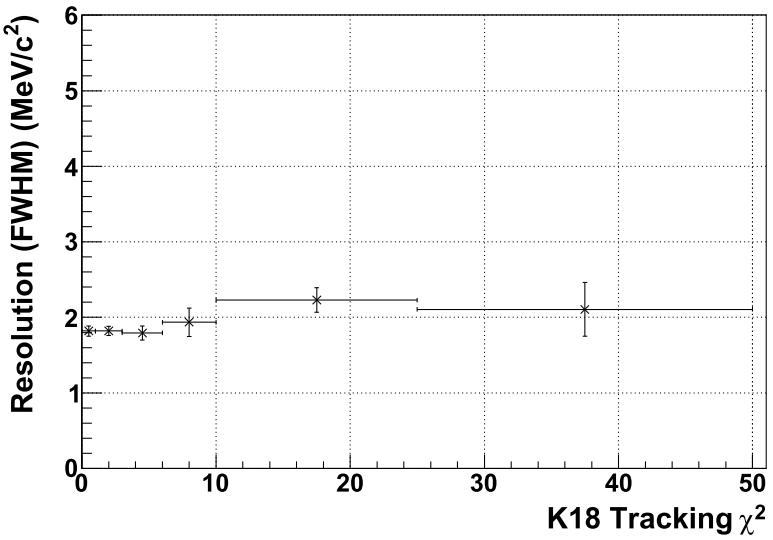

Figure 3.12: The missing mass resolution of Σ^+ as a function of the χ^2_{K18}.

Figure 3.13 shows momentum distribution for a 1.37 GeV/c π^+ beam (a) and 1.92 GeV/c π^- beam (b), respectively. The single-track events were selected in those figures. The momentum bite was typically $\pm 2\%$. The momentum distribution was different for a different slit condition.

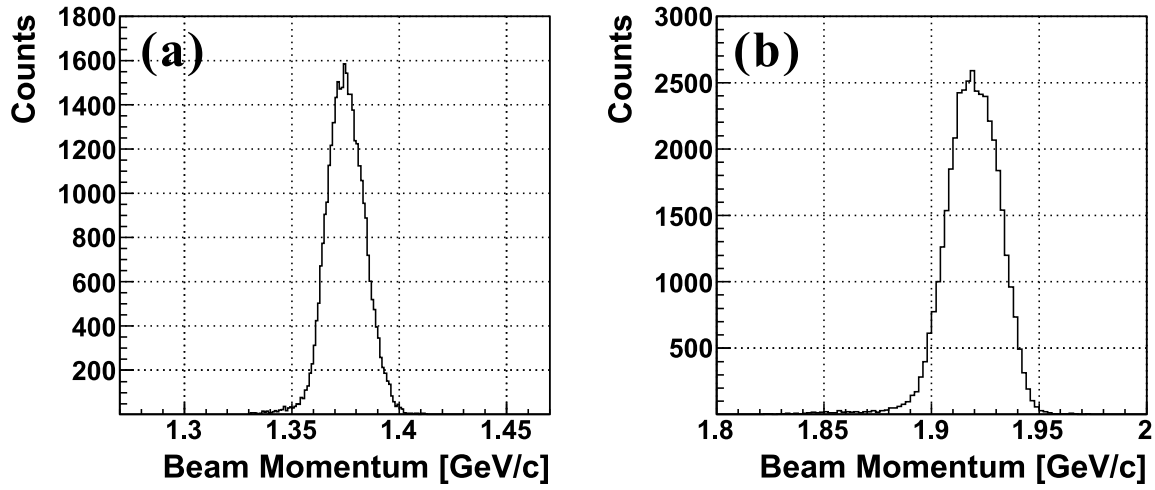

Figure 3.13: Typical distribution of the momentum for a π^+ beam of 1.37 GeV/c (a) and a π^- beam of 1.92 GeV/c (b).

3.3 Analysis of scattered particles

3.3.1 Hodoscope cut

In order to reduce background particles and the analyzing time, hodoscope cuts were applied to TOF-ADC,TDC and LC-ADC,TDC before the SKS tracking analysis. The ADC values of each channel was normalized so that the most probable peak position for the π data should be the same after subtracting the ADC pedestal. The TDC values was converted to the time using the TDC conversion gain and the flight time from BH2. Then, the ADC and TDC spectra of each detector were summed up for all the channels. The K events are shown in the figures. The selection of scattered particles is described in Sec. 3.3.3.

Figure 3.14 shows the hodoscope cut region of TOF-ADC,TDC. The black and red lines in (a) and (b) are the PIK triggered and K events, respectively. The figure (c) and (d) are the scatter plots between TOF-ADC,TDC and the scattered particle mass, respectively. The K events of more than 99% were selected by these TOF cuts.

Figure 3.15 shows the hodoscope cuts region of LC-ADC,TDC. The black and red lines in (a) and (b) are the PIK triggered and K events, respectively. The figure (c) and (d) are the scatter plots between LC-ADC,TDC and scattered particle mass, respectively. The K events which had a small ADC values were the K decay events after passing though AC2. Those decay events were also true K events so that the lower boundary was determined to be as low as possible.

Figure 3.16 shows the hodoscope cut region of the combination check between TOF and LC hit segments (the hit segment ID difference between the TOF and the LC counter) and that of the time difference between TOF and LC. The black and red lines in (a) and (b) are the PIK triggered and K events, respectively. The figure (c) and (d) are the scatter plots between the hit segment number difference between the TOF and the LC segment, and between the time difference between TOF and LC and the

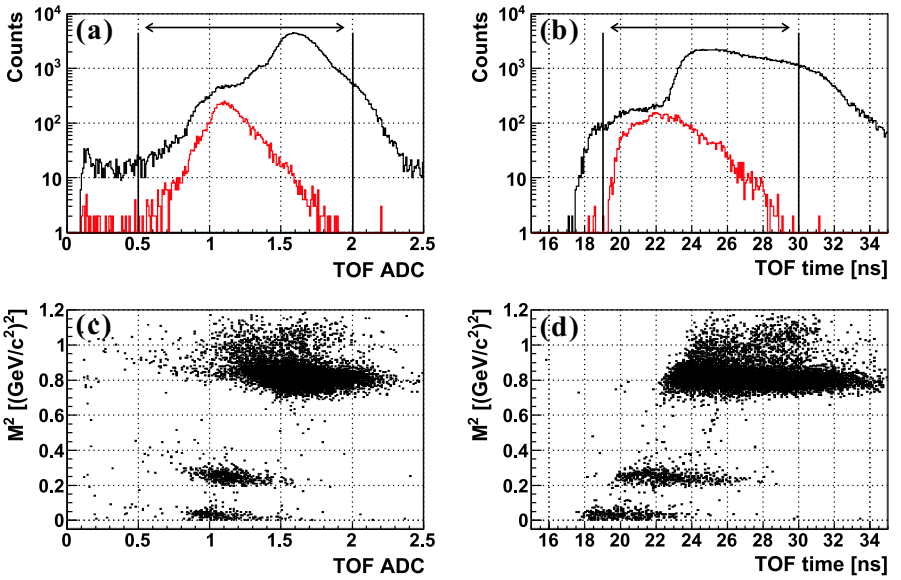

Figure 3.14: The hodoscope cut region of TOF-ADC (a) and TOF-TDC (b). The figure (c) and (d) are the scatter plots between TOF-ADC,TDC and the scattered particle mass, respectively.

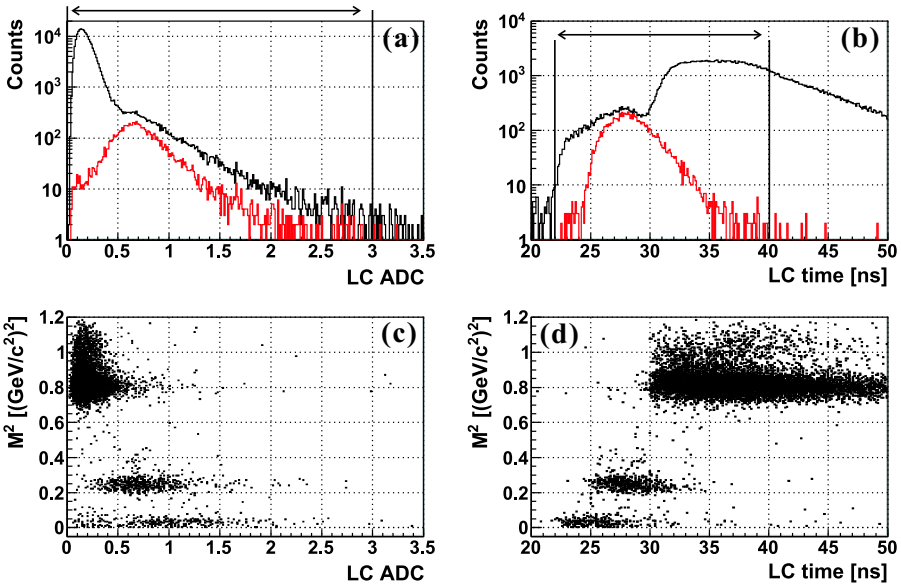

Figure 3.15: The hodoscope cut region of LC-ADC (a) and LC-TDC (b). The figure (c) and (d) are the scatter plots between LC-ADC,TDC and the scattered particle mass, respectively.

scattered particle mass, respectively. The combination check was applied to reduce the background events as described in Sec. 2.5.

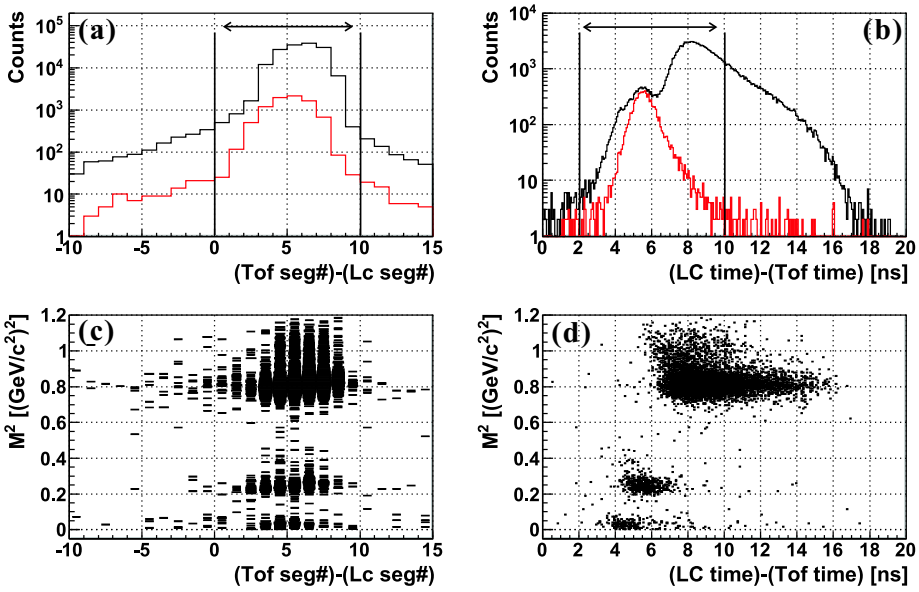

Figure 3.16: The hodoscope cut region of the hit segment number difference between the TOF and the LC segment (a) and the time difference between TOF and LC (b). The figure (c) and (d) are the scatter plots between the hit segment number difference between the TOF and the LC segment and the time difference between TOF and LC, respectively versus the scattered particle mass.

In addition, the K events were selected using the horizontal scattering angle measured by SDC1·2 and the flight time between BH2 and TOF as shown in Fig. 3.17. The K events were selected as shown in the figure. This selection was applied after finishing the local track search of the SDC1·2 tracking.

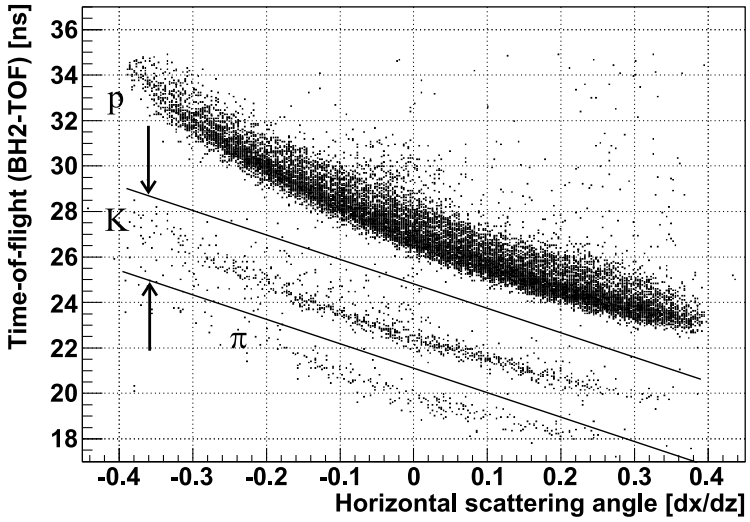

Figure 3.17: Scatter plot between the horizontal scattering angle measured by SDC1·2 and the flight time between BH2 and TOF. The selected region for K was indicated in the figure.

3.3.2 Momentum reconstruction of scattered particles

Overview

The momentum of a scattered particle was calculated from the SDC data as follows. At first, local straight tracks were determined at the entrance and the exit of the SKS magnet by SDC1·2 and SDC3·4 using the least square method, respectively. For both SDC1·2 and SDC3·4 trackings, all combinations of hit positions on the plane were examined with a pre-tracking routine to reduce the number of the combination. This analysis procedure is the same as that of the BC3·4 tracking.

Next, the momentum of the scattered particle was determined by reconstructing a trajectory from the hit positions. The reconstruction was carried out with the Runge-Kutta method [58] for each particle using a calculated magnetic field map. The magnetic field map was calculated by the ANSYS code using the finite element method. The calculation and accuracy of the field map is described in Appendix A. The trajectory and the momentum were optimized by minimizing the following χ^2 values iteratively. The fitting parameters were the momentum (p), the horizontal (x) and vertical (y) positions and their derivatives (dx/dz, dy/dz) at the target position. The χ^2 value of each track is defined as

$$\chi^2_{SKS} \equiv \frac{1}{n-5} \sum_{i=1}^{n} \left(\frac{x_i^{tracking} - x_i^{data}}{w_i} \right)^2 ,$$

where n is the number of the chamber planes with a hit, $x_i^{tracking}$ and x_i^{data} are the hit position on the i-th plane in the tracking in and the data, and w_i is the position resolution of the i-th plane. The convergence criterion in the iteration is $\delta\chi^2 = (\chi^2_{k+1} - \chi^2_k)/\chi^2_k <$

10^{-3}, where k is the number of iteration and χ^2_k is the tracking χ^2 for the k-th iteration.

Local straight track search of SDCs

The analysis procedure for both SDC1·2 and SDC3·4 tracking is the same as that of the BC3·4 tracking. The timing information of SDC1·2 was digitized by the TKO Multi-hit TDC (MHTDC) modules, while that of SDC3·4 was digitized by the TKO Dr.II single-hit TDC modules. The analysis of SDC1·2 was completely the same as that of BC3·4.

For converting the TDC value to the time information of the SDC3·4 hits, the TKO Dr.II TDC module was calibrated by using the TDC calibrator (ORTEC 462). The TDC calibrator generated the start and stop signals. The time interval between start and stop signals automatically changed within the setting range. Its resolution was much better than the resolution of the TKO Dr.II TDC module (∼0.35 ns).

The drift length was obtained by the same analysis procedure as in the BC3·4 tracking. We chose the 5th-order polynomial function which gives the best tracking χ^2 value. Since the position of SDC2 was close to the SKS magnet gap, the straight track was slightly bended by the magnetic field inside of SDC2. In the SKS track reconstruction, the track bending was taken into account. The correction of the drift velocity in the magnetic field was not applied.

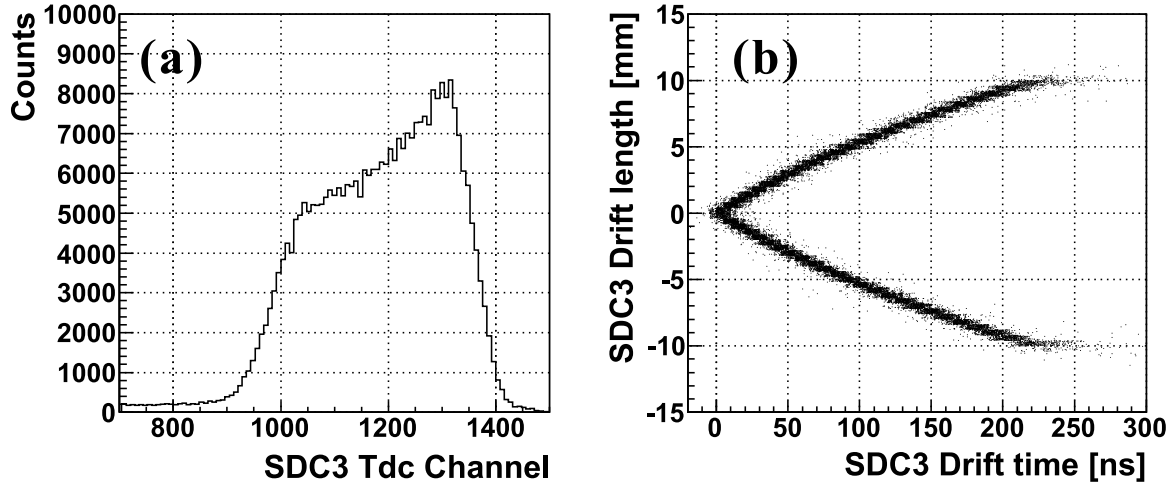

Figure 3.18: Typical TDC distribution (a) and a scatter plot between the drift time and the drift length (b) of one of the SDC3 layers. Those distributions were made from the sum of all hits in a layer.

Figure 3.18 shows a typical distribution of the TDC (a) and the drift length (b) of one of the SDC3 layers. After determining the drift length, local straight tracks were found by using the least square method. As the origin of the the local coordinate of the SDC1·2 tracking, the center of the experimental target position was used. For the SDC3·4 local tracking, the origin was arbitrarily assigned. In the present analysis, the origin was defined as the central position of the first later of SDC3. Those coordinates for the local tracking were defined in the local coordinate systems, while for the SKS tracking

as the global coordinate as shown in Fig. 3.19. The origin of the global coordinate system was arbitrarily assigned. In the present analysis, the origin in the SKS magnet coil was defined as the same origin to calculate the magnetic field map.

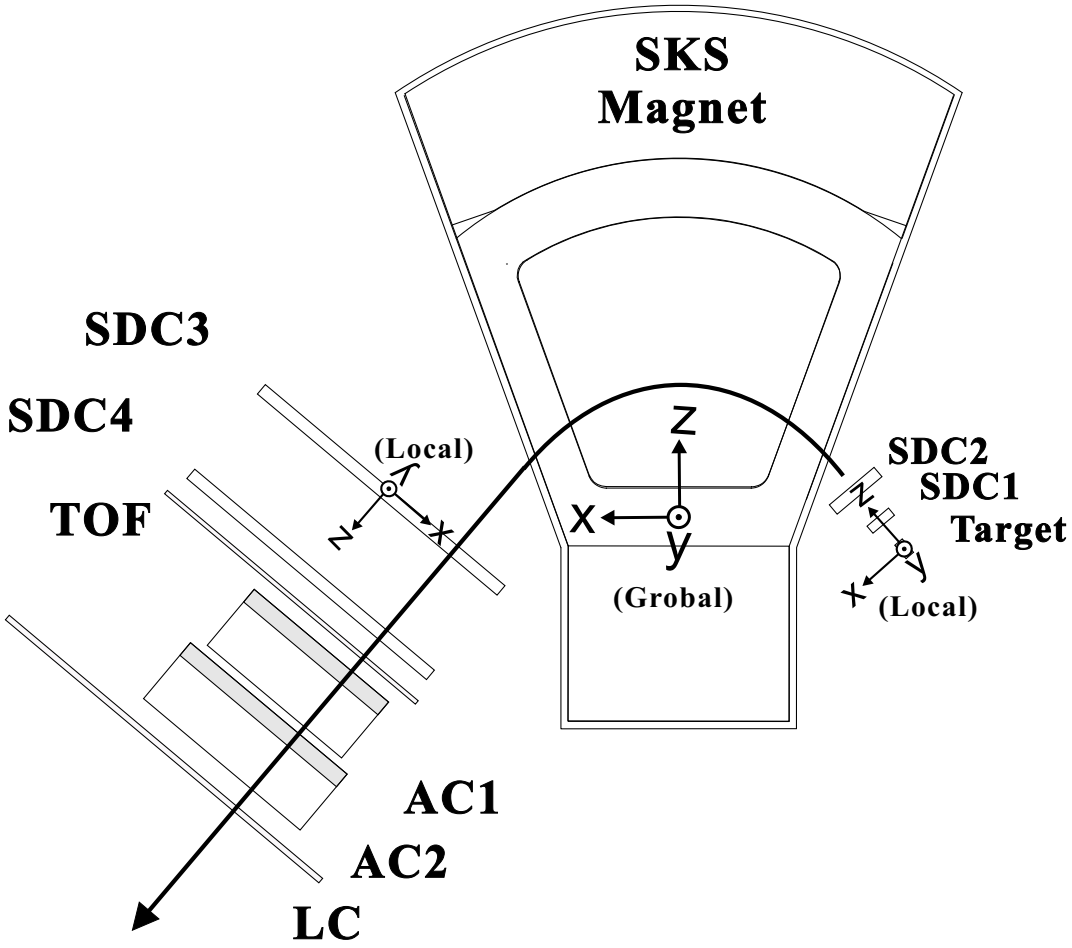

Figure 3.19: The origin of the coordinates of the local tracking of SDC1·2 and SDC3·4 and the SKS tracking.

The analysis procedure was also the same as of the beam line chamber tracking. Figure 3.20 shows the χ^2 distribution of SDC1·2 tracking (a) and SDC3·4 tracking (b). In the local track search, the accepted χ^2 value was selected to be less than 20 which included more than 99.5% of single tracks. The black and the red lines show the total and the single-track events, respectively. The quality of the SKS spectrometer tracking and the χ^2_{SKS} selection criteria was described later in the section for the SKS tracking efficiency.

Figure 3.21 shows the residual distribution of one of the SDC2 layers (a) and one of the SDC3 layers (b). In the calculation of the residual distribution, the calculated layer was not included in the tracking analysis. Typical residual widths of SDC2 and SDC3 were 200 μm and 300 μm in rms, respectively.

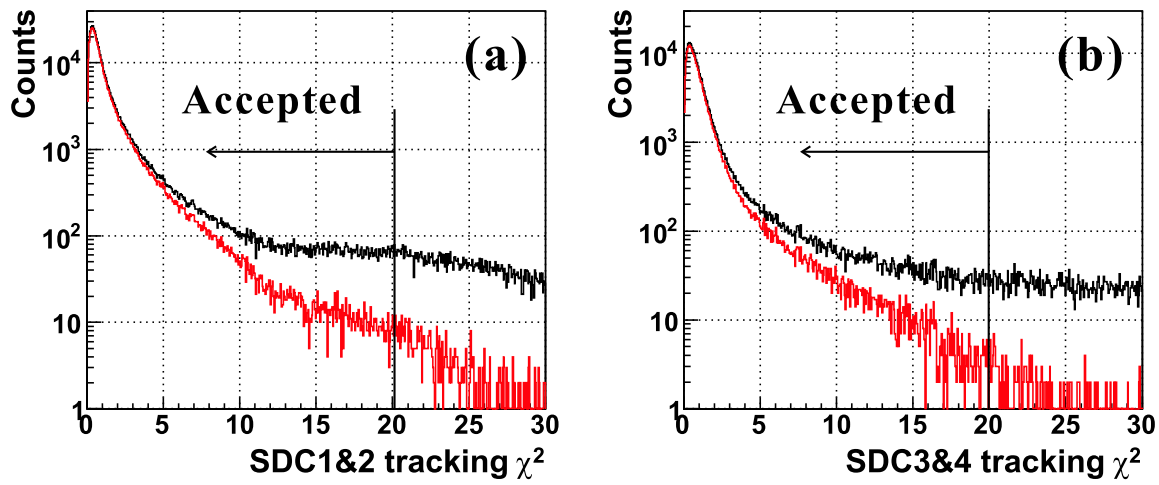

Figure 3.20: Typical χ^2 distributions of SDC1·2 tracking (a) and SDC3·4 tracking (b). The black and the red lines show the total and the single-track events, respectively.

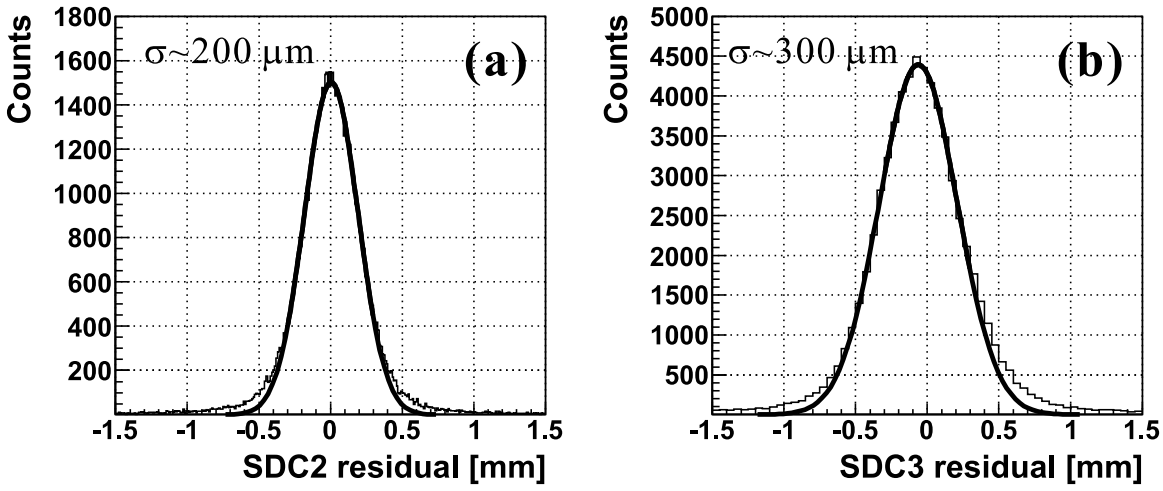

Figure 3.21: Typical residual distribution of one of the SDC2 layers (a) and one of the SDC3 layers (b).

The SKS tracking

The momentum of the scattered particle was determined by reconstructing a trajectory from the hit positions. The reconstruction was carried out with the Runge-Kutta method [58] for each particle using a calculated magnetic field map. The first step of the SKS tracking started from a position at the exit of SKS because the number of multi-track events was much smaller than that of the entrance. In the present analysis, the initial position was on the TOF counter position which was calculated from the local straight track of SDC3·4. The initial momentum value was input to a momentum near the scattered particle momentum. Then, the particle trajectory was calculated step by step using the magnetic field map from the position on the TOF counter to that of the target. Since the trajectory was calculated by using the global coordinate as shown in Fig. 3.19, the local coordinates of the SDC1·2 and SDC3·4 layers hit positions were converted to the global coordinates. The element of the magnetic field map was a 20 mm cube and the normal step size was set to be 25 mm. In the step calculation, the magnetic field value at every point was interpolated by a linear function. Since the hit position on each layer was used to trace the particle trajectory, the track bending by the fringing magnetic field inside of the drift chambers were considered in the SKS tracking calculation. The first calculation by using the initial momentum value. By satisfying the convergence criterion, the calculation was iterated by changing the momentum and other parameters.

Figure 3.22 shows a typical χ^2_{SKS} distribution. The χ^2_{SKS} selection criteria is described in the section of the SKS tracking efficiency. In the SKS tracking analysis, the ratio of multi-track K events were found to be negligibly small, less than 0.1%.

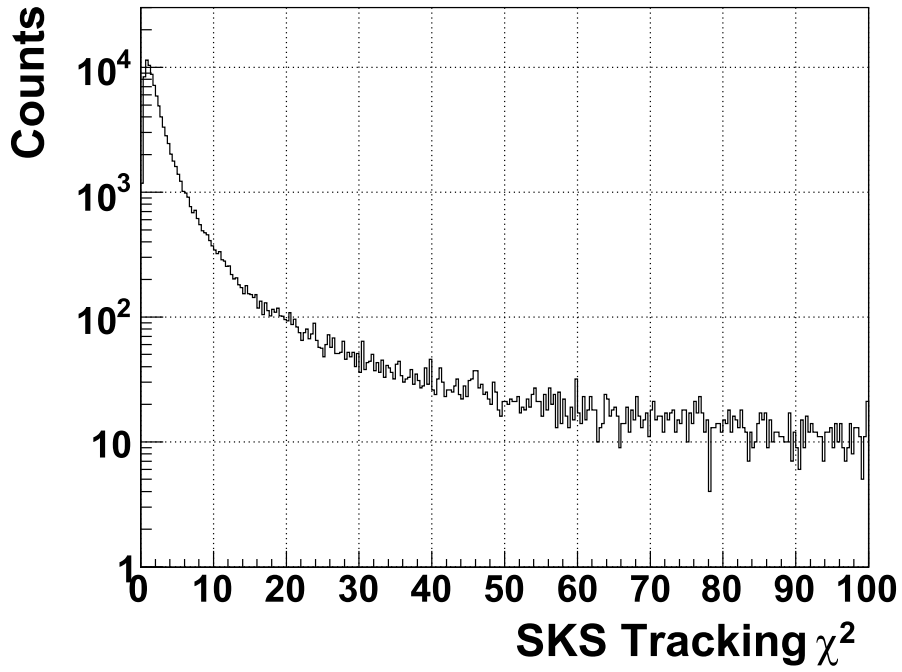

Figure 3.22: Typical distribution of χ^2_{SKS}.

3.3.3 Particle identification in the SKS

The PIK trigger cannot completely remove all background. The background particles were fast protons which fired LC and pions which cannot be detected by AC1 and AC2 because of its inefficiency. The background particles were roughly identified and rejected by using ADC and TDC cuts of the TOF and LC counters before the tracking in order to reduced the number of events to be analyzed in the time-consuming Runge-Kutta tracking routine. Those rough selections were applied in the first stage of the offline analysis. The selection using ADC and TDC cuts of the TOF and LC counters was discussed in the section of the particle identification efficiency.

After the Runge-Kutta tracking, the mass of a scattered particles (M_{scat}) was finally reconstructed as

$$M_{scat} = \frac{p}{\beta}\sqrt{1-\beta^2}$$

where β is the velocity of a scattered particle obtained from the time-of-flight and the flight path length between BH2 and TOF, and p is the momentum obtained from the SKS tracking. Figure 3.23 shows a typical mass spectrum for the $p(\pi^-, K^+)\Sigma^-$ data without any event selection by the ADC and TDC information of the TOF and LC counters (the PIK triggered event). The momentum range of the scattered particles were 0.7−1.0 GeV/c.

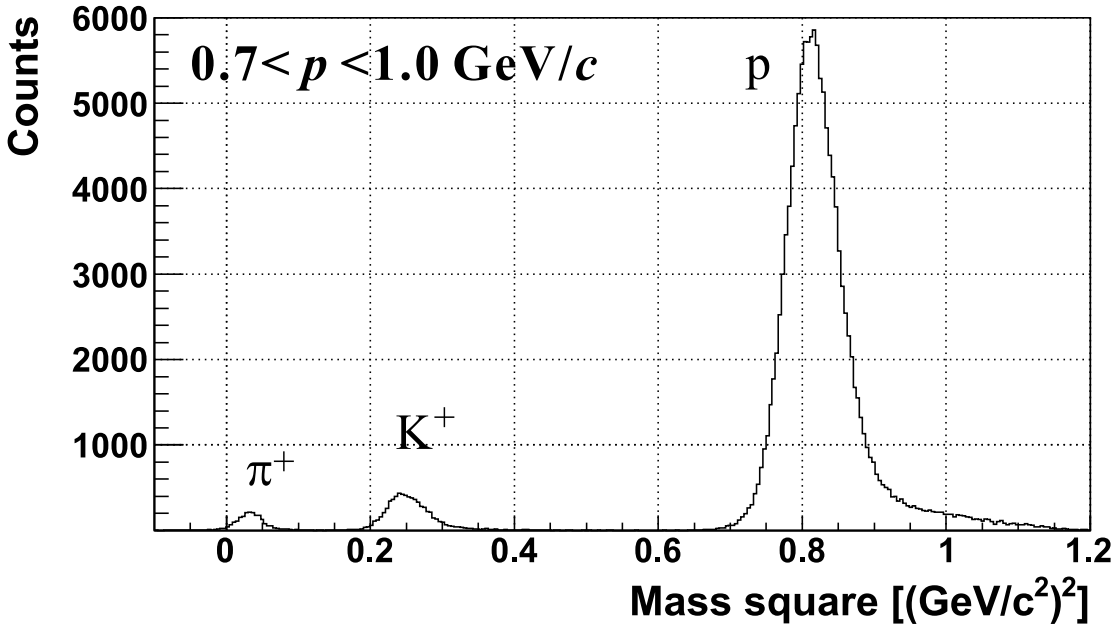

Figure 3.23: Scattered particle mass distribution for the $p(\pi^-, K^+)\Sigma^-$ data. The tail of the proton distribution was from the reaction events at the BH2 counter.

3.4 Vertex reconstruction

The scattering angle and the vertex point were obtained from both incident beam and scattered particle trajectories which were obtained by the track reconstruction in the K1.8 beam line spectrometer and the SKS, respectively. Figure 3.24 shows distribution of the horizontal (x) (a) and vertical (y) (b) scattering angle difference measured by both spectrometers for the beam-through data with the π^- of 0.85 GeV/c. We obtained the horizontal and vertical angular resolutions of 2.7 mrad and 4.1 mrad in rms, respectively. The vertical resolution was worse than the horizontal one because of the wire configuration of the drift chambers.

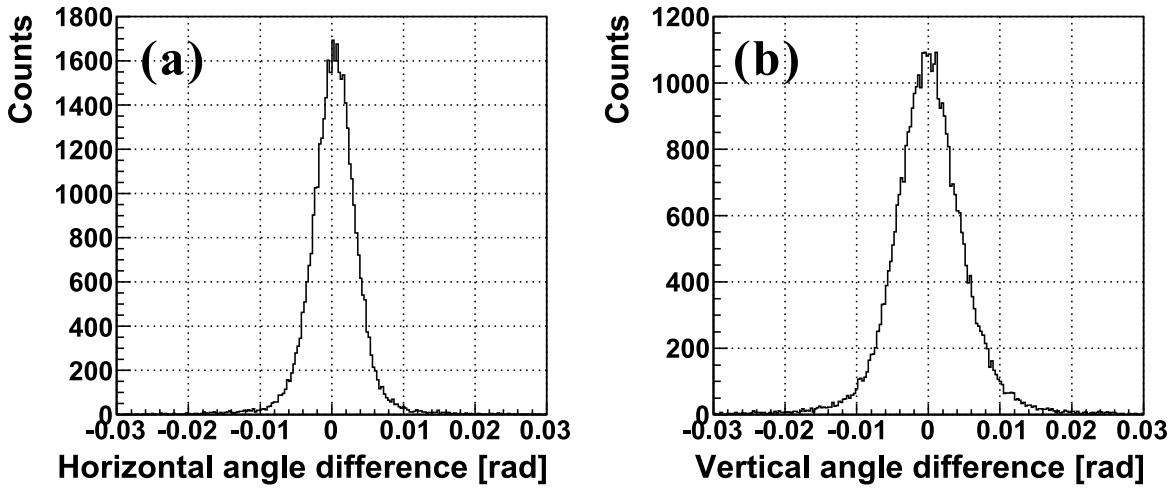

Figure 3.24: Typical distribution of the horizontal (a) and vertical (b) scattering angle difference measured by both spectrometers for the π^- of 0.85 GeV/c in the empty target data. The horizontal and vertical angular resolutions were 2.7 mrad and 4.1 mrad in rms, respectively.

The reaction vertex point was obtained from the closest distance between the tracks of beam π and scattered K. Figure 3.25 shows a distribution of the vertex position and the closet distance for the (π^-, K^-) events, where z-axis was defined as the beam direction. The bump around 200 mm was due to the event from SDC1 and the tail around the target region included the events from the target cell materials. The center of the z-vertex distribution was consistent with the survey of the target position, the upstream from the designed target point by 10 mm. The sizes of the horizontal (x) and vertical (y) distributions were smaller enough than the target size, and their distributions were consistent with the beam profile.

Figure 3.26 shows a scatter plot between the scattering angle and z-vertex distribution. As shown in the figure, the reconstruction of the z-vertex for very forward scattering angles failed because of difficulty to obtain the closest distance between the forward track of the beam π and the scattered K. For the scattering angle less than 2°, the z-vertex resolution was worse than the other angles. The background of very forward angle was higher than the other angles as discussed in Sec. 3.7 Thus, the scattering angle

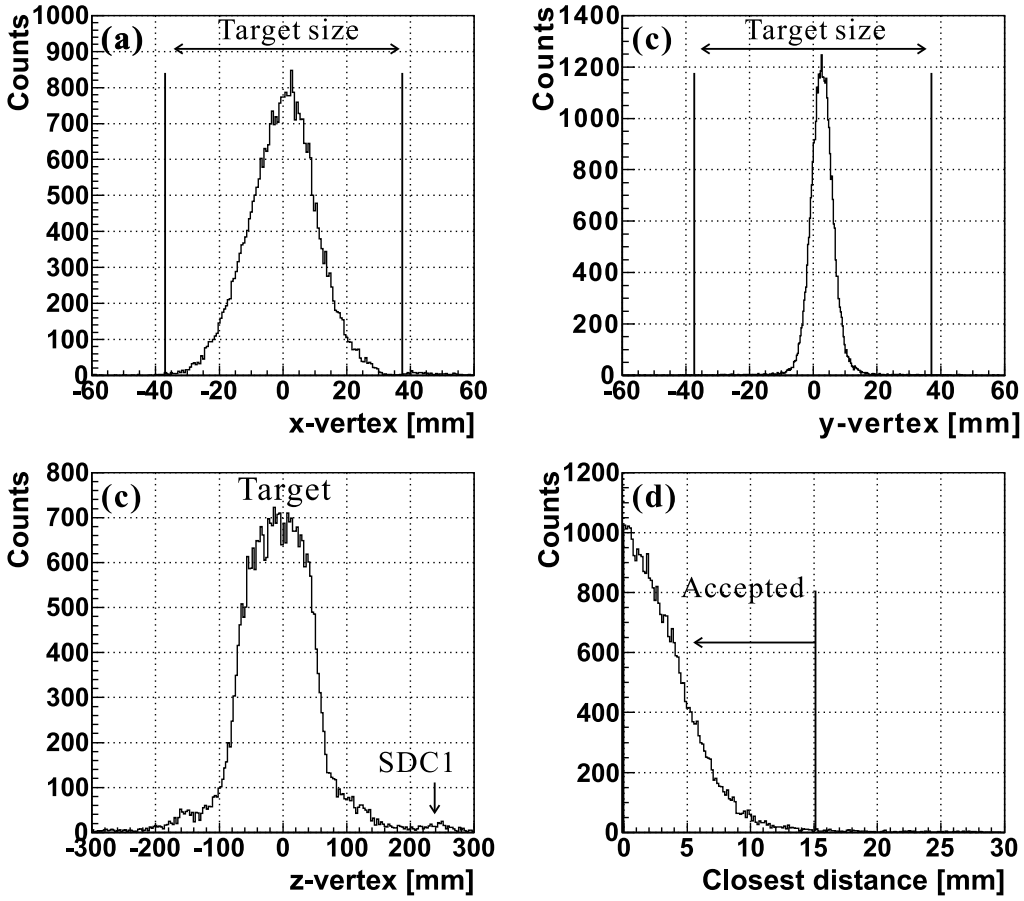

Figure 3.25: Vertex distribution for the (π^-, K^-) data. The distributions of the x-vertex (a), y-vertex (b), z-vertex (c), and the closest distance (d) were shown. The target size and the selected region were indicated by arrows.

cut ($\theta \geq 2^\circ$) was applied as indicated in Fig. 3.26.

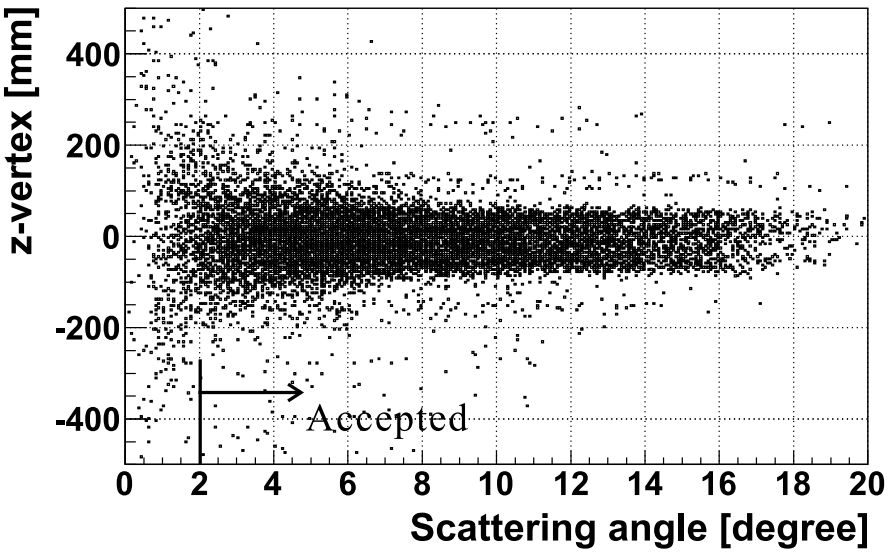

Figure 3.26: Scatter plot between the scattering angle and z-vertex distribution for the (π^-, K^-) data.

3.5 Cross section

The cross section was calculated from the experimental yield as

$$\left(\frac{d\sigma}{d\Omega}\right) = \frac{A}{(\rho x)\cdot N_{Avo}} \cdot \frac{1}{(N_{Beam}\cdot f_{Beam}\cdot \epsilon_{K1.8})} \cdot \frac{1}{(\epsilon_{daq}\cdot f_{abs}\cdot \epsilon_{vertex})} \cdot \frac{N_K}{\epsilon_{SKS}\cdot \Delta\Omega}$$

$$\epsilon_{K1.8} = \epsilon_{BC1\cdot2}\cdot\epsilon_{BC3\cdot4}\cdot\epsilon_{K1.8track}\cdot\epsilon_{single-track}$$
$$\epsilon_{SKS} = \epsilon_{TOF}\cdot\epsilon_{LC}\cdot f_{AC}\cdot\epsilon_{SDC1\cdot2}\cdot\epsilon_{SDC3\cdot4}\cdot\epsilon_{SKStrack}\cdot\epsilon_{PID}\cdot f_{decay}\cdot\epsilon_{matrix}$$

where A is the target mass number (A=1 in the present analysis), ρx the target thickness in g/cm^2, N_{Avo} Avogadro's number, N_{Beam} the number of the total beam particles measured as the scaler counts of the BEAM trigger, N_K the number of good (π, K) events, $\Delta\Omega$ the effective solid angle of the SKS, and ϵ's and f's the experimental efficiency factors. The factors represent the detector and analysis efficiencies, the data acquisition efficiency, the muon contamination effects in the beam, the K decay effects, the K absorption effects and the matrix trigger efficiency for the $p(\pi^-, K^-)$ data, where symbols are defined in Table 3.1. The precision of the cross section is determined by those of ρx, $\Delta\Omega$ and efficiency factors. The acceptance of the SKS was calculated by a Monte Carlo simulation, and each efficiency factor was estimated with various calibration data or Monte Carlo simulations. In this section, we discuss how they were obtained, and

finally we estimate the total systematic error of the cross section. The stability of the detector efficiencies during the Θ^+ production run is described in Appendix B.

Table 3.1: The list of the experimental efficiency factors.

Factors	Meaning	Values (%)
ϵ_{daq}	Data-acquisition efficiency	75.2±0.1
f_{beam}	Beam normalization factor	92.4±2.0
$\epsilon_{BC1\cdot2}$	BC1·2 efficiency	94.3±1.0
$\epsilon_{BC3\cdot4}$	BC3·4 efficiency	99.3±0.2
$\epsilon_{K1.8track}$	K1.8 tracking efficiency	93.1±0.8
$\epsilon_{single-track}$	Single track ratio	85.0±0.8
ϵ_{TOF}	TOF efficiency	99.7±0.1
ϵ_{LC}	LC efficiency	98.5±0.1
f_{AC}	AC1·2 accidental veto factor	89.8±1.2
$\epsilon_{SDC1\cdot2}$	SDC1·2 efficiency	95.6±0.2
$\epsilon_{SDC3\cdot4}$	SDC3·4 efficiency	99.8±0.2
$\epsilon_{SKStrack}$	SKS tracking efficiency	96.0±0.2
ϵ_{PID}	PID efficiency in SKS	92.9±0.5
f_{decay}	K decay factor	41.7±2.0
f_{abs} (K^+)	K^+ absorption factor	96.8±0.5
f_{abs} (K^-)	K^- absorption factor	89.4±0.5
ϵ_{vertex}	Event vertex cut efficiency	75.4±0.7
ϵ_{matrix}	The matrix trigger efficiency	99.0±0.1
	Total relative error	±6

3.5.1 Efficiency

Several efficiencies and factors are mainly the averaged values during the Θ^+ production. These values are the average for about one-fourth of the Θ^+ production runs whose event number is statistically large enough. The error is determined from the root mean square of the efficiency fluctuation of these runs.

Data acquisition efficiency

The data acquisition efficiency (ϵ_{daq}), caused by the dead time of the data acquisition system, was obtained as a ratio of the number of events accepted by the data acquisition system to that of the triggers. ϵ_{daq} was obtained as a function of the trigger rate, and a typical value of ϵ_{daq} was 75.2$\pm$0.1% at the trigger rate of $\sim$350/2.2 sec spill. The main contribution of the dead time was the data transfer time of the TKO multi-hit TDC modules.

Beam normalization factor

The beam normalization factor (f_{beam}) represents the fraction of π out of N_{Beam}.

The electron (or positron) contamination of the beam was 12$-$14%, and they were rejected by GC with an efficiency of 99.5% in the trigger level. The number of remaining electrons (or positron) was negligibly small compared with that of the π beam. The proton contamination in the positive pion beam was also almost completely rejected by requiring the timing coincidence between BH1 and BH2.

However, muons in the beam, which are the decay products of pions, could not be separated from pions. The μ contamination in the beam at 1.92 GeV/c was estimated to be 3.5$\pm$2.0% by using the Decay Turtle code [59]. The Decay Turtle calculated the properties of beam, such as the beam profile and the number of beam particles, at each beam line component. For the Decay Turtle calculation, the profile of the incident beam generated from the T1 target and the properties of the beam line components were parametrized as the input file. For example, the properties of a dipole magnet, such as the aperture, the effective length of the central track, the field strength and gradient, were input. The particle trajectories were calculated by the transfer matrix constructed by the input parameters of the beam line magnets, while in the electrostatic separators, the trajectories were calculated by using the Runge-Kutta calculation method. The trajectories which stopped at the several slits or went outside of the magnet aperture were rejected.

In the present experiment, the number of muons in the beam was not able to be measured. The systematic error was estimated from the measured and calculated results for the previous KEK experiment [60], assuming that the Decay Turtle calculation achieved the same accuracy.

The accidental coincidence rate (f_{acc}) between BH1 and BH2 was estimated by using the BEAM trigger data mixed in the (π, K) data as

$$1 - f_{acc} = \frac{N_{BH1,2}}{N_{Beam}},$$

where $N_{BH1,2}$ is the number of events for which the time-of-flight between BH1 and BH2 was proper for π as shown in Fig. 3.2. The averaged values of $1 - f_{acc}$ during the Θ^+ production run was 95.7±0.5%.

In total, the value of $f_{Beam} \equiv (1 - f_{mu})\cdot(1 - f_{acc})$ was estimated to be 92.4±2.0%.

BC1·2, BC3·4 and K1.8 tracking efficiency

In order to obtained the BC1·2 efficiency ($\epsilon_{BC1\cdot2}$), the BC3·4 efficiency ($\epsilon_{BC3\cdot4}$), and the K1.8 tracking efficiency ($\epsilon_{K1.8track}$), we used the BEAM trigger events mixed in the (π, K) data after selecting pions in the BH1−BH2 time-of-flight. The efficiency includes the detection efficiency and the analysis efficiency to find a good track. The local tracking efficiency was defined as

$$\epsilon = \frac{N(Track \times PiBeam)}{N(PiBeam)},$$

where $N(PiBeam)$ is the number of events for which the time-of-flight between BH1 and BH2 was proper for π, and $N(Track \times PiBeam)$ the number of good track found in the proper π event. The beam line tracking efficiencies are the average values during the Θ^+ production run.

The BC efficiency was the total efficiency including the detection efficiency and the analysis efficiency to find a good straight track. Due to the bad time structure of the beam, the instantaneous beam rate at the entrance of the K1.8 beam spectrometer was extremely high. To reduce the track finding time and the multi-track event, events with a large number of cluster hits were rejected (multiplicity cut) before the track search. The required number of cluster hits was less than 6 clusters per layer. The BC1·2 efficiency ($\epsilon_{BC1\cdot2}$) during the production run was found to be 94.3±1.0%.

For the BC3·4 analysis, all combinations of hit positions on the plane were examined, while the multiplicity cut before the track search was not applied. The BC3·4 efficiency ($\epsilon_{BC3\cdot4}$) was found to be 99.3±0.2%.

Figure 3.27 shows typical track multiplicity of the BC1·2 and BC3·4 local tracking. The maximum number of tracks obtained in the BC3·4 local tracking was large because the layer multiplicity cut was not applied. A typical ratio of the multi-track event to the total tracks was ∼15% and ∼7% for BC1·2 and BC3·4, respectively.

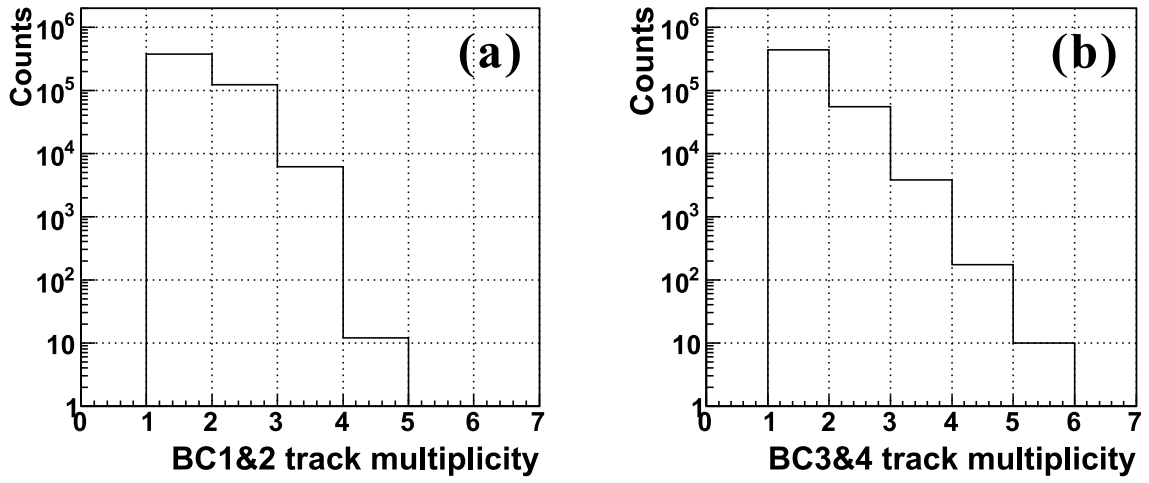

Figure 3.27: Typical track multiplicity of the BC1·2 (a) and BC3·4 (b) local tracking.

The K1.8 tracking efficiency ($\epsilon_{K1.8track}$) was the analysis efficiency to reconstruct a particle trajectory in the beam spectrometer defined as

$$\epsilon_{K1.8track} = \frac{N(K18track \times BC1 \cdot 2\ track = 1 \times BC3 \cdot 4\ track = 1)}{N(BC1 \cdot 2\ track = 1 \times BC3 \cdot 4\ track = 1)},$$

where $N(BC1 \cdot 2\ track = 1 \times BC3 \cdot 4\ track = 1)$ was the number of single good tracks found in the BC1·2 ($\chi^2 < 30$) and BC3·4 ($\chi^2 < 20$) local tracking, and $N(K18track \times BC1 \cdot 2\ track = 1 \times BC3 \cdot 4\ track = 1)$ the number of good K1.8 track found in the single good tracks of both BC1·2 and BC3·4 local tracking. It was found to be 93.1±0.8%. The efficiency was estimated from a ratio of the number of events with a good particle trajectory ($\chi^2 < 50$) by the K1.8 tracking to the number of events which have good straight local tracks both at the entrance and at the exit of the spectrometer.

Due to the bad time structure of the beam, the ratio of multi-track events with two or more good particle trajectories in the K1.8 tracking was high. We cannot find which of those trajectories is a true track which reacted in the target or not. They made a combinatorial background in the missing mass spectrum as shown in Fig. 3.28. Thus, all multi-track events were rejected in the present analysis to reduce the background in the missing mass spectrum as much as possible. In addition, in multi-track events in the beam line tracking, the miss connection between local tracks at the entrance and the exit was included. Thus, to reject both multi-track event and miss connection, we selected events with single local tracks both at the entrance and at the exit before reconstructing the beam line track. The selection of a single-track was defined as a single-track efficiency:

$$\epsilon_{single-track} = \frac{N(BC1 \cdot 2\ track = 1 \times BC3 \cdot 4\ track = 1)}{N(BC1 \cdot 2\ track > 0 \times BC3 \cdot 4\ track > 0)},$$

where $N(BC1{\cdot}2\ track > 0 \times BC3 \cdot 4\ track > 0)$ and $N(BC1{\cdot}2\ track = 1 \times BC3 \cdot 4\ track = 1)$ were the number of good tracks and single good tracks found in the BC1·2 ($\chi^2 < 30$) and BC3·4 ($\chi^2 < 20$) local tracking, respectively. The single-track efficiency was found to be 85.0±0.8%.

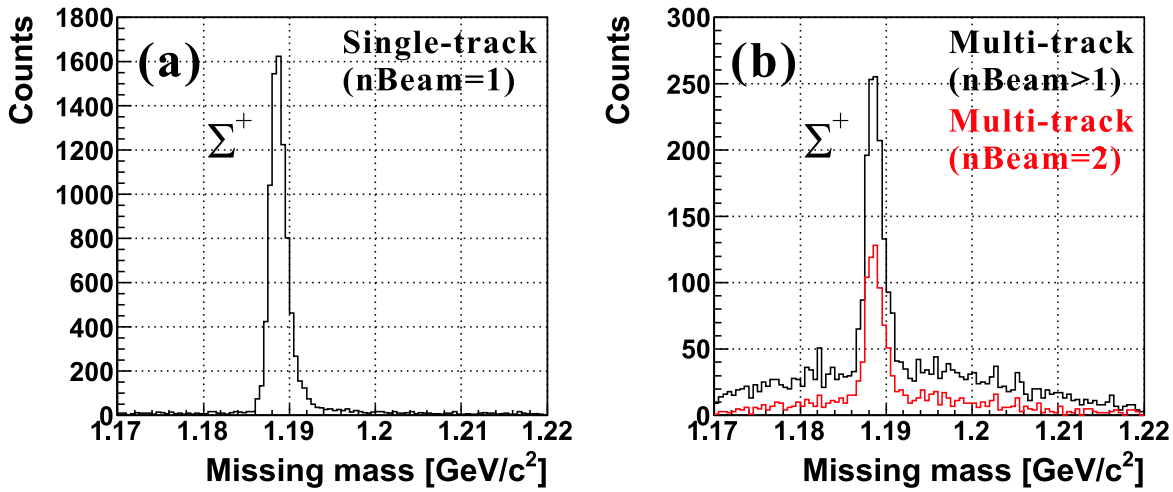

Figure 3.28: The Σ^+ missing mass spectrum with the single-track selection (a) and the multi-track one (b). The combinatorial background was increased by the multi-track selection (b).

Efficiency of TOF and LC

The detection efficiency of TOF was estimated from the (π^-, K^-) reaction data by taking data with the controlled trigger defined as

$$LC\ Trigger \equiv BEAM \times LC,$$

where hits of the TOF counter was not required. The LC timing was used for the STOP signal of the TDC's for SDC3·4, while the TOF timing was used in the normal trigger. The TOF efficiency was obtained as

$$\epsilon_{TOF} = \frac{N(TOF \times Track \times AC1 \cdot 2 \times LC)}{N(Track \times AC1 \cdot 2 \times LC)},$$

where $N(Track \times AC1 \cdot 2 \times LC)$ is the number of π^- track which should pass through the effective area of TOF selected by the TDC information of AC1·2 and LC, and $N(TOF \times Track \times AC1 \cdot 2 \times LC)$ the number of those π^- track detected by TOF. The momentum range of scattered π^- of 0.75−1.00 GeV/c was selected by reconstructing a particle trajectory in the SKS. The efficiency averaged in the whole region of TOF was found to be ϵ_{TOF}=99.7±0.1% for the the controlled trigger data. The efficiency was assumed to be the same for K because of a small energy loss difference from π. The error was determined from the difference between the efficiencies fro different π^- momenta.

The detection efficiency of LC was estimated from the π^- beam-through data by changing the beam momentum from 0.75 GeV/c to 0.95 GeV/c keeping the magnetic field of the SKS magnet at 2.5 T. The beam-through data was taken with the controlled trigger defined as

$$TOF\ Trigger \equiv BEAM \times TOF,$$

where hits of the LC counter was not required. The LC efficiency was obtained as

$$\epsilon_{LC} = \frac{N(LC \times Track \times TOF \times AC1 \cdot 2)}{N(Track \times TOF \times AC1 \cdot 2)},$$

where $N(Track \times TOF \times AC1 \cdot 2)$ is the number of π^- track which should pass through the effective area of LC selected by the TDC information of TOF and AC1·2, and $N(LC \times Track \times AC1 \cdot 2 \times LC)$ the number of those π^- track detected by LC. The average efficiency for π^- on the whole region of the LC counter was found to be ϵ_{LC}=98.5±0.1% for the the controlled trigger data. The μ^- events from the π^- decay after passing through TOF was included in the efficiency. The error was determined from the difference between the efficiencies fro different π^- momenta. The efficiency was assumed to be the same for K because the yield of Čerenkov photons by K in the momentum range from 0.75 GeV/c to 0.95 GeV/c was high enough than the discriminator threshold.

The efficiencies of TOF and LC were estimated only by the controlled trigger data. As described in Appendix B, the gain and noise level (ADC pedestal value) were stable enough so that the time dependence of the error of the efficiency was ignored.

AC1·2 K detection

The accidental veto factor of AC1·2 was estimated from the controlled trigger data in which the information of AC1·2 was not required. The trigger condition was defined as,

$$NoAC\ Trigger \equiv BEAM \times TOF \times LC.$$

For the estimation, we used scattered proton events which should not be detected by AC1·2. The coincidence width between TOF and AC1·2 selected by each TDC information was set at 20±5 ns, being the same as that for the PIK trigger. The AC1·2 accidental veto factor was obtained from

$$f_{AC1\cdot2\ acc} = 1 - \frac{N(AC1 \cdot 2 \times Track \times TOF)}{N(Track \times TOF)},$$

where $N(Track \times TOF)$ is the number of proton track which should pass through the effective area of AC1·2, and $N(AC1 \cdot 2 \times Track \times TOF)$ the number of those proton track detected by AC1·2. The accidental veto factor was thus estimated to be 93.1±0.7% for the controlled trigger data. The error was determined by changing the TDC timing selection of the coincidence width between TOF and AC1·2.

In addition, the K detection by δ ray emission was estimated in the simulation using the Geant4 code. The realistic shape of AC2 (box size, PMT position and reflector shape) and the reflection properties of materials were input in the simulation. Pencil beams of kaons with momentum of 0.75−0.95 GeV/c were irradiated to the center position of the vertical area by changing the incident horizontal position (X direction with Y=0 in Fig. 2.18). The detection of K event was defined that photons generated by δ rays reached to the PMT window considering the quantum efficiency of PMT (∼20%). We found that 1.8±0.8% of K events fired AC2. The error was determined from the difference by changing the momentum within 0.75−0.95 GeV/c. Thus, the total accidental veto

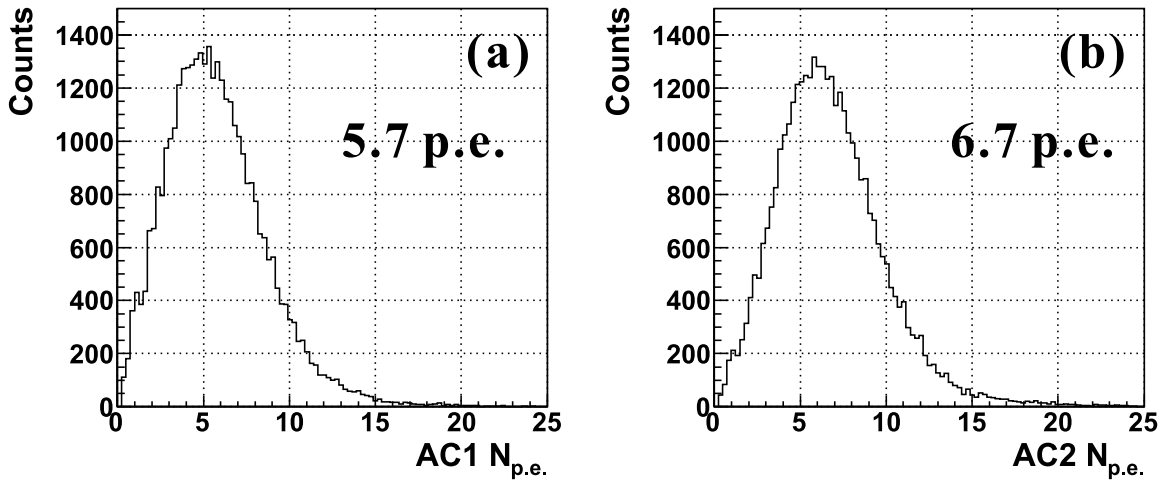

Figure 3.29: The number of photo-electrons detected by AC1 (a) and AC2 (b) for the π^- events.

factor (f_{AC}) including the effect of AC1 and AC2 δ-ray detection was estimated to be 89.8±1.2%.

Figure 3.29 show the sum of the number of photo-electrons detected by AC1 (a) and AC2 (b) for the π events in the $p(\pi^-, K^+)\Sigma^-$ run data with the momentum range of 0.75−0.95 GeV/c. The π detection efficiencies of AC1 and AC2 were 97.9±0.1% and 99.2±0.1%, respectively. The efficiency of AC1 was lower than that of AC2, because of a gap of the aerogel radiators due to a partition of the radiator box, while AC2 had no gap and partitions. The partitions of the box deteriorate light transmission and also decreased the number of photo-electron.

SDC1·2 efficiency

The efficiency of SDC1·2 ($\epsilon_{SDC1\cdot2}$) is the total efficiency including the detector efficiency and the analysis efficiency to find straight tracks at the entrance of the SKS magnet. It was estimated by the same way as that of BC3·4 by using the BEAM trigger events mixed in the (π, K) data. The SDC1·2 efficiency was determined as

$$\epsilon_{SDC1\cdot2} = \frac{N(SDC1\cdot2\,Track \times PiBeam \times BC3\cdot4\,Track)}{N(PiBeam \times BC3\cdot4\,Track)},$$

where $N(PiBeam \times BC3\cdot4\ Track)$ is the number of events for the proper for π and tracks which should pass through the effective area of SDC1·2 were chosen from straight tracks determined by the BC3·4 local tracking, and $N(SDC1\cdot2\ Track \times PiBeam \times BC3\cdot4\ Track)$ the number of good tracks to these π^- events found in the SDC1·2 ($\chi^2 < 20$) local tracking. It was found to be 95.6±0.2%. Since the efficiency is not affected for a small energy-loss difference between π (1.37−1.92 GeV/c) and K (0.75−1.00 GeV/c), we assumed that the efficiency is the same for K. The SDC1·2 local tracking efficiency is the average value during the Θ^+ production run.

SDC3·4 efficiency

The efficiency of SDC3·4 ($\epsilon_{SDC3\cdot4}$) is the total efficiency including the detector efficiency and the analysis efficiency to find straight tracks at the exit of the SKS magnet. We estimated the efficiency using scattered proton events recorded in the PIK trigger data (the $(\pi, p)X$ events) in which the particle does not decay in flight. Figure 3.30 shows the scatter plot between the horizontal scattering angle measured by SDC1·2 and the flight time between BH2 and TOF. The proton events were selected as shown in the figure. The SDC3·4 efficiency was estimated from the number of those selected proton events ($N(Proton)$) as

$$\epsilon_{SDC3\cdot4} = \frac{N(SDC3\cdot4\, Track \times Proton)}{N(Proton)},$$

where $N(SDC3\cdot4\, Track \times Proton)$ was the number of good tracks of these proton events found in the SDC3·4 ($\chi^2 < 20$) local tracking. It was found to be 99.8±0.2% which was the average of typical runs whose event number was statistically large enough during the Σ production run. The error was determined from the root mean square of the efficiency fluctuation for each run. Figure 3.31 shows a layer's efficiency of one of the SDC4 layers as a function of the hit position. There was no dependence on the horizontal position. We assumed the efficiency is the same for K because of a small energy loss difference between proton and K in the momentum range of 0.75−1.00 GeV/c.

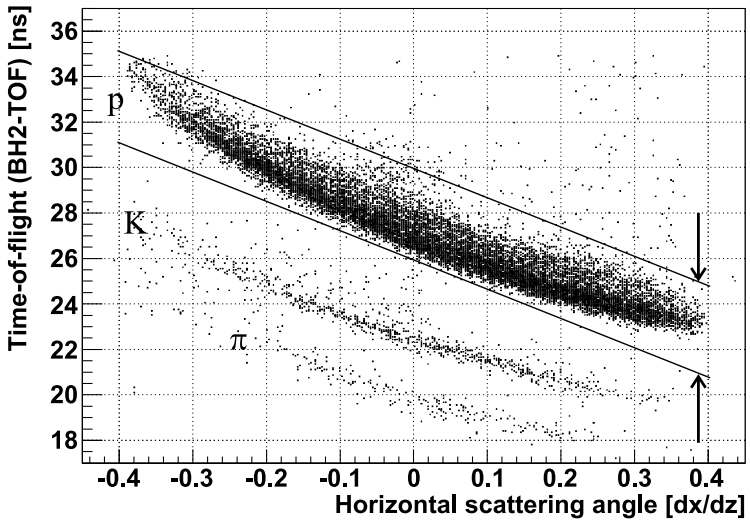

Figure 3.30: Scatter plot between the horizontal scattering angle measured by SDC1·2 and the flight time between BH2 and TOF. The selected region for protons was indicated in the figure.

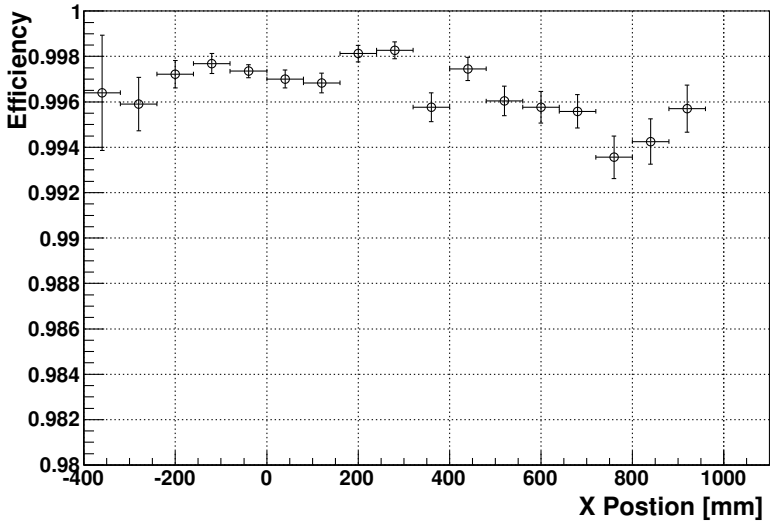

Figure 3.31: The layer's efficiency of one of the SDC4 layers as a function of the horizontal hit position.

SKS tracking efficiency

The SKS tracking efficiency ($\epsilon_{SKStrack}$) was estimated by using the (π, p)X events recorded in the PIK trigger because the proton does not decay in flight. The quality of the SKS tracking χ^2 was estimated from the missing mass resolution of the Σ^+ data. Figure 3.32 shows the missing mass resolution of Σ^+ as a function of the χ^2_{SKS}. In the figure, the bin width whose χ^2 was more then 6 was determined to have the same number of events included in each bin. It was found that the events whose χ^2_{SKS} is less than 30 kept the missing mass resolution of less than 2.3 MeV/c^2 (FWHM). In order to keep the achievable sensitivity, the acceptable Σ^+ missing mass resolution which corresponded to the estimated Θ^+ missing mass resolution of less than 2.0 MeV/c^2 (FWHM) was estimated to be less than 2.5 MeV/c^2 (FWHM). In addition, the ratio of the peak tail of Σ^+ was drastically increased in χ^2_{SKS} of more than 30. Thus, we selected the events of χ^2_{SKS} less than 30 as good trajectory.

The SKS tracking efficiency ($\epsilon_{SKStrack}$) was the analysis efficiency to reconstruct a particle trajectory in SKS, which is obtained as

$$\epsilon_{SKStrack} = \frac{N(SKStrack \times SDC1 \cdot 2\, track = 1 \times SDC3 \cdot 4\, track = 1)}{N(SDC1 \cdot 2\, track = 1 \times SDC3 \cdot 4\, track = 1)},$$

where $N(SDC1 \cdot 2\, track = 1 \times SDC3 \cdot 4\, track = 1)$ was the number of single good tracks of proton events found in the SDC1·2 ($\chi^2 < 20$) and SDC3·4 ($\chi^2 < 20$) local tracking, and $N(SKStrack \times SDC1 \cdot 2\, track = 1 \times SDC3 \cdot 4\, track = 1)$ the number of good SKS track found in the single good tracks of both SDC1·2 and SDC3·4 local tracking.

Figure 3.33 shows the efficiency as a function of the scattering angle. The SKS tracking efficiency for each angle (θ_{SKS}) was estimated as a ratio of the number of events accepted as a good trajectory within the selected scattering angle region by the tracking

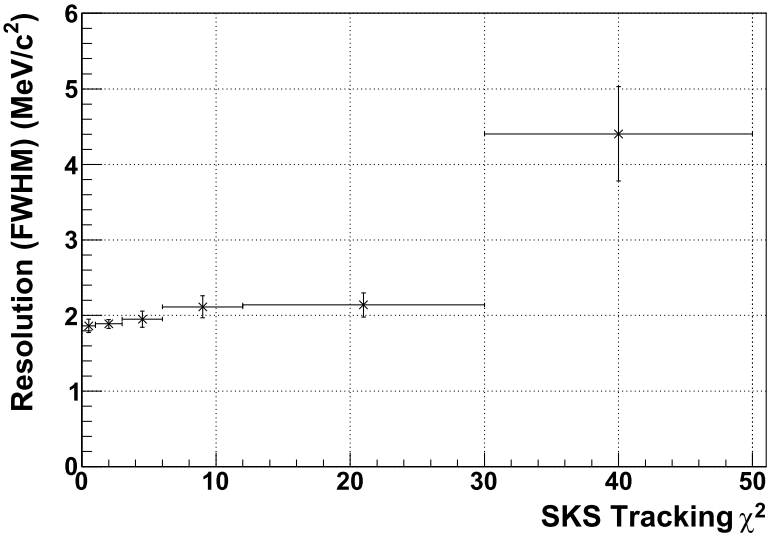

Figure 3.32: The missing mass resolution of Σ^+ as a function of the χ^2_{SKS}.

analysis to the number of events which have good straight tracks within the selected scattering angle calculated by SDC1·2 trajectory ($\theta_{SDC1\cdot2}$) as,

$$\epsilon_{SKS\theta} = \frac{N(SKStrack \times \theta_{SDC1\cdot2} \times SDC1\cdot2\ track = 1 \times SDC3\cdot4\ track = 1)}{N(\theta_{SDC1\cdot2} \times SDC1\cdot2\ track = 1 \times SDC3\cdot4\ track = 1)},$$

The scattering angle ($\theta_{SDC1\cdot2}$) was calculated by using the horizontal and vertical angles measured by SDC1·2 tracking. Good straight tracks at both of the entrance and exit of SKS were also required. The efficiency for the scattering angle more than 15° was worse than the other angles because the magnetic field was not reproduced well in the fringing field region, namely the region near the pole edge and the coil of the SKS magnet, by the ANSYS code.

Fig. 3.34 shows the missing mass resolution of Σ^+ as a function of the SKS scattering angle. The resolution of scattering angle more than 15° is worse than the acceptable missing resolution of less than 2.5 MeV/c^2. In addition, the peak shape of Σ^+ was distorted in the large scattering angle region. Thus, for the calculation of the cross section, the events with the scattering angle of $2^\circ - 15^\circ$ were selected, and the scattering angle dependence of the SKS tracking efficiency was taken into account.

The efficiency of the SKS tracking (ϵ_{SKS}) was estimated to be 96.0±0.2% with the tracking χ^2 cut of less than 30. It was the average of typical runs whose event number was statistically large enough during the Σ production run. The error was determined from the root mean square of the efficiency fluctuation for each run. The present total SKS tracking efficiency was 91.6±0.3% from the efficiencies of SDC1·2 (96%), SDC3·4 (>99%) and the SKS tracking (96%). For the previous KEK experiment, the total efficiency was ∼72% (SDC1·2: 91%, SDC3·4: 81% and SKS: 97%) [47]. The improvement was due to the better tracking efficiency in the tracking chambers.

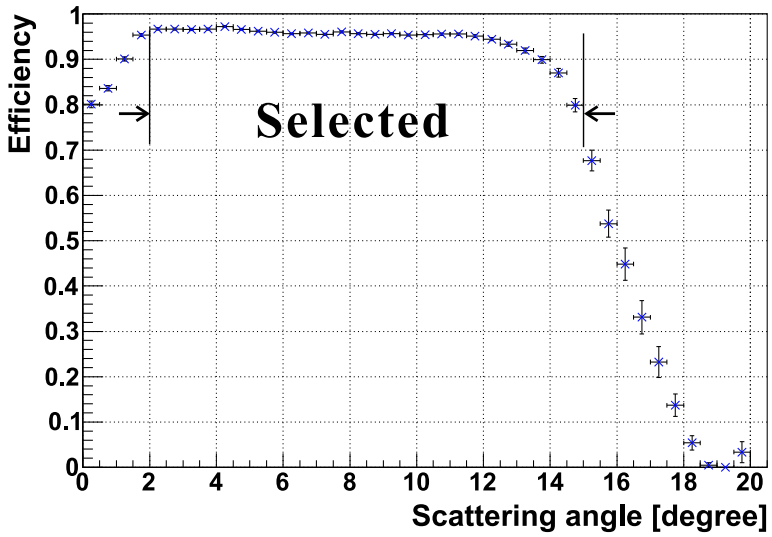

Figure 3.33: The SKS tracking efficiency as a function of the scattering angle.

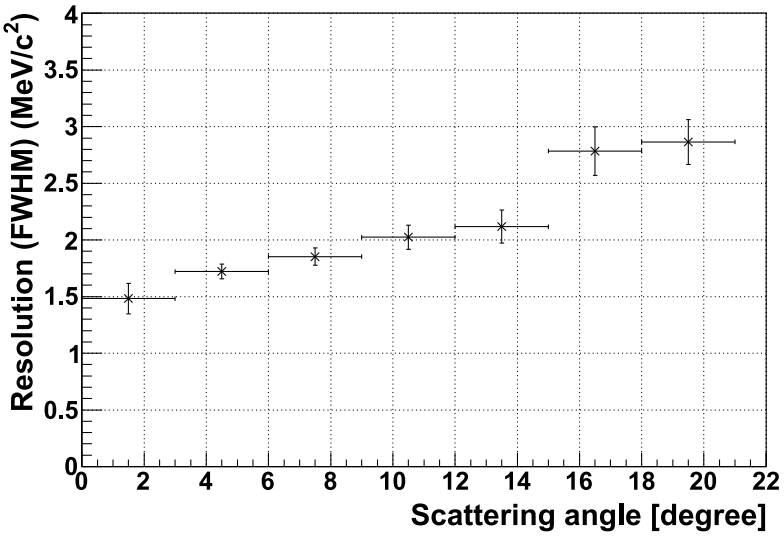

Figure 3.34: The missing mass resolution of Σ^+ as a function of the SKS scattering angle.

Efficiency of the particle identification in the SKS

The event selection by the hodoscope cuts were described in Sec. 3.3. The efficiency of the total hodoscope cuts (ϵ_{Hodo}) was estimated to be 93.3±0.3%. The error is statistical one.

Figure 3.35 shows a typical mass spectrum for the $p(\pi^-, K^+)\Sigma^-$ data. The PIK triggered events are shown in the black histogram and the K selected events after the hodoscope cuts in red one. The tail around the K peak is due to the time walk of the TOF-TDC which was not corrected. The tail of the proton distribution comes from the reaction events at the BH2 counter. Kaons are clearly separated from pions and protons, and the selected region ($0.17 < m^2 < 0.50$) is indicated in arrow. By fitting a Gaussian function to the K distribution, the selected region was determined as -3σ for the lower boundary to avoid the tail of π distribution. The higher one was determined at the edge of the tail. The selection efficiency was estimated to be 99.6±0.3% as a ratio of the number of events in the selected region above to the number of events $[N(M^2\ without\ cut)]$ for a loose selection ($(0.15 < m^2 < 0.55)$). The selected region of the $p(\pi^-, K^-)$ data was the same as that for the $p(\pi^-, K^+)\Sigma^+$ data.

The overall cut efficiency was estimated by

$$\epsilon_{PID} = \epsilon_{Hodo} \times \frac{N(M^2\ with\ cut \times M^2\ without\ cut)}{N(M^2\ without\ cut)}.$$

The efficiency was estimated to be 92.9±0.5% from the $p(\pi^-, K^+)\Sigma^-$ data. The error was determined from the selection efficiencies of different production runs.

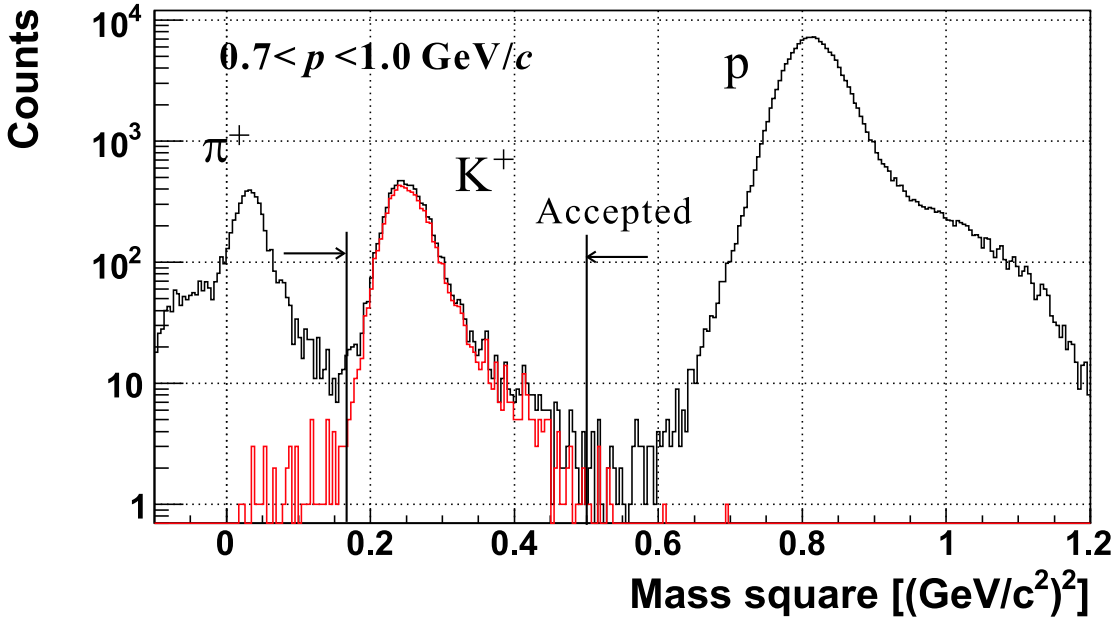

Figure 3.35: Scattered particle mass distribution for the $p(\pi^-, K^+)\Sigma^-$ data. The tail around the K peak was due to the decay events. The tail of the proton distribution was from the reaction events at the BH2 counter.

Vertex cut efficiency

As mentioned in Sec. 3.4, the vertex cut was applied to select good (π, K) events from the target region. The vertex resolution for very forward scattering angle events was worse than the other events as shown in Fig. 3.26. By selecting events with the z-vertex in just the target length, the z-vertex efficiency had a scattering angle dependence. We accepted the events inside of the target region as the good (π, K) events. For the calculation of the cross section, the scattering angle dependence of the z-vertex cut efficiency was taken into account. The liquid hydrogen target consisted of several materials, which caused background events. The background events in the selected region are discussed in Sec. 3.7. The efficiency (ϵ_{vertex}) was obtained to be 75.4±0.7% in average for $2^\circ - 15^\circ$.

K decay factor

Since the $\beta\gamma c\tau$ of 0.75−1.00 GeV/c K is 5.6−7.5 m, a part of the kaons produced in the target decay before they reach the SKS downstream detectors. The survival rate in the SKS track reconstruction process was studied with a Monte Carlo simulation. In the simulation, events were generated at the target with a uniform momentum distribution (0.75−0.95 GeV/c), a uniform angular distribution ($\theta < 20^\circ$) and a realistic reaction point distribution (Gaussian with $\sigma_{x,y,z} = 10.0,\ 5.50,\ 120$ mm). The events of the K decay before reaching the TOF counter were completely rejected by the track reconstruction process. If a kaon decayed after passing through TOF but before passing through AC2, AC2 fired and such a event was rejected. The events of the K decay after passing through AC2 were partly rejected by checking the combination between hit segments of TOF and LC as shown in Fig. 3.16. The rejection rate (0.5%) was included into ϵ_{PID}. The survival rate from K decay is listed in Table 3.2. The total survival rate (f_{decay}) was estimated to be 41.7±2.0%. The error was determined by the ambiguity of the K decay inside of the AC2 radiator.

For the calculation of the cross section, the survival rate before reaching TOF was corrected event by event taking into account the momentum and the flight path length. Then, after passing through TOF, we took into account the downstream survival rate, whose dependence on the scattering angle and momentum was small and averaged.

Table 3.2: The rejection of K decay events and the total survival rate.

Decay	Fraction [%]
No decay at TOF	44.9
Rejected by the SKS tracking	55.1
Rejected by AC1·2	3.2
Total survival rate	41.7

K absorption factor

Some of the kaons produced in the target interacted with materials in the spectrometers along the flight path. The K^+N and K^-N inelastic cross sections around 0.85 GeV/c are 2.0 mb and 20.0 mb, respectively. The absorption rate (f_{abs}) was estimated by the simulation, in which the target, the counters, the drift chamber gas and widows, the helium bags and air between the detectors were considered as materials in the spectrometer as shown in Table 3.3. Along the path of the scattered kaons, the thickness of TOF (3.10 g/cm^2) and AC1·2 (4.52 g/cm^2) was dominant, while the total material thickness was ∼10 g/cm^2. We took into account both inelastic and elastic interactions in the simulation. The K events were generated at the target with a uniform momentum distribution (0.75−0.95 GeV/c), a uniform angular distribution ($\theta < 20^\circ$) and a realistic reaction point distribution (Gaussian with $\sigma_{x,y,z} = 10.0,\ 5.50,\ 120$ mm). The absorption rate (f_{abs}) of the kaons was obtained as

$$f_{abs} = 1 - \frac{N_{K\ hit\ on\ LC}}{N_{K\ generated}}.$$

The rate was estimated to be 3.2±0.5% for K^+ and 10.6±0.5% for K^- respectively. The error was estimated by the difference of the material thickness along the particle trajectories, due to overlapping of the black sheet of the TOF counter (∼0.03 g/cm^2) and insulators inside of the target chamber (∼0.02 g/cm^2).

Table 3.3: Typical materials in the spectrometers along the flight path.

Material	length (cm)	Density (g/cm^3)	Thickness (g/cm^2)
Target	12.0	0.0709	0.85
TOF	3.0	1.03	3.10
AC1	11.3	0.20	2.26
AC2	11.3	0.20	2.26
AC frame (Al)	0.2	2.70	0.54

Efficiency of the matrix trigger

In the Θ^+ production data, the pre-scaled PIK trigger data without the matrix trigger was also taken with the pre-scale factor of 10. The efficiency of the matrix trigger (ϵ_{matrix}) was estimated by following equation,

$$\epsilon_{matrix} = \frac{N_{on}}{10 \times N_{off}},$$

where N_{on} and N_{off} are the number of kaons selected in the scattered particle mass distribution with and without the matrix trigger data, respectively. The efficiency had no dependence on the scattering angle and the scattered particle momentum so that the matrix trigger made no bias on the missing mass spectrum. We estimated the efficiency of the matrix trigger to be ϵ_{matrix}=99.0±0.1%. The error come from the statistical one.

3.6 Acceptance of SKS

The effective solid angle of the SKS ($\Delta\Omega$) was calculated with a simulation. For a fixed interval of the scattering angle $\Delta\theta$, the effective solid angle was calculated as a function of scattering angle θ and momentum p as follows,

$$\Delta\Omega(\theta, p; \Delta\theta) = 2\pi \int_{\theta-\frac{1}{2}\Delta\theta}^{\theta+\frac{1}{2}\Delta\theta} d\cos\theta \times \frac{\text{number of accepted events}}{\text{number of generated events}}.$$

In the event generation, the distribution of the beam profile defined as a function of (x_b, y_b, u_b, v_b) was produced from the experimental data, where x_b, y_b, u_b and v_b are the horizontal and vertical positions and their direction cosines of a beam particle at the target. The scattered kaons were generated uniformly from $\theta - \frac{1}{2}\Delta\theta$ to $\theta + \frac{1}{2}\Delta\theta$ in the polar angle (uniformly generated from $\cos(\theta + \frac{1}{2}\Delta\theta)$ to $\cos(\theta - \frac{1}{2}\Delta\theta)$ in the simulation), from 0 to 2π in the azimuthal angle and from $p - \frac{1}{2}\Delta p$ to $p + \frac{1}{2}\Delta p$ in the momentum.

In the simulation, the combination of the TOF and LC counters used in the matrix trigger was also taken into account. In the present analysis, we selected events in the scattering angle from 2^o to 15^o in which the efficiency of the SKS tracking is flat. Therefore, the effective solid angle was calculated for $2^o \leq \theta \leq 15^o$.

In addition, the size of AC1·2 was smaller than that of TOF and LC. For the present experiment, the TOF and LC segments used in the trigger were restricted after precise adjustment of their coverages considering the scattered particle momentum and the trigger rate. The coverages of TOF and LC were from the segment number 11 to 32 (last) and from 10 to 28 (last), respectively. In the simulation, the acceptance of AC1·2 was considered after selecting those segments of TOF and LC. The acceptance without any selection (a) and the selected one (b) are shown in Fig. 3.36. The acceptance is represented by the ratio of the number of accepted events divided by the number of generated events. Figure 3.37 shows the acceptance projected to the polar angle at the scattered particle momentum of 0.85 GeV/c (a) and the projection to the momentum (b) with the TOF and LC segment selection.

The momentum region of the scattered particle of 0.80−0.95 GeV/c corresponds to the region of the Θ^+ missing mass of 1.51−1.54 GeV/c^2. The momentum region wide enough is covered by selecting the segments of TOF and LC.

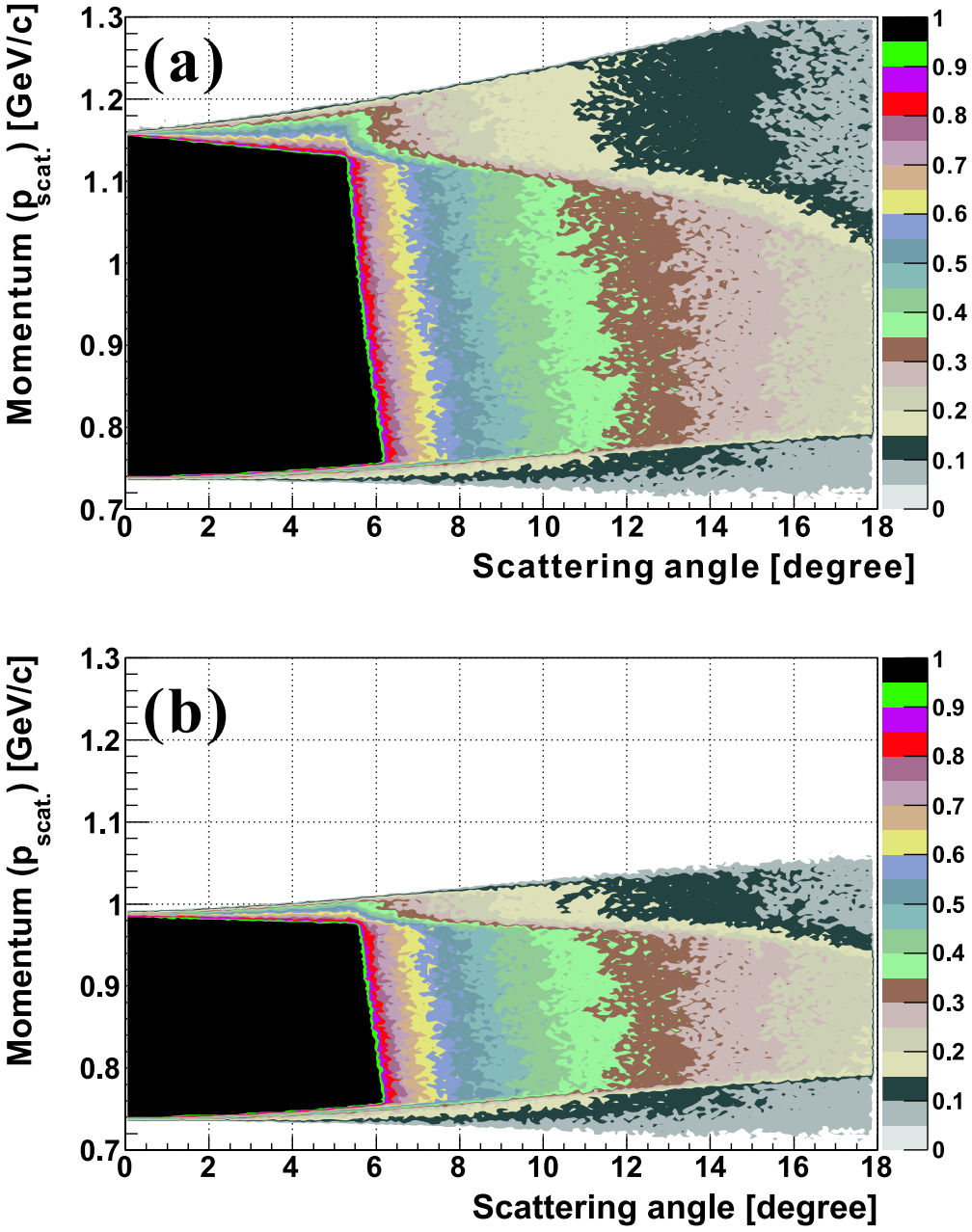

Figure 3.36: The acceptance of SKS in the 2.5 T mode. It shows the total acceptance without the TOF and LC segment selection (a) and with the TOF and LC segment selection (b). The acceptance is represented by the ratio of the number of accepted events to the number of generated events.

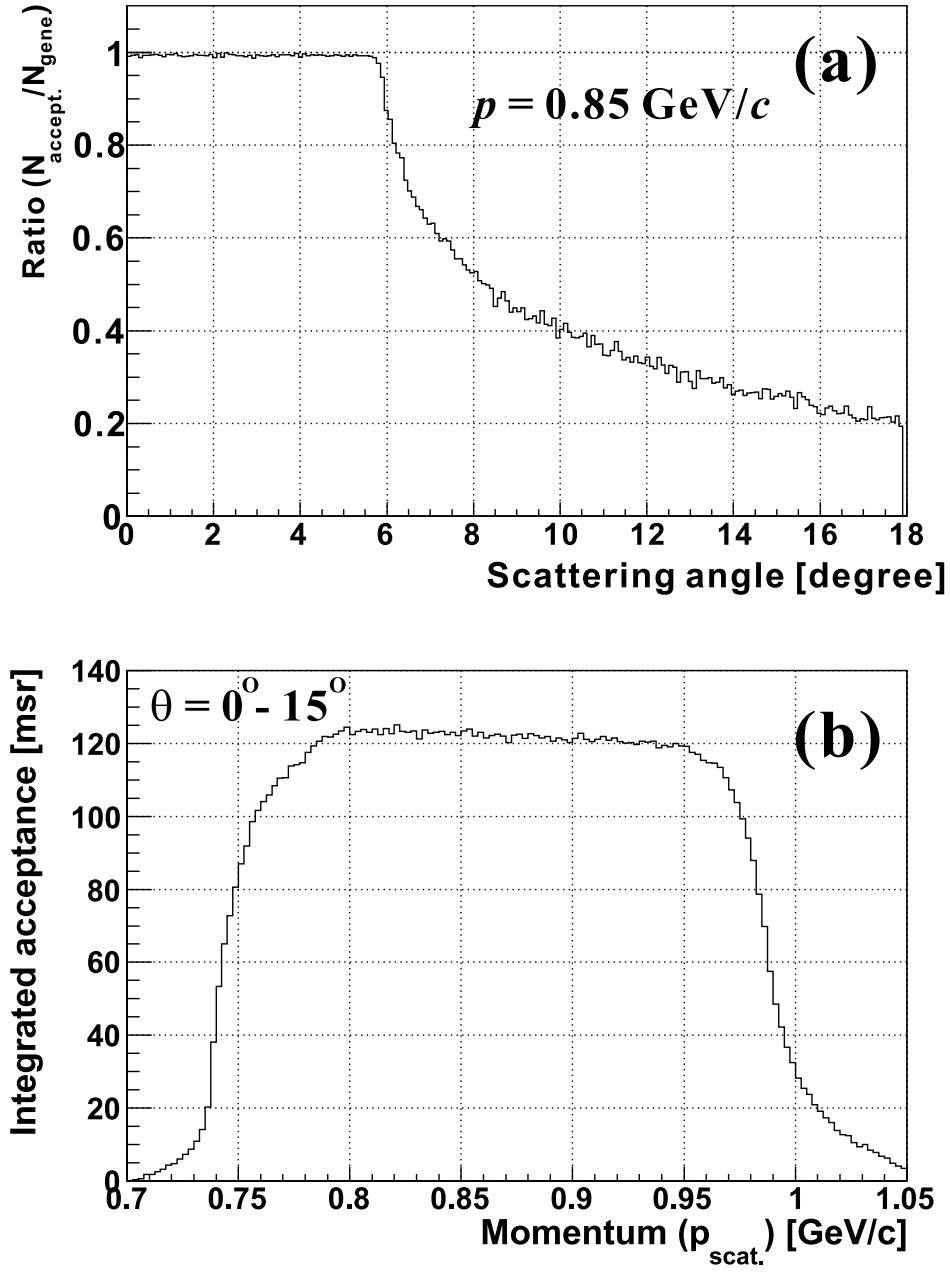

Figure 3.37: The acceptance of SKS in the 2.5 T mode. It shows the acceptance projected to the polar angle for the scattered particle momentum of 0.85 GeV/c (a) and the projection to the momentum (b) with the TOF and LC segment selection. The acceptance (a) is represented by the ratio of the number of accepted events to the number of generated events. The acceptance (b) is the solid angle integrated from 0° to 15°, respectively.

3.7 Background

In order to estimate the statistical significance of a Θ^+ peak in the missing mass spectrum, the background of the spectrum was estimated from the empty target data and a Monte Carlo simulation.

3.7.1 Empty target data

The target cell of the liquid hydrogen target was made of PET and Mylar as described in Sec. 2.7. We took empty target data to estimate the number of events from those target cell materials. To accumulate a large number of events, we used the (π^-, π^-) reaction for reconstructing the reaction vertex point instead of the (π^-, K^-) reaction.

For the very forward scattering angle, the z-vertex distribution of both events from the liquid hydrogen target and from the target materials were largely smeared as shown in Fig. 3.38, where the events with the scattering angle over 0° to 2° (a) and 2° to 4° (b) are shown. The black and the red lines are the empty target and the liquid hydrogen target data, respectively. The empty target data was normalized by the beam flux. The number of events from the liquid hydrogen was not much enhanced from the empty target data for the event of scattering angle over 0° to 2°. Thus, most of the background events with the scattering angle over 0° to 2° were ascribed to the beam decay events within the target region. From the (π^-, π^-) data, the beam decay μ^- in the target region could not be distinguished from the reaction π^-. In this analysis, the very forward angle region was cut away in order to reduce the ambiguity of the vertex selection efficiency. The scattering angle cut ($\theta \geq 2°$) was applied as indicated in Fig. 3.26.

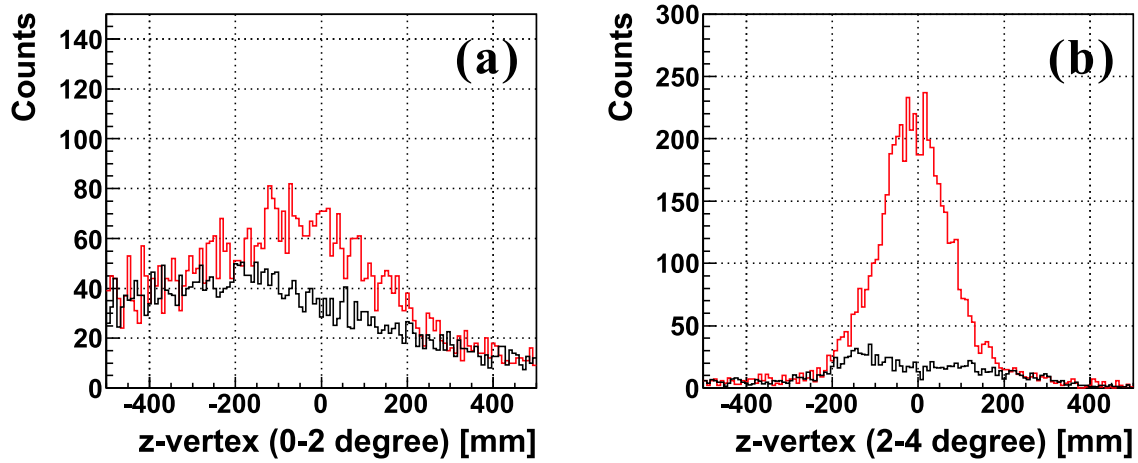

Figure 3.38: The z-vertex distribution of scattering angle over 0° to 2° (a) and 2° to 4° (b). The black and the red lines are the empty target and the liquid hydrogen target data, respectively. The empty target data was normalized by the beam flux.

Figure 3.39 shows the vertex distributions along the beam axis (a), and the horizontal (b) and vertical (c) directions. The red line histogram shows the vertex distribution

obtained from the liquid hydrogen target data. The empty target data normalized by the beam flux was also shown in the histogram.

Figure 3.40 shows the vertex distribution obtained by subtracting the contribution of the target cell materials in the empty target data from the vertex distribution obtained for the liquid hydrogen target data. As shown in the figure, the region of the vertex cut was tightly applied for the horizontal and vertical directions of $|x| < 25$ mm and $|y| < 20$ mm, respectively. The z-vertex region was selected to be $-70 < z < 50$ mm according to the subtracted distribution and the target center position. The vertex selection efficiency was obtained to the subtracted vertex distribution as

$$\epsilon_{vertex} = \frac{N_{With\ vertex\ selection}}{N_{Without\ vertex\ selection}},$$

where $N_{With\ vertex\ selection}$ is the number of events in the selected vertex region and $N_{Without\ vertex\ selection}$ events in the whole region of the subtracted vertex distribution.

In the selected region, the ratio of remaining background events was 2.8±0.1%. The contribution of those events to the error of the cross section was included as a systematic error, where the background in the (π^-, π^-) reaction data was assumed to be the same as of the (π^-, K^-) reaction.

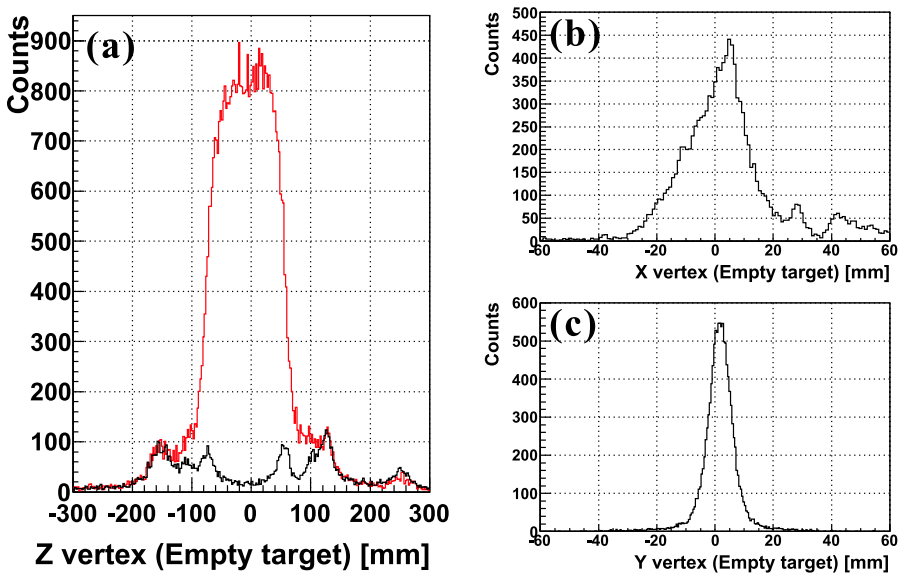

Figure 3.39: The vertex distribution of the empty target data along the beam axis (a), and the horizontal (b) and vertical (c) directions. The red line histogram shows the vertex distribution obtained from the liquid hydrogen target data. The black line shows the empty target data normalized by the beam flux.

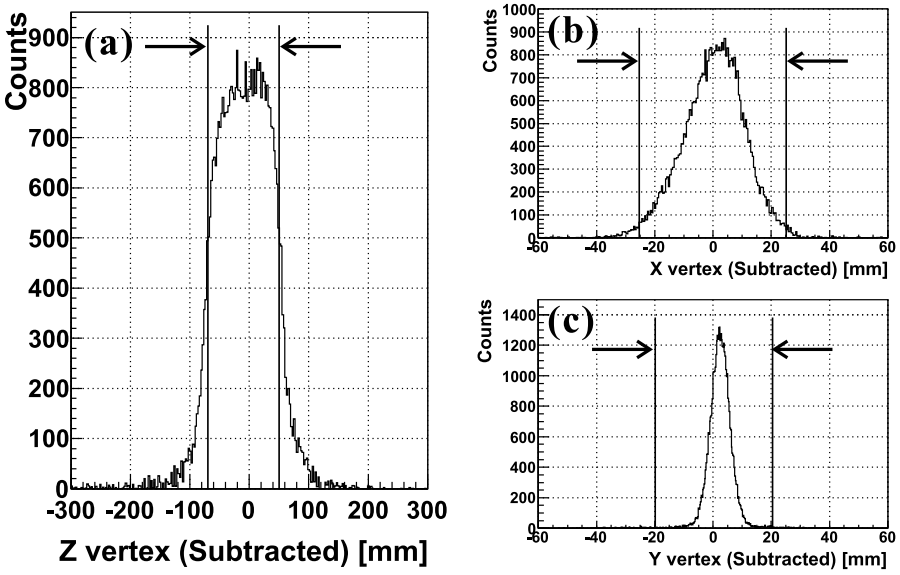

Figure 3.40: The subtracted vertex distribution from the liquid hydrogen data along the beam axis (a), and the horizontal (b) and vertical (c) directions. The selected region was indicated by arrows.

3.7.2 Associated reactions

The main backgrounds using the $p(\pi^-, K^-)X$ reaction are the ϕ production, the $\Lambda(1520)$ production and the K^-K^+n and K^-K^0p productions following the 3-body phase space as following.

$$\begin{aligned} \phi \text{ production} : \pi^- p &\rightarrow \phi\, n \rightarrow K^-K^+n && (\sigma = 30.0 \pm 8.0\ \mu\text{b}) \\ \Lambda(1520) \text{ production} : \pi^- p &\rightarrow \Lambda(1520)\, K^0 \rightarrow K^-K^0p && (\sigma = 20.8 \pm 5.0\ \mu\text{b}) \\ \text{phase space} : \pi^- p &\rightarrow K^-K^+n \text{ and } K^-K^0p && (\sigma \sim 25\ \mu\text{b}) \end{aligned}$$

We estimated the background events from those associated reactions by using the Geant4 simulation code.

The angular dependence of the cross section for the ϕ production and the $\Lambda(1520)$ production was reported in Ref. [61] and Ref. [62], respectively. For the ϕ production, the cross section has a slight angular dependence as shown in Fig. 3.41 (a). In the simulation, the isotropic production was used because the data is not inconsistent with the isotropic distribution. For the $\Lambda(1520)$ production, we used the angular dependence of the cross section of $\propto 1 + \cos^2(\theta_{CM})$ as indicated in Fig. 3.41 (b). Figure 3.42 shows the background shape of those associated reactions. In the spectrum, the acceptance of SKS, the decay of scattered K^-, the distribution of the beam profile and the beam momentum bite were included. The relative yield of the three processes in the figure was normalized by the ratio of each measured cross section. The comparison with the obtained data was discussed in Sec. 4.1.

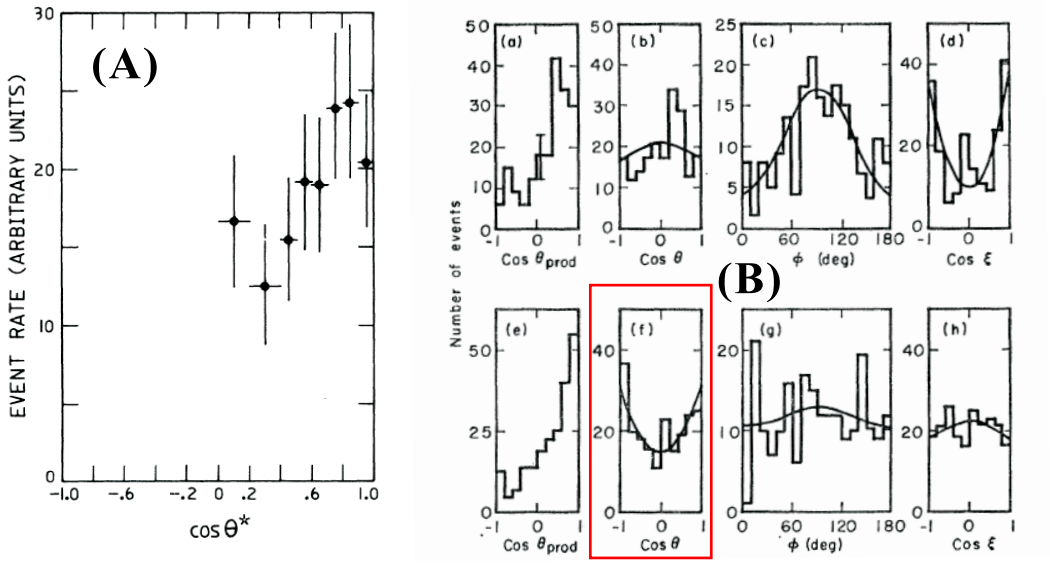

Figure 3.41: The angular dependence of the cross section of the ϕ [61] (A) and the $\Lambda(1520)$ [62] (B) production. The upper and bottom histograms are the angular distributions of the $\Sigma(1385)$ and the $\Lambda(1520)$ production, respectively. (f) is the angular dependence used in the simulation.

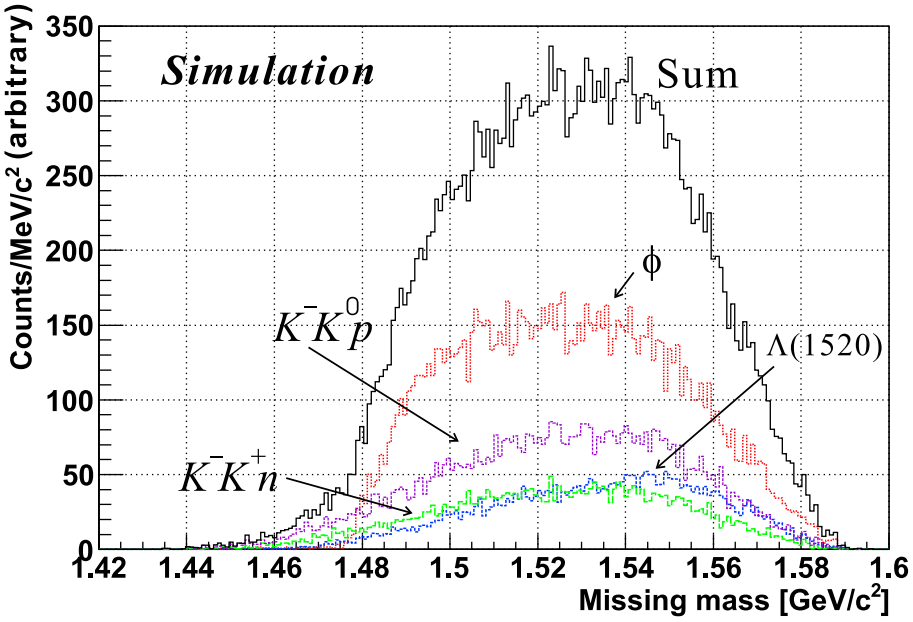

Figure 3.42: The estimated background shape of the associated reactions.

3.8 The Σ production cross section

Using the elementary Σ production, the consistency between the obtained cross section and the reference cross sections was checked. For the cross section calculation, the efficiencies which were estimated from the $\Sigma^{\pm}$ data were used. Figure 3.43 shows the missing mass spectrum for Σ^+ and Σ^- obtained from the analysis of the $p(\pi^+, K^+)$ and $p(\pi^-, K^+)$ data, respectively. The peaks of Σ^+ and Σ^- were clearly observed.

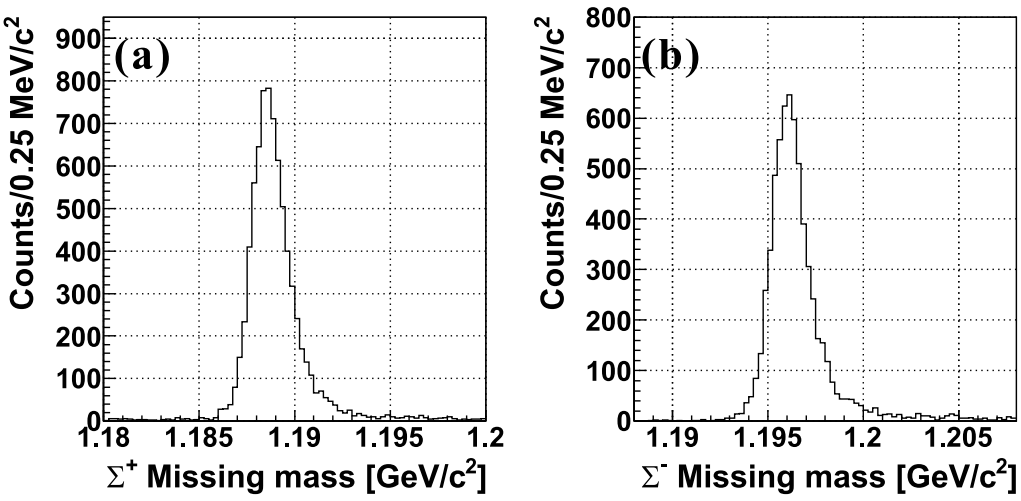

Figure 3.43: The missing mass spectrum of Σ^+ (a) and Σ^- (b).

The differential cross section of Σ^+ production is shown in Fig. 3.44. The cross section reported in old experiments [63] is also shown in the figure. The old data was taken via the $p(\pi^+, K^+)$ reaction with the beam momentum of 1.377 GeV/c, while the present data was taken with that of 1.375 GeV/c. Since the past experimental data was given in the center of mass system, it was transfered to the laboratory system for comparison. The present data is indicated in cross and the previous data is shown in open circles.

The differential cross section of Σ^- production is shown in Fig. 3.45 with the old experiments [64]. The present data taken with the beam momentum of 1.389 GeV/c is shown in cross, and the open circle and the open square show the old data with the beam momentum of 1.275 GeV/c and 1.325 GeV/c, respectively.

The present data agrees well with the previous measurements and improves statistics.

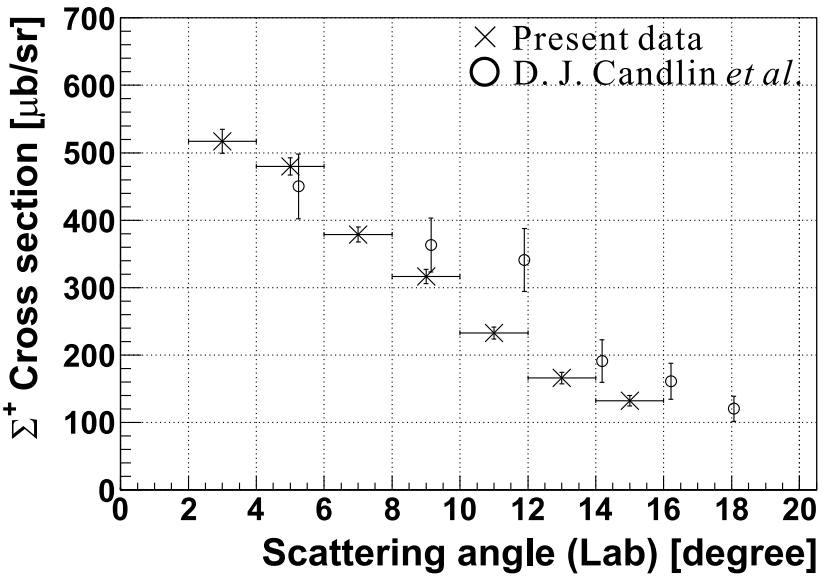

Figure 3.44: The differential cross sections of Σ^+ production. The angular distribution reported in old experiment [63] is also shown in open circle.

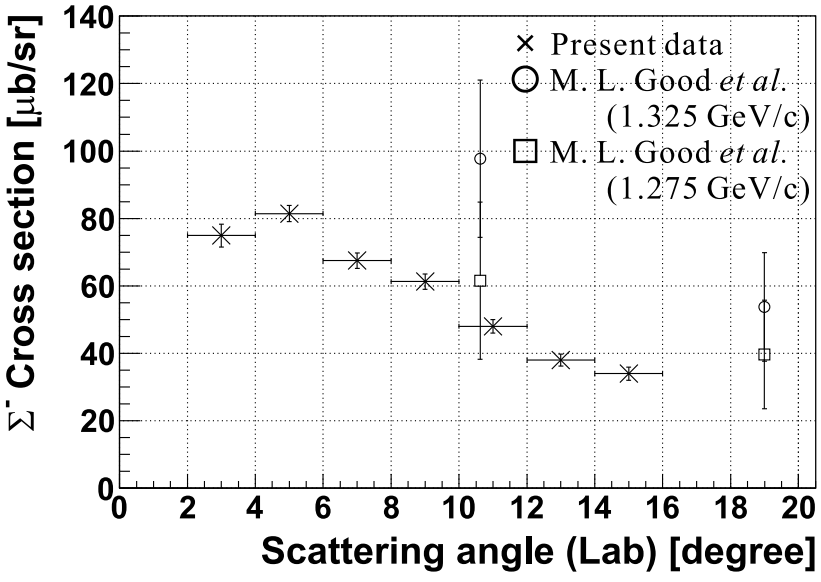

Figure 3.45: The differential cross sections of Σ^- production. The angular distribution reported in old experiments [64] is also shown in open circle and open square.

3.9 Systematic errors

The systematic error of the total cross section for $\Sigma^{\pm}$ and that for Θ^{+} is summarized in Table 3.4. It was obtained from the experimental efficiency (ϵ_{total}) and the acceptance of the SKS ($\Delta\Omega$). The error for $\Sigma^{\pm}$ was estimated from only the $\Sigma^{\pm}$ production data. The error was smaller than that of the Θ^{+} production run because of the small time dependence of the fluctuation of the efficiency values. The stability of the detector efficiencies during the Θ^{+} production run is described in Appendix B. The time dependence of the efficiency values was included in the systematic errors.

Table 3.4: The systematic error of the cross section for each data.

Data	Cycle	ϵ_{total} [%]	$\Delta\Omega$ [%]	Total [%]
$\Sigma^{\pm}$	October	±3	±1	±4
Θ^{+}	October/November	±6	±1	±7

3.10 Energy precision and resolution

The energy precision and resolution are discussed in this section. In the (π^-, K^-) reaction with the beam momentum of 1.92 GeV/c, there are no monochromatic mass peaks around the Θ^+ mass which can be used for the mass calibration, as we used to calibrate the mass scale in hypernuclear spectroscopy experiments [47]. In addition, the momentum of scattered particles was reconstructed by the calculated magnetic field map of the SKS magnet, while a precisely measured field map was used in the previous KEK experiments using SKS. The accuracy of the absolute value and the resolution of the missing mass were estimated by the beam-through data with the empty target and by the $p(\pi^\pm, K^+)\Sigma^\pm$ reaction data. The beam momentum setting for the $p(\pi^\pm, K^+)\Sigma^\pm$ reaction data was 1.37 GeV/c, where the momentum range of scattered particles was the same as that for the (π^-, K^-) reaction with the beam momentum of 1.92 GeV/c.

Beam-through data

In order to check the linearity of the SKS momentum, the π^- beam-through data without a target were taken at several central momenta from 0.75 GeV/c to 0.95 GeV/c. The magnet setting of SKS was fixed at the negative polarity of 2.5 T.

Figure 3.46 shows the mean values of the difference of momenta measured by the two spectrometers ($\Delta p = p_{SKS} - p_{K1.8}$) as a function of the central momentum of the beam line spectrometer. The average offset of the momentum difference ($\sim$4 MeV/c) was corrected to be zero. We assumed the central momentum of the beam spectrometer was proportional to the magnetic field of the beam line magnet. The momentum difference was fluctuated within $\pm$0.4 MeV/c. For the beam-through data, only a special path of the π^- beam trajectory was examined and the position dependence of the inaccuracy of the calculated magnetic field map enhanced the fluctuation. Figure 3.47 shows the distribution of the difference of momenta measured by the two spectrometers without any offset correction. The beam momentum setting was 0.85 GeV/c.

Figure 3.48 shows the width of the distribution for the momentum difference between the two spectrometers (Δp) as a function of the central momentum of the beam line spectrometer. This width gives the sum of the momentum resolution for the two spectrometers (σ_{SKS} and $\sigma_{K1.8}$) because the width (rms) could be given as $\sigma_{\Delta p} = (\sigma_{SKS}^2 + \sigma_{K1.8}^2)^{1/2}$. The width is $\sim$0.2% (FWHM) for the central momentum. We found that the central momentum dependence of Δp width (the sum of the momentum resolutions) was negligibly small. As described in Appendix A, since the resolution was determined by the magnetic field of the uniform region which had a larger BL, the effect of inaccuracy of the magnetic field was small for the beam-through data.

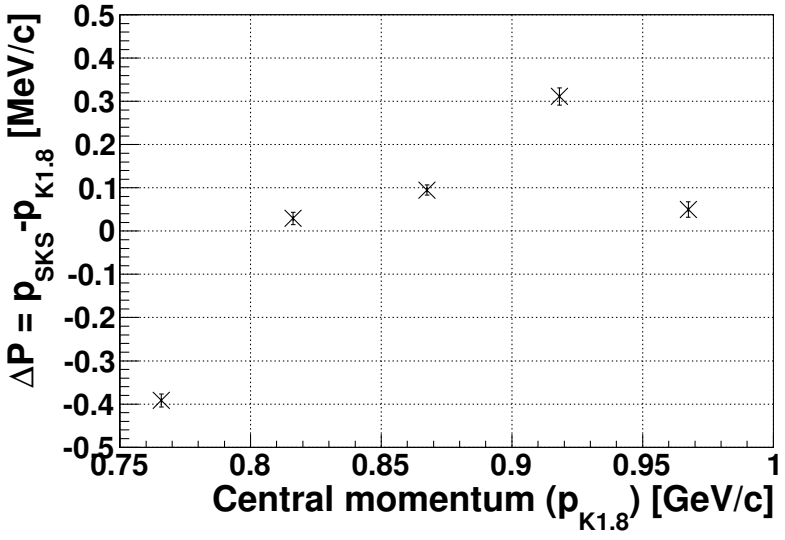

Figure 3.46: The momentum difference between the two spectrometers as a function of the central momentum of the beam line spectrometer. It was fluctuated because the position dependence of the inaccuracy of the calculated magnetic field map caused the SKS momentum shift for the beam-through data.

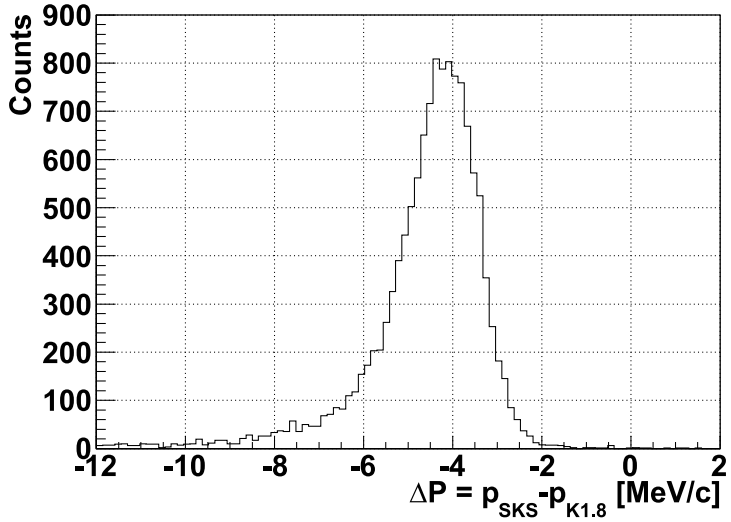

Figure 3.47: The momentum difference between the two spectrometers without any offset correction. The beam momentum setting was 0.85 GeV/c.

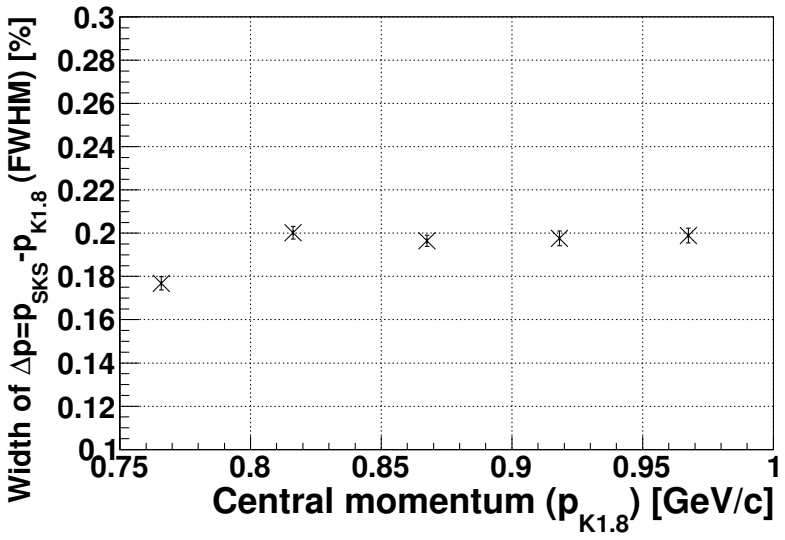

Figure 3.48: The width of the distribution for the momentum difference between the two spectrometers as a function of the central momentum of the beam line spectrometer.

Energy loss correction

Energy loss in target

The missing mass was calculated from the momentum vectors of the incident beam particle and the scattered particle. The energy loss by the materials on the path of the particle trajectory affected the absolute values of the momentum.

The effect of the energy loss by the target materials was estimated by a simulation. In the simulation, only the liquid hydrogen was considered. The angular distribution of the scattered particles was assumed to be uniform in the center-of-mass system. Figure 3.49 shows the simulated missing mass spectrum of the $p(\pi^-, K^+)\Sigma^-$ reaction without the target (a) and with the target (c). The mass center was shifted to M_Σ+2.15 MeV/c^2 with the missing mass resolution of 0.74 MeV/c^2 (FWHM). Compared with the simulated resolution without the target of 0.48 MeV/c^2 (FWHM), the effect of the energy loss by the target material was estimated to be ΔE_{target}=0.56 MeV/c^2 (FWHM). This effect included not only the energy loss straggling but also the difference of the path length in the target. In the case of the $p(\pi^-, K^-)\Theta^+$ reaction as shown in Fig. 3.49 (b, d), the mass was expected to shift to M_Θ+1.57 MeV/c^2, assuming the Θ^+ mass of 1.53 GeV/c^2 and the uniform production angular distribution in the center-of-mass system. The effect of the energy loss by the target material was estimated to be ΔE_{target}=0.41 MeV/c^2 (FWHM).

In the analysis of the $p(\pi^\pm, K^+)\Sigma^\pm$ reaction data, the energy loss can be calculated event by event from the vertex position using the Bethe Bloch formula. Only the liquid hydrogen was considered as the material. The corrected shift was 2.45±0.04 MeV/c^2 in average. To the missing mass calculation, the event-by-event correction of the target energy loss was applied. The error of the correction was included in the energy scale calibration.

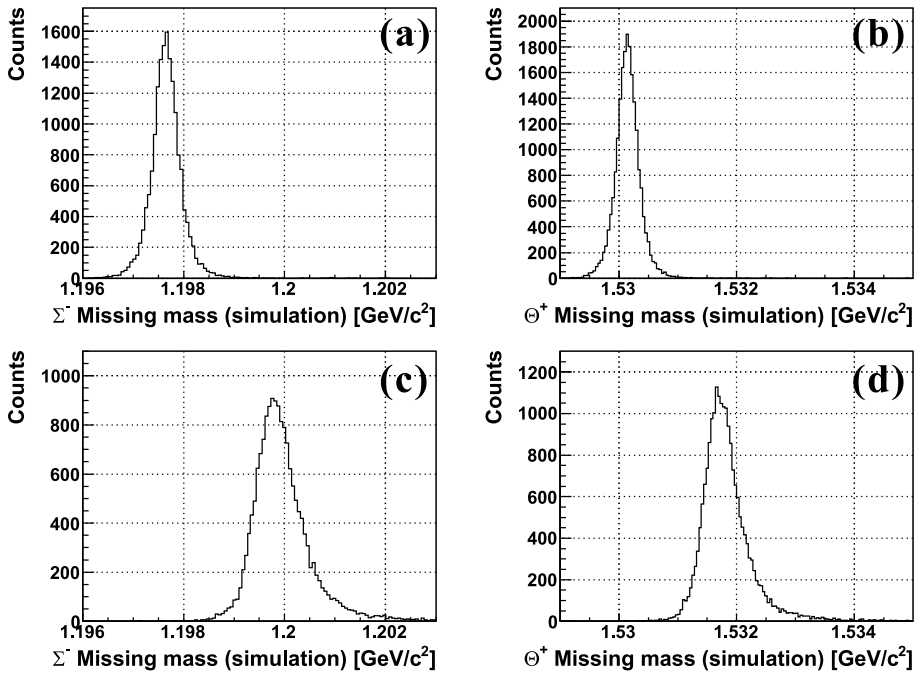

Figure 3.49: The simulated missing mass spectra of the $p(\pi^-, K^+)\Sigma^-$ reaction without the target (a) and with the target (c), and those of the $p(\pi^-, K^-)\Theta^+$ reaction without the target (b) and with the target (d).

Energy loss in BH2

The energy loss effect of the overlapping BH2 segments were estimated by using the Σ^+ production data. Figure 3.50 (a) shows the missing mass spectrum of Σ^+ with the selection of the number of the hit BH2 segments. The black line shows the missing mass spectrum without any selection, and the red and blue lines were the events of which the single, and the double BH2 hits were required, respectively. The double BH2 hits required the adjoining hit. The single BH2 hit corresponded to the beam particle passing through no overlapping region. The double BH2 hits spectrum was shifted due to the energy loss difference by the overlapping BH2 segments. Figure 3.50 (b) shows the beam profile of the horizontal position at the BH2 counter measured by the beam tracking by selecting a single beam track, and double and adjoining BH2 hits. The overlapped regions of BH2 segments were clearly selected. In addition, the missing mass resolution for the double BH2 hits events was 2.1±0.1 MeV/c^2(FWHM) which was worse than that for the single BH2 hit events (1.9±0.1 MeV/c^2 (FWHM)). However, the resolution of the double BH2 hits was acceptable so that the energy loss difference for the double BH2 hits events was corrected to the beam momentum by selecting the overlapping regions. The corrected shift of the beam particle passing through the overlapping region was estimated to be 1.1 MeV/c by the Bethe Bloch formula. The same correction value was used for the correction of the $p(\pi^-, K^-)\Theta^+$ reaction. The ratio of the number of BH2 hits more than 2 to the total number of the BH2 hit was ∼0.5%. In the present analysis, the effect of those events were negligibly small. Figure 3.51 shows the corrected missing

mass spectrum of Σ^+ with the selection of the number of the BH2 hit segments. The black line shows the missing mass spectrum without any selection, and the red and blue lines show the events in which the single, and the double and adjoining BH2 hits were required, respectively.

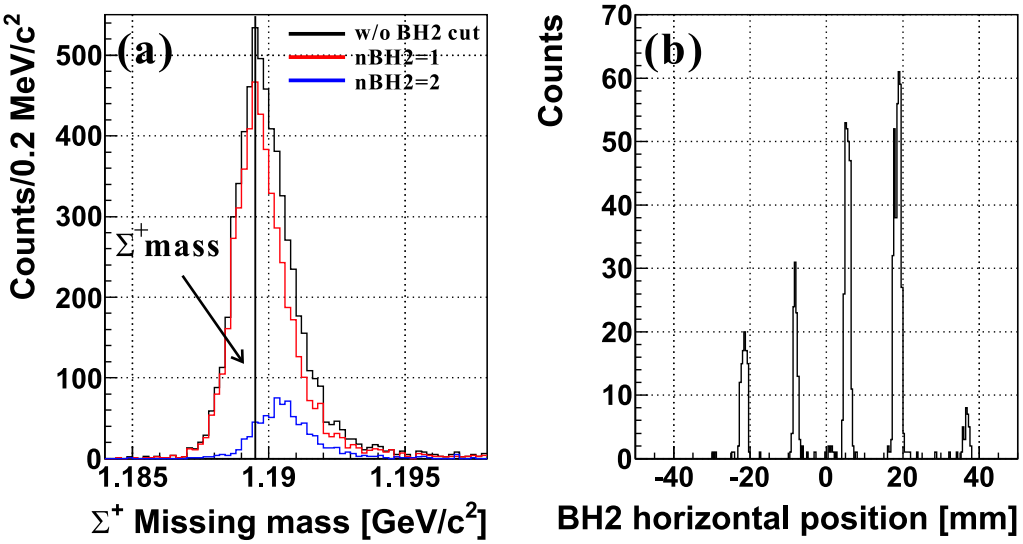

Figure 3.50: The missing mass spectrum of Σ^+ with the selection of the number of the hit BH2 segments (a). The black line shows the missing mass spectrum without any selection, and the red and blue lines show the events in which only single BH2 hit, and double and adjoining BH2 hits were required, respectively. The proper Σ^+ mass is indicated in (a). The beam profile of the horizontal position at the BH2 counter measured by the beam tracking by selecting a single beam track, and double and adjoining BH2 hits (b). The position of the overlapping BH2 segments are clearly selected.

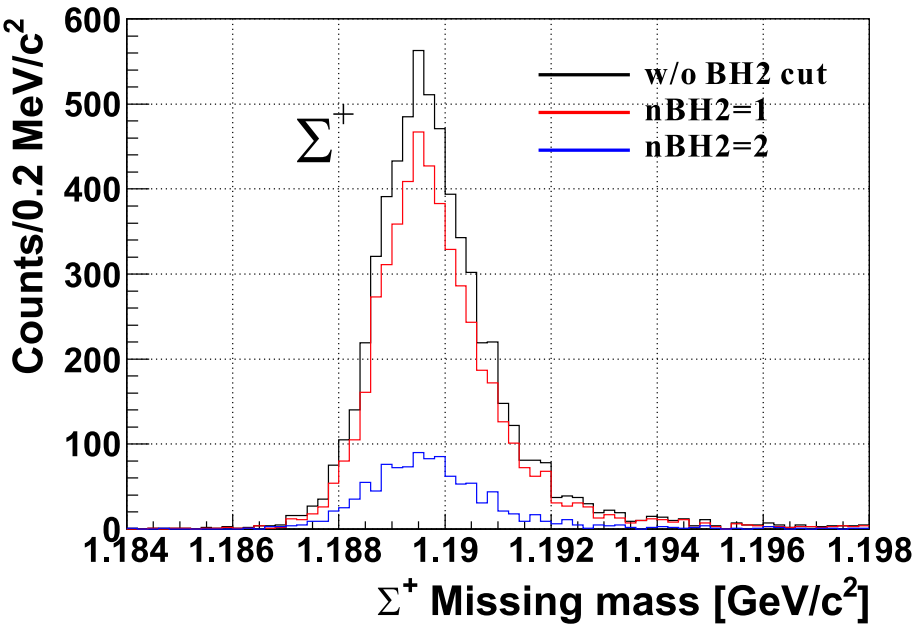

Figure 3.51: The corrected missing mass spectrum of Σ^+ with the selection of the number of the BH2 hit segments. The black line shows the missing mass spectrum without any selection, and the red and blue lines show the events in which only single BH2 hit, and double and adjoining BH2 hits were required, respectively.

Momentum correction

In the present experiment, the momentum of the scattered particles was reconstructed by using the calculated magnetic field map, while using the precisely measured field map in the previous KEK experiment. We used the SKS magnetic field of 2.5 T, where the magnetization of iron was saturated. It is difficult to completely reproduce the magnetic field map from the calculation so that the position or scattering angle dependence of the scattered particle momentum might exist. Such dependence was checked by the $p(\pi^{\pm}, K^+)\Sigma^{\pm}$ reaction data.

Figure 3.52 shows a scatter plot between the derivatives of horizontal ($\frac{dx}{dz}$) or vertical ($\frac{dy}{dz}$) positions at the target point and the missing mass for the $p(\pi^-, K^+)\Sigma^-$ reaction data. The higher order correlation between the the derivatives and the missing mass is seen in the figure (a, c). The correlations are caused by the position dependence of the inaccuracy of the calculated magnetic field map.

To optimize the energy resolution, this correlation was corrected by the SKS momentum and the derivatives of the horizontal and vertical positions. For the correction, the momentum difference ($P_{calc} - P_{analyzed}$) was used. The analyzed momentum ($P_{analyzed}$) was obtained from the momentum reconstruction by the SKS tracking. This momentum has some correlation with the derivatives. The calculated momentum (P_{calc}) was obtained from the calculation by the scattering angle and the beam momentum, where the kinematics of the $p(\pi^-, K^+)\Sigma^-$ reaction was assumed. This momentum has no correlation with the derivatives. Thus, the subtraction ($P_{calc} - P_{analyzed}$) has the information of

the correlation. The correction for the SKS momentum was made with the fourth-order polynomial in $\frac{dx}{dz}$ and $\frac{dy}{dz}$ as shown in the figure (b, d).

A strong correlation was found in the region of $\frac{dx}{dz} < -0.12$. Except for this region, almost no correlation remained before the correction. Since it was found that the correction parameters can be commonly used for both the $p(\pi^+, K^+)\Sigma^+$ and the $p(\pi^-, K^+)\Sigma^-$ reaction data, the same parameters were also applied for the correction of the $p(\pi^-, K^-)$ reaction data.

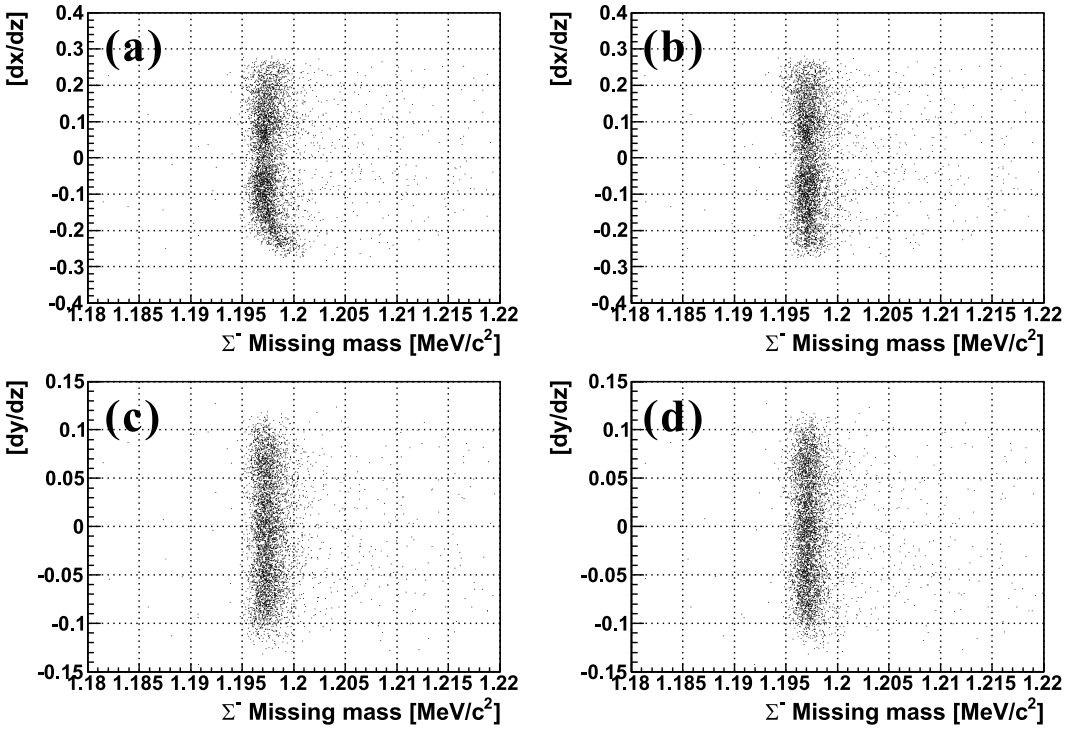

Figure 3.52: A scatter plot between the derivatives of horizontal ($\frac{dx}{dz}$) or vertical ($\frac{dy}{dz}$) positions at the target point and the Σ^- missing mass. The figures after corrected for the correlation are shown in (b, d).

Energy calibration and precision

In order to calibrate the momentum of both of the K1.8 beam line spectrometer and the SKS spectrometer, $\pi^{\pm}$ beam-through data without a target were taken at several central momenta (-0.75 GeV/c to -0.95 GeV/c, and $+0.85$ GeV/c) in addition to the $p(\pi^{\pm}, K^{+})\Sigma^{\pm}$ reaction data. The SKS magnet setting was fixed at the positive polarity of 2.5 T for the $p(\pi^{\pm}, K^{+})\Sigma^{\pm}$ reaction data, and both positive and negative polarities of 2.5 T for the beam-through data, respectively.

From the analysis without any correction, the missing mass values of $\Sigma^{\pm}$ and the momentum difference between the two spectrometers ($\Delta p = p_{SKS} - p_{K1.8}$) were obtained as listed in Table 3.5. The Σ^{+} mass (1189.37$\pm$0.07 MeV/c^2 in PDG [65]) was obtained to be 1186.18$\pm$0.08 MeV/c^2, the Σ^{-} mass (1197.45$\pm$0.03 MeV/c^2 in PDG [65]) was obtained to be 1196.21$\pm$0.08 MeV/c^2, and the Δp ($p_{SKS} - p_{K1.8}$) values which should be zero were obtained to be -4.08 ± 0.01 MeV/c for the average of the negative polarity and -0.21 ± 0.03 MeV/c for the positive polarity, respectively. Those inconsistencies can be removed or reduced by shifting or scaling the absolute reconstructed momentum values of the beam line spectrometer and the SKS spectrometer.

From the NMR probe value of SKS, the positive and negative magnetic field values for the same coil current were the same within $\sim10^{-4}$ so that we assumed the absolute momentum of SKS can be scaled but without any offset. On the other hand, from the Hall probe value of the dipole magnet of the K1.8 beam line spectrometer, the positive and negative magnetic field values with the same coil current were different with a shift to the negative side by $\sim2\times10^{-3}$ T. Thus, it was assumed that the momentum of the beam line spectrometer has an offset.

Table 3.5: The condition of the calibration process and the obtained values by correcting the parameters.

	No correction (MeV)	+SKS scale +K1.8 offset (MeV)	+K1.8 scale (MeV)
ΔM_{Σ^+}	-3.2	-0.8	0
ΔM_{Σ^-}	-1.2	-1.4	0
Δp_{+}	-0.2	0	0
Δp_{-}	-4.1	0	0
Condition	(1)	(2)	(3)

The offset of the momentum of the beam line spectrometer and the scale of the SKS magnetic field were the parameters to be determined. Table 3.5 shows the condition of the calibration process ((1)$-$(3)) and the obtained values by correcting the parameters. We obtained the $\Delta p = p_{SKS} - p_{K1.8}$ values of -4.08 ± 0.01 MeV/c and -0.21 ± 0.03 MeV/c for negative and positive polarities, respectively. By changing the offset of the momentum of the beam line spectrometer and the scale of the SKS magnetic field, this difference can be corrected to be zero. Then, by using those correction parameters determined from the Δp correction, the $\Sigma^{\pm}$ mass difference between the PDG value and the obtained

missing mass peak centers with the target energy loss correction was obtained to be $M_{Analysis} - M_{PDG} = -0.8$ MeV/c^2 and -1.4 MeV/c^2. To correct the remaining mass difference, the scale factor of the beam momentum was added to the iteration. Finally, the $\Sigma^{\pm}$ mass values agreed with the PDG values by adjusting the scale factor of the SKS spectrometer and both of the scale factor and offset of the beam line spectrometer. By changing the scale factor of the beam line spectrometer, the $\Sigma^{\pm}$ mass values were changed from (2) to (3) in Table 3.5 within the mass difference of 1.4 MeV/c^2. Thus, the error of the calibration was estimated to be ± 1.4 MeV/c^2. The absolute value was determined by the (3) condition.

For the measurement of the (π^-, K^-) reaction with the beam momentum of 1.92 GeV/c, we used the SKS magnet setting fixed at the negative polarity of 2.5 T. The momentum scale of SKS was calibrated with the beam-through and the $\Sigma^{\pm}$ data as described above. On the other hand, the beam momentum of 1.92 GeV/c has to be extrapolated. The initial beam momentum was calculated from the monitored magnetic field value and the effective length of the D4 magnet. The accuracy of the initial momentum of the beam line spectrometer was estimated from the accuracy of the field measurement by the Hall probe. It was negligibly small compared with the error of the calibration. For the effective length, a calculated value was used and the realistic value had to be estimated from the data. Since the error of the scale factor of the beam line spectrometer was regarded as including the error of the effective length, the mass difference of 1.4 MeV/c^2 was scaled by the beam momentum (scale = 1.92/1.37). Thus, the total error of the absolute vales of the missing mass of Θ^+ was determined to be ± 2.0 MeV/c^2.

3.11 Missing mass resolution

The missing mass resolution is estimated as follows,

$$\Delta M^2 = \Delta^2_{Beam} + \Delta^2_{SKS} + \Delta^2_{\theta} + \Delta E^2_{target},$$

where the first term in r.h.s. is the mass resolution coming from the momentum resolution of the beam line spectrometer and the second is that of SKS. The third term comes from the resolution of the scattering angle and the last term from the energy loss straggling in target materials. From the measured missing mass resolution of the Σ production data, we can estimate the Θ^+ missing mass resolution. Each term of the missing mass resolution is calculated from the following equations,

$$\begin{aligned}
\Delta M^2 &= (\frac{\partial M}{\partial p_{Beam}})^2 \Delta {p_{Beam}}^2 + (\frac{\partial M}{\partial p_{SKS}})^2 \Delta {p_{SKS}}^2 + (\frac{\partial M}{\partial \theta})^2 \Delta\theta^2 + \Delta E^2_{target} \\
\frac{\partial M}{\partial p_{Beam}} &= \frac{1}{M}[\beta_\pi (M_p - E_K) + p_K \cos\theta] \\
\frac{\partial M}{\partial p_{SKS}} &= -\frac{1}{M}[\beta_K (M_p + E_\pi) - p_\pi \cos\theta] \\
\frac{\partial M}{\partial \theta} &= -\frac{p_\pi p_K}{M} \sin\theta,
\end{aligned}$$

where E_π and p_π are the total energy and momentum of a pion, E_K and p_K are those of a kaon, M_p is the proton mass, and θ is the scattering angle of the reaction, Δp_{Beam} and Δp_{SKS} the momentum resolution of the K1.8 beam line and the SKS spectrometer, respectively, and $\Delta\theta$ the resolution of the scattering angle.

The design value of the momentum resolution ($\Delta p_{Beam}/p$) of the beam line spectrometer was 3.3×10^{-4}(FWHM). If the design value was achieved, the contribution of the resolution of the beam spectrometer was negligibly small. During the experiment, the magnetic field of the dipole magnet was monitored by the Hall probe. We found a fluctuation of the magnetic field synchronized to the accelerator cycle. The fluctuation had a dependence on the magnetic field strength. At the beam momenta of 1.37 GeV/c and 1.92 GeV/c, the fluctuations were $\pm3.0\times10^{-4}$ and $\pm4.0\times10^{-4}$, respectively. We assumed the momentum resolution of the beam line spectrometer was determined by the sum of the design value and the fluctuation of the magnetic field as $\Delta p_{Beam}/p = 4.5 \times 10^{-4}$ and 5.2×10^{-4} for the beam momenta of 1.37 GeV/c and 1.92 GeV/c, respectively.

The SKS momentum was obtained by using the calculated magnetic field map. The resolution might be determined by the accuracy of the map because accurate calculation is difficult at the strength of 2.5 T due to saturation of the iron magnetization. The accuracy of the map was estimated by comparing with the measured map which was previously used in the KEK experiment. The difference of the magnetic field values between the measured map and the calculated one is described in Appendix A. The difference was $\sim10^{-3}$ in the uniform region (the center of the SKS pole), while in the region near the SKS coil, it was $\sim10^{-2}$. Similarly, in the fringing field region and the region close to the SKS pole edge, the difference was larger than that of the central region. They correspond to the regions where the efficiency of the SKS tracking dropped. From the beam-through analysis, the position dependence enhanced the SKS momentum shift

of $\pm$0.4 MeV/c, which corresponded to the accuracy of 4.7×10^{-3} at the momentum of 0.85 GeV/c on the mid-plane. From those factors, the inaccuracy of the magnetic filed was obvious. Thus, the contribution of the resolution of the SKS momentum (Δp_{SKS}) is considered to be dominant.

Table 3.6 shows the contribution of each factor and the estimation of the missing mass resolution of Θ^+. The missing mass resolution of the Σ production was obtained to be ΔM =1.86$\pm$0.08 MeV/c^2(FWHM). The resolution of the scattering angle was estimated to be Δ_θ=5 mrad(FWHM) in Sec. 3.4. This contribution was small enough for the missing mass resolution. The effect of the target energy loss ΔE_{target} was estimated in Sec. 3.10. This effect included not only the energy loss straggling but also the difference of the path length in the target. The unknown SKS momentum resolution Δ_{SKS} was estimated from the measured ΔM and the estimated Δ_{Beam}, Δ_θ and ΔE_{target} to be $\Delta p_{SKS}/p$=3.2×10^{-3}(FWHM). By using those resolution values, the missing mass resolution for Θ^+ was estimated to be 1.4$\pm$0.1 MeV/c^2(FWHM).

Table 3.6: The estimation of missing mass resolution of Θ^+. Each value is shown in FWHM. In the calculation, the scattered particle momentum at the scattering angle of 5° was used.

	$\Sigma^\pm$	Θ^+
$\Delta p_{Beam}/p$	4.5×10^{-4}	5.2×10^{-4}
Δp_{Beam} (MeV/c)	0.62	1.00
$\lvert\frac{\partial M}{\partial p_{Beam}}\rvert$	0.68	0.53
Δ_{Beam} (MeV/c^2)	0.42	0.53
$\Delta p_{SKS}/p$	3.2×10^{-3}	3.2×10^{-3}
Δp_{SKS}	2.96	2.93
$\lvert\frac{\partial M}{\partial p_{SKS}}\rvert$	0.56	0.40
Δ_{SKS} (MeV/c^2)	1.66	1.17
$\Delta\theta$ (rad)	5.0×10^{-3}	5.0×10^{-3}
$\lvert\frac{\partial M}{\partial \theta}\rvert$	92.4	100
Δ_θ (MeV/c^2)	0.46	0.50
ΔE_{target} (MeV/c^2)	0.56	0.41
Total ΔM (MeV/c^2)	1.86$\pm$0.08 (data)	1.44

Chapter 4

Experimental results and discussion

4.1 Missing mass spectrum of the $\pi^- p \to K^- \Theta^+$ reaction

The missing mass spectrum for the the $\pi^- p \to K^- \Theta^+$ reaction with the momentum of 1.92 GeV/c is shown in Figure 4.1. The scattering angles of 2° to 15° were selected. Three spectra with different binnings of 0.5 MeV/c^2, 1.0 MeV/c^2 and 2.0 MeV/c^2 per bin are presented. In the missing mass spectrum, any peak corresponding to the Θ^+ pentaquark has not been observed by considering for the expected missing mass resolution of 1.4 MeV/c^2 (FWHM).

Background shape

The backgrounds were generated by using the Geant4 simulation code as discussed in Sec. 3.7. Figure 4.2 shows the calculated backgrounds in the $\pi^- p \to K^- X$ missing mass spectrum, which are the ϕ production, the $\Lambda(1520)$ production and the $K^- K^+ n$ and $K^- K^0 p$ productions following the 3-body phase space. The backgrounds were generated by considering the acceptance of SKS, the decay of scattered K^-, the distribution of the beam profile and the beam momentum bite were included. The relative ratio of the sum of three processes in the figure was normalized by the ratio of each measured cross section. The vertical scale of the simulation data was normalized by using the beam flux and the the experimental efficiency factors. In the figure, the obtained data was also shown for the comparison. The simulation data agrees well with the backgrounds of the present data within the errors of cross section (20−30%).

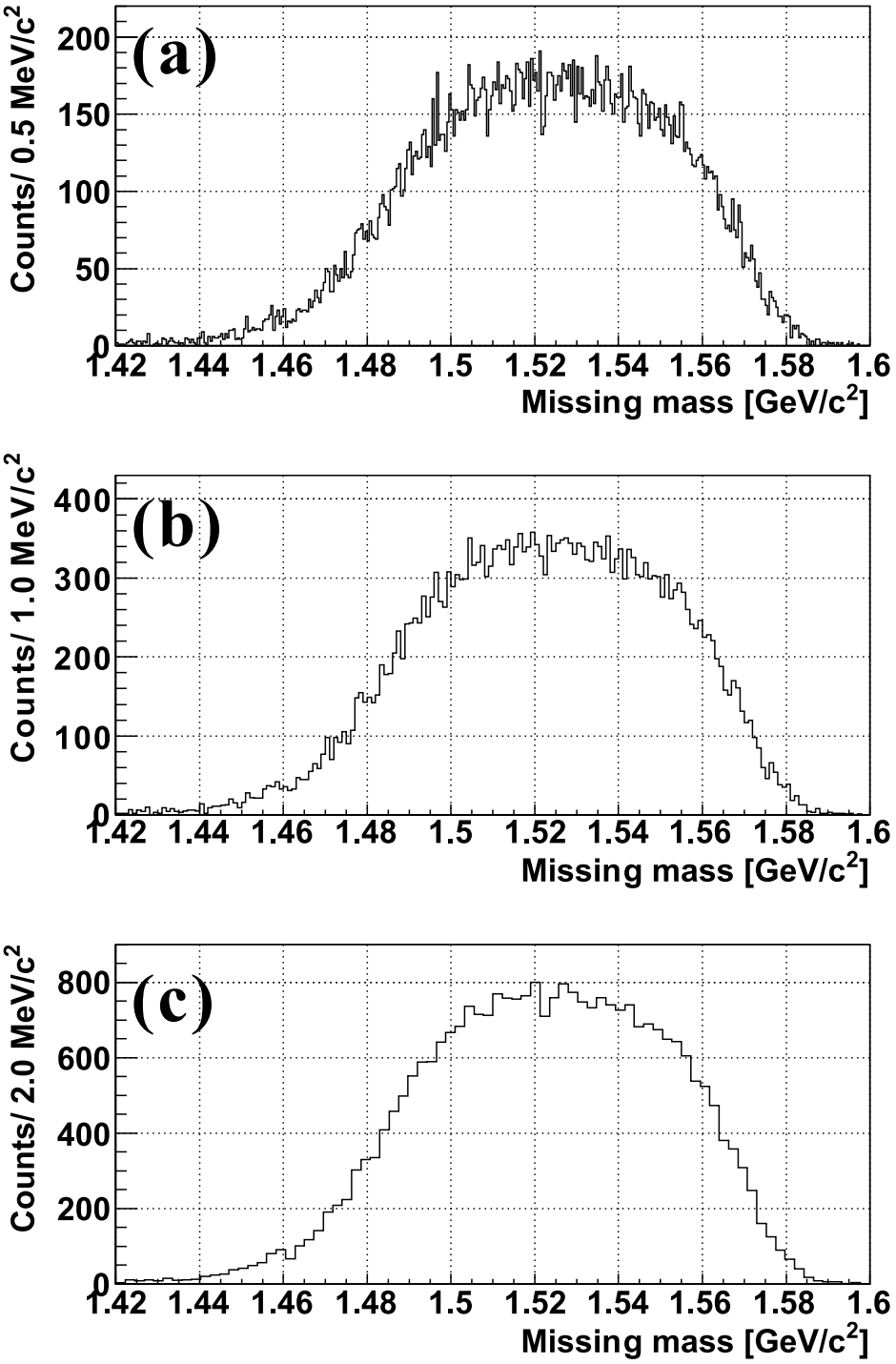

Figure 4.1: The missing mass spectrum for the the $\pi^- p \to K^- \Theta^+$ reaction with the momentum of 1.92 GeV/c. with different binning of 0.5 MeV/c^2 (a), 1.0 MeV/c^2 (b) and 2.0 MeV/c^2 (c) per bin.

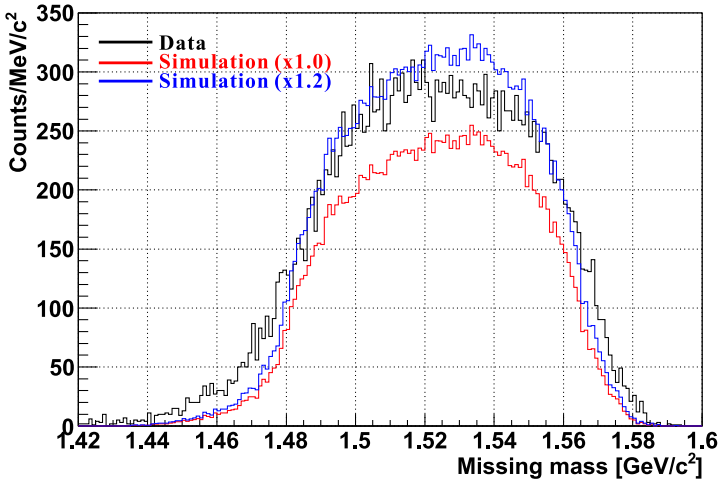

Figure 4.2: The background spectrum for the the $\pi^- p \to K^- \Theta^+$ reaction with the momentum of 1.92 GeV/c. The backgrounds were generated by using the Geant4 simulation code as discussed in Sec. 3.7. The relative ratio of three process was calculated by the ratio of each measured cross section. The vertical scale of the simulation data was normalized by using the beam flux and the the experimental efficiency factors. The red and blue lines show the normalization spectra multiplied by 1.0 and 1.2, respectively. In the figure, the obtained data was also shown for the comparison.

4.2 Upper limit of production cross section

Figure 4.3 shows the missing mass spectrum in the scale of averaged differential cross section for the $\pi^- p \to K^- \Theta^+$ reaction over 2° to 15° in the laboratory frame. The averaged differential cross section is defined as

$$\overline{\sigma}_{2^o-15^o} = \int_{2^o}^{15^o} \left(\frac{d\sigma}{d\Omega} \right) d\Omega / \int_{2^o}^{15^o} d\Omega.$$

For the derivation of the upper limit, the spectrum was fitted with a peak to obtain the cross section. The peak was assumed to be a Gaussian with the fixed width of 1.4 MeV/c^2 (FWHM), and the 3rd-order polynomials function was used for the background shape. Figure 4.4 shows one of the fitting result. In the figure, the peak with the 90% confidence level upper limit was also shown.

The upper limit of the peak cross section in the missing mass region over 1.50 GeV/c^2 to 1.55 GeV/c^2 is shown in Fig. 4.5. On the top of figure, the averaged differential cross section of the fitted peak in the missing mass spectrum for the $\pi^- p \to K^- \Theta^+$ reaction averaged over 2° to 15° in the laboratory frame was shown. The the 90% confidence level upper limit of the cross section was shown in the bottom. The upper limit of the cross section is 0.20 μb/sr in the missing mass region over 1.52 GeV/c^2 to 1.54 GeV/c^2. The upper limit of 1.53 GeV/c^2 was obtained to be 0.10 μb/sr. Assuming that K^- is produced in the S-wave and isotropically emitted in the center of mass system, 8.0% of K^- is accepted by the spectrometer at the Θ^+ mass of 1.53 GeV/c^2. In this assumption,

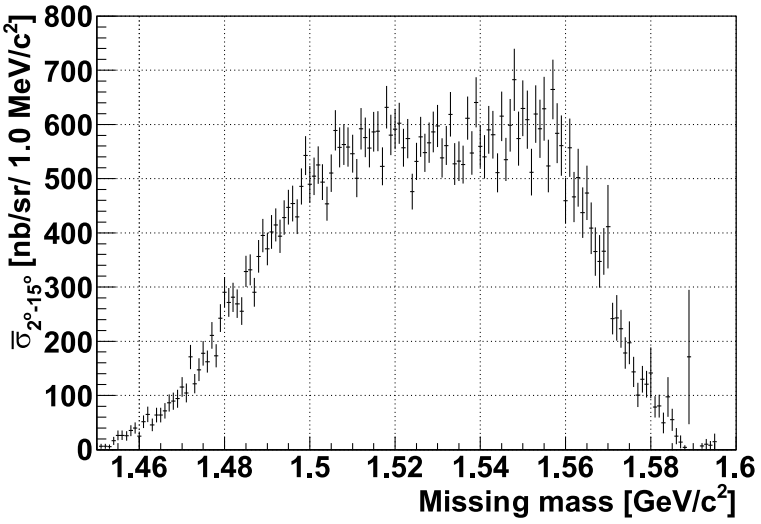

Figure 4.3: The differential cross section of the missing mass spectrum for the $\pi^- p \to K^- \Theta^+$ reaction averaged over 2° to 15° in the laboratory frame.

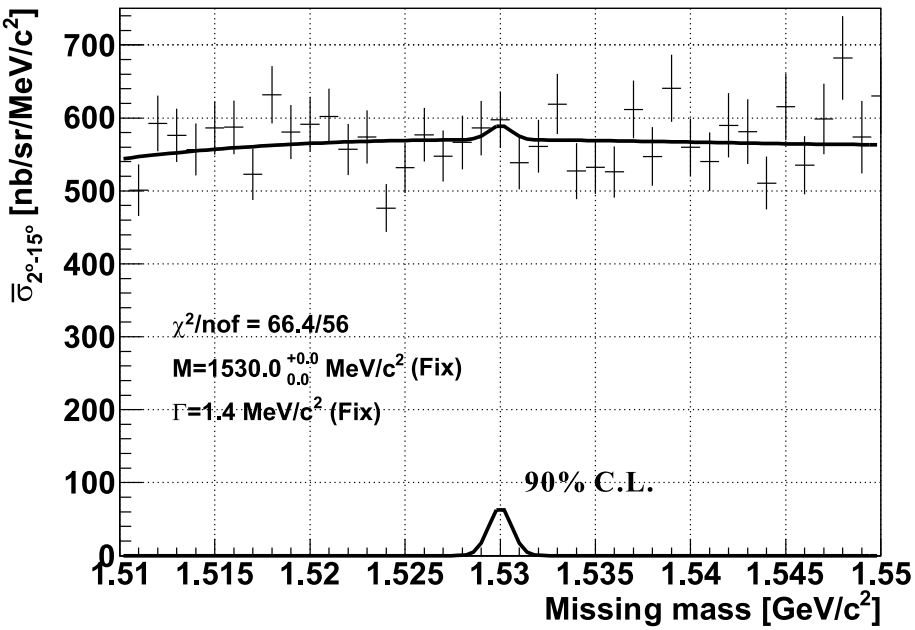

Figure 4.4: The missing mass spectrum of the $\pi^- p \to K^- \Theta^+$ reaction with a fitting result. One of the fitting result was shown in the figure. For the fitting, we used a Gaussian peak shape and the background shape of the 3rd-order polynomials function. The width was fixed to be the experimental resolution of 1.4 MeV/c^2 (FWHM). The peak with the 90% confidence level upper limint were also shown.

the upper limit of the total cross section were obtained to be 0.15 μb at the mass of 1.53 GeV/c^2. For comparison, the upper limit was obtained with the Θ^+ width fixed to be 2.0 MeV/c^2 (FWHM) as shown in Fig. 4.6.

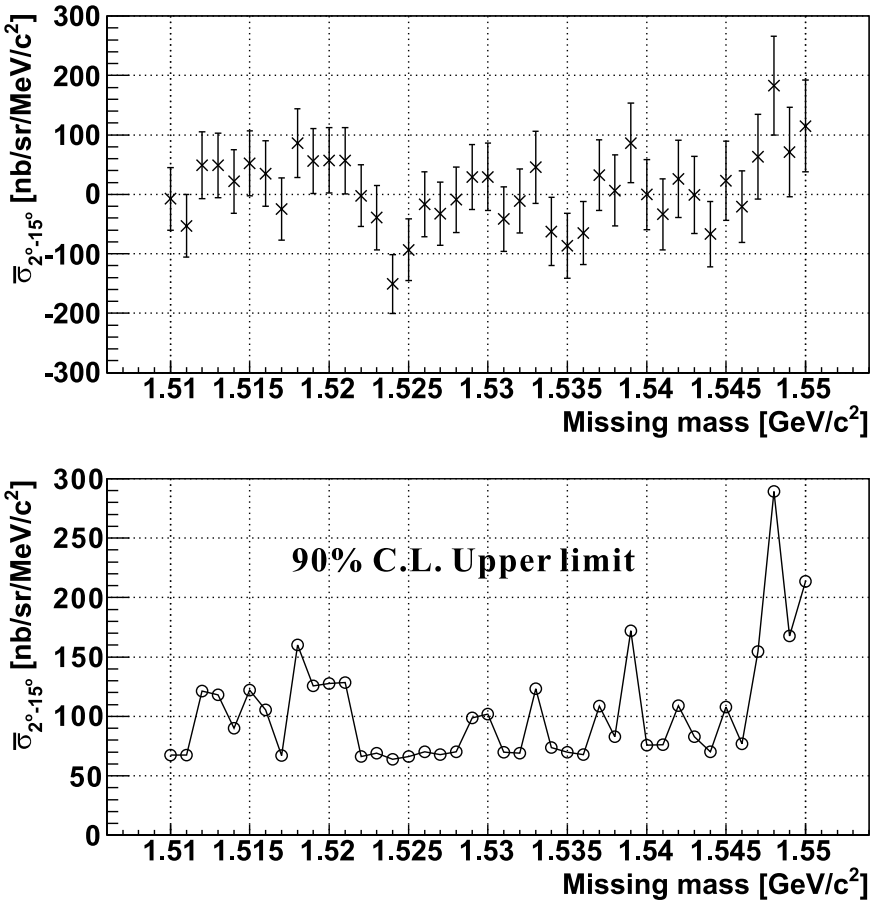

Figure 4.5: Top: the differential cross section of the $\pi^- p \to K^- \Theta^+$ reaction averaged over 2° to 15° in the laboratory frame with the Θ^+ width fixed at 1.4 MeV/c^2 (FWHM). Bottom: the upper limit of the differential cross section of the $\pi^- p \to K^- \Theta^+$ reaction averaged over 2° to 15° in the laboratory frame. The line show the 90% upper limit of the differential cross section.

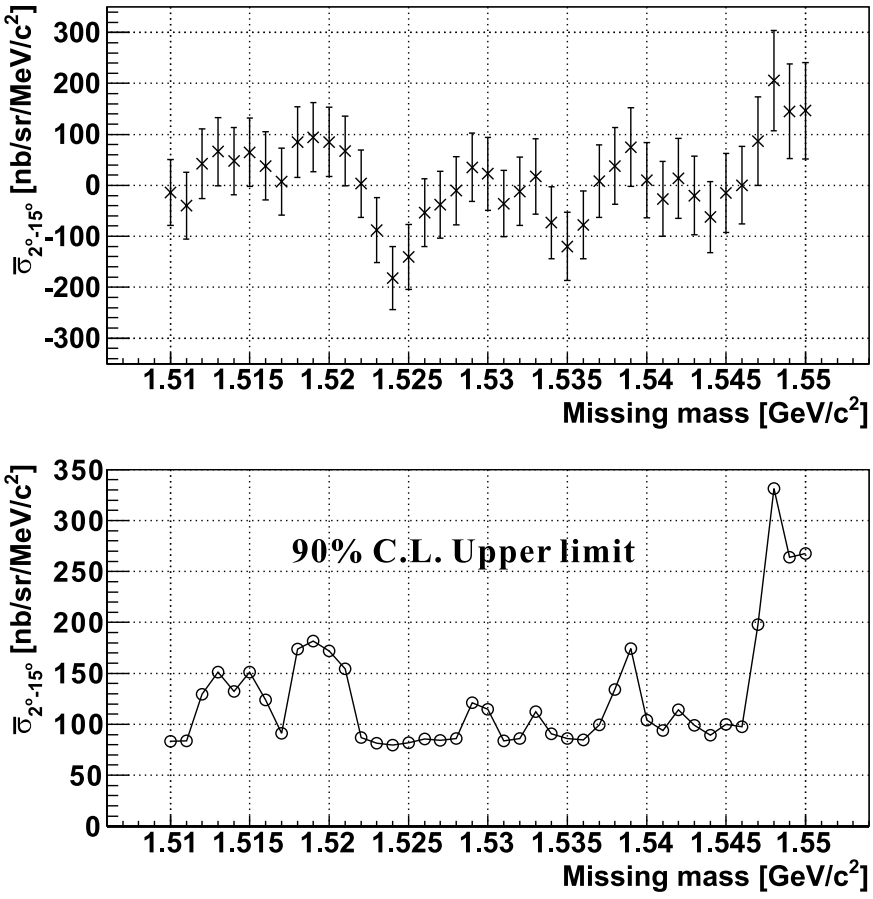

Figure 4.6: Top: the differential cross section of the $\pi^- p \to K^- \Theta^+$ reaction averaged over 2° to 15° in the laboratory frame with the Θ^+ width fixed at 2.0 MeV/c^2 (FWHM). Bottom: the upper limit of the differential cross section of the $\pi^- p \to K^- \Theta^+$ reaction averaged over 2° to 15° in the laboratory frame. The line show the 90% upper limit of the differential cross section.

4.3 Discussion

Comparison with the previous experiment

In the previous KEK-E522 experiment, the bump with a width consistent with the experimental resolution has been suggested at the mass of $M = 1530.6^{+2.2}_{-1.9}(\text{stat.})^{+1.9}_{-1.3}(\text{syst.})$ MeV/c^2. However, in the present J-PARC E19 experiment, any peak in the corresponding mass region has not been observed. We carried out the experiment with the missing mass resolution of 1.4 MeV/c^2(FWHM) which is almost 10 times better than the previous experiment of 13.6 MeV/c^2(FWHM). The bump suggested in the previous experiment has been denied.

We obtained a new value of the upper limit of the differential and the total cross section of the $\pi^- p \to K^- \Theta^+$ reaction with the momentum of 1.92 GeV/c. At the mass of 1.53 GeV/c^2, the upper limit of the differential cross section averaged over 2° to 15° in the laboratory frame was 0.10 μb/sr, and that of the total cross section assuming the S-wave production was 0.15 μb, while those of the previous experiment were 2.9 μb/sr (2°−15°) and 3.9 μb, respectively. Both of the upper limits were for the 90% confidence level. The 20 times lower upper limit was obtained from the present experiment. Since the sensitivity of the present experiment was high enough, the production mechanism of Θ^+, if it exist, is strongly constrained.

Comparison with the theoretical calculation

The theoretical calculation via the $\pi^- p \to K^- \Theta^+$ reaction was discussed in Sec. 1.3. Theoretical calculations was calculated by several authors [38, 39]. As shown in Fig. 1.5, the calculated cross section ranges from about 2 μb to 190 μb, controlled by both coupling constants of $g_{KN\Theta}$ and $g_{K^*N\Theta}$. The calculated cross section for the $\pi^- p \to K^- \Theta^+$ reaction took into account the s-channel and the t-channel diagrams [38]. From the results of the previous KEK-E522 and KEK-E559 experiments, we understood the $g_{K^*N\Theta}$ should be quite small. The smaller coupling of $g_{K^*N\Theta}$ means that the contribution of the t-channel process to the cross section of the $\pi^- p \to K^- \Theta^+$ reaction is small. In addition, $g_{KN\Theta}$ should be small to explain both experimental results.

The cross section of the $\pi^- p \to K^- \Theta^+$ reaction was calculated using the small coupling constant of $g_{K^*N\Theta}$ by [40] as shown in Fig. 1.7. They assumed the width of Θ^+ of 1 MeV/c^2 and positive parity. The cross section of the s-channel process is 0.5 μb at $\sqrt{s} = 2.25$ GeV. The present result is smaller than this theoretical calculation so that the small coupling constants of both $g_{KN\Theta}$ and $g_{K^*N\Theta}$ are obvious. The cross section is related to the width of Θ^+ for the s-channel process and the small cross section implies the narrow width. In the calculation in Ref. [40], they assumed the width of Θ^+ of 1 MeV/c^2 and obtained the cross section of the s-channel process to be 0.5 μb. Thus, the present result implies the width of Θ^+ to be less than several hundred keV/c^2.

Chapter 5

Conclusion

The Θ^+ pentaquark predicted by Diakonov *et al.* has an unusual nature of quark contents of $uudd\bar{s}$ and a narrow width. The observation of Θ^+ reported by SPring-8/LEPS triggered the investigation of Θ^+. Several experiments reported positive results immediately. On the other hand, negative results have been reported from several high-energy experiments with higher statistics. Thus, the confirmation of the existence (or non-existence) of the Θ^+ is crucially important, particularly by high statistics experiments in low energy region with hadronic reactions.

Previously, the search for Θ^+ using hadron beams was performed in the KEK-PS E522 experiment via the $\pi^- p \to K^- \Theta^+$ reaction and the KEK-PS E559 experiment via the $K^+ p \to \pi^+ \Theta^+$ reaction. Those experiments found no clear evidence for Θ^+, but a hint of a 2.6σ Θ^+ peak was observed in E522. The total cross section of the Θ^+ production related to the decay width and the s-channel process with the $g_{KN\Theta}$ coupling is expected to be dominant in the $\pi^- p \to K^- \Theta^+$ reaction. We can expect the cross section for the width of 1 MeV/c^2 amounts to less than 1 μb/sr. Thus, experimental information on the cross section is important to understand the nature of Θ^+.

The J-PARC E19 experiment was carried out at the J-PARC K1.8 beam line from October to November in 2010. This was the first experiment in the J-PARC hadron experimental facility. The experiment was proposed aiming to confirm the existence of Θ^+ using the $\pi^- p \to K^- \Theta^+$ reaction by high-resolution spectroscopy. We measured the missing mass spectrum of the $\pi^- p \to K^- X+$ reaction with the beam momentum of 1.92 GeV/c. This experiment was a natural expansion of the E522 experiment but much improved in resolution and statistics. For the E19 experiment, we used the K1.8 beam line spectrometer and the SKS spectrometer both of which have an excellent momentum resolution of $\Delta p/p \sim 10^{-3}$. The SKS spectrometer, which was previously used at KEK, was reconstructed for the J-PARC experiments with new detectors and a new data acquisition system.

In the experiment, we irradiated 7.8×10^{10} π^- mesons on the liquid hydrogen target. For the calibration of the spectrometer system, the $\Sigma^\pm$ production data were taken via the $\pi^\pm p \to K^+ \Sigma^\pm$ reactions. The analysis was carried out to pay attention the resolution of the spectrometer. The missing mass resolution for the Θ^+ is estimated to be 1.4 MeV/c^2 (FWHM) from the $\Sigma^\pm$ data. The selection of good (π^-, K^-) events were also determined. In the missing mass of the $\pi^- p \to K^- \Theta^+$ reaction, any structure

corresponding to Θ^+ was not observed. Therefore we have obtained the upper limit of the production cross section of the $\pi^- p \to K^- \Theta^+$ reaction at the beam momentum of 1.92 GeV/c. The upper limit of the differential cross section averaged for the scattering angle over 2^o to 15^o at the laboratory frame have been obtained to be 0.20 μb/sr in the missing mass region over 1.52 GeV/c^2 to 1.54 GeV/c^2. That of the total cross section was obtained to be 0.15 μb at the 90 % confidence level at the mass of 1.53 GeV/c^2.

From the results of the present experiment along with the previous experiment at KEK, we understood the coupling constants of both $g_{KN\Theta}$ and $g_{K^*N\Theta}$ are quite small, using both π^- and K^+ beams to produce Θ^+ with beam momenta less than 2 GeV/c. In addition, we found that the width of Θ^+ is possibly less than several hundred keV/c^2. The experimental result gives the extremely strong constraint to the production mechanism or the existence of Θ^+.

Acknowledgements

First of all, I would like to acknowledge the J-PARC E19 collaborators and every person whom I had a fortune to work with. Were not for their contributions and advices, I would have never been able to complete this work.

I would like to express my sincere gratitude to Prof. Hirokazu Tamura, my supervisor. He opened my eye to an experimental hadronic and hypernuclear physics world. I have gained from his passion toward research and his attitude of always being at the fronter of science. I am blessed by a chance of getting involved in the first physics experiment and of writing the first doctoral thesis out of J-PARC. This exciting opportunity gave me both many joys and challenges of physics research with invaluable experiences. His advices and encouragements made me come through with a successful completion of this work.

I would like to express my great thanks to Dr. M. Naruki who is the spokesperson of the J-PARC E19 experiment. She made me a great part of the first J-PARC physics experiment and guided me throughout the experiment. I would also like to greatly thank Prof. T. Takahashi. He valued my judgements every time when we faced problems, and let me take a major responsibility of the entire experiment from which I have gained many important things. Mr. T. N. Takahashi, who started out the same year as me, is thanked for sharing the joy of the experiment and enduring a tough time together.

I would like to greatly acknowledge the Hyperball group members. Dr. T. Koike encouraged me many times, when I was overwhelmed by the worries of my graduate study. He helped me to keep my motivation. Dr. M. Ukai showed me an uncompromising attitudes toward experiments. It was fun to do experiments with her playfulness. Her warm advices gave me a strength to overcome problems faced in this work. Dr. K. Miwa gave me a lot of technical advices, and told me many important insights in performing and designing an experiment. His hard work with a high motivation toward an experimental physics inspired me greatly. I would like to thank colleges of the Hyperball group, who supported me every time and enjoyed experiments with me; they are Dr. Y. Miura, Ms. S. Kinoshita, Dr. Y. Ma, Mr. K. Hosomi, Mr. M. Mimori, Mr. T. Otani, Ms. M. Sato, Mr. Y. O. Yamamoto, Mr. T. Wang, Mr. R. Honda, Mr. K. Yagi, Mr. Y. Yonemoto, Mr. K. Sugihara, Mr. F. Hiruma, Mr. A. Sasaki, and Mr. Y. Matsumoto. I owe the experimental success to their strong help. I would like to deeply express my thanks to Mr. D. Kawama who started graduate study at the same year. We enjoyed university life, when we entered the Strangeness Nuclear Physics group. I consider him as my good rival and to improve each other.

I have spent my graduate school days as a member of the Strangeness Nuclear Physics group in Tohoku University. I would like to acknowledge Prof. O. Hashimoto for his advices and for giving me a chance to lean greatly in my school days. I am very much impressed by his leadership in overseeing every aspect of our research activities. I would like to acknowledge Prof. S. N. Nakamura, Dr. Y. Fujii, Dr. M. Kaneta and Dr. T. Maruta for their advice and great support at university. I would like to thank Dr. K. Futatsukawa who always lad me as an elder student. I would like to acknowledge Dr. Y. Okayasu, Dr. K. Tsukada and Dr. A. Matsumura for their advices and encouragements. I would like to express my thanks to those who leaned with me in the Strangeness

Nuclear Physics group, Mr. B. Brian, Mr. T. Gogami, Mr. A. Okuyama, Mr. A. Chiba, Mr. D. Doi, Mr. S. Nagao, Mr. S. Kato, Mr. K. Makabe, Mr. S. Hirose, Mr. N. Arai and Mr. D. Uchiyama. My special thanks goes to Mr. N. Chiga. He told me many of technical method expertise in constructing detectors and supporting frames. Because of his marvelous skill and excellent design, the SKS detectors were successfully constructed.

I would like to express my great thanks to members of the Experimental Nuclear and Hadronic Physics group in Kyoto University. I am indebted to Prof. T. Nagae and Dr. H. Fujioka for valuable supports for the experiment. I would like to thank Mr. A. Okamura, Mr. M. Moritsu, Mr. S. Adachi, Mr. H. Sugimura and Mr. Y. Ichikawa who supported me and enjoyed the experiment with me. I could not carry out the experiment without their great contributions. It was indeed a great pleasure to work with them.

I would like to express my thanks to Prof. A. Sakaguchi who worked with me to construct the SKS down stream detectors. I learned about detectors from his deep understanding of detectors. I would like to specially thank Ms. R. Iwasaki. Her humorous and funny personality made the collaborators cozy. On the other hand, I am surprised by her hard work with an attention to details. I would like to acknowledge Dr. R. Kiuchi for his advice and his great collaboration in constructing the K1.8 experimental area. I would like to thank Mr. K. Yoshida, Mr. N. Ishibashi and Mr. T. Tanaka for constructing the K1.8 experimental area and the SKS down stream detectors. I would like to express my great thanks to Prof. K. Tanida for his advice and thinking always of our wellbeing. Minouchi residence he organized in renting provided me an comfortable home in Tokai. I would like to acknowledge other collaborators, Prof. K. Imai, Prof. H. Noumi, Prof. K. B. Tanaka, Prof. Y. Sato, Prof. S. Sawada, Dr. T. Suzuki, Dr. H. Takahashi and Dr. C. J. Yoon.

The present experiment was made possible by the staffs of J-PARC and KEK. I would like to express my great thanks to the Hadron beam channel group, accelerator group and electronics group for their strong support for the experiment.

Finally, but not the least, I want to express my sincere gratitude to my parents, Hisaya Shirotori and Kiku Shirotori, and my sisters, Kasumi Shirotori and Misaki Shirotori, and my grand-mother, Noriko Shirotori. This thesis is dedicated in memory of late Kanemi Shirotori and Shizue Shirotori.

Appendix A

Field map calculation

Introduction

In order to realize the SKS specifications which are a good momentum resolution of $\sim 10^{-3}$ and a large angular acceptance of 100 msr in the 1 GeV/c momentum range, the precision of the magnetic field is one of the essential factors. Since the SKS magnet has a large gap and a strong magnetic field, the transfer matrix cannot be used due to the saturation of iron and the complicated fringing field shape. The measured magnetic field map of SKS was used to reconstruct the scattered particle momentum with the Runge-Kutta method in the previous KEK experiments. The magnetic filed of SKS was measured by a precisely calibrated Hall probe with an accuracy of 0.02%. The automated measurement for a large volume of SKS ($\sim$6 m^3) was performed using a special apparatus whose position accuracy is 0.1 mm as described in Ref. [60]. More than 10^5 magnetic field points were measured for several current values and the inconsistency between the measured points were examined and corrected point by point. It was estimated that the precision of the field map almost determined the momentum resolution of SKS. From the measured accuracy of the field map, the momentum resolution was estimated to be 0.12$-$0.15%(FWHM) which was consistent to the measured momentum value of 0.14%(FWHM) obtained from the beam through data. Figure A.1 show the measured 2.2 T and 2.7 T map, respectively. The magnetic field strength of the z-direction on the mid-plane (Z=0) is shown. Due to the physical interference between the SKS coil vessel and the Hall probe, the field map was not completely measured.

SKS coil specification and problem

The SKS coil was divided into two parts which are the high (HF) and the low (LF) magnetic field coil, respectively. Figure A.2 shows the schematic view of the SKS coil. Both HF and LF consist of three parts. The HF and LF coils are inner and outer sides, respectively. Each coil unit has a layer structure along the vertical direction. The coil turn is listed in Table A.1.

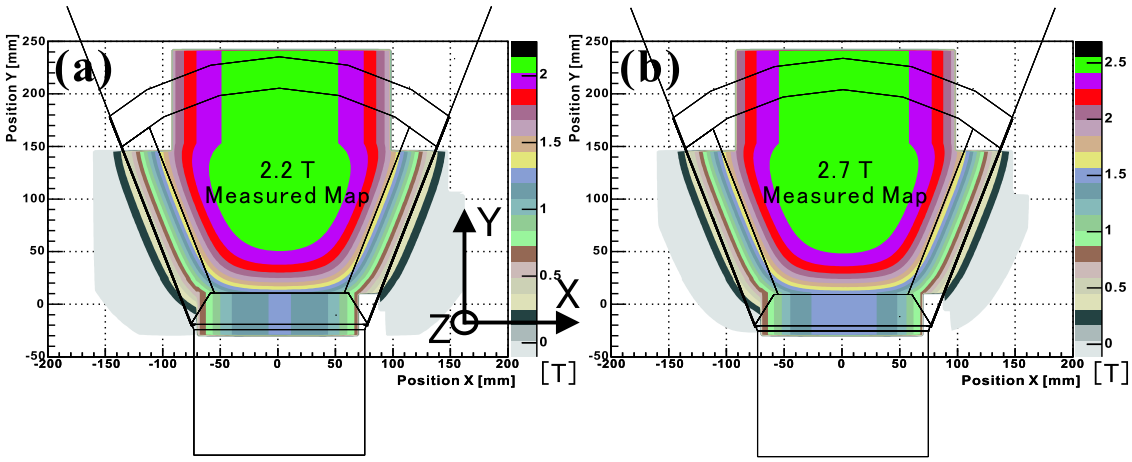

Figure A.1: The measured 2.2 T (a) and 2.7 T (b) map.

Table A.1: The number of coil turns. The HF1 and LF3 are the most inner and outer side, respectively.

	#turns	Total
HF1	330	989
HF2	330	
HF3	329	
LF1	350	1119
LF2	350	
LF3	419	
Total	2108	

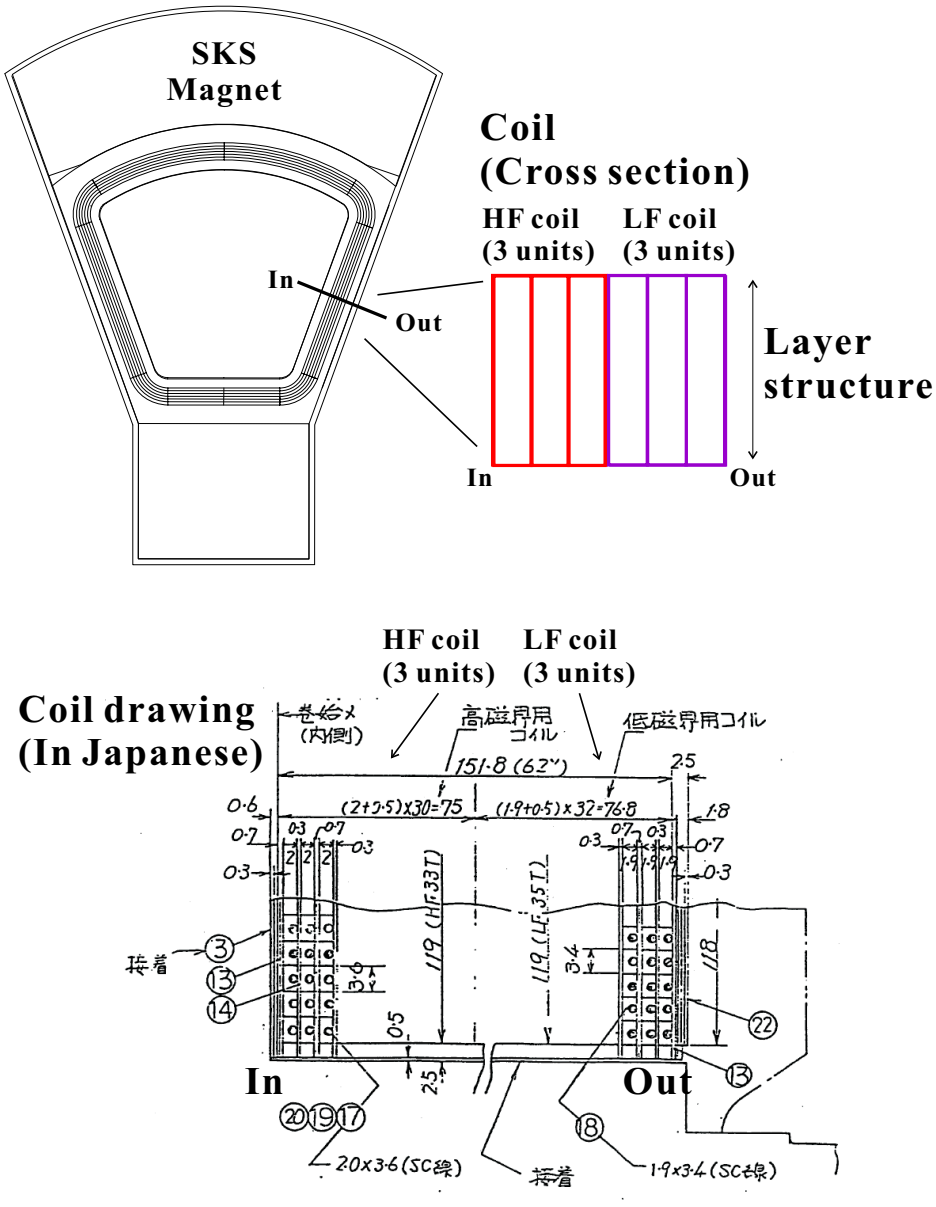

Figure A.2: The top figure show the schematic view of the SKS coil. The bottom figure shows the drawing of the coil (in Japanese).

The SKS magnet was moved to the J-PARC. The magnet was disassembled and the SKS coil was checked and tested before the J-PARC experiment. During the electrical insulating test by applying a high voltage, the resistance of one of the coil piece was found to be drastically decreased. It was found that in the most internal piece of the coil (HF1) as shown in Fig. A.3 was shorted. The shorted part could not be repaired because of its location at the most inner part of the coil. In addition, the point was not checked by a nondestructive way due to the thick coil vessel (3 cm stainless). Thus, one of the HF coil including the shorted part was disconnected by electrically insulating the section. The number of the coil turn unit was decreased to 5/6. The previous and the present SKS coil specification was listed in in Table A.2.

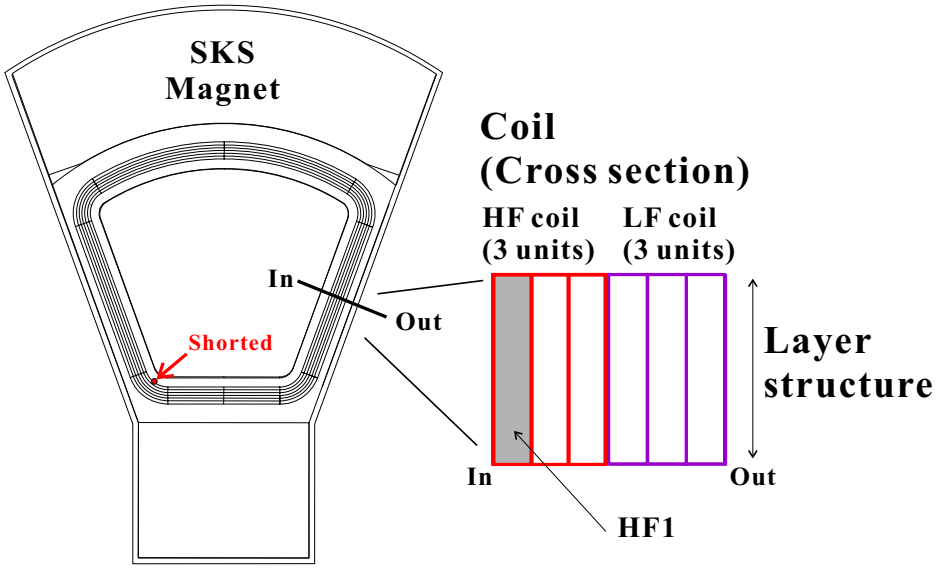

Figure A.3: The shorted points of the SKS coil and the removed coil unit.

Table A.2: The present SKS coil specification. The 470A data was the quench limit of the SKS coil.

	Default	Present	Present (limit)
Max current (A)	500	400	470
Total #turns	2108	1778	1778
Max field strength (T)	3.0	2.48	2.70
Stored energy (MJ)	11.3	6.3	8.7

Unfortunately the most severer problem has happened. At the magnetic field strength of around 2 T, the magnetic field shape was determined by the current of coil because of the saturation of iron. The change of the coil shape might drastically affect the magnetic field shape and the measured map which was used in the previous experiments cannot

be used. The best way of achieving the same resolution was to re-measure the magnetic field map. However, the preparation schedule allowed no time for the measurement. Therefore, we decided to use a calculated magnetic field map. The calculation of the magnetic field is described in the next section.

Field map calculation

The magnetic field map was calculated by the ANSYS code. In the ANSYS calculation, the finite element method (Scaler Potential Method) is used. Given an arbitrary current distribution, static three dimensional magnetic fields was calculated. In the regions where the current density is zero, the magnetic field was defined in terms of a scalar potential which is a solution of the Laplace's equation. The inputs for the calculation were the shape of the SKS coil and yoke from the drawings of the SKS magnet, the measured B-H curve of iron and the current distribution of coils. Figure A.4 show the B-H curve of iron. The yellow line which was made by the measured data was used for the present calculation. For comparison, the blue and red line are that of the TOSCA default and the Toshiba standard, respectively.

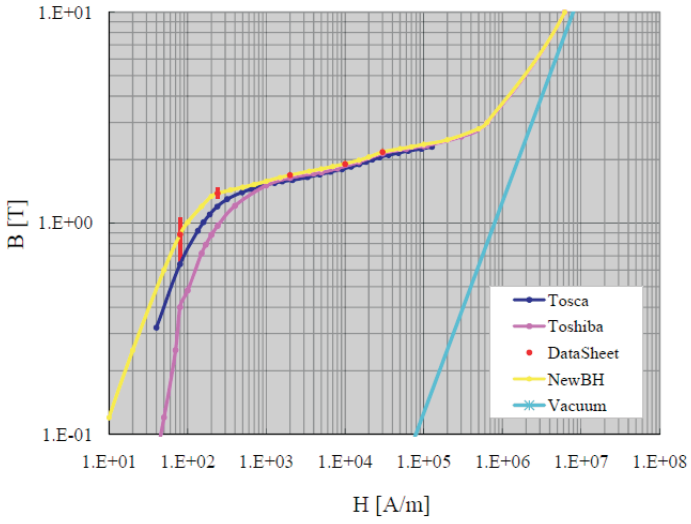

Tosca: TOSCA default iron
Toshiba: used at Toshiba
NewBH: manually generated

SKS data sheet

H [A/m]	B [T]		
	Av.	Max	Min
80	0.88	1.06	0.66
240	1.39	1.48	1.31
2000	1.69	1.71	1.66
10000	1.91	1.93	1.86
30000	2.17	2.10	2.20

Figure A.4: The B-H curve of iron of the SKS magnet. The table in the figure show the data sheet.

Figure A.5 shows the coordinate of the magnetic field map. The origin of the coordinate was arbitrarily determined in the inside of the coil. For the calculation, the half of the SKS magnet model (Z>0) divided by the mid-plane (Z=0) was the only input. The symmetry of the SKS magnet shape with respect to the Y axis as shown in Fig. A.5 was assumed.

The current distribution of the coil was divided into the LF and HF coil parts. The current values were accordingly determined by the number of the coil turns.

For the calculation, the size and shape of mesh (element) to be calculated had to be set into the ANSYS code. For the default setting, according to the input shape, the

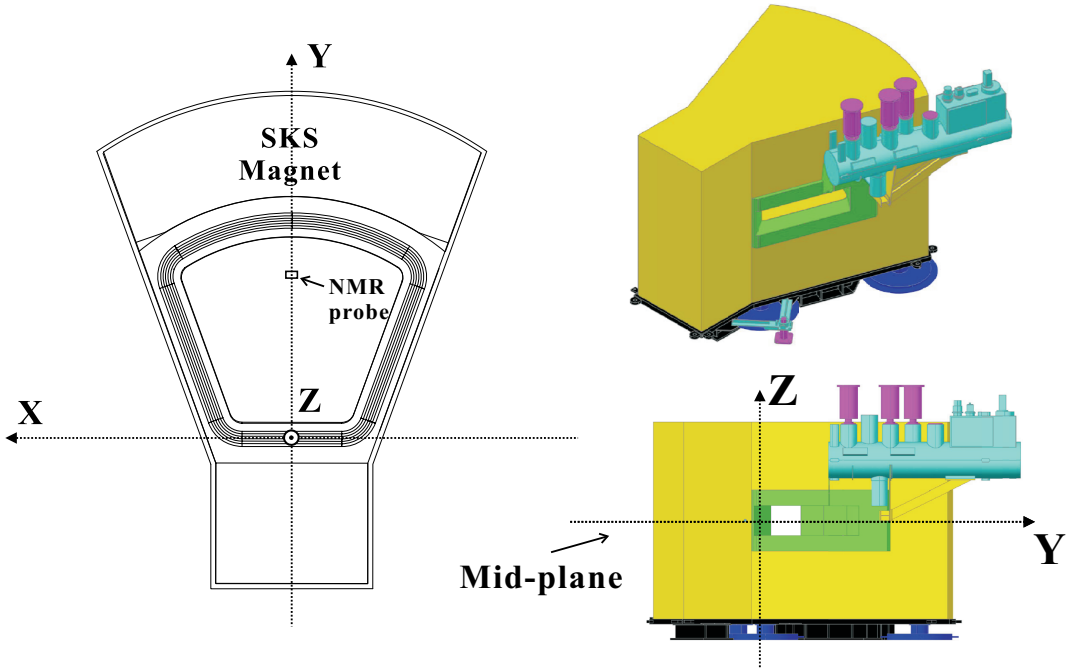

Figure A.5: The coordinate of the calculation. The NMR probe position is indicated in the figure.

element size and shape were automatically determined by the ANSYS code. The default element shape was regular tetrahedron (free mesh). For the SKS magnet calculation, the element shape for the important was hexahedron (mapped mesh) put by hand for the more precise calculation. This procedure was applied for yoke, gap and positions around drift chambers. The element of the other parts uses the default. The element and input region size were as small and precise as possible allowed by the computer memory, respectively.

As a boundary condition, zero magnetic field at infinity was taken. In addition, the symmetrical magnetic field points where the field element should be zero were also to be boundaries. As shown in Fig. A.5, the points along the y-axis (X=0, B_x=0) and on the mid-plane (Z=0, B_x=B_y=0) are boundaries. The scalar potential value on each mesh was calculated and the solution was obtained by satisfying the boundary condition.

The calculated map was not corrected by the measurement of the present SKS magnetic field. On the SKS pole face, the NMR probe was installed as shown in Fig. A.5. The NMR only measured the magnetic field value near the pole face (distance of $\sim$10 mm). For the momentum reconstruction, the calculated field map was normalized by using the NMR value.

Comparison with measured map

The calculated magnetic field map was compared to the measured one. The full SKS coil was used and the calculated magnetic field was 2.2 T. Figure A.6 shows one of the result of the field map calculation. In the top figure, the difference (ΔB_z) of the magnetic field value of z-direction between the measured and calculated map are shown. The compared region was indicated in the bottom figure (x=0, z=0). For the tuned calculation (b), the difference of the uniform region (the center of the SKS pole) was $\sim 10^{-3}$ T, while in the region near the SKS coil, it was more than 0.01 T. Similarly, the fringing field region and the region close to the SKS pole edge were worse than that of the central region. They correspond to the regions where the efficiency of the SKS tracking dropped.

Figure A.7 shows the difference (ΔB_z) along the central track. The absolute value of the difference was similar to the compared region in Fig. A.6. In particular, the ΔB_z values around the coil were worse that of the uniform region. The asymmetry along the path was due to that of the measured field map.

The several magnetic field maps were calculated by changing input parameters, different B-H curves (measured or ANSYS default curve), the default and the shifted coil position ($\pm$10 mm to z-direction), the smaller and larger coil shape ($\pm$10 mm) for considering the reduction and expansion of the coil by the magnetic force. However, the accuracy and the shape of the magnetic field were not drastically improved. In addition, the improvement by charging the mesh was not also drastic. The accuracy of the magnetic filed was partially achieved in the uniform region to the previous value of 1.4×10^{-3}(FWHM), while the fringing field region and the region close to the SKS pole edge and coil were worse. The difference of the accuracy makes the position dependence of the central value of the momentum as described in Sec. 3.10. The beam through data (Sec. 3.10.) shows that the sum of the momentum resolution ($\sigma_{\Delta p} = (\sigma_{SKS}^2 + \sigma_{K1.8}^2)^{1/2}$) was 2.0×10^{-3}(FWHM). Since the resolution was determined by the magnetic field of the uniform region which had a larger BL, the effect of the inaccurate region near the SKS coil was small for the beam-through data.

The accuracy of the calculated field map was an order of 10^{-3} for the uniform region, while the region near the SKS coil, the fringing field region and the region close to the SKS pole edge were more than 10^{-2}. Due to the saturation of iron, the magnetic field calculation of the worse accuracy regions were quite difficult. We need a further study or the re-measurement of magnetic field measurement for improvement.

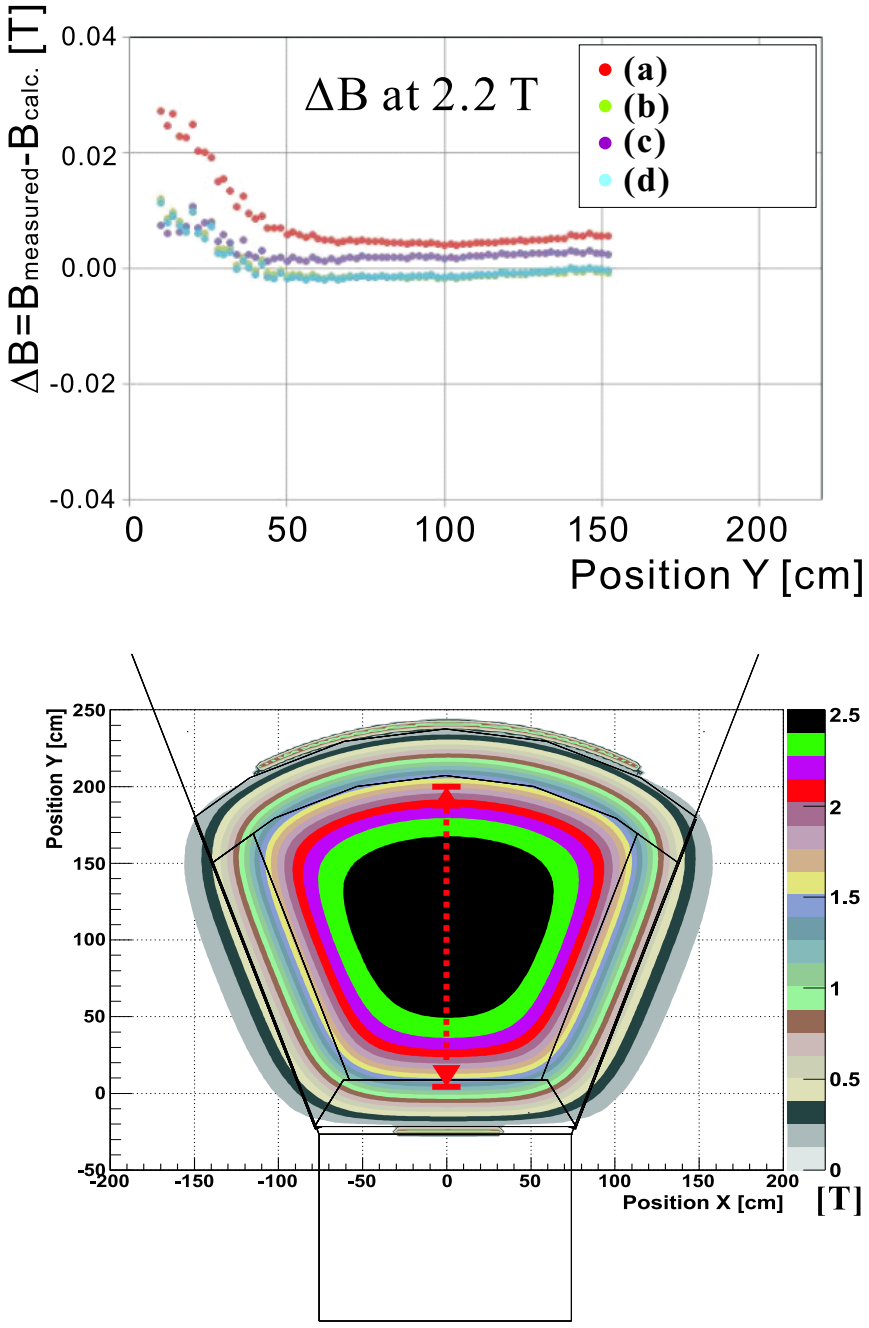

Figure A.6: The difference of the magnetic field value (ΔB) between the measured map and the several calculated maps (top) and the distribution of the calculated magnetic field (z component) of 2.2 T (bottom). The points in different colors in the top figure correspond to the calculated maps with different calculating condition. (a) The result of the first calculation including the bag of the input parameters, (b) that of the calculation with the finalized parameters, (c) that of the 10-mm smaller coil shape to the inner size, and (d) that of the bag of (a) corrected. The compared region was indicated in the bottom figure (x=0, z=0).

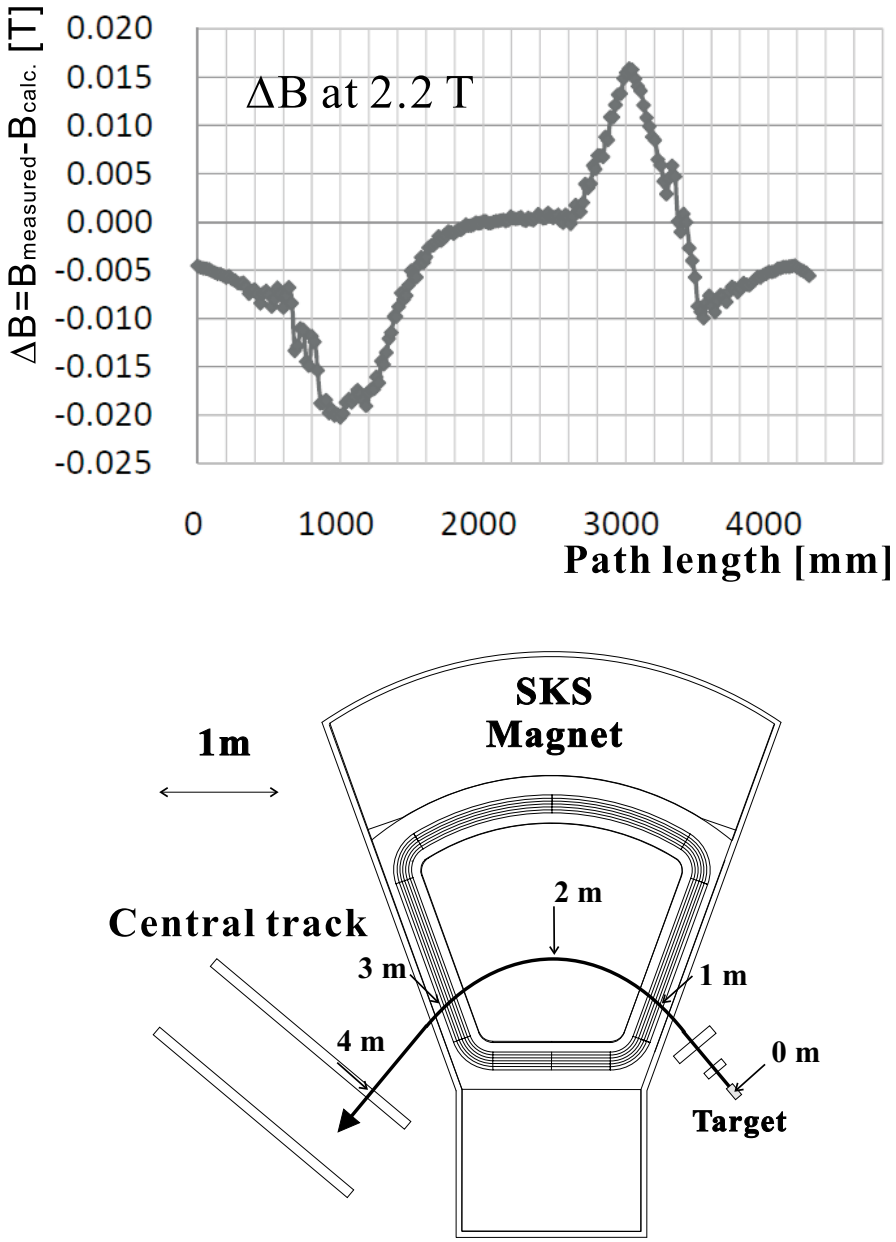

Figure A.7: The difference of the magnetic field value (ΔB) between the measured and calculated map along the central track (top). The central track and the position of the path are shown and indicated in the bottom figure.

Appendix B

Efficiency time dependence

The time dependence of efficiency was checked during the Θ^+ production run. The data are arbitrarily selected at every 4∼6 hour. The horizontal axis of all spectrum indicates order in which the data were taken. Actual time laps between data point denoted as ΔT($\sim$ 5 hours) is about 5 hours. The first half is from the 1st Θ^+ production run (1−13) and the later half from the 2nd run (21−34).

Beam

Beam intensity

The beam intensity was adjusted to be 1 M/spill. Figure B.1 shows the average of beam intensity of one run during the Θ^+ production run. The beam intensity fluctuated by $\pm$5%.

Beam accidental rate

The accidental coincidence rate (f_{acc}) between BH1 and BH2 during the Θ^+ production run was shown in Fig. B.2. The accidental rate was changed between the 1st and 2nd run due to the accelerator condition.

Horizontal and vertical beam position

The horizontal (X) and vertical (Y) beam position during the Θ^+ production run was shown in Fig. B.3 and Fig. B.4, respectively. The beam position was changed accordingly by beam tuning. The shift of the beam positions was acceptable because the beam profile was much smaller than the target size.

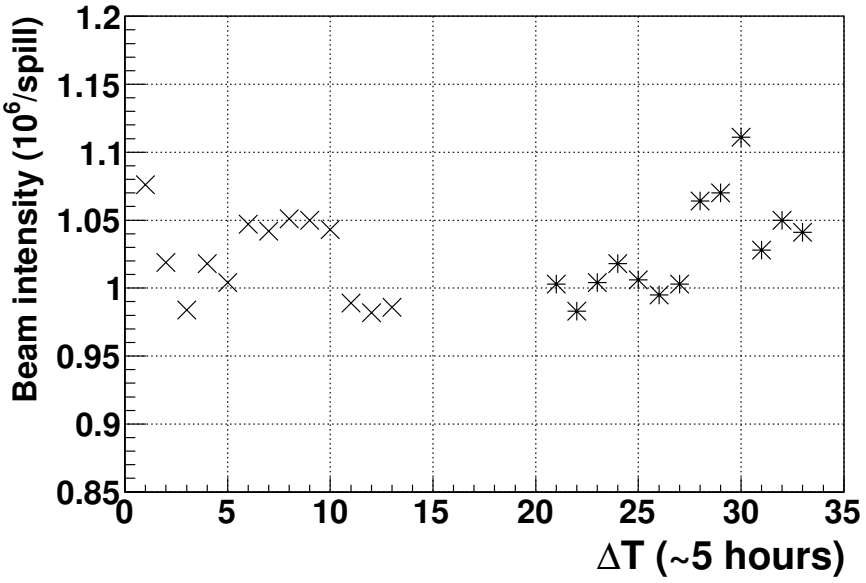

Figure B.1: The beam intensity during the Θ^+ production run. The value of the 1st and 2nd run are shown in cross and star, respectively.

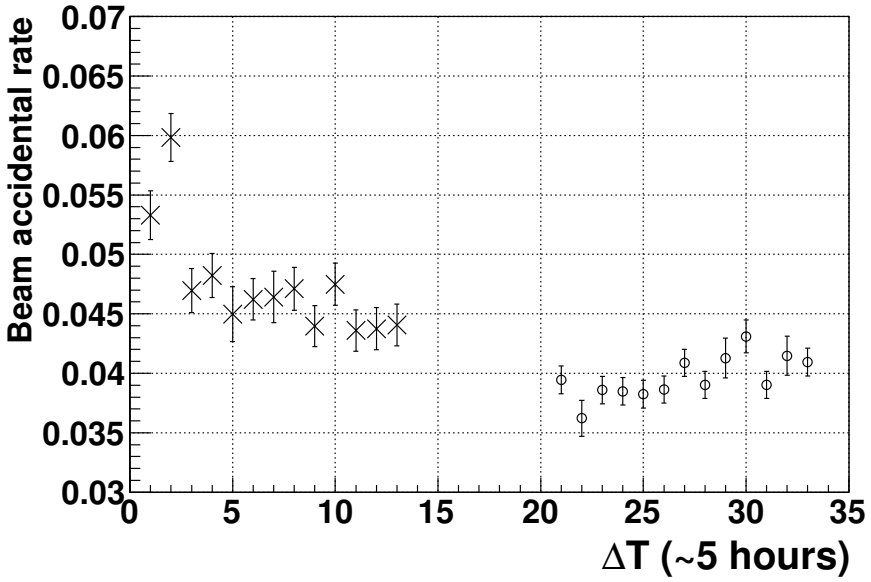

Figure B.2: The beam accidental coincidence rate during the Θ^+ production run. The value of the 1st and 2nd run are shown in cross and open circle, respectively.

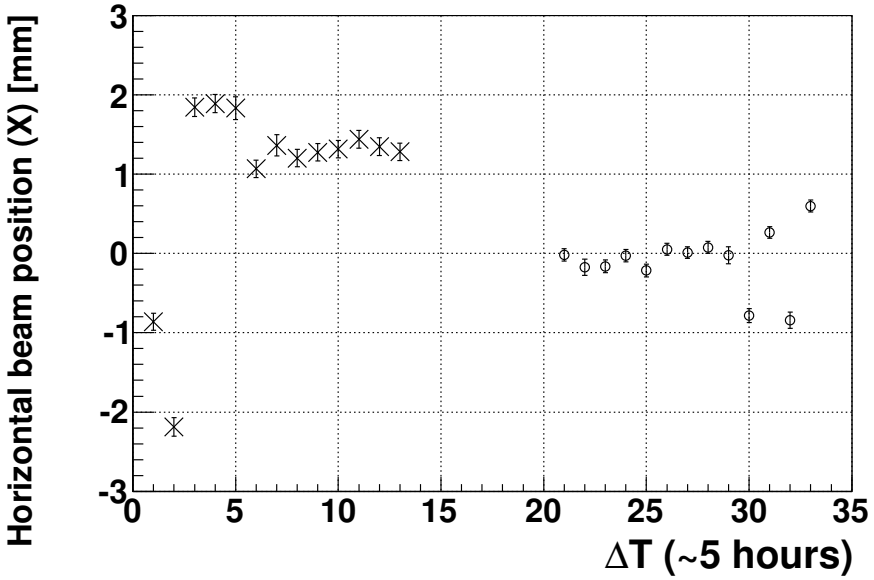

Figure B.3: The horizontal (X) beam position during the Θ^+ production run.

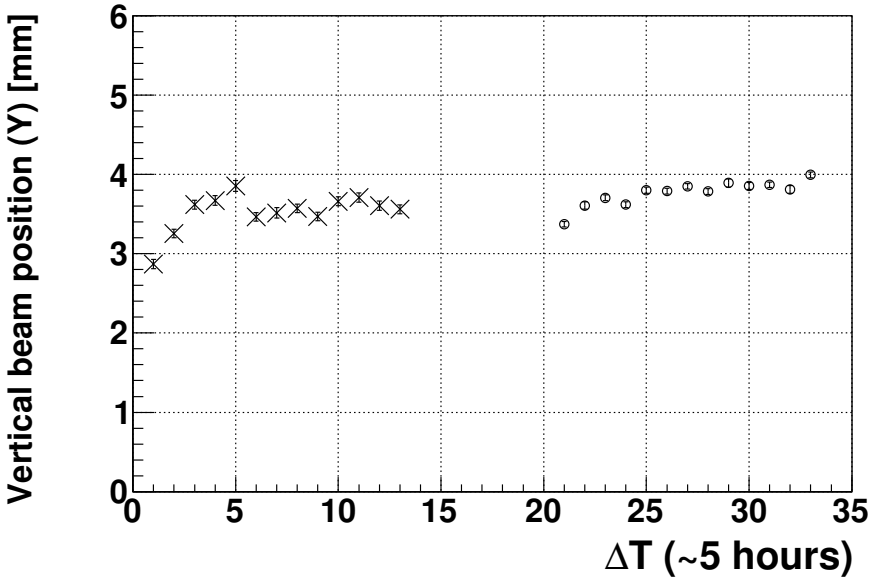

Figure B.4: The vertical (Y) beam position during the Θ^+ production run.

Chamber and tracking

The chamber efficiency was included the detection efficiency and the analysis efficiency to find a good track as described in Sec 3.5. All chamber were installed in the air conditioning house where the temperature was be maintained constant ($\sim 20°$C).

BC1·2 efficiency

Figure B.5 shows the average of the BC1·2 efficiency of one run during the Θ^+ production run. In the beginning of the 1st run, we searched for the available beam rate and the high voltage condition of the BC1·2. Thus, the efficiency was largely fluctuated. The run in which the efficiency was dropped was due to the accidental stop of the gas follow.

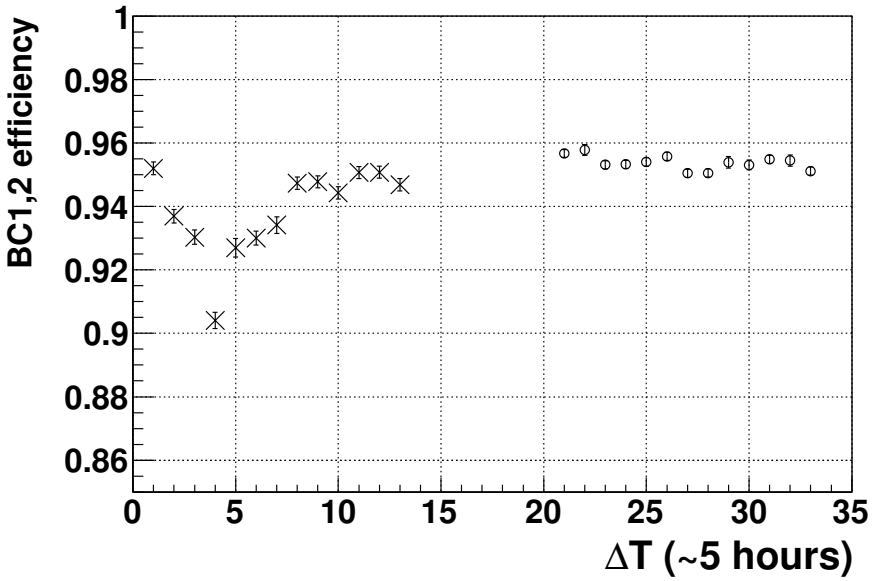

Figure B.5: The BC1·2 efficiency during the Θ^+ production run. The value of the 1st and 2nd run are shown in cross and open circle, respectively.

BC3·4 efficiency

Figure B.6 shows the average of the BC3·4 efficiency of one run during the Θ^+ production run. The efficiency was quite stable.

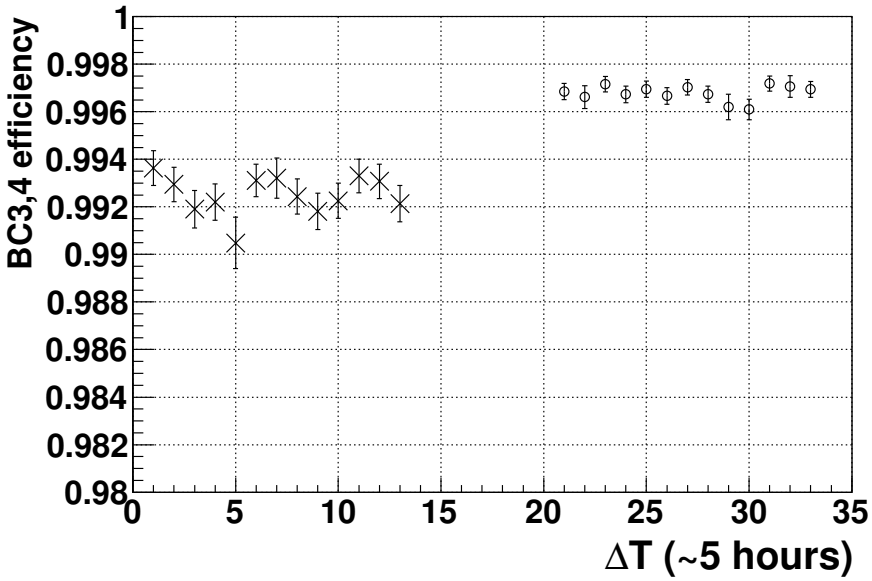

Figure B.6: The BC3·4 efficiency during the Θ^+ production run. The value of the 1st and 2nd run are shown in cross and open circle, respectively.

Beam line tracking efficiency

Figure B.7 shows the average of the K1.8 beam line tracking efficiency of one run during the Θ^+ production run. At the beginning of the 1st run, the efficiency BC1·2 was quite unstable. Thus, we searched for the available beam rate by changing the beam line magnet setting in order to defocus the beam profile at the BC1·2 position. After tuning magnets, the BC1·2 worked with 10% more beam intensity, but the defocussing of the beam caused the 5% efficiency drop of the beam line tracking becase the $\chi^2_{K1.8}$ became worse.

Single beam track efficiency

Figure B.7 shows the average of single beam track efficiency of one run during the Θ^+ production run. After tuning magnets for the stable operation for BC1·2, we found that the multi-track events were increased.

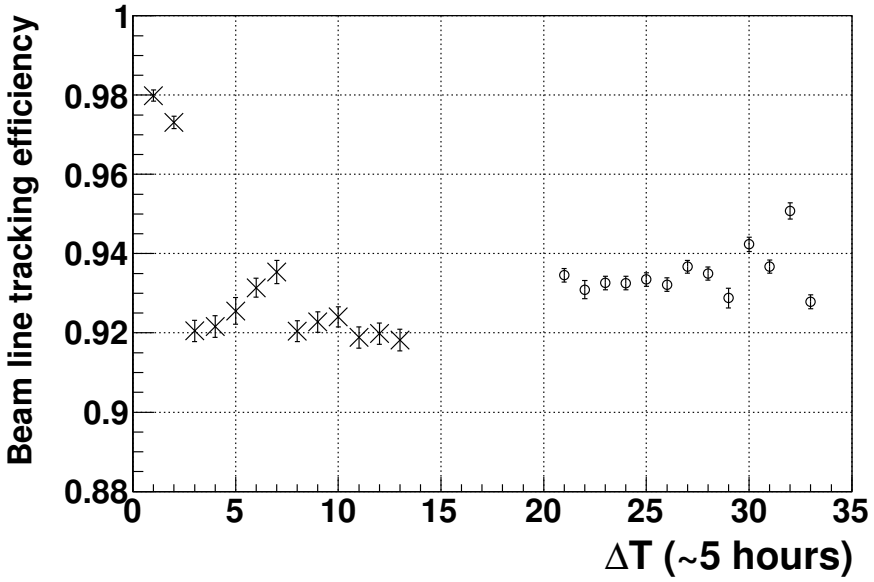

Figure B.7: The K1.8 beam line tracking efficiency during the Θ^+ production run. The value of the 1st and 2nd run are shown in cross and open circle, respectively.

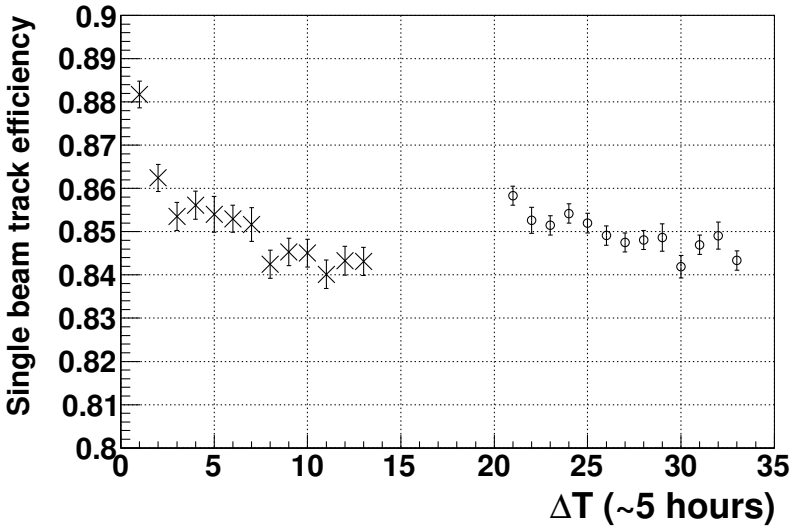

Figure B.8: The single beam track efficiency during the Θ^+ production run. The value of the 1st and 2nd run are shown in cross and open circle, respectively.

SDC1·2 efficiency

Figure B.9 shows the average of the SDC1·2 efficiency of one run during the Θ^+ production run. The efficiency was quite stable.

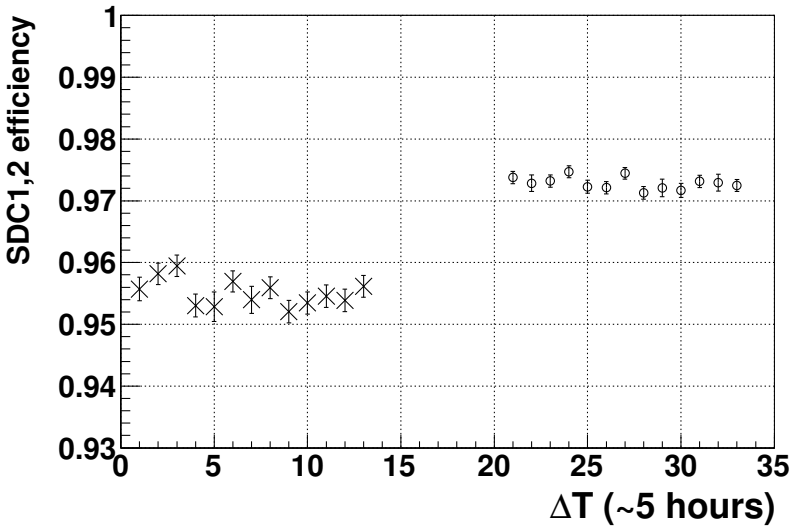

Figure B.9: The SDC1·2 efficiency during the Θ^+ production run. The value of the 1st and 2nd run are shown in cross and open circle, respectively.

SDC3·4 efficiency

Figure B.10 shows the average of the SDC3·4 efficiency of one run during the Θ^+ production run. The fluctuation of the efficiency during the Θ^+ production run was estimated by using the scattered π^- events recorded in the PIK trigger data (the $(\pi^-, \pi^-)X$ events). We selected π^- events by using the scatter plot between the horizontal scattering angle measured by SDC1·2 and the flight time between BH2 and TOF as described in Sec 3.5. The efficiency was quite stable.

The SKS tracking efficiency

The SKS tracking efficiency can not be estimated by using the the scattered π^- events recorded in the PIK trigger data (the $(\pi^-, \pi^-)X$ events). In the case of the the SDC3·4 tracking, scattered particles which decay in-flight before reaching the SKS down stream detectors make the straight track and the local track can be found by the SDC3·4 tracking. On the other hand, those decay events can not be reconstructed by the SKS tracking because the trajectory is largely changed by the decay. In addition, the background events which are generated at the SKS coil vessel also make $(\pi^-, \pi^-)X$ events. Similarly, those events can not be reconstructed by the SKS tracking. The ratio was changed according to the number of beam hitting the coil vessel. Thus, the efficiency cannot be defined for the SKS tracking. Since the efficiencies of the SDC1·2 and SDC3·4 local

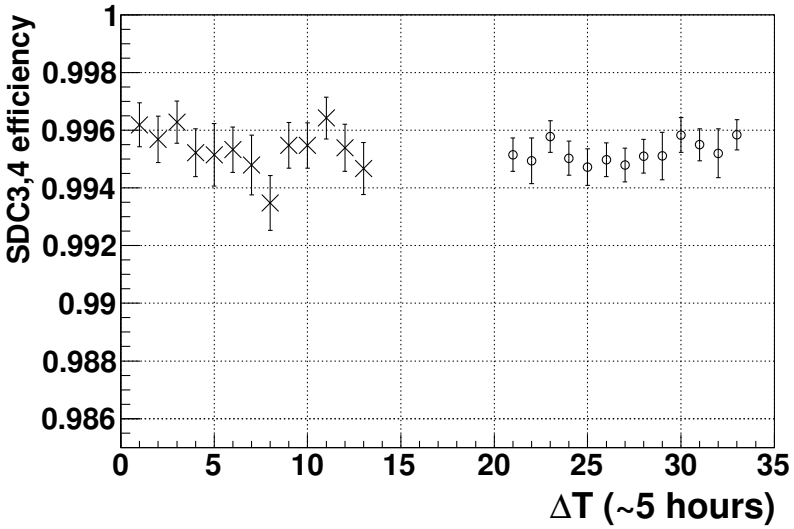

Figure B.10: The SDC3·4 efficiency during the Θ^+ production run. The value of the 1st and 2nd run are shown in cross and open circle, respectively.

tracking and the monitored magnetic field fluctuation ($\sim 10^{-4}$) are quite stable, the SKS tracking efficiency might be stable.

Trigger counter

Figure B.11, B.12, B.13, B.14, B.15 and B.16 show the time dependence of mean value and width of the pedestal, and the ADC gain (normalized value or most probable peak) of one of those counters. The pedestal information which indicates the noise level is one of the important one for the stable operation for the trigger counters. Since the GC signal was always used to be veto, the raw ADC signal in the proper π timing was not taken during the production run. BH2, TOF, AC, TOF and LC were installed in the air conditioning house where the temperature was be maintained constant ($\sim$ 20°C). GC and BH1 were installed outside of the house. The temperature was also stable during the beam time (15$\sim$ 20°C). Those histograms show one of the counter's channel, but all channel are also stable during the the Θ^+ production run.

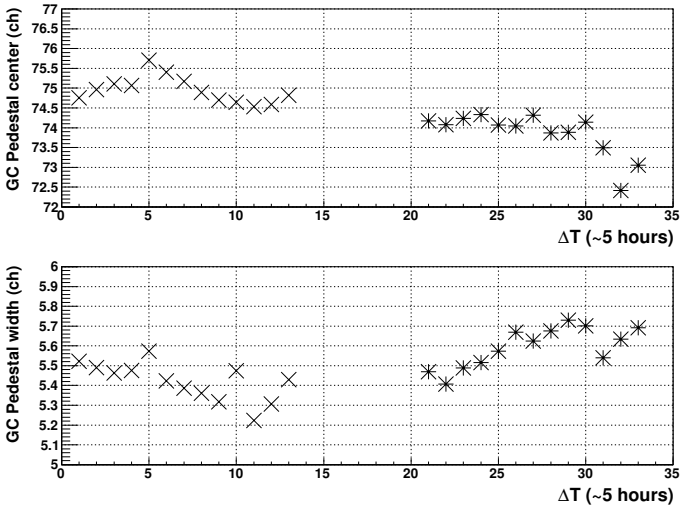

Figure B.11: The mean value and width of the pedestal of GC during the Θ^+ production run.

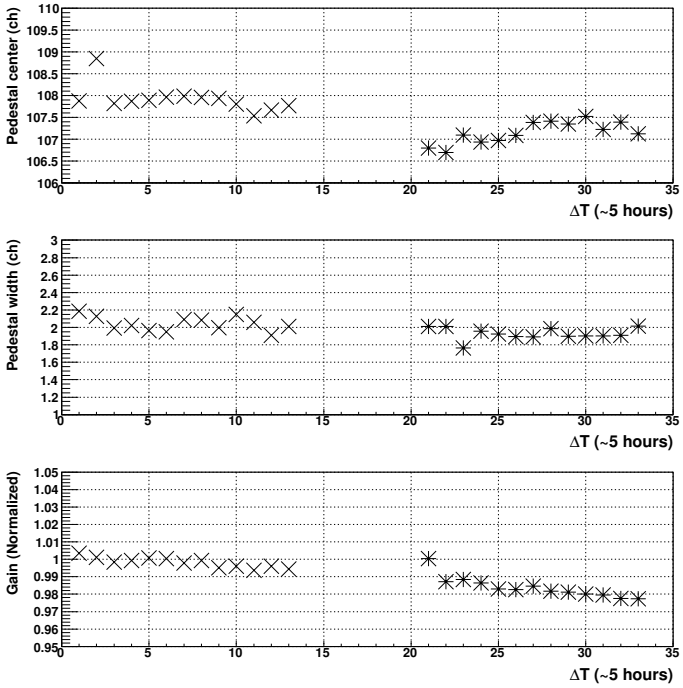

Figure B.12: The mean value and width of the pedestal, and the ADC gain of BH1 during the Θ^+ production run.

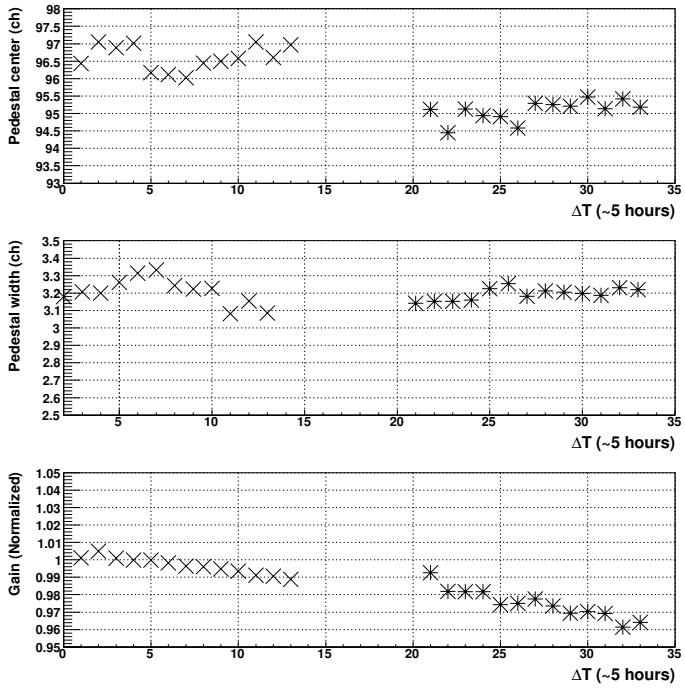

Figure B.13: The mean value and width of the pedestal, and the ADC gain of BH2 during the Θ^+ production run.

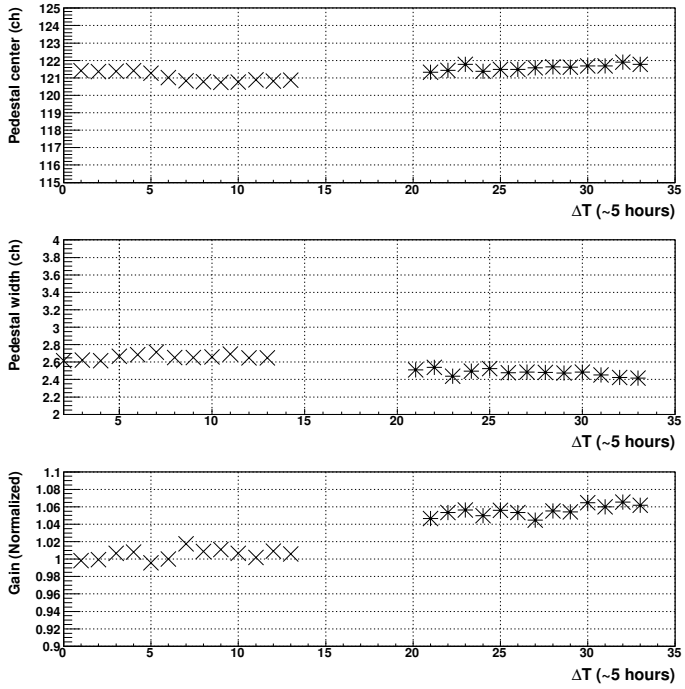

Figure B.14: The mean value and width of the pedestal, and the ADC gain of TOF during the Θ^+ production run.

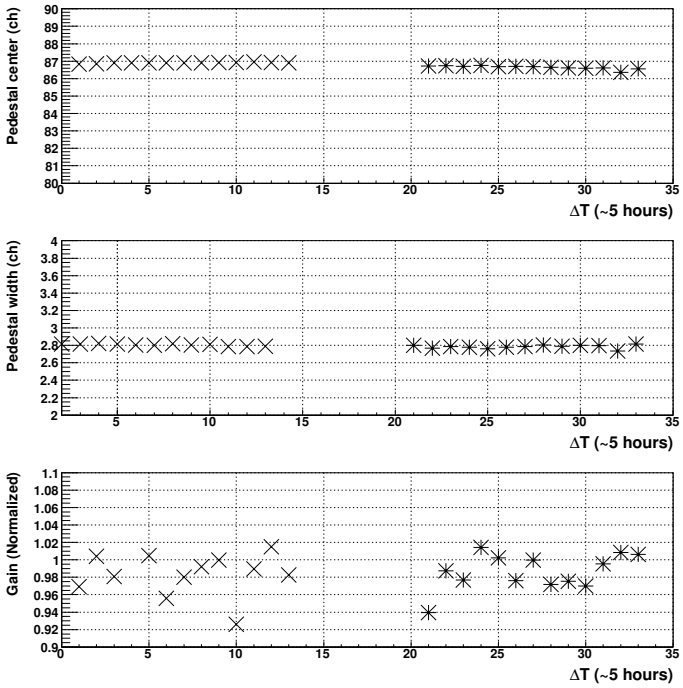

Figure B.15: The mean value and width of the pedestal, and the ADC gain of AC during the Θ^+ production run.

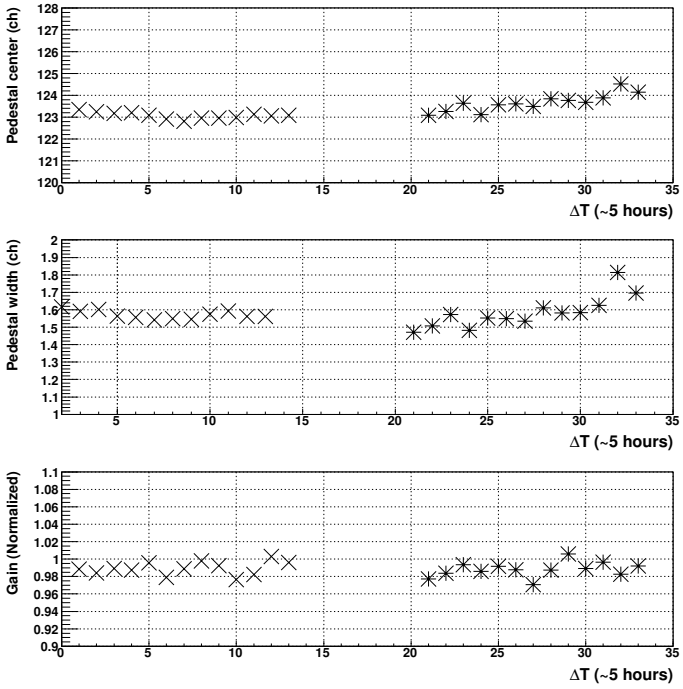

Figure B.16: The mean value and width of the pedestal, and the ADC gain of LC during the Θ^+ production run.

Bibliography

[1] R. L. Jaffe, Proc. Topical Conference on Baryon Resonances, Oxford, July 1976, SLAC-PUB-1774.

[2] S.-K. Choi *et al.*, Phys. Rev. Lett. **100**, 142001 (2008).

[3] D. Diakonov, V. Petrov, M. Polyakov, Z. Phys. A **359**, 305 (1997).

[4] T. Nakano *et al.*, Phys. Rev. Lett. **91**, 012002 (2003).

[5] R. Jaffe, F. Wilczek, Phys. Rev. Lett. **91**, 232003 (2003).

[6] T. Nakano *et al.*, Phys. Rev. C. **79**, 025210 (2009).

[7] DIANA Collaboration, V. V. Barmin *et al.*, Phys. Atom. Nucl. **66**, 1715 (2003).

[8] DIANA Collaboration, V. V. Barmin *et al.*, Phys. Atom. Nucl. **73**, 1168 (2010).

[9] CLAS Collaboration, S. Stepanyan *et al.*, Phys. Rev. Lett **91**, 252001 (2003).

[10] CLAS Collaboration, V. Kubarovsky *et al.*, Phys. Rev. Lett **92**, 032001 (2004).

[11] SAPHIR Collaboration, J. Barth *et al.*, Phys. Lett. B **572**, 127 (2003).

[12] A. E. Asratayn, A. G. Dolgolenko and M. A. Kubantsev, Phys. Atom. Nucl. **67**, 682 (2004).

[13] HERMES Collaboration, A. Airapetian *et al.*, Phys. Lett. B **585**, 213 (2004).

[14] COSY-TOF Collaboration, M. Abdel-Bary *et al.*, Phys. Lett. B **595**, 127 (2004).

[15] ZEUS Collaboration, S. Chekanov *et al.*, Phys. Lett. B **591**, 7 (2004).

[16] NOMAD Collaboration, L. Camilleri *et al.*, Nucl. Phys. B **143**, 129 (2005).

[17] SVD Collaboration, A. Aleev *et al.*, arXiv:hep-ex/0401024.

[18] SVD Collaboration, A. Aleev *et al.*, arXiv:hep-ex/0509033.

[19] BES Collaboration, J. Z. Bai *et al.*, Phys. Rev. D **70**, 012004 (2004).

[20] ALEPH Collaboration, S. Schael *et al.*, Phys. Lett. B **599**, 1 (2004).

[21] BABAR Collaboration, B. Aubert *et al.*, hep-ex/0502004.

[22] BABAR Collaboration, K. Goetzen *et al.*, Nucl. Phys. (Proc. Suppl.) **164**, 117 (2007).

[23] Belle Collaboration, K. Abe *et al.*, hep-ex/0409010.

[24] Belle Collaboration, R. Mizuk *et al.*, hep-ex/0411005.

[25] CDF Collaboration, D. O. Litvintsev *et al.*, Nucl. Phys. B (Proc. Suppl.) **142**, 374 (2005).

[26] SPHINX Collaboration, Yu. M. Antipov *et al.*, Eur. Phys. J. **A21**, 455 (2004).

[27] HERA-B Collaboration, I. Abt *et al.*, Phys. Rev. Lett **93**, 212003 (2004).

[28] Hyper-CP Collaboration, M. J. Longo *et al.*, Phys. Rev. D **70**, 111101(R) (2004).

[29] FOCUS Collaboration, J. M. Link *et al.*, Phys. Lett. B **639**, 604 (2006).

[30] PHENIX Collaboration, C. Pinkenburg *et al.*, J. Phys. G **30**:S1201 (2004).

[31] WA89 Collaboration, M. I. Adamovich *et al.*, Phys. Rev. C **72**, 055201 (2005).

[32] CLAS Collaboration, M. Battaglieri *et al.*, Phys. Rev. Lett **96**, 042001 (2006).

[33] CLAS Collaboration, B. McKinnon *et al.*, Phys. Rev. Lett **96**, 212001 (2006).

[34] CLAS Collaboration, S. Niccolai *et al.*, Phys. Rev. Lett **97**, 032001 (2006).

[35] COSY-TOF Collaboration, M. Abdel-Bary *et al.*, Phys. Lett. B **649**, 252 (2007).

[36] NOMAD Collaboration, O. Samoylov *et al.*, Eur. Phys. J.C **49**, 499 (2007).

[37] A. I. Titov, A. Hosaka, S. Date, Y. Ohahi, Phys. Rev. C **70**, 042202 (2004).

[38] Y. Oh, H. Kim, and S. H. Lee, Phys. Rev. D **69**, 014009 (2004).

[39] Y. Oh, H. Kim, and S. H. Lee, Phys. Rev. D **69**, 074016 (2004).

[40] C. M. Ko and W. Liu, nucl-th/0410068.

[41] K. Miwa *et al.*, Phys. Lett. B **635**, 72 (2006).

[42] K. Miwa *et al.*, Phys. Rev. C **77**, 045203 (2008).

[43] T. Hyodo, and A. Hosaka, Phys. Rev. C **72**, 055202 (2005).

[44] M. Naruki *et al.*, J-PARC Proposal E19, "High-resolution search of Θ^+ pentaquark in $\pi^- p \to K^- X$ reactions" (2006).

[45] K. H. Tanaka *et al.*, The technical report of the hadron experimetal facility, KEK internal 2007-1.

[46] K. L. Brown *et al.*, CERN 80-04 (1980).

[47] H. Hotchi et al., Phys. Rev. C **64**, 044302 (2001).

[48] T. Takahashi et al., Nucl. Phys. A **835**, 88 (2010).

[49] Digital Teslameter 151 (DTM-151), http://www.group3technology.com/meters/dtm151.php

[50] S. Adachi, Master Thesis of Graduate school, Kyoto University (2009).

[51] O. Sasaki and M. Yoshida, IEEE Trans. Nucl. Sci., vol **46**, 1871 (1999).

[52] EFM-3000AX, "http://echo-denshi.co.jp/nmr_magnetic.htm"

[53] http://lambda.phys.tohoku.ac.jp/ takahasi/TUL-8040/.

[54] Y. Igarashi IEEE Trans. Nucl. Sci., vol **52**, 2866 (2005).

[55] Y. Igarashi IEEE Trans. Nucl. Sci., vol **57**, 618 (2010).

[56] S. Agostinelli *et al.*, Nucl. Instrum. Methods. A **506**, 250 (2003).

[57] S. Morinobu, privete communication.

[58] J. Myrheim and L. Bugge, Nucl. Instr. Meth. **160**, 43 (1979).

[59] K.L. Brown, Ch. Iselin, D.C. Carey: Decay Turtle, CERN 74-2 (1974), Urs Rohrer: Compendium of Decay Turtle Enhancements.

[60] T. Hasegawa, Doctor Thesis of Graduate school, University of Tokyo, INS-IM-15 (1994).

[61] H. Courant *et al.*, Phys. Rev. D **16**, 1 (1977).

[62] O. I. Dahl *et al.*, Phys. Rev. B **163**, 1377 (1967).

[63] D. J. Candlin *et al.*, Nucl. Phys. B **226**, 1 (1983).

[64] M. L. Good and R. R. Kofler, Phys. Rev. **183**, 1148 (1969).

[65] K. Nakamura *et al.*, (Particle Data Group), J. Phys. G **37**, 075021 (2010).